(2)

Analytical Methods Report 8903

THE APPLICATION OF ADVANCED PANEL METHODS TO PROPELLER/HULL CONFIGURATIONS

FINAL REPORT
Contract N00014-86-C-0474 December 1990

Analytical Methods Report 8903

THE APPLICATION OF ADVANCED PANEL METHODS TO PROPELLER/HULL INTERACTION

FINAL REPORT

Prepared for:

Office of Naval Research
800 North Quincy
Arlington, Virginia 22217

by:

Analytical Methods, Inc.
2133 - 152nd Avenue N.E.
Redmond, Washington 98052
(206) 643-9090

Under Contract N00014-86-C-0474

December 1990

TABLE OF CONTENTS

Section			Page No.
LIST OF FIGURES			ii
1.0	INTRODUCTION		1
2.0	PROPELLER ANALYSIS		3
	2.1	Uniform Flow	6
	2.2	Nonuniform Inflow	8
		2.2.1 Comparison with Exact Solution	8
3.0	HUB AND SHROUD INTERACTION		
	3.1	Basic Modeling	16
	3.2	Applications	25
4.0	ISOLATED HULL ANALYSIS		45
	4.1	Potential Flow	45
	4.2	Viscous Flow	49]
5.0	PROPELLER-HULL INTERACTION		53
	5.1	Technical Approach	53
	5.2	Frequency Band Analysis	54
	5.3	Time-Dependent Analysis	
		5.3.2 Method Outline	57
		5.3.3 Method Formulation	58
6.0	DISCUSSION OF RESULTS		65
	6.1	Propeller in Uniform Flow	65
	6.2	Propellers in Simple Nonuniform Flow	85
	6.3	Propeller in Fully Nonuniform Flow	85
		6.3.1 Frequency Band Analysis	85
		6.3.2 Time-Dependent Analysis	91
		6.3.2.1 Uniform Flow Analysis	91
		6.3.2.2 Nonuniform Flow Analysis	100
	6.4	Simple Propeller-Hull Interaction	123
7.0	CONCLUSIONS		136
8.0	REFERENCES		138

LIST OF FIGURES

Fig. No.	Title	Page No.
2.1	Two Triangles in Version C.0 Wake Panels	7
2.2	Sphere in Nonuniform Flow	7
2.3	Comparison of Velocity Potentials on a Sphere	9
2.4	Comparison of X Components of Velocity on a Sphere	10
2.5	Comparison of Total Velocity on a Sphere	11
2.6	Sphere in Nonuniform Flow	
(a)	Modeling with Option 1	13
(b)	Modeling with Option 2	14
(c)	Modeling with Option 3	15
3.1	Comparison of Measured and Predicted Boundary Layer Development on U.S. Airship Akron	26
3.2	Comparison of Measured and Predicted Boundary Layer Developments	27
3.3	Propeller-Shroud-Hub Assembly	
(a)	View Showing Tip Shroud Clearance	29
(b)	Oblique View Showing Shroud Paneling	30
3.4	Pressure Distribution on Propeller with Shroud and Hub	
(a)	Radial Location 2.2	31
(b)	Radial Location 4.4	32
(c)	Radial Location 5.5	33
3.5	Pressure Distribution in Radially Nonuniform Flow	
(a)	Radial Location, r = 2.2	34
(b)	Radial Location, r = 4.4	35
(c)	Radial Location, 4 = 5.5	36
3.6	Pressure Distribution on Hub	
(a)	Buttline Cut, Y = 0	37
(b)	Station Cut, X = 0	38
3.7	Propeller, Hub and Shroud Assembly in the Nonuniform Flow Induced by Stator, Hub and Shroud	
(a)	Radius, r = 2.2	39
(b)	Radius, r = 4.4	40
3.8	Stator, Hub and Shroud Assembly	
(a)	Axial View	41
(b)	Oblique View Showing Wake	42

LIST OF FIGURES

Fig. No.	Title	Page No.
3.9	Pressure Distribution on Stator Section	43
3.10	Velocity Scan Data Showing Flow Nonuniformity	44
4.1	Airship Akron Boundary Layer Characteristics Correlated with Experiment	
(a)	Momentum Thickness before Changes to MPROP	46
(b)	Momentum Thickness after Changes to MPROP	46
4.2	Experimental Correlation of Boundary Layer Characteristics	
(a)	Boundary Layer Thickness before Changes to MPROP	47
(b)	Boundary Layer Thickness after Changes to MPROP	47
4.3	Velocity Profile Inside Boundary Layer Correlated with Experiment	48
4.4	The Axisymmetric Afterbodies	50
4.5	Grid for Afterbody 1	
(a)	Large-Domain Grid for Afterbody 1	51
(b)	Small-Domain Grid for Afterbody 1	51
4.6	Pressure Distribution on Afterbody 1 at Re = 6.6 Million	52
5.1	General Arrangement	59
5.2	USAERO Configuration Breakdown	64
6.1	Blade Paneling and Wake. Propeller Model No. 0123, Ship Research Institute, Tokyo, Japan (40)	66
6.2	Surface Pressure Correlation on Propeller 0123 (40)	
(a)	J = V/nD = 0.9, R = 0.77R	67
(b)	J = V/nD = 0.7 , R = 0.77R	68
6.3	Hoshino Propeller Paneling for Analysis	69
6.4	Experimental Correlation, 5-Bladed Hoshino Propeller; Advance Ratio = 0.7, R = 11.80	70
6.5	Experimental Correlation, 5-Bladed Hoshino Propeller; Advance Ratio = 0.7, R = 10.05	71
6.6	Hoshino Propeller Experimental Correlation; Advance Coefficient = 0.5, R = 11.80	72
6.7	Hoshino Propeller Experimental Correlation; Advance Coefficient = 0.5, R = 10.05	73

LIST OF FIGURES

Fig. No.	Title	Page No.
6.8	Hoshino Propeller Experimental Correlation; Advance Coefficient = 0.3 (Off Design), R = 11.80	74
6.9	Hoshino Propeller Experimental Correlation; Advance Coefficient = 0.3 (Off Design), R = 10.05	75
6.10	van Gent 4-Bladed Propeller Paneled for Analysis	76
6.11	Experimental Correlation for van gent Propeller at Radial Section, R = 10.19, Advance Coefficient = .4	77
6.12	Experimental Correlation for van gent Propeller at Radial Section, R = 12.20, Advance Coefficient = .4	78
6.13	Experimental Correlation for van gent Propeller at Radial Section, R = 14.50, Advance Coefficient = .4	79
6.14	Experimental Correlation for van gent Propeller at Radial Section, R = 19.40, Advance Coefficient = .4	80
6.15	Experimental Correlation for van gent Propeller at Radial Section, R = 10.19, Advance Coefficient = .4	81
6.16	Experimental Correlation for van gent Propeller at Radial Section, R = 12.20, Advance Coefficient = .4	82
6.17	Experimental Correlation for van gent Propeller at Radial Section, R = 14.50, Advance Coefficient = .6	83
6.18	Experimental Correlation for van gent Propeller at Radial Section, R = 19.40, Advance Coefficient = .6	84
6.19	Propeller with a Skew of 72° in Uniform Flow	86
6.20	Cp Distribution on Blade Section at R = 4.4	
(a)	Uniform Flow	87
(b)	Radially Nonuniform Flow	88
6.21	Wake Fractions, Reproduced from Ref. 40	89
6.22	Pressure Correlation on a 6-Bladed Propeller in Nonuniform Wake; r = 0.77R, x/c = 0.2, Suction Side	90
6.23	Wake Fraction Contours for nonuniform Inflow, Reproduced from Ref. 42	92
6.24	Comparison between 8-Term Solution and Experiment (42) .	93

LIST OF FIGURES

Fig. No.	Title	Page No.
6.25	USAERO Paneling for the SRI-MP0123 6-Bladed Propeller . .	94
6.26	USAERO Calculations for the SRI MP 0123 6-Bladed Propeller in Uniform Flow at J = .7	
(a)	General View Showing Computed Wake and Spectrum Plot of Surface Pressure (Hydrostatic Term Included)	95
(b)	Buttline Cut through Wake	96
(c)	Station Cut One Diameter Downstream from Propeller . . .	97
(d)	Time History of CD and CMX	98
(e)	Comparison of Calculated and Measured Thrust and Torque Coefficients	99
(f)	Comparison of Calculated and Measured Pressure Distribution at 0.77 Radius at J = 0.7	101
(g)	Comparison of Calculated and Measured Chordwise Pressure Distribution at .77 Radius for J = 0.9	102
(h)	Comparison of Calculated and Measured Chordwise Pressure Distribution at 0.77 Radius at J = 1.1	103
6.27	Resulting Onset Flow Computed on a 1.2 D Disc Just Up-Stream of Propeller	104
6.28	General View of the MP0123 Propeller in Nonuniform Flow Showing USAERO Computed Surface Pressure Distribution . .	105
6.29	Waterline Cuts through the Blades and Local Wake	
(a)	Z/R = 0.24	107
(b)	Z/R = 0.56	108
6.30	Details of the Computed Pressure Distribution near the Blade Root	109
6.31	Computed Chordwise Pressure Distribution at .77R at Various Azimuthal Stations	
(a)	0° (Top)	110
(b)	90° (Side)	111
(c)	180° (Bottom)	112
(d)	270° (Side)	113
6.32	Comparison of Calculated and Measured Pressure Histories--Time-Dependent Analysis	
(a)	Position A	114
(b)	Position B	115
(c)	Position C	116
(d)	Position D	117
(e)	Position E	118
6.33	Details of the Pressure History Terms	
(a)	Position A	120
(b)	Position D	121

LIST OF FIGURES

Fig. No.	Title	Page No.
6.34	Computed Phasing of the Pressure Terms Relative to the Onset Flow Variation	122
6.35	Propeller/Hull Arrangement for Propeller-Hull Interaction	124
6.36	Axial Velocity Distribution in the Plane of the Propeller Calculated by RANSTERN; Re = 4.56 Million	125
6.37	Propeller Pressure Contours Calculated by MPROP to Highlight Viscous Hull Interaction	
(a)	No Hull; J = 0.4, Suction Side	126
(b)	No Hull; J = 0.4, Pressure Side	127
(c)	Full Hull; J = 0.4, Suction Side	128
(d)	Full Hull; J = 0.4, Pressure Side	129
(e)	Slender Hull; J = 0.4, Suction Side	130
(f)	Slender Hull; J = 0.4, Pressure Side	131
(g)	No Hull; J = 0.6, Suction Side	132
(h)	No Hull; J = 0.6, Pressure Side	133
(i)	Full Hull; J = 0.6, Suction Side	134
(j)	Full Hull; J = 0.6, Pressure Side	135

1.0 INTRODUCTION

Propeller-hull interaction arises in two related but distinct ways. Unsteady forces and moments developed by the propeller operating in the spatially nonuniform hull wake and transmitted to the hull through the propeller shafting are known as bearing forces. Periodic pressure forces induced on the hull due to the hydrodynamic action of unsteady propeller velocity and pressure field are termed surface forces. The increase of shaft output power and restrictive profile of current single-screw designs give rise to vibration and noise problems. In the past, propeller-induced ship hull vibration has been handled primarily as in-service engineering modifications. Recently, however, many articles have appeared on the topic of ship vibration and noise arising from pressure excitation (1), (2). A fund of theoretical knowledge on the various hydrodynamic aspects of the interaction problem has emerged from the collective works of groups of investigators such as Breslin et al. (3), Cox et al. (4), Kaplan (5), Noordzij (6), Huse (7) and others. In spite of these advances in the understanding of the flow, there is no satisfactory answer to the question of whether some particular wake, together with a given propeller configuration, will cause vibration problems at a given speed.

Briefly, lifting surface methods have been developed to calculate the unsteady flow field around an isolated propeller operating in the prescribed velocity field of the hull wake (8) and (9). The introduction of the hull into the known flow field of the propeller results in a time-dependent boundary condition on the hull surface which must be satisfied by placing time-dependent singularities on the hull surface. The force and moments on the hull follow by an application of the extended Lagally theorem. Vorus (10) has suggested an alternative to the calculation of the hull diffraction potential in the presence of the propeller onset flow. He has shown that the unsteady forces and moments on the hull can be calculated by combining the solution for the potential about a bare hull in simulated motion with the solution for the isolated propeller flow field. In both of these approaches the feedback of the hull singularities on the propeller flow field is neglected.

The mechanism producing large pressure pulse excitation involves a complicated interaction between cavitating flow over the propeller blades and rapidly changing velocities associated with nonuniform wakes. The development of methods to model the generation and volume variation of a transient cavity is an important prerequisite for calculating propeller-hull interaction. Although the methodology for calculating propeller-hull interaction in an approximate manner is available, the prediction of cavity geometry is not well developed.

The objective of the present work is to further the understanding of the propeller-hull interaction process by numerical simulation. Specifically, the aim was to couple the three-dimensional inviscid flow procedures developed at Analytical Methods, Inc. (AMI) with a companion viscous flow program at Scientific Research Associates, Inc. During the term of the contract the previously proposed investigation was revised in the light of discussions held with the Office of Naval Research. The major change proposed by the Navy was an emphasis on the hub and tip vortex modeling for a shrouded propeller in nonuniform flow without the participation of the viscous

flow program from Scientific Research Associates. The redirection of efforts at AMI lead to a comprehensive computational approach aimed at solving specific areas of concern to the Navy. Special emphasis was given to propeller analysis in prescribed hull wakes and to the solution of the complete inviscid hull interaction problem. The basic approach used a superposition of the solution for several harmonics of the prescribed nonuniform velocity distribution. This capability was developed in the program, MPROP, a marine propeller version of VSAERO. The case of a propeller in nonuniform flow was also analyzed using an existing time-dependent program, USAERO, developed at Analytical Methods, Inc. These two approaches are particularly suitable for certain types of nonuniformity of flow. The frequency-based approach provides the basic features of the interaction in a simple, cost effective way. The time-dependent solution is computationally less efficient, but it may be the only way to solve an arbitrary inflow problem; also it has the potential for a complete simultaneous analysis of the hull/propeller mutual interaction. Both these approaches have to be applied to analyze the interaction problem.

2.0 PROPELLER ANALYSIS

Predicting the performance of marine propellers, even in isolation or in the ideal conditions found in most laboratory test environments, is a challenging task. The high levels of skew and twist, the high solidity of the multi-blade configurations now being studied, and a basic inability to model leading-edge flows (important for cavitation studies) have forced the designer away from the simpler lifting line and lifting surface analyses that have laid the foundations of the theoretical understanding of propeller flows. This has led to the introduction of first generation surface singularity models where the full blade geometry, including thickness, is represented.

Even these methods were unable to properly model the flows around the blade root sections although leading-edge effects were now more correctly represented. The use of simple source or vortex-lattice models of the sections has led to problems associated with mass flow loss through the surface (leakage). This was particularly problematic when the flows were channel-like, as in the interblade passages at the roots of the blades of today's high solidity marine propellers.

They were also generally unable to allow for the mutual deformation of the blade wakes and, more importantly, although some limited representation of the tip-edge shedding was possible, they did not have the capability to model the rolling up of the edge wakes and their subsequent development over the tip surface. Finally, the ability to include any viscous flow effects was severely limited and prediction and modeling of regions of separated flow was not possible.

These problems, the poor representation of the root channel flows, the wake development and the viscous flow effects, have been resolved with a second generation panel method, program VSAERO (11) (for **V**ortex **S**eparation **AERO**dynamics). Developed originally for generalized aero-/hydrodynamic configuration modeling purposes, the program uses a compound source/doublet singularity to represent the surface and applies a Dirichlet boundary condition to solve for the unknown potential. This contrasts with earlier panel methods which applied the Neumann boundary condition to solve for a locally unknown velocity. Program VSAERO is also able to calculate the development of the wake using an iterative procedure and uses a streamline tracking calculation, together with a quasi-three-dimensional boundary layer analysis to determine the viscous flow behavior.

The program differs from other second generation panel methods (Ref. 12 is typical) in that a low-order (i.e., flat panel) representation of the surface, with all the benefits of ease of configuration assembly, has been retained. Other methods, while retaining a simple singularity model, have gone to a higher-order surface representation. This has resulted in high levels of effort to prepare the input deck even for the simple cylindrical surfaces of aircraft.

A special version of program VSAERO, named MPROP, has been developed for the marine propeller application. The major changes to the program were a move to a helical wake relaxation scheme and the addition of the blade rotations to the conventional translation motions in the original program.

In this regard, it has much in common with another special version of VSAERO developed to model hovering rotors or aircraft propellers in axial flight (13). The major difference, of course, is the geometric representation of the blades with the marine version developing the highly skewed, twisted and cambered sections found in present practice. The modeling has been updated to enforce the Kutta condition, especially for propeller shapes without a sharp trailing edge.

All of the earlier marine propeller analysis methods made some assumptions regarding the axisymmetry of the flow and here MPROP was no different. Consequently, application of the analyses was limited to uniform onset flow, flows far removed from the normal operating environment of the marine propeller.

The following assumptions are made in the analysis of bodies moving through a mass of fluid.

1. The fluid is at rest when the body is stationary.

2. The fluid boundaries are sufficiently far away from the body and their movement is negligible.

3. The fluid is homogeneous and is of uniform density.

4. The effects of viscosity are negligible everywhere except inside idealized thin layers across which the velocity potential is discontinuous.

5. The speed of motion of the body is negligible compared to the speed of sound in the fluid.

All of the above assumptions are conventional and a variety of problems important to a marine engineer can be adequately modeled within the framework of the above assumptions. Section 5 discusses how to analyze the motion of a body in a fluid which is not at rest. The modeling of the nearby boundaries is explained in Section 2.4. Section 3 deals with flow situations where the effects of viscosity may not be negligible. The fifth condition above may be relaxed provided the flow is subsonic everywhere. In other words, all steady flow problems arising in moderately subsonic speeds are included. No assumptions or approximations regarding the shape of the body are made. There are no limitations in the analysis which preclude the application of the code to blunt, abrupt, or uneven body geometry. In the case of massive flow separation, the analysis must be repeated with different parameters or with a different code as dictated by the nature of the problem. Boundary layer analysis of patches with roughness is possible. Cavitation control devices such as mass injection or suction can be modeled. The basic theory is contained in two documents already submitted to the Navy (13), (14). A brief summary is presented for completeness.

Tne velocity vector in potential flow can be expressed as the gradient of a scalar potential, ϕ. The mathematical conditions to be satisfied by ϕ are:

(a) $\nabla^2\phi = 0$ everywhere in the flow field except inside the idealized wake layers,

(b) $\nabla\phi \cdot \mathbf{n} = V_s$ on the surface of the body. V_s is nonzero only when mass is injected or drawn in to induce the desired flow pattern, and

(c) $\nabla\phi = 0$ sufficiently far away from the body for the disturbance to vanish.

Let w denote the wake surface of bodies with nonzero circulation such that there is a discontinuous jump in velocity potential across it. In the domain excluding the potential barrier of the wake, the flow is non-circulatory and the velocity potential at any point, P, in the flow following Lamb (Ref. 7, p. 59, Eq. (7)) is

$$\phi_p(x,y,z,t) = -1/4\pi \iint 1/r \; \partial\phi/\partial n \; ds + 1/4\pi \iint_{sW} \phi \; \partial/\partial n \; (1/r) \; ds \qquad (2.1)$$

where

$$r = \frac{1}{\sqrt{(x_p - x_1)^2 + (y_p - y_1)^2 + (z_p - z_1)^2}}$$

and x_1, y_1 and z_1 represent a point on the body surface. The integration must extend over all points on the body and wake surface. ϕ is the disturbance potential due to body motion and vanishes at infinity. When point P is on the surface, the locally singular kernel, 1/r, must be replaced by appropriate limiting value and should be excluded from the region of integration.

Discretization of S into N panels assuming that ϕ is constant on each of the panels and $\partial\phi/\partial n$ takes the value of prescribed normal velocity, provides the following matrix equation for the unknown velocity potential on the surface, ϕ_s.

$$[A] \; [\phi_s] = [\phi_n] \qquad (2.2)$$

Elements of matrix A are geometric quantities defined by $\iint \partial/\partial n \; (1/r) ds$,

and ϕ_N is the velocity potential induced at a control point by the sum of all constant strength sources of known strength. The former may be recognized as the velocity potential induced at a control point by a unit strength doublet whose axis is normal to the panel surface. The above matrix equation is the basic equation and is sometimes referred to as an internal Dirichlet formulation for the velocity potential.

2.1 Uniform Flow

In the case of a propeller, we have a steady linear velocity of advance along the shaft axis and rotation with a constant angular velocity, ω, about the shaft axis. The normal velocity at a control point, P, due to a combination of translation and rotation is given by $\mathbf{V} \cdot \mathbf{n} + (\mathbf{w} \times \boldsymbol{\gamma}) \cdot \mathbf{n}$, where $\boldsymbol{\gamma}$ is the position vector of the point, P. The change in the expression for the source strength is one major change in the boundary condition. The other change is the fact that the trailing wake has a component of swirl velocity added to it.

In developing MPROP for analyzing marine propellers several technical problems arose which had to be solved before smooth surface pressures could be calculated.

1. The standard geometry interpolation package led to excessive distortion and displacement in the location of panel edges along a column. This was corrected by adding a new interpolation routine which constructs panel edge coordinates based on direct interpolation of pitch, camber and thickness.

2. The existing wake models for wings and helicopter rotor blades were unsuitable for modeling marine propeller wakes due to major differences in spanwise loading. A new wake model has been synthesized based mainly on Min's experimental studies at M.I.T. (16).

3. The severe correction to pitch due to large skew or warp caused difficulty for the existing scheme of satisfying the Kutta condition, especially near the hub. An alternative formulation of the Kutta condition was introduced along with changes in the wake routines to restore correct loading behavior.

4. In the existing panel model the singularity distributions are placed on the mean plane of the quadrilateral. On quadrilaterals whose sides are not coplanar (i.e., skewed panels), the corner points are equidistant from the constructed mean plane (two above and two below). This model, therefore, leaves gaps between the singularity distributions on neighboring panels; as a result, the influence coefficient acting at nearby control points can be in error. The most often seen effect of this is after wake relaxation when some of the wake panels become highly skewed. If part of the surface paneling is close by, such as in close vortex/surface interaction for tip vortices or propeller-hub juncture vortices, then significant local errors occur in the doublet solution and, hence, in the local velocities and pressures. Skewed surface panels are also a source of error, but the associated error can be alleviated by repaneling. The most obvious treatment is to divide the skewed panel into two triangles having a common edge in one of the diagonals of the quadrilateral, Figure 2.1. This treatment has proven adequate for wake panels with little cost penalty.

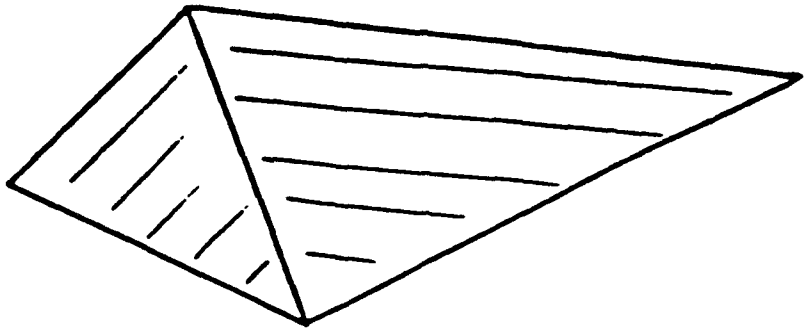

Figure 2.1. Two Triangles in Version C.Ø Wake Panels.

$$U = 1.0 - \frac{5Y^2}{2R^2}$$

¢ on the Surface of the

sphere = $\frac{R}{8}$ $(5\cos^3\theta - 3\cos\theta)$

where $r = R \sin\theta$

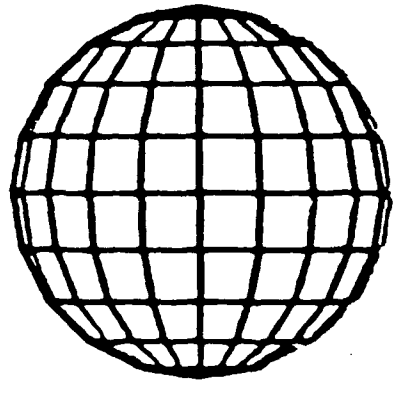

Figure 2.2. Sphere in Non-uniform Flow.

5. Practical propeller designs allow thick and abrupt trailing edges. Correct modeling of such edges poses a technical problem. The usual practise of relaxing the sectional circulation until the satisfaction of the Kutta Condition at the trailing edge is not enough. Such an approach results in unacceptable errors in overall performance predictions. To correct this problem a Y-wake attachment has been developed which leads to satisfactory solutions for the cases analyzed. The use of two parallel wake surfaces leads to numerical errors in the calculated value of circulation. In the Y-wake model the wakes from the upper and lower surfaces are brought to a line and merged as a single sheet. Such an approach eliminates the numerical errors.

2.2 Nonuniform Inflow

MPROP allows the specification of a general field of inflow velocity. A nonuniform velocity field may be specified in three different ways. The three components of the velocity field may have an arbitrary radial variation, planar variation or spatial variation. Cartesian polar coordinates may be used to specify the inflow field. A three-dimensional interpolation scheme has been devised to obtain the velocity components at any given point from a field specification of velocity components.

2.2.1 Comparison with Exact Solution

In order to verify the modeling of nonuniform inflow, a test case was constructed. There is a very special exact nonuniform flow about a sphere for which the Laplacian field can be constructed assuming such flow is possible without viscosity. The flow and its inviscid solution are shown in Figure 2.2.

For such a flow the normal velocity induced on the sphere is

$$\partial\phi/\partial\gamma = -U \cos\theta$$

$$= -\frac{1}{2}(3 - 5\cos^2\theta)\cos\theta$$

$$= P_3(\mu)$$

where $\mu = \cos\theta$ and $P_3(\mu)$ is a Legendre polynomial of the third order. By invoking the property of zonal harmonics it is possible to write down the expression for the velocity potential on the sphere in similar fashion to solving for uniform flow past a sphere (6), (see Article 90 in Ref. 15). ϕ on the sphere = R/8 (5 $\cos^3\theta$ - 3f $\cos\theta$).

The solution was also calculated using VSAERO. Figures 2.3, 2.4 and 2.5 compare the velocity potential, X component of velocity and total velocity of the calculation with the analytical solution.

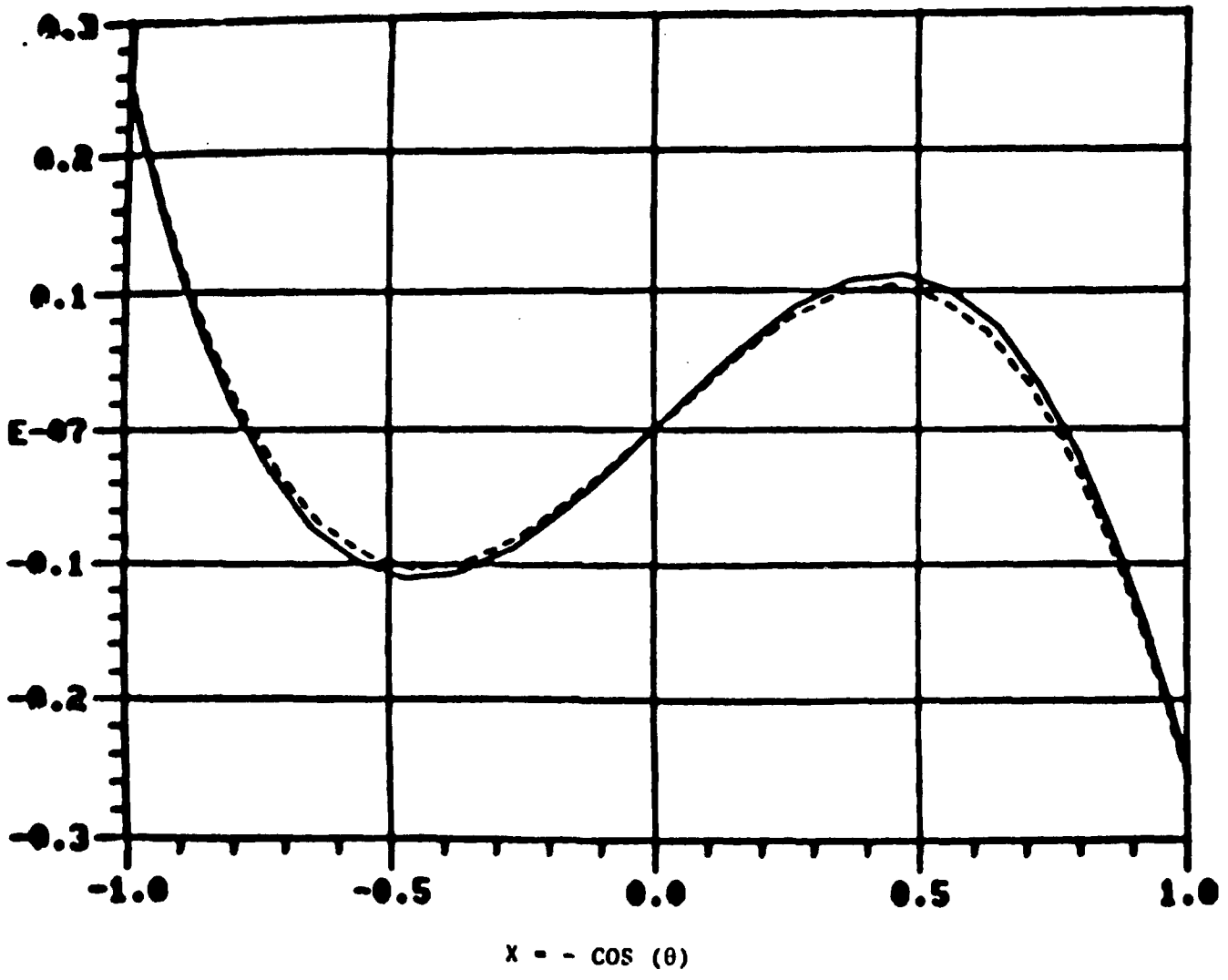

Figure 2.3. Comparison of Velocity Potentials on a Sphere.

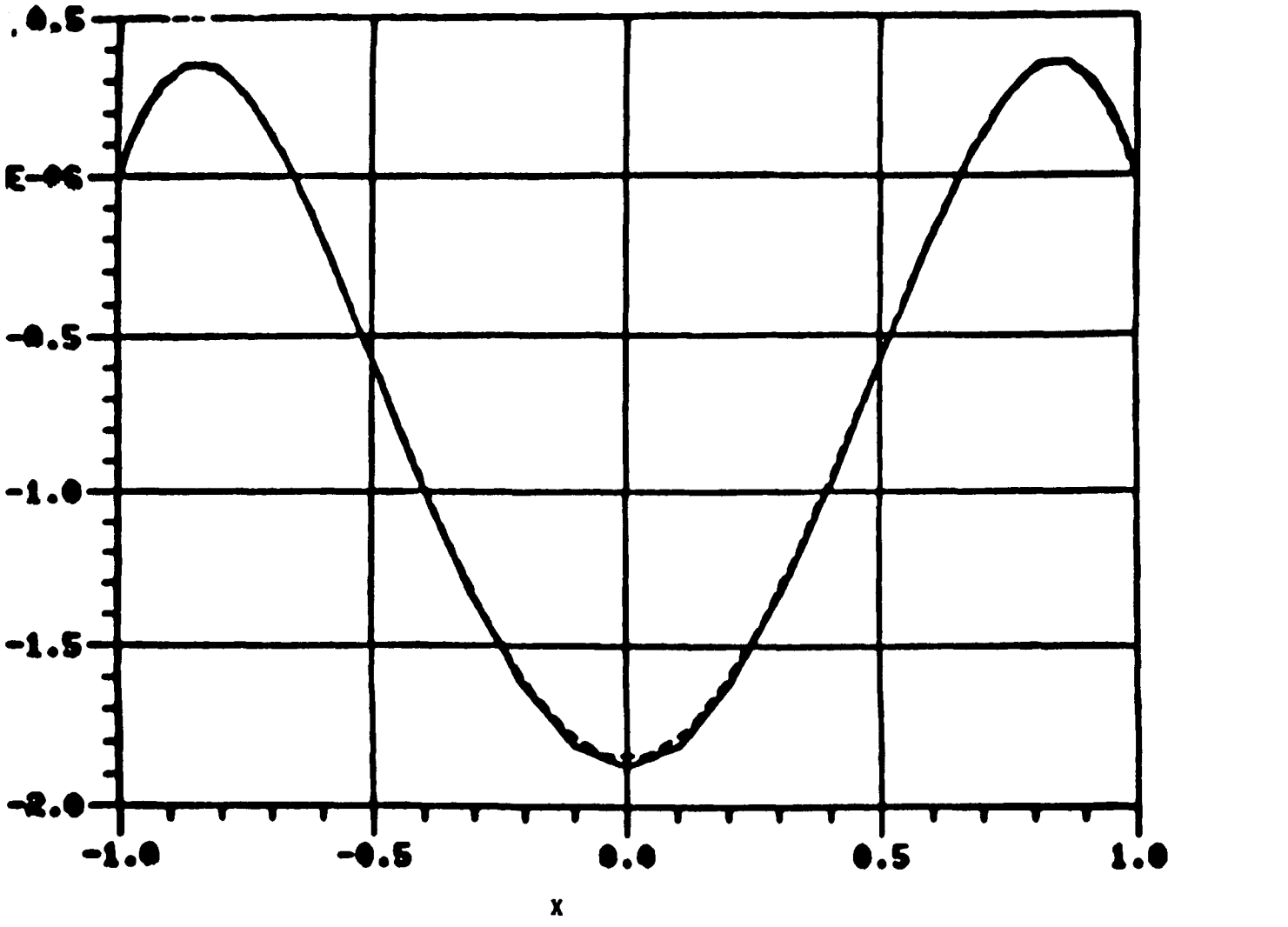

Figure 2.4. Comparison of X Components of Velocity on a Sphere.

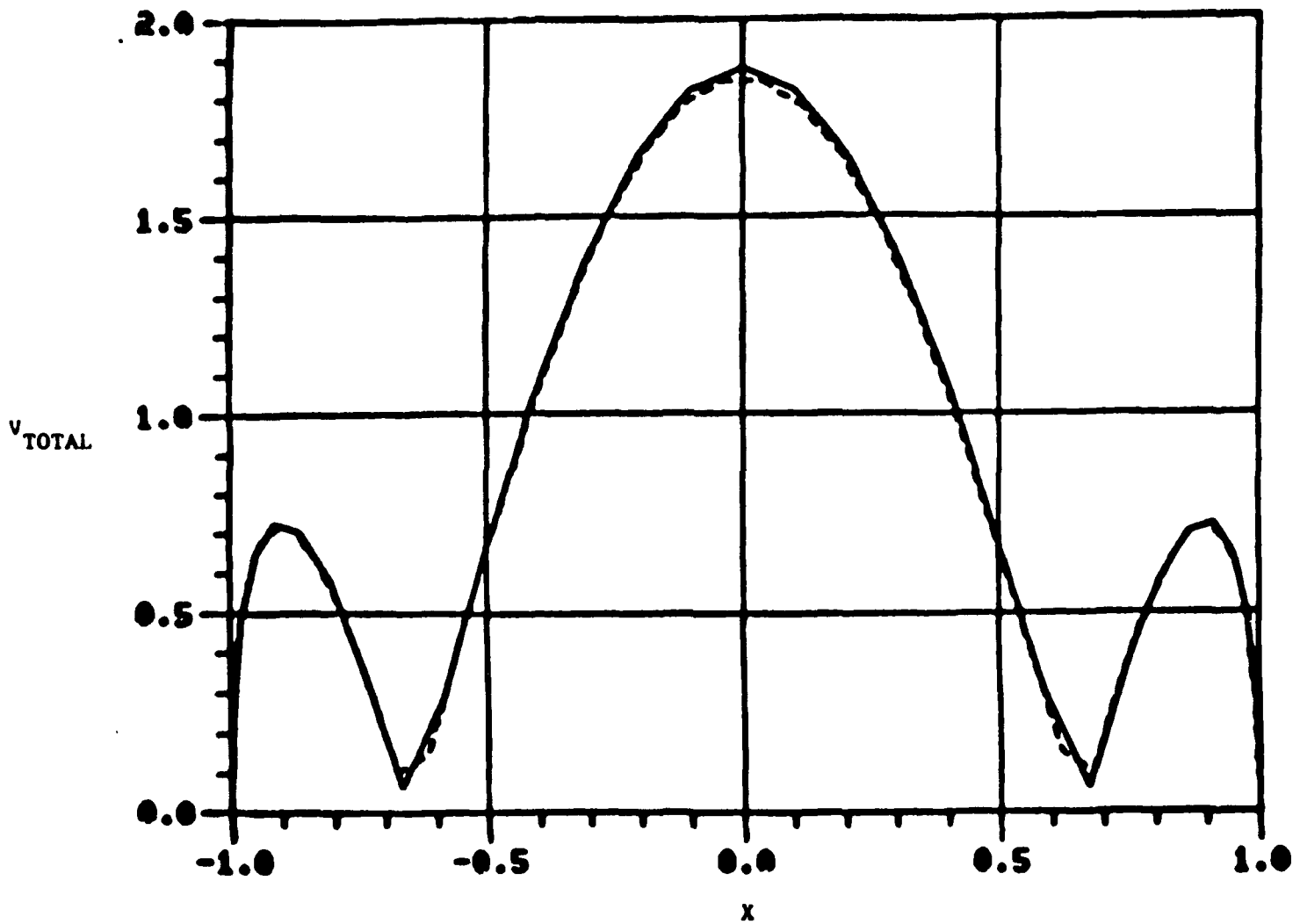

Figure 2.5. Comparison of Total Velocity on a Sphere.

The above calculations were performed with the nonuniform inflow prescribed on a radial line. Two additional calculations were made on a sphere with nonuniformity prescribed along a two-dimensional plane and a three-dimensional volume, respectively. The doublet solution for three different nonuniform inputs is presented in Figures 2.6(a), (b), and (c). All three forms are thus verified. A fourth form of representing the nonuniform flow is also provided in terms of polar x, r and θ components. This option is useful when the geometry of the velocity scan is annular.

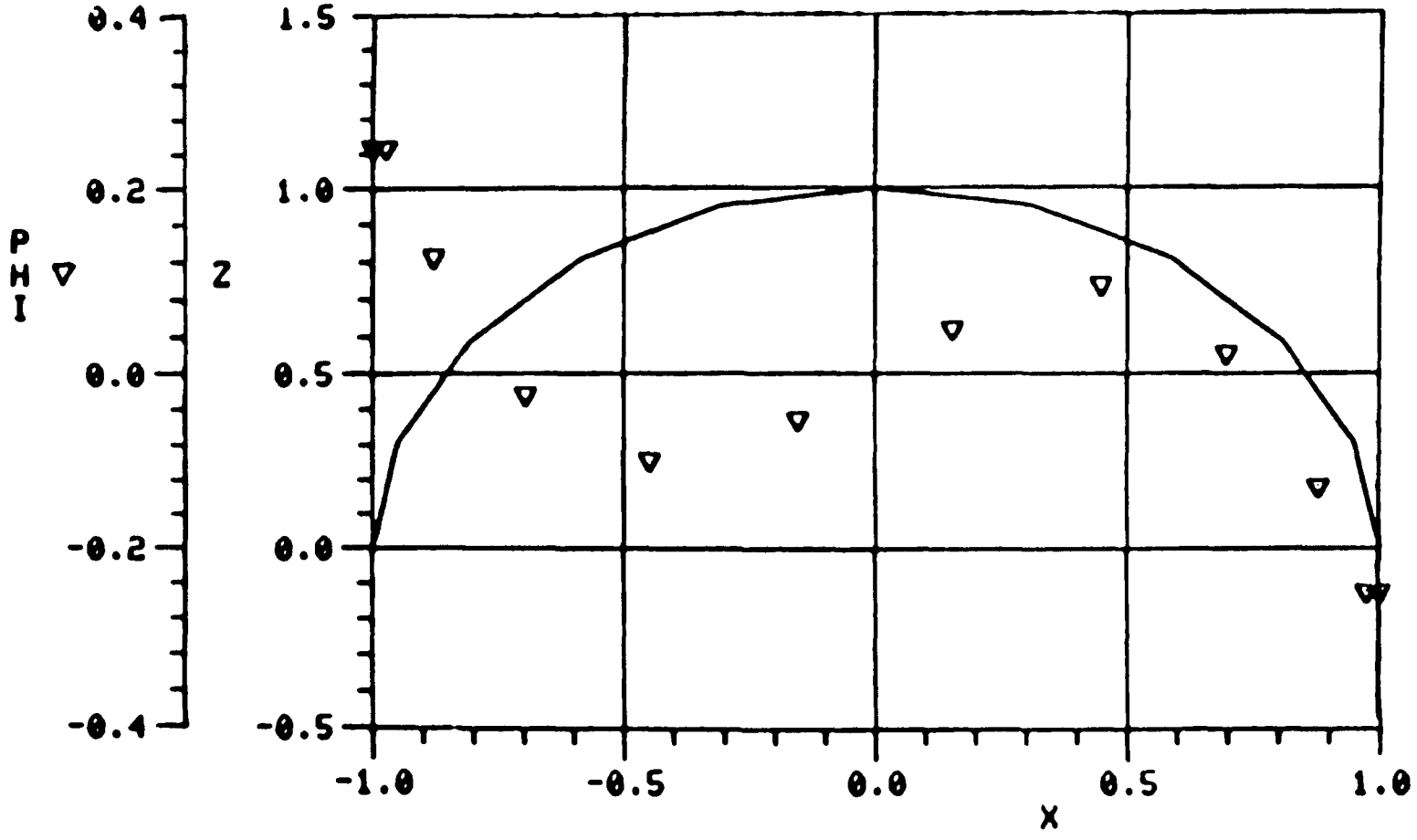

(a) Modeling with Option 1

Figure 2.6 Sphere in Non-Uniform Flow.

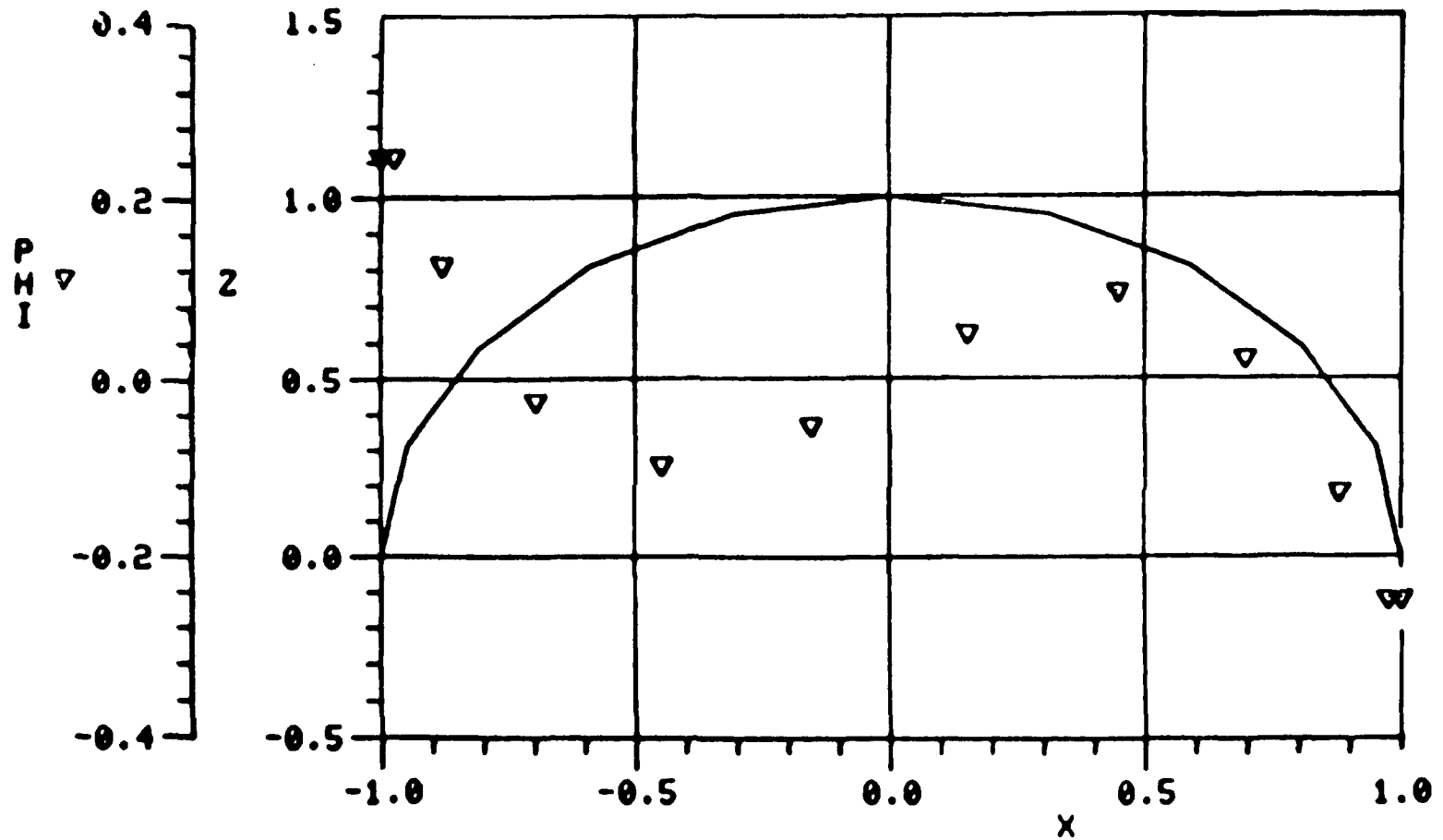

(b) Modeling with Option 2

Figure 2.6. Continued.

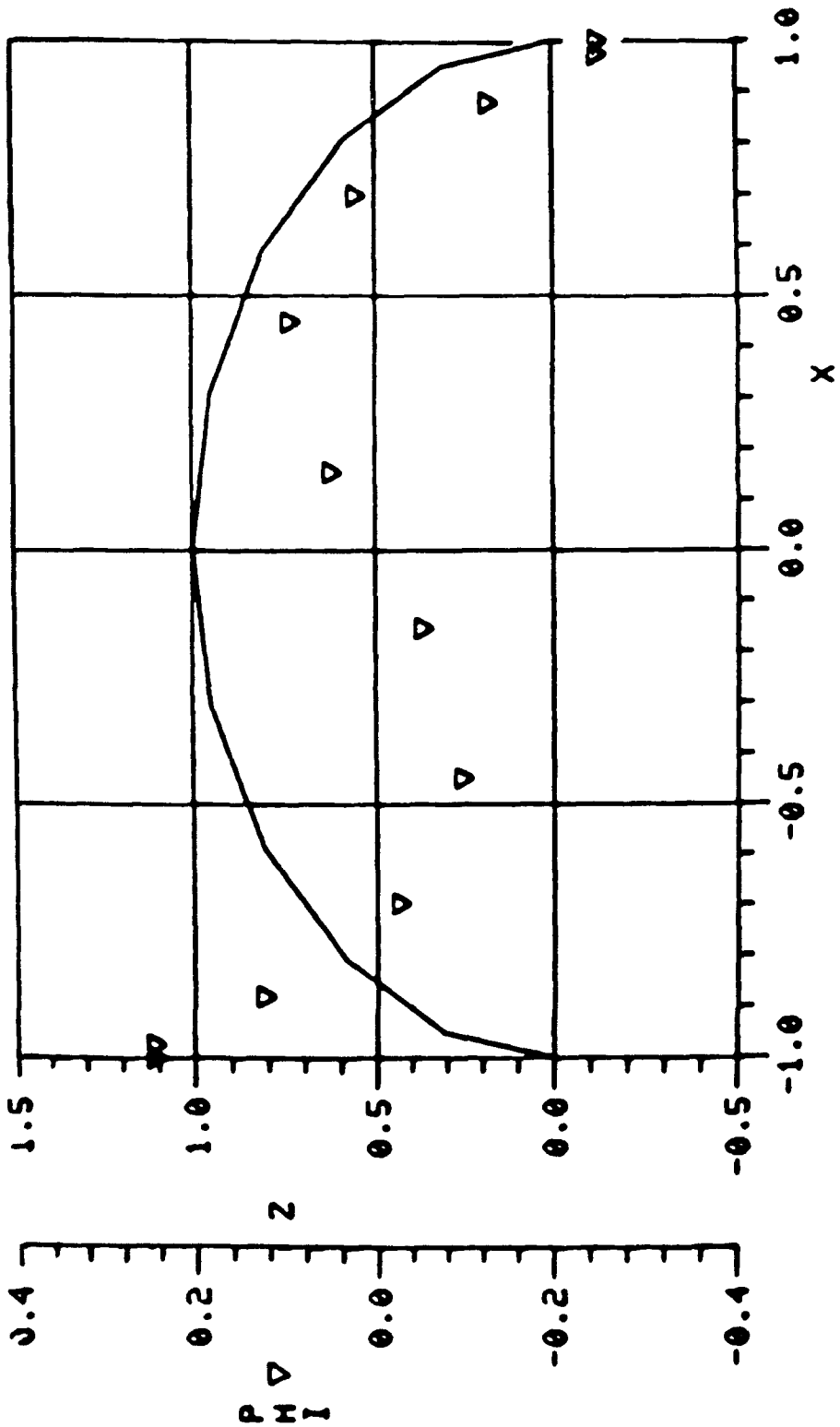

(c) Modeling with Option 3

Figure 5.6. Concluded.

3.0 HUB AND SHROUD INTERACTION

MPROP was modified to accept an axisymmetric duct, an axisymmetric hub and an arbitrary number of blade rows. The modification allows for some components to rotate while keeping other components stationary. For example, the propeiler and hub may rotate while the duct and other components are held stationary. In the following the special changes to the program, MPROP, which help in modeling the hub and shroud are discussed.

3.1 Basic Modeling

In applying MPROP to model close surface interactions, three major difficulties were encountered. These are related to off-body velocity calculations wake relaxation and streamline/boundary layer analysis.

Off-body velocity calculations have had difficulties in the past when performed near a surface or inside a duct or between nearby components. New schemes have been installed to improve this calculation. A velocity calculation is regarded as "safe" when beyond a panel "size" from the panel center. The initial size of a panel is the average distance between opposite mid-points. Once the surface velocities have been evaluated, the distances between opposite mid-points are now weighted by the local velocity components in these directions. Thus, large aspect ratio panels with flow predominantly across the small width have a reduced near-field "size" relative to the old model. In the new velocity scan all "safe" velocities along a scan line are computed first. All points falling within the near-field zone of a panel are marked and their velocities are derived later by interpolation through the "safe" set. The surface velocity values on the panels intersected by the scan line are included in the interpolation. A warning is printed if an isolated near-field point is detected with no external "safe" velocity information. The interpolations are performed independently within each flow region in cases where a scan line has several intersections. Points falling inside a closed body are not treated except that the first point inside a surface is transferred to the surface and takes on the local panel value. At present, there is a scheme installed to interpolate for the velocity at the intersection point--the nearest panel value is used. With reasonable panel density this should not cause a major discrepancy; however, should it appear necessary, a local interpolation scheme has also been installed to improve this calculation.

New scan options have been installed in MPROP to allow panel-to-panel and point-to-panel scan lines. These give good results except very close to the surface. The boundary layer velocity profile has been incorporated in the off-body velocity scan to give a realistic velocity profile near the surface.

In wake relaxation calculations on complicated configurations involving multiple wakes, wake lines from different wakes have been observed to pair up to form a doublet couple which proceeds to track alarmingly off to the side. While this usually does not seriously affect the solution on the upstream components, it can change local wake roll-up and affect downstream components. A scheme has been installed in MPROP which allows the formation of multiple wake lines. If any two wake lines approach within a certain

distance, they are identified together. A bundle can include a number of wake lines and new members may join at the downstream wake grid planes. Only the trajectory of the wake line with the smallest subscript in each bundle is computed; the movement vectors are then transferred to the other members of the bundle.

Clearly, the action of the new bundle scheme supersedes the earlier coincident vortex line routine and makes it unnecessary to input coincident vortex line information where wake lines become coincident at some downstream wake grid plane.

The small distance parameter used as a criterion for bundle formation is presently formed on the basis of the segment lengths on the wake attachment line projected in the y-z plane. A reasonable size parameter has been established on the basis of a number of test cases.

The wake geometry was contained in 251 x 31 arrays. The maximum number of wake lines was 251 and the maximum number of grid planes was 31. The small number of wake grid planes is inadequate for the relaxation of tip vortices. In MPROP, the arrays were converted to single-subscript arrays, so that for those cases which use fewer than 251 wake lines, the number of wake grid planes available is:

$$\text{Maximum grid planes} < 7{,}781/(\text{Total number of wake lines}) \qquad \text{(i)}$$

$$\text{Maximum grid planes} < 155 \qquad \text{(ii)}$$

A streamline procedure has been installed which is more robust and includes previously unavailable options, such as automated streamline starts and laminar/turbulent starts; that is, boundary layer analyses along streamlines which do not start at stagnation points. Also, a significant effort has been expended in improving the reliability of the boundary layer analysis itself.

The streamline routine that generates data for use in the boundary layer code has been modified to correct the convergence term. The convergence term measures how quickly the surface velocity vectors appear to converge. For external flow over an axisymmetric body it is equal to

$$(1/r)(dr/dx)$$

where r is the radius of the body. For any body the convergence is

$$\left[-1/V\right] \quad \left[\partial(V \cdot t)/\partial t\right]$$

where t is the vector transverse to the streamline direction. This is identical to the equation for a body of revolution.

The streamline routine at one time made the assumption that the surface potential satisfied Laplace's equation in two dimensions. That is,

$$\left[\partial V/\partial s\right] + \left[\partial(V \cdot t)/\partial t\right] = 0$$

Under this assumption the convergence term was calculated as

$$\left[+1/V\right] \quad \left[\partial V/\partial s\right]$$

which is a simple calculation.

Unfortunately, no physical basis exists for the above assumption. The simplest illustration of this is the flow at the centerline of a high aspect ratio wing. The surface streamlines have zero convergence because they remain parallel; however, the above equation will produce sizable values. The correction of this error is even more important to internal flows where a converging duct is associated with increasing velocities.

The correct general formula has been coded into the streamline routine and the computed values are written to the plot file for display as the variable, Rf, under the streamline/two-dimensional option.

Boundary Layer Methods

The integral method is an adaptation by Curle (17) of a method developed by Thwaites (18). In Thwaites' method, the momentum integral equation,

$$d\theta/dx = C_f/2 - (H + 2)(\theta/U)(dU/dx) - (\theta/r)(dr/dx) \qquad (3.1)$$

is written in the form,

$$(d/dx)(K/U) = L/U - (K/r)(dr/dx)/(dU/dx) \qquad (3.2)$$

where

$$K = \theta^2/\nu(dU/dx)$$

$$L = (\ell - K(H + 2))$$

$$\ell = (\theta/U)(\partial U/\partial y)_{y=0} \qquad (3.3)$$

θ = Momentum Thickness

H = Shape Factor

C_f = Skin Friction

u = Local Velocity

$(1/r)(dr/dx)$ = a measure of the streamline divergence or convergence.

In Thwaites' method, the divergence term is not considered, although the method was later extended to include this term by Rott and Crabtree (19).

Thwaites used exact solutions to a variety of laminar flows to determine the relationship between L and K,

$$L = 0.45 - 6K \tag{3.4}$$

Curle has pointed out that Eq. (3.4) is not adequate in flows approaching separation, and he has suggested an extension or correction giving

$$L = 0.45 - 6K + g(K,\mu) \tag{3.5}$$

The parameter, μ, is a function of both the pressure gradient and the curvature or second derivative of velocity,

$$\mu = K^2U(d^2U/dx^2)/(dU/dx)^2 \tag{3.6}$$

Curle rewrote Eq. (3.5) in the form

$$L = F_o(K) - \mu G_o(K) \tag{3.7}$$

where F_o and G_o are universal functions determined from a series of exact solutions to laminar flows in the same way as they are in Eq. (3.4). After substitution of Eq. (3.5) into Eq. (3.2), and with subsequent integration, the result can be rearranged in the form

$$\theta = 0.45\nu/(U^6r^2)\int_o^x r^2(1 + 2.22g)U^5dx \tag{3.8}$$

This equation is conveniently solved by iteration, g initially equal to zero. With values of K and μ determined in the first iteration, a second iteration is carried out using Eq. (3.7). At each step in the calculation, the local skin friction coefficient, C_f, and the shape factor, H, can be calculated using Eq. (3.3). The local skin friction coefficient has been defined as

$$C_f = (\mu/\rho\theta U)\ell \tag{3.9}$$

where ℓ in Eq. (3.3) is determined in a similar manner to L from a series of known solutions to give

$$\ell^2 = F_1(K)k - G_1(K) \tag{3.10}$$

The functions, F_0, F_1, G_0 and G_1 are tabulated in the computer program. Calculations begin at the stagnation point, with the initial momentum thickness, θ, given as a function of K. For bluff bodies, K takes an initial

$$\theta_o = \left[\frac{.0604}{dU/dx}\right]^{1/2} \tag{3.11}$$

The calculation proceeds either to laminar separation or to the end of the airfoil, whichever occurs first. The calculated boundary layer development is then interrogated to determine if transition, laminar separation or forced transition (boundary layer tripping) has taken place. If any of these phenomena have occurred, the downstream flow is assumed to be turbulent.

Boundary Layer Transition and Laminar Separation

Boundary layer transition is a very complex phenomenon. Reynolds number is a controlling parameter, but it has been shown that the Reynolds number at transition can be increased a considerable amount by careful elimination of disturbances. At very low Reynolds numbers, laminar boundary layers are stable to small disturbances. However, at higher Reynolds numbers, the boundary layer is unstable, and small disturbances can be amplified. Amplification of these disturbances causes the flow to become turbulent. The point at which flow breakdown occurs depends on the strength and dominant frequency of the initial disturbance. Disturbances may be due to free-stream turbulence, surface roughness, noise or vibration of the surface. As there is no detailed analysis of the transition process, transition prediction is accomplished by means of empirical correlations. Granville (Ref. 20) has developed a procedure based on the determination of the neutral stability point and the transition point. The neutral stability point is defined as that point downstream from which small disturbances are amplified within the boundary layer. It is this amplification of small disturbances that ultimately leads to transition. The neutral stability point is reached when the Reynolds number, based on the local momentum thickness and local flow properties, attains some critical value, $R_{\theta ins}$. Schlichting and Ulrich (21) have shown that $R_{\theta ins}$ can be correlated with the local pressure gradient parameter, $K = (\theta^2/\nu)(dU/ds)$. Correlations by Smith (22) and others have been reduced to analytical form as follows.

Instability Curves

$$K = -0.4709 + 0.11066\ \ln R_\theta - 0.0058591\ \ln^2 R_\theta \tag{3.12a}$$

$$\text{for } 0 < R_{\theta ins} \leq 650$$

and

$$K = 0.69412 - 0.23992\ \ln R_\theta + 0.0205\ \ln^2 R_\theta \tag{3.12b}$$

$$\text{for } 650 < R_{\theta ins}$$

If for a given R_θ the pressure gradient parameter, K, as calculated by Eq. (3.12), is greater than determined by the boundary layer development, the flow has passed from a stable to an unstable region. Once the flow passes into the unstable region, the transition process begins; and Granville has been able to show that a correlation similar to the instability process can be used to determine the transition point. He formed an average pressure gradient parameter, $\bar{K}$, defined as

$$\bar{K} = \frac{\int_{s_{ins}}^{s_{trans}} K \, ds}{s_{trans} - s_{ins}} \tag{3.13}$$

which correlated reasonably well with with the momentum thickness Reynolds number at transition, $R_{\theta trans}$. This correlation is presented in analytical form as follows.

Transition Curves

$$\bar{K} = -0.0925 + 7.0 \times 10^{-5} R_\theta \tag{3.14a}$$

$$\text{for } 0 < R_{\theta trans} \leq 750,$$

$$K = -0.12571 + 1.14286 \times 10^{-4} R_\theta \tag{3.14b}$$

$$\text{for } 750 < R_{\theta trans} \leq 1{,}100$$

and

$$\bar{K} = 1.59381 - 0.45543 \ln R_r + 0.032534 \ln^2 R_\theta \tag{3.14c}$$

$$\text{for } 1{,}100 < R_{\theta trans}$$

When the $\bar{K}$ calculated by Eq. (3.14) for a given R_θ is greater than the value determined from the boundary layer development, transition is predicted.

With transition predicted, initial values of the momentum thickness, θ, and shape factor, H, are required to start the turbulent boundary layer calculation. Because the boundary layer growth is continuous, the momentum thickness at transition is used as the initial turbulent momentum thickness. Since the shape factor varies from values greater than 2.0 to less than 1.5 through the transition region, an empirical expression is used to determine the initial turbulent shape factor. The empirical relation between H and $R_{\theta trans}$ was determined from the data obtained by Coles (23):

$$H_t = \frac{1.4754}{\text{Log}_{10} R_{\theta trans}} + 0.9698 \qquad (3.15)$$

In many cases, the pressure gradient is of sufficient strength to separate the laminar boundary layer prior to transition. Except in extreme cases, the boundary layer will then reattach, usually as a turbulent boundary layer. Researchers been able to analyze this phenomenon (24), but the procedure is extremely complicated and cumbersome; consequently, empirical relationships are required. From the measurements of Gaster (25) and others, a correlation is formed which is capable of predicting both the occurrence of a separation and later the reattachment as a turbulent boundary layer or the catastrophic separation. The correlation is of the form,

$$K = 0.0227 - 0.0007575\ R_\theta - 0.000001157\ R_\theta^2 \qquad (3.16a)$$

for $R_\theta > 125$

and

$$K = -.09 \qquad (3.16b)$$

for $R_\theta < 125$.

The value of K determined by the boundary layer development must be less than that calculated by Eq. (3.16) before separation without reattachment is predicted. If reattachment is predicted, the turbulent boundary layer calculation is initiated using the momentum thickness calculated at the separation point.

Turbulent Method

Methods for the calculation of turbulent boundary layers in two dimensions have been developed by many investigators. These methods were reviewed at a conference held in 1968 at Stanford University (26). One of the methods, an integral method by Nash and Hicks (27), compared very favorably with the more complex finite difference methods. The method remains (White (28)) an excellent approach for application to the current problem, both in terms of accuracy and speed.

The Nash-Hicks method is based on momentum and moment of momentum equations coupled with a skin friction law derived from Coles' velocity profile family (29). An additional equation is obtained by relating the shear stress integral to its equilibrium value using a simple first-order differential equation. The equations have been derived in (30) and (31), and are repeated herein for completeness.

A family of integral equations can be derived taking higher moments of the equation of motion. The resulting equations can be expressed as

$$\int_o^\delta \left(u \frac{\partial u}{\partial x} - \frac{1}{r} \frac{\partial u}{\partial y} \int_o^\delta \frac{\partial (ur)}{\partial x} dy\right) y^\alpha dy = \frac{U\delta^{\alpha+1}}{\alpha + 1} \frac{dU}{dx} + \frac{1}{\rho} \int_o^\delta y^\alpha \frac{\partial \tau}{\partial y} dy \quad (3.17)$$

where

α = 0 gives the momentum integral equation, and

α = 1 gives the moment of momentum integral equation

The velocity distribution across the boundary layer can be represented by Coles' velocity profile family, given by

$$u = \frac{u_\tau}{\kappa} \left(\ln\left(y \frac{u_\tau}{\nu}\right) + C\right) + \frac{u_\beta}{2} \left(1 - \cos \frac{(\pi y)}{\delta}\right) \quad (3.18)$$

where

u_τ = friction velocity, $(\tau_w/\rho)^{1/2}$,

u_β = free parameter having units of velocity,

δ = boundary layer thickness,

κ = .41, and

C = 2.05.

Substitution of this equation into Eq. (3.17) results in two equations of the form:

$$A \frac{du_\tau}{dx} + B \frac{du_\beta}{dx} + \frac{C}{\delta} \frac{d\delta}{dx} + \Phi = D \frac{dU}{dx} - \frac{E}{r} \frac{dr}{dx} \quad (3.19)$$

A third equation of the same form is obtained by evaluating Eq. (3.18) at y = δ followed by the differential with respect to x. The parameter, Φ, is represented by the following relations:

$$\text{(i)}\ \alpha = 0 \qquad \Phi = \frac{-1}{\delta} u_\tau^2$$

$$\text{(ii)}\ \alpha = 1 \qquad \Phi = \frac{-1}{\delta^2} \int_o^\delta \frac{\tau}{\rho}\, dy$$

$$\text{(iii)}\ \alpha = \infty \qquad \Phi = 0 \tag{3.20}$$

The shear stress integral, $\int_o^\delta \frac{\tau}{\rho}\, dy$, appearing in Eq. (3.20) was evaluated by Nash and Hicks using an equation of the form:

$$\frac{d\, C_\tau}{dx} = \frac{.15}{\delta} (C_{\tau eq} - C_\tau) \tag{3.21}$$

where

$$C_\tau = \frac{1}{1/2\ \rho U^2 \delta} \int_o^\delta \tau\, dy$$

The equilibrium value of C_τ, $(C_{\tau eq})$, was determined by Nash and Macdonald (30) from measured shear stress distributions giving

$$C_{\tau eq} = .025\ (1 - \frac{1}{H})^2 \tag{3.22}$$

where H is the local shape factor. Equation (3.22) can be expressed in terms of the parameters, u_τ, u_β and U, by evaluation of the integral relations used to define H; that is,

$$H = \frac{\delta^*}{\theta} = \frac{\int_o^\delta (1 - \frac{u}{U})\, dy}{\int_o^\delta \frac{u}{U} (1 - \frac{u}{U})\, dy} \tag{3.23}$$

with the aid of Eq. (3.18). The equations for the four unknowns, u_τ, u_β, δ, and C_τ, can be integrated once the pressure distribution, U(x), and the streamline divergence, $1/r(dr/dx)$, are prescribed. Initial conditions are obtained from the transition analysis. In this case, initial values of the momentum thickness, θ, and the shape factor, H, are known. Initial values of u_τ, u_β and δ can be determined from the known θ and H using Eq. (3.18).

The starting value for C_τ is obtained by making the assumption that in the region of transition, $C_\tau \approx C_{\tau eq}$.

The accuracy of the calculation method is demonstrated in Figure 3.1. This figure shows a comparison between measured and calculated boundary layer developments along a streamline on the U.S. Airship Akron. A further comparison is shown in Figure 3.2 for the case of a boundary layer in a strong, adverse pressure gradient approaching separation. Particular reference should be made to the good agreement between calculated and measured skin friction coefficients.

3.2 Applications

Several test cases have been constructed to verify the working of the code under conditions of engineering interest. Cases involving radially nonuniform flow through propeller, hub and duct assemblies have been run successfully. The propeller chosen had a skew of 72° with a very small clearance of 0.01R between the duct wall and the propeller tip. Multiple stator blades were constructed using the NACA 0012 profile. These were positioned forward of the propeller. Separate cases were run with and without the stators. The flow with stator, hub and duct was calculated with a velocity survey at the grid points of a three-dimensional mesh. The calculated velocity was used in a separate run as a nonuniform inflow around the propeller, hub and duct assemblies. Provision was made for the user to provide the nonuniform inflow data either by means of a separate tape file or as part of the input file. The latter option is easier when radially nonuniform inflow is present or when the volume of inflow data is not very large. The former mode of specification requires some user manipulation of input such as providing the data in the auxiliary tape unit in the desired format. For minimum user manipulation, a direct solution with all the component parts in place would, of course, be preferable.

The number of panels used on the propeller was 320, and was not regarded as sufficient for accurate Cp calculation. Five blades were used in all propeller calculations. Hub and duct were input as axisymmetric components over a basic region of angular width, 360/5 = 72°. When a different number of blades was used, an appropriate change must be made so that with NBLADE rotational reflections, a full body was simulated. The cases documented are as follows.

1. Five-bladed propeller in axisymmetric duct and hub. The hub was regarded as fixed. It may be changed to rotating by a single input change. The entire assembly was subject to nonuniform radial flow as specified above.

2. Five-bladed stator (NACA 0012 section) in axisymmetric duct and hub subject to radially nonuniform flow.

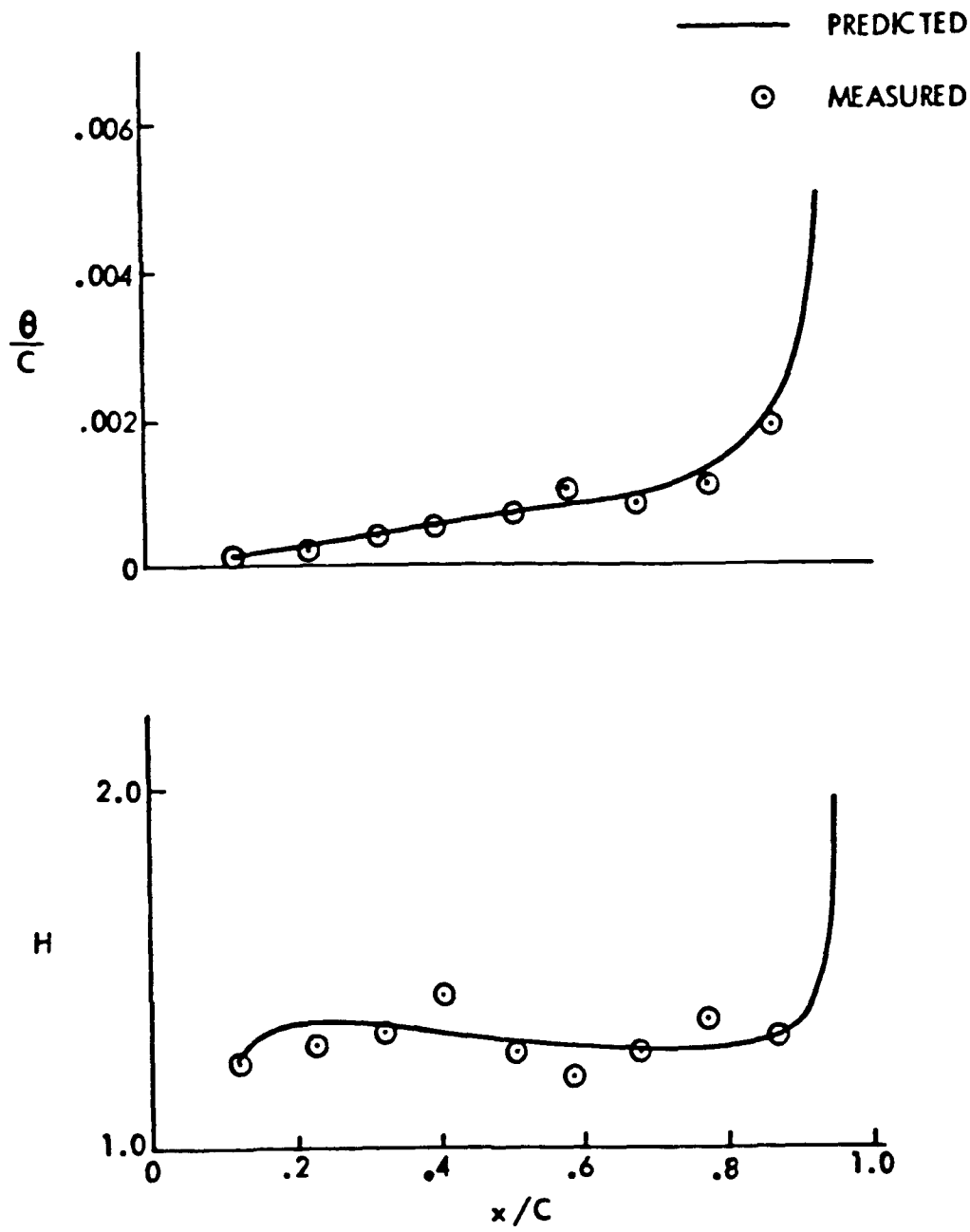

Figure 3.1. **Comparison of Measured and Predicted Boundary Layer Developments on U. S. Airship Akron.**

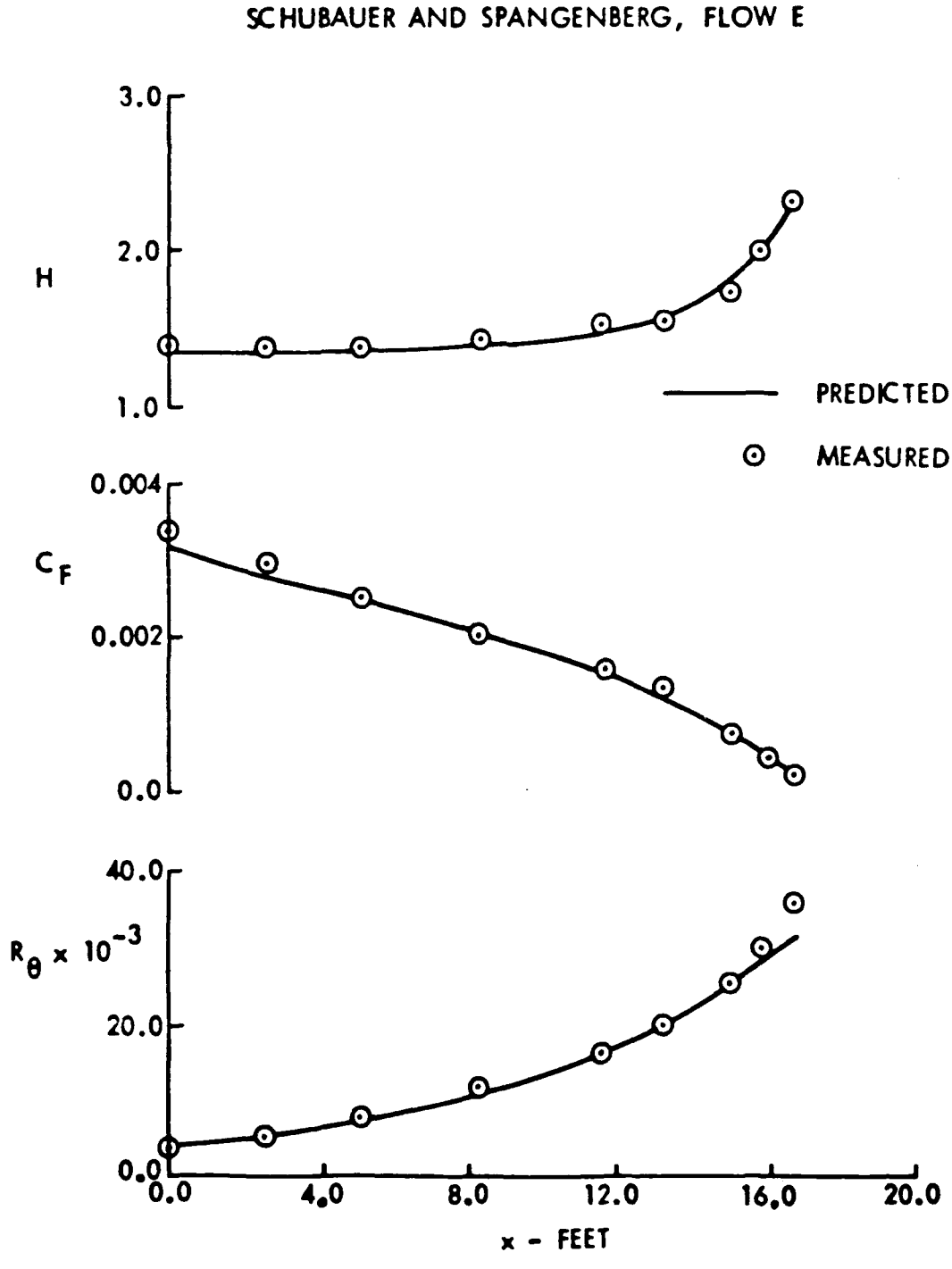

Figure 3.2. **Comparison of Measured and Predicted Boundary Layer Developments.**

Figures 3.3(a) and (b) are two views of the propeller, hub and duct assembly. As mentioned earlier, the duct and hub are defined over a basic region which is reflected NBLADE times to provide complete definition over 360°. Figures 3.4(a), (b) and (c) show the sectional Cp distribution at the three radial locations. The Cp distribution without the duct and the hub (Figure 3.5) is also shown to highlight the difference. The solution near the hub is more strongly influenced compared to the tip region. Figures 3.6(a) and (b) are sectional Cp plots along a longitudinal (constant Y) station and a lateral station (constant X). Figure 3.7(a) and (b) show the imfinal calculation without a stator.

Figures 3.8(a) and (b) are views of the five-bladed stator, duct and hub. Figure 3.9 shows the sectional Cp plot on the primary stator. The Cp is symmetric as the stators are carrying zero load. The inflow is radially nonuniform as before, but preserves symmetry. Figure 3.10 shows contour plots of a velocity scan. Care is necessary in interpreting the velocity scan from a rotating propeller. The flow is time-dependent and the value of velocity at a point is what an observer rotating with the point at the angular speed of the propeller will see as a steady velocity. An azimuthal averaging scheme has been added which provides a time-averaged velocity calculation in addition to the time history of the velocity components. The velocity scan models in an approximate but realistic way the influence of the stator, hub and duct assembly on the surrounding flows.

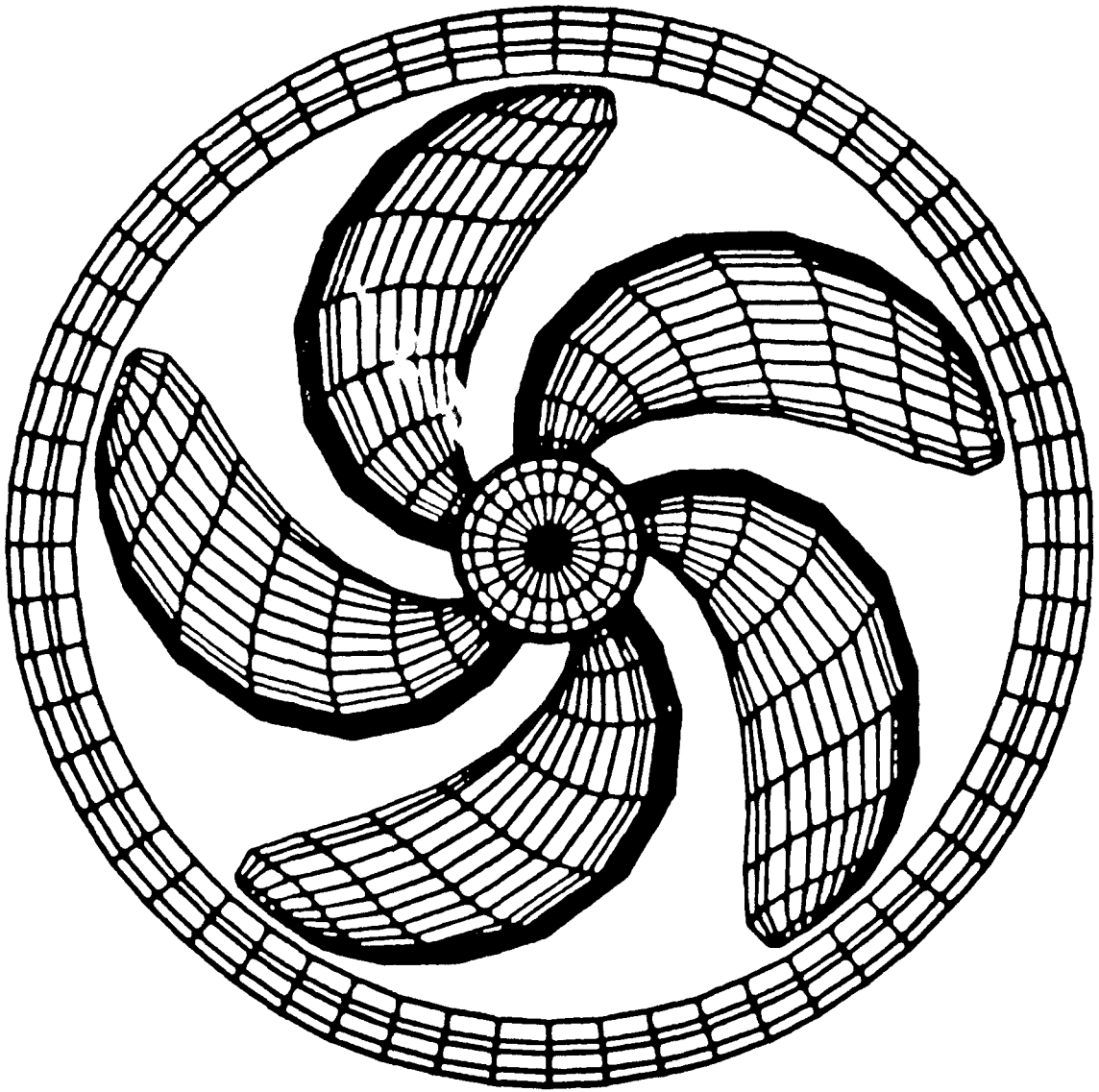

(a) View Showing Tip Shroud Clearance

Figure 3.3. Propeller-Shroud-Hub Assembly.

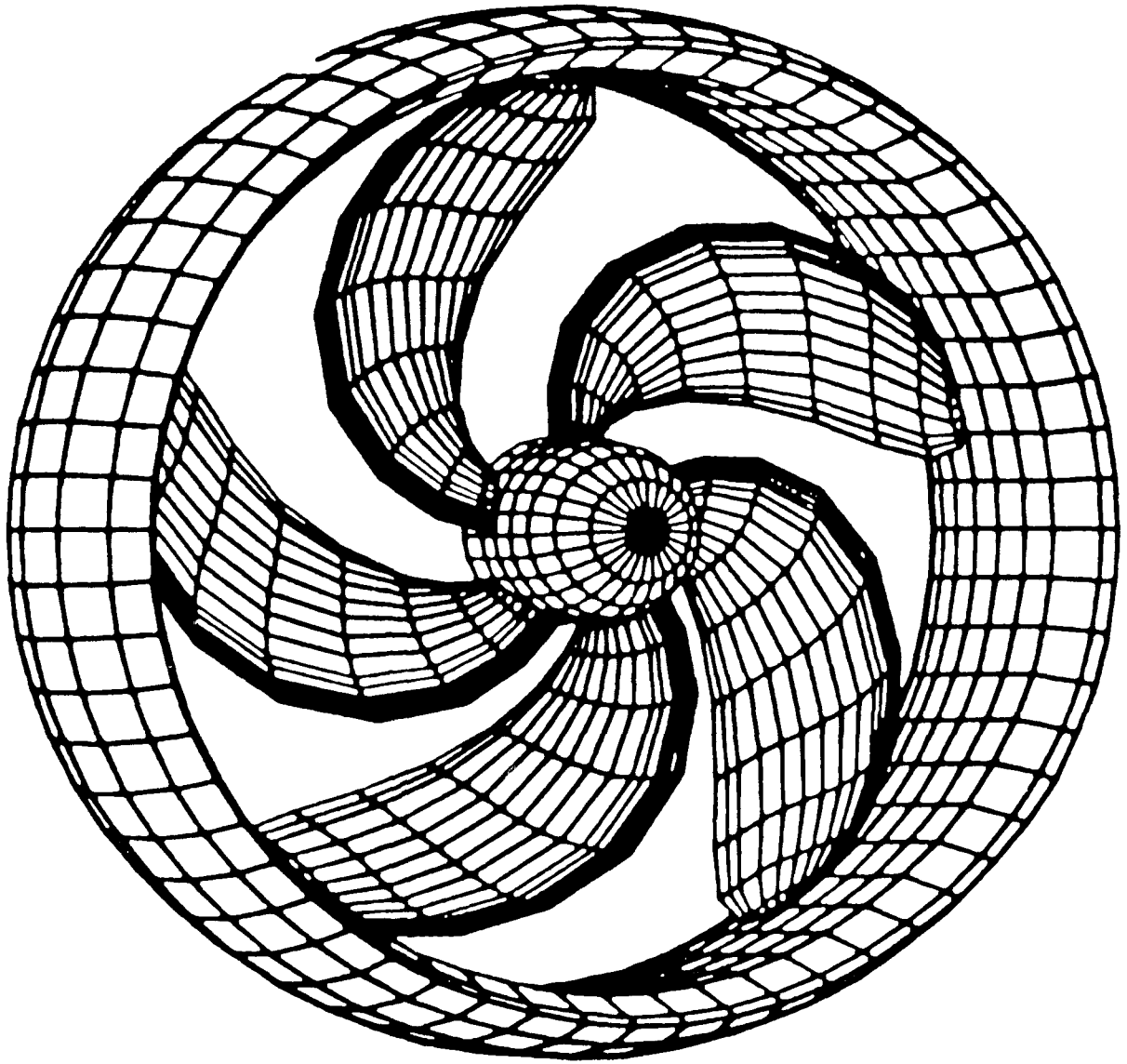

(b) Oblique View Showing Shroud Paneling

Figure 3.3. Concluded.

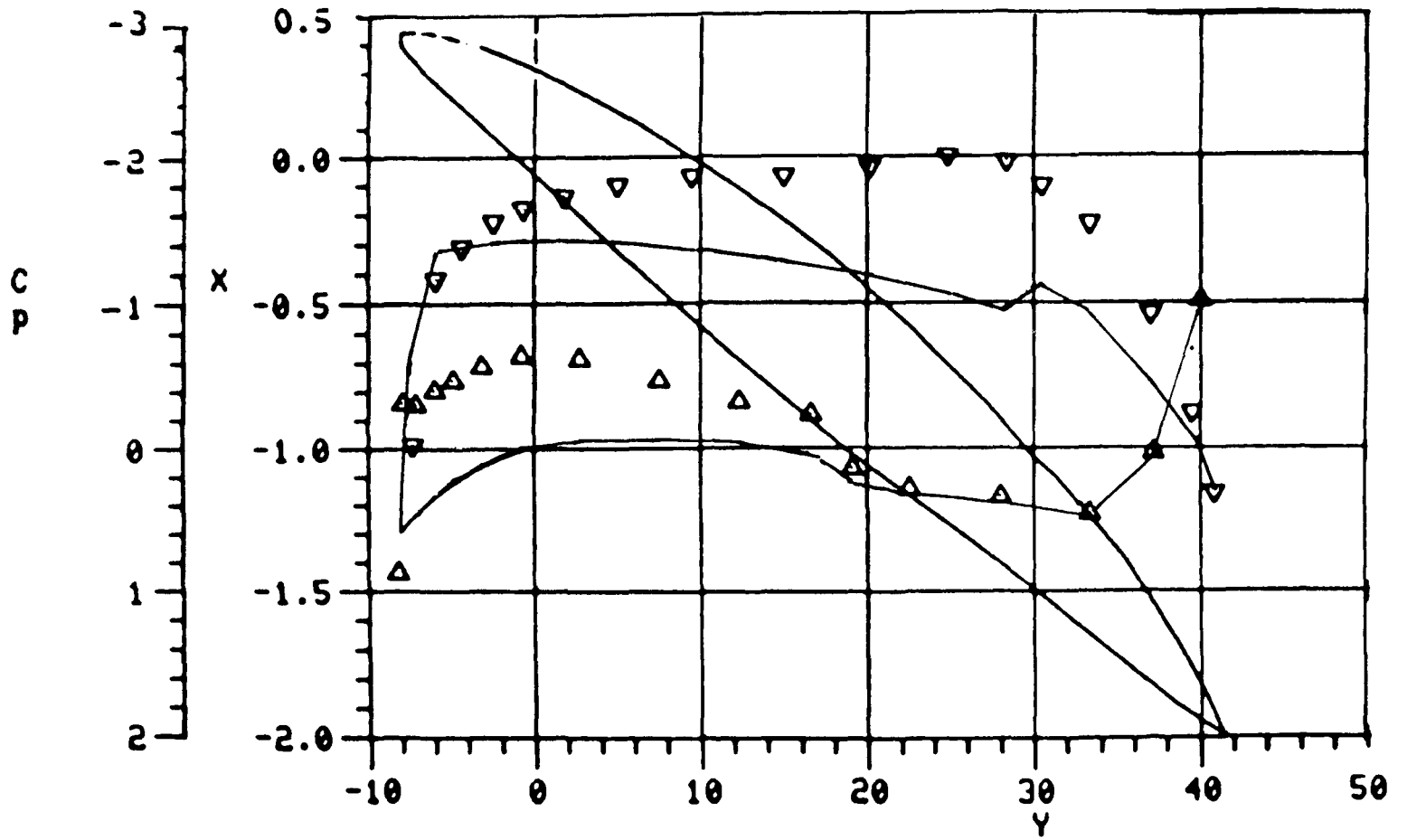

(a) Radial Location 2.2

Figure 3.4 . Pressure Distribution on Propeller with Shroud and Hub.

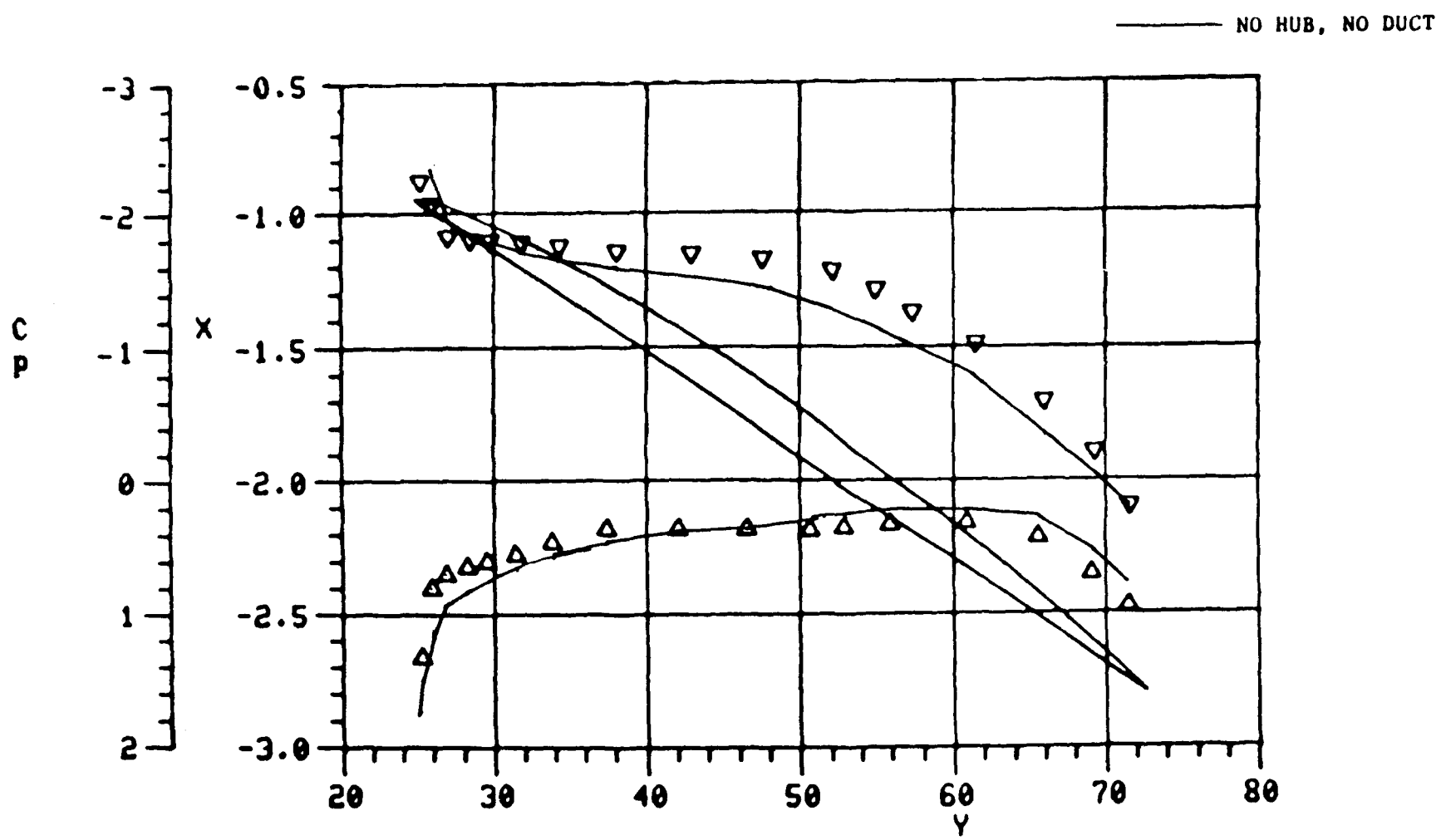

(b) Radial Location 4.4

Figure 3.4. Continued.

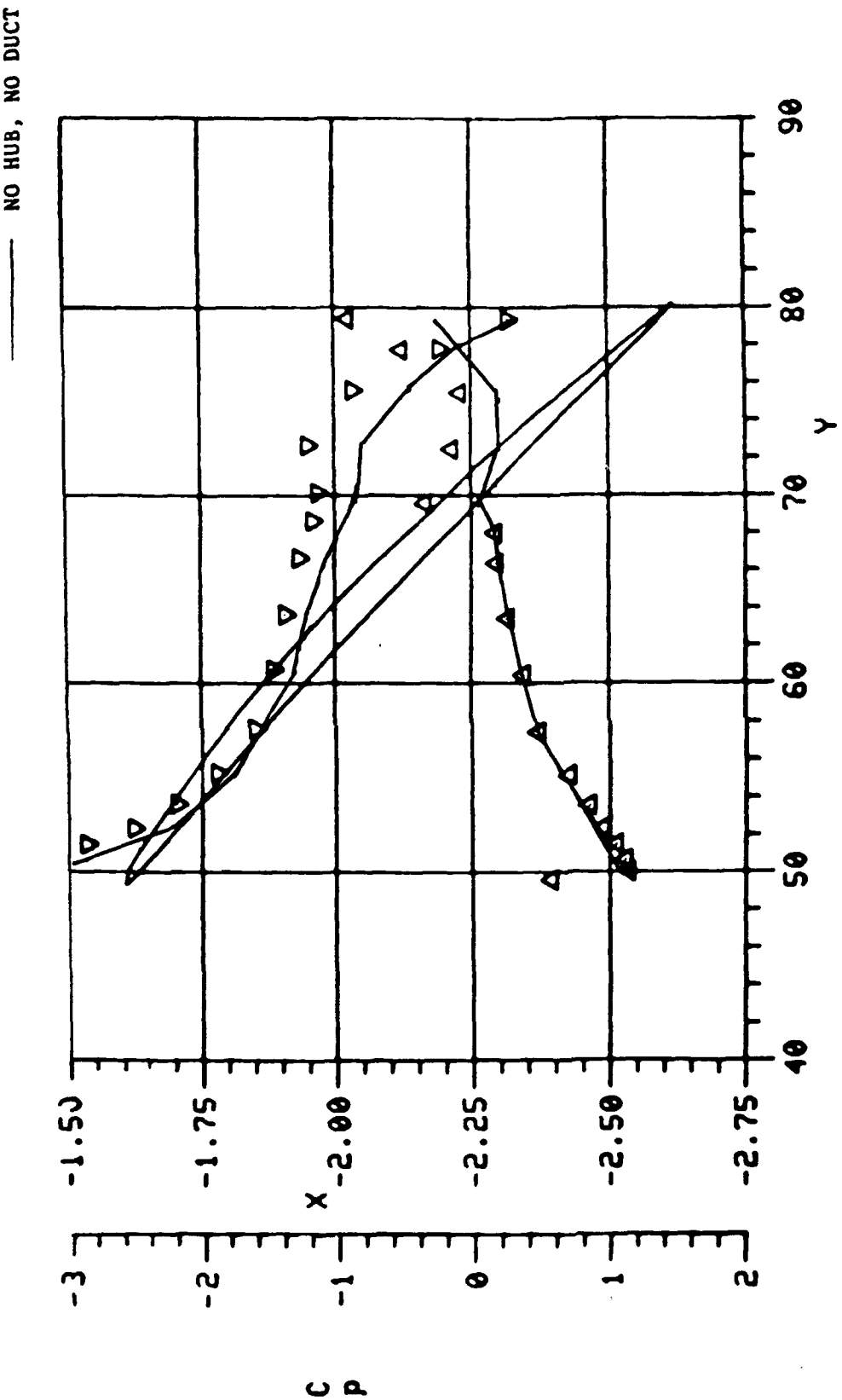

(c) Radial Location 5.5

Figure 3.4. Concluded.

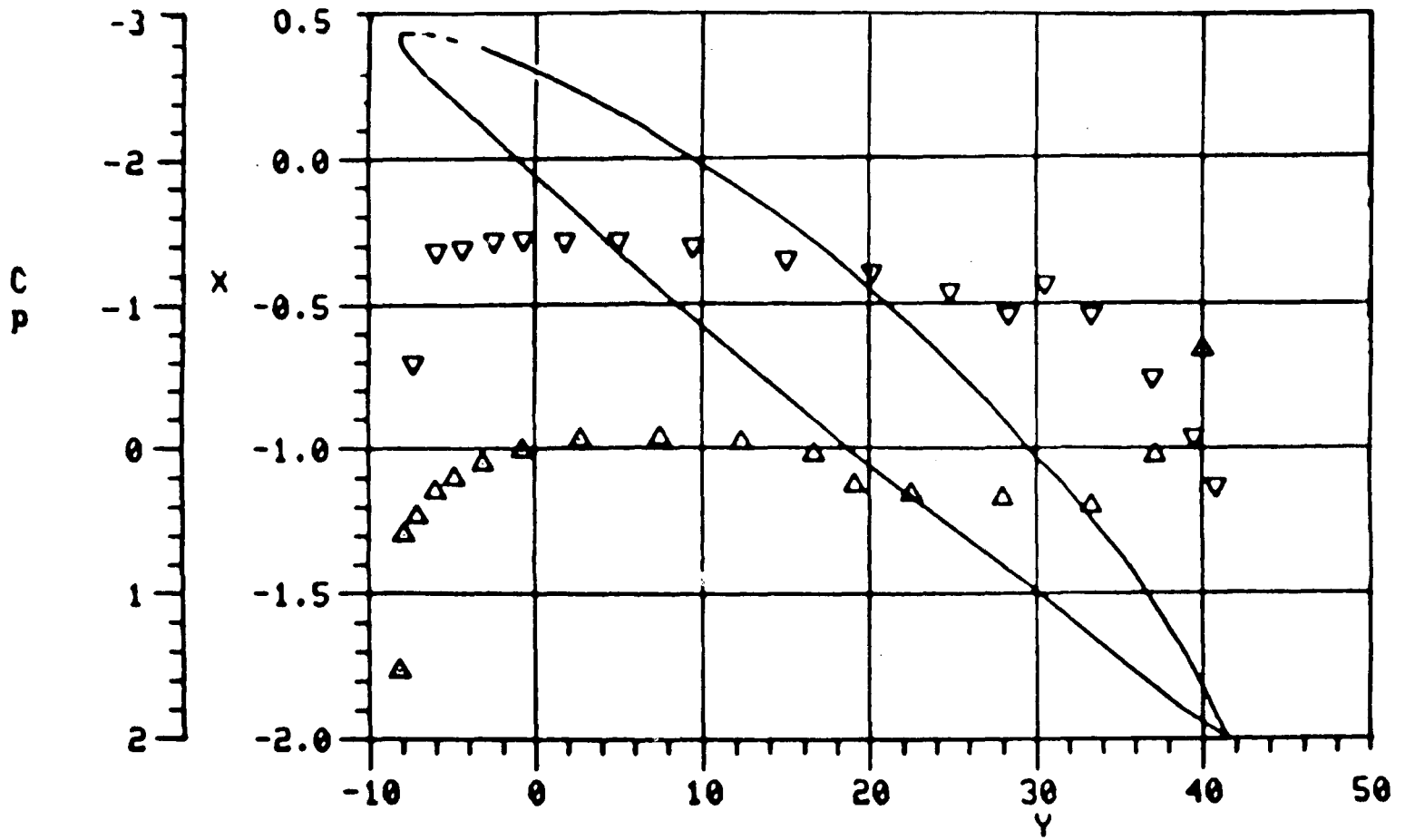

(a) Radial Location, r = 2.2

Figure 3.5. Pressure Distribution in Radially Non-Uniform Flow.

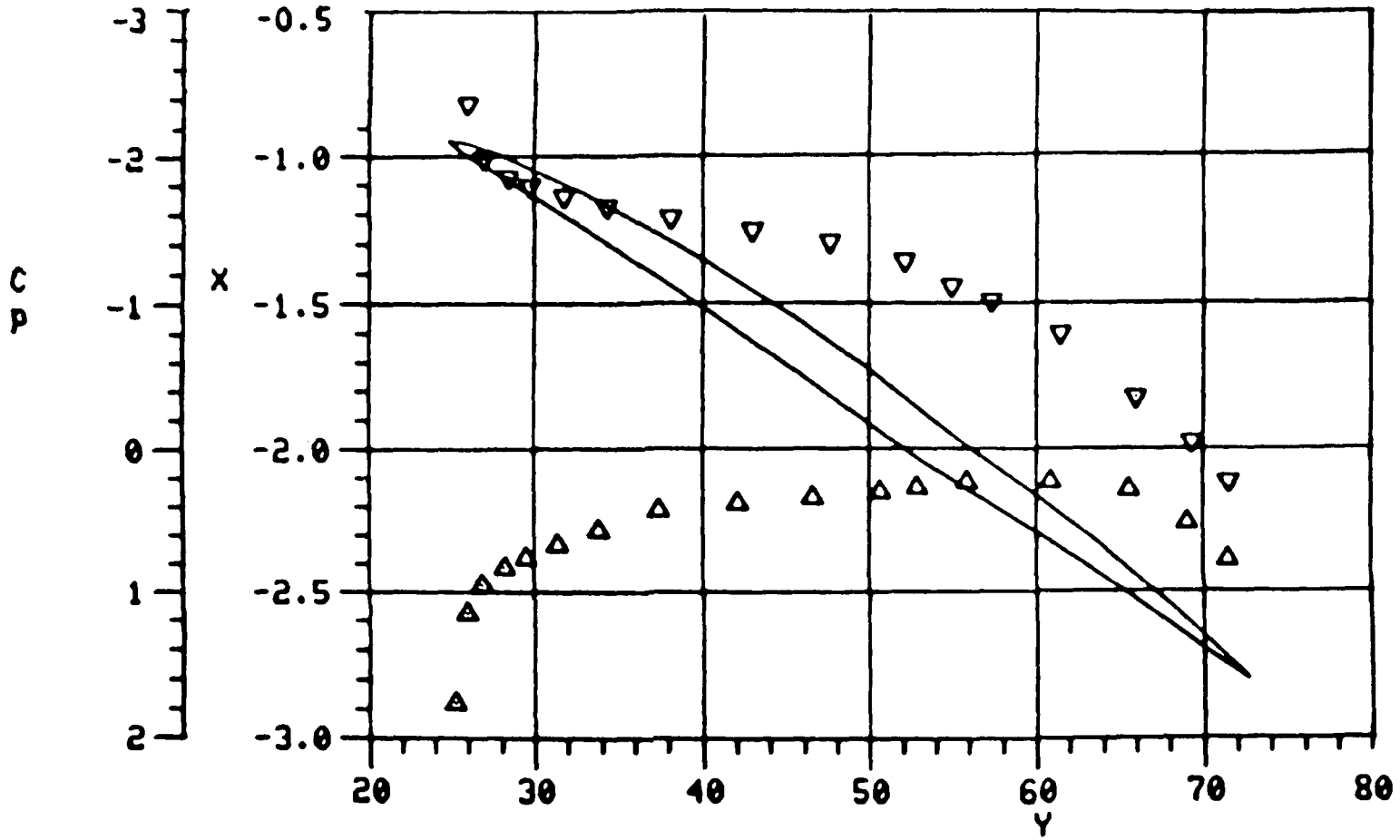

(b) Radial Location, r = 4.4

Figure 3.5. Continued.

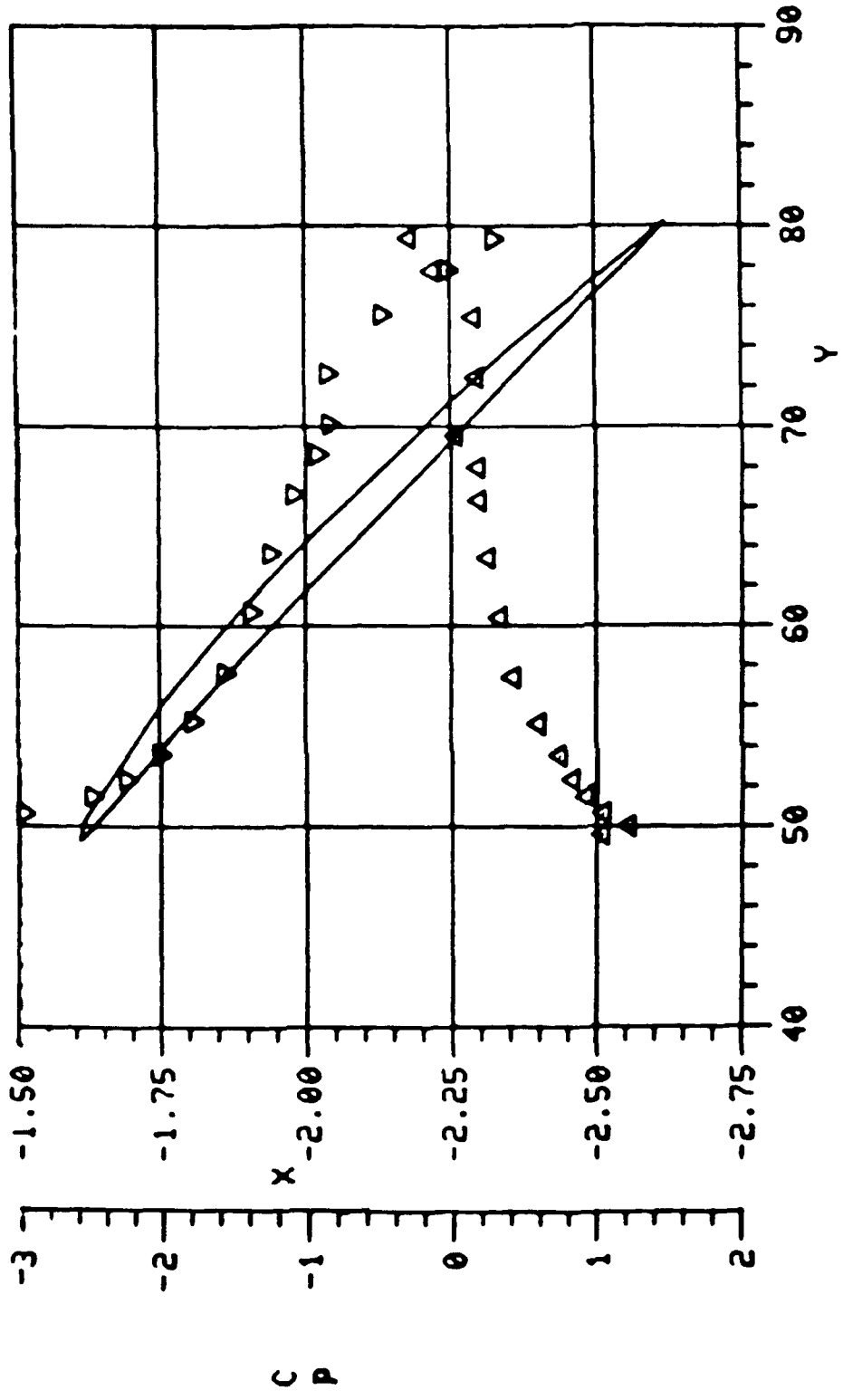

(c) Radial Location, r = 5.5

Figure 3.5. Concluded.

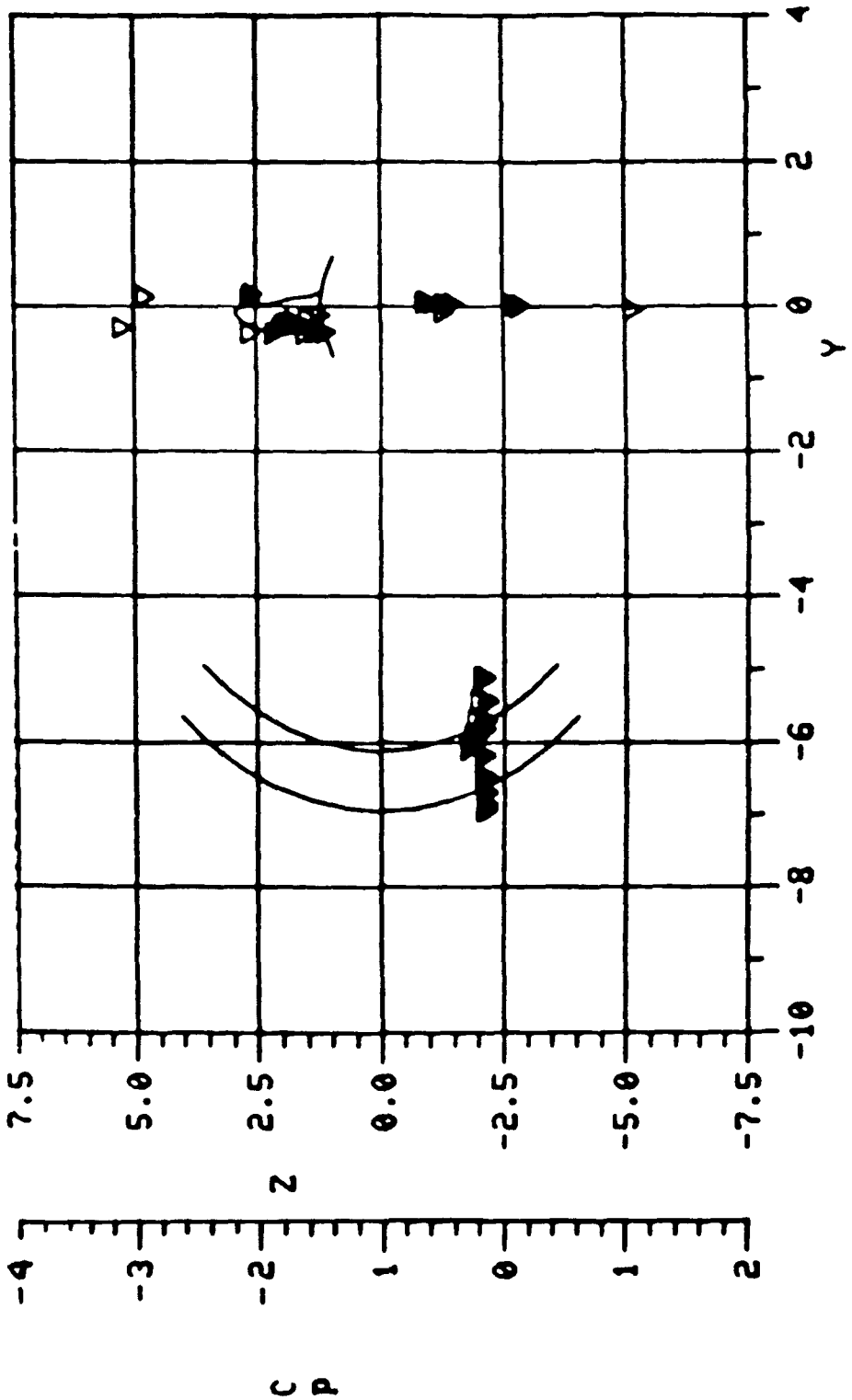

(a) Buttline Cut, Y = 0

Figure 3.6. Pressure Distribution on Hub.

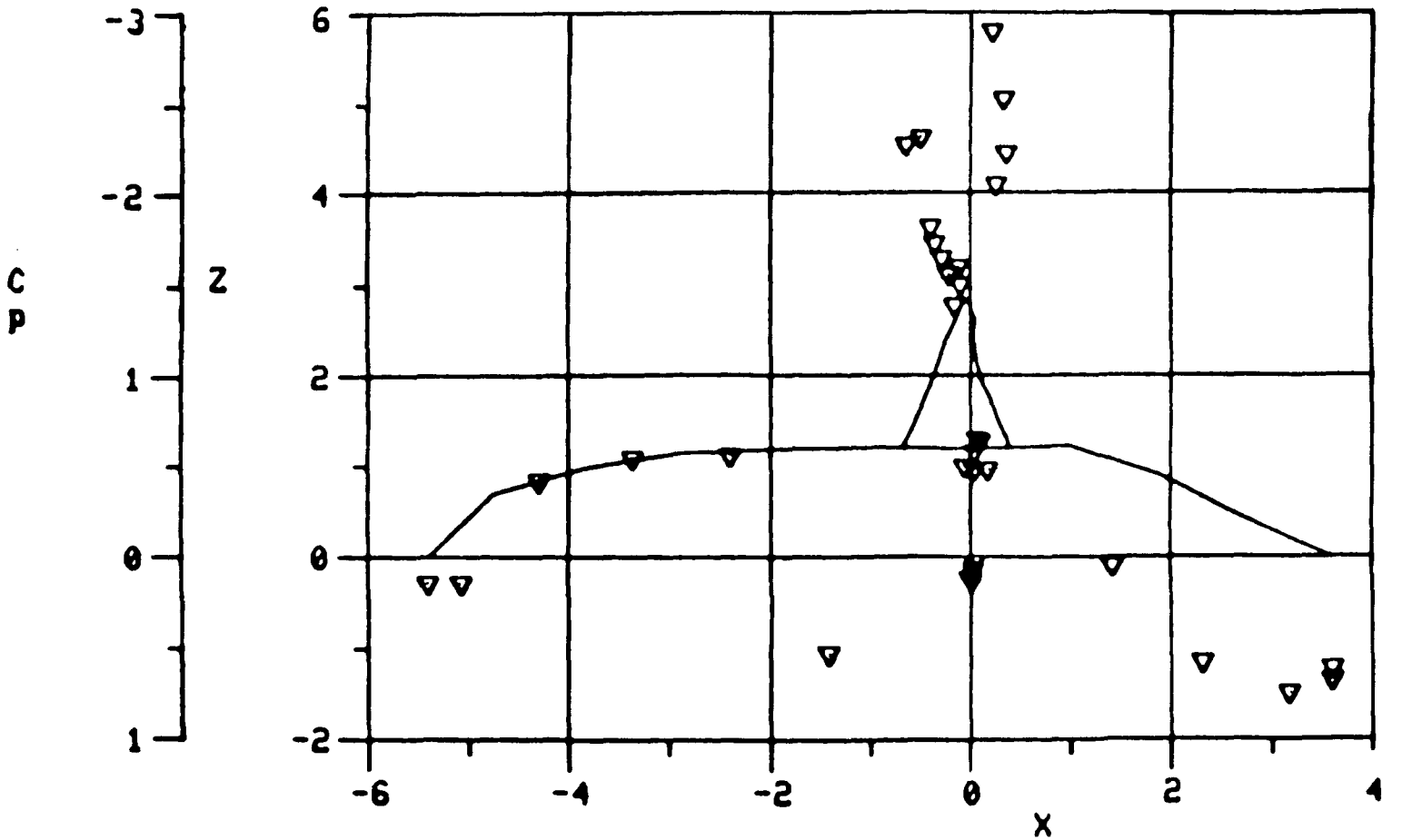

(b) Station Cut, X = 0

Figure 3.6 . Concluded.

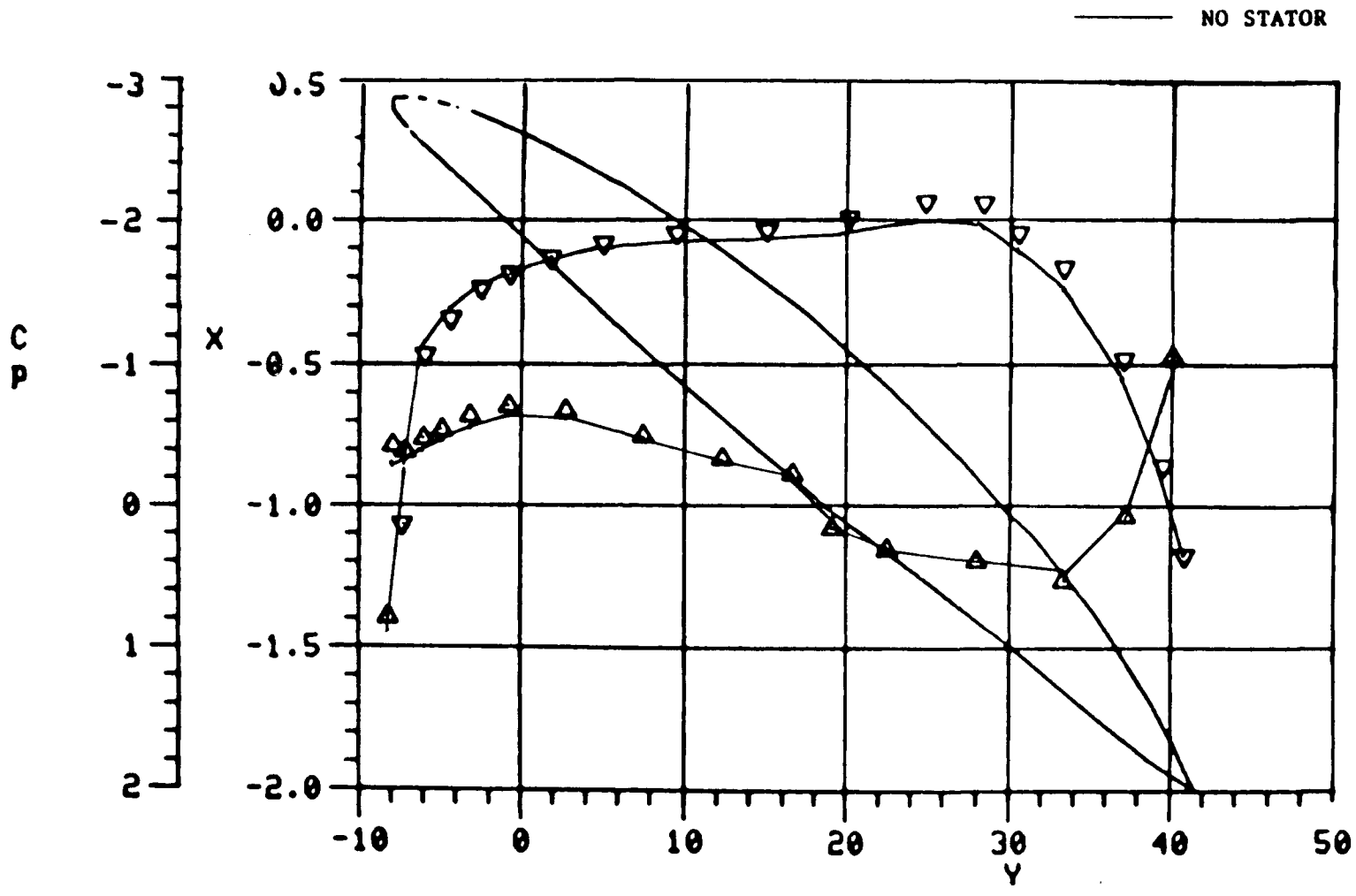

(a) Radius r = 2.2

Figure 3.7. Propeller, Hub and Shroud Assembly in the Non-Uniform Flow Induced by Stator, Hub and Shroud.

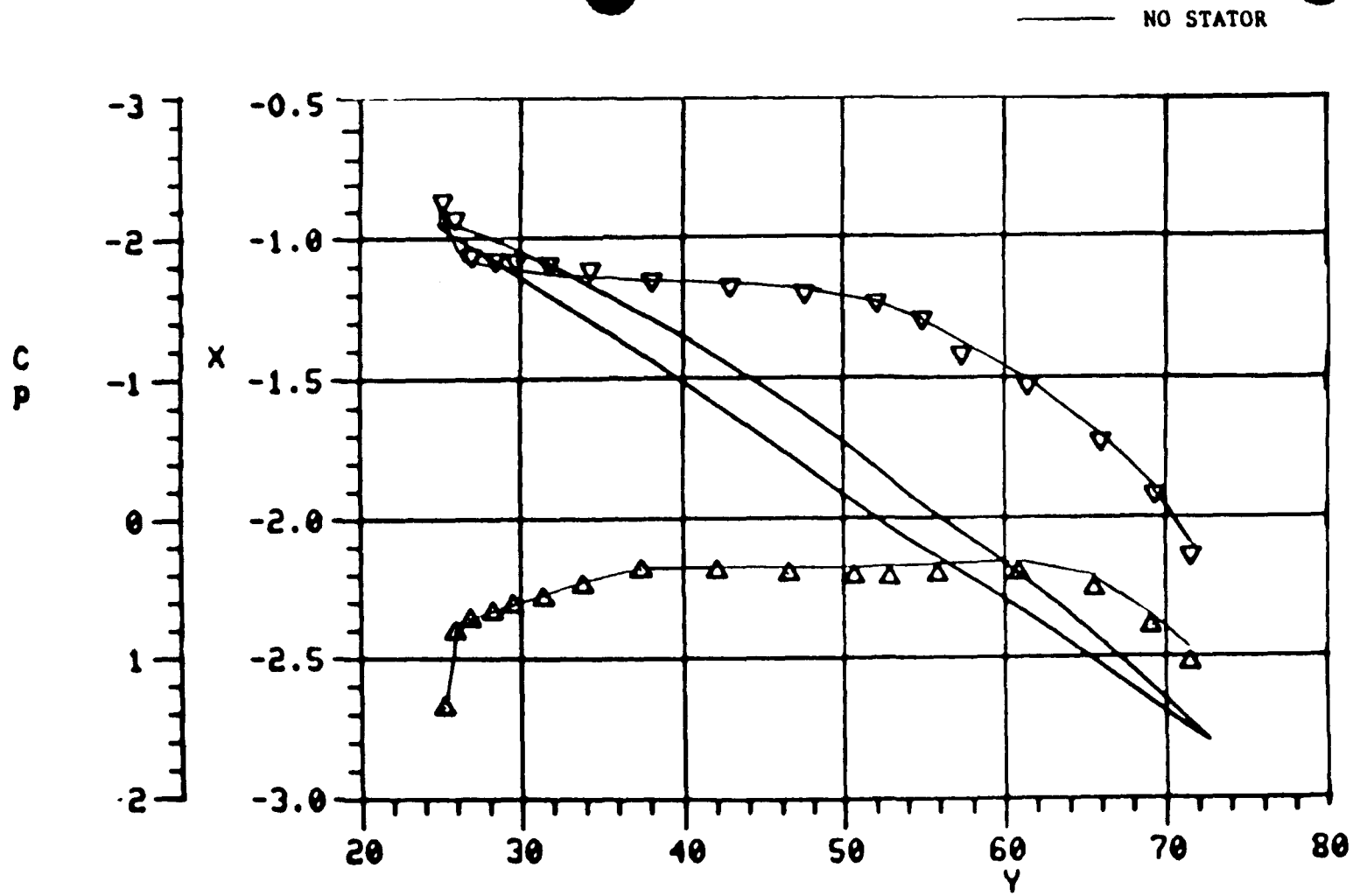

(b) Radius = 4.4

Figure 3.7. Concluded.

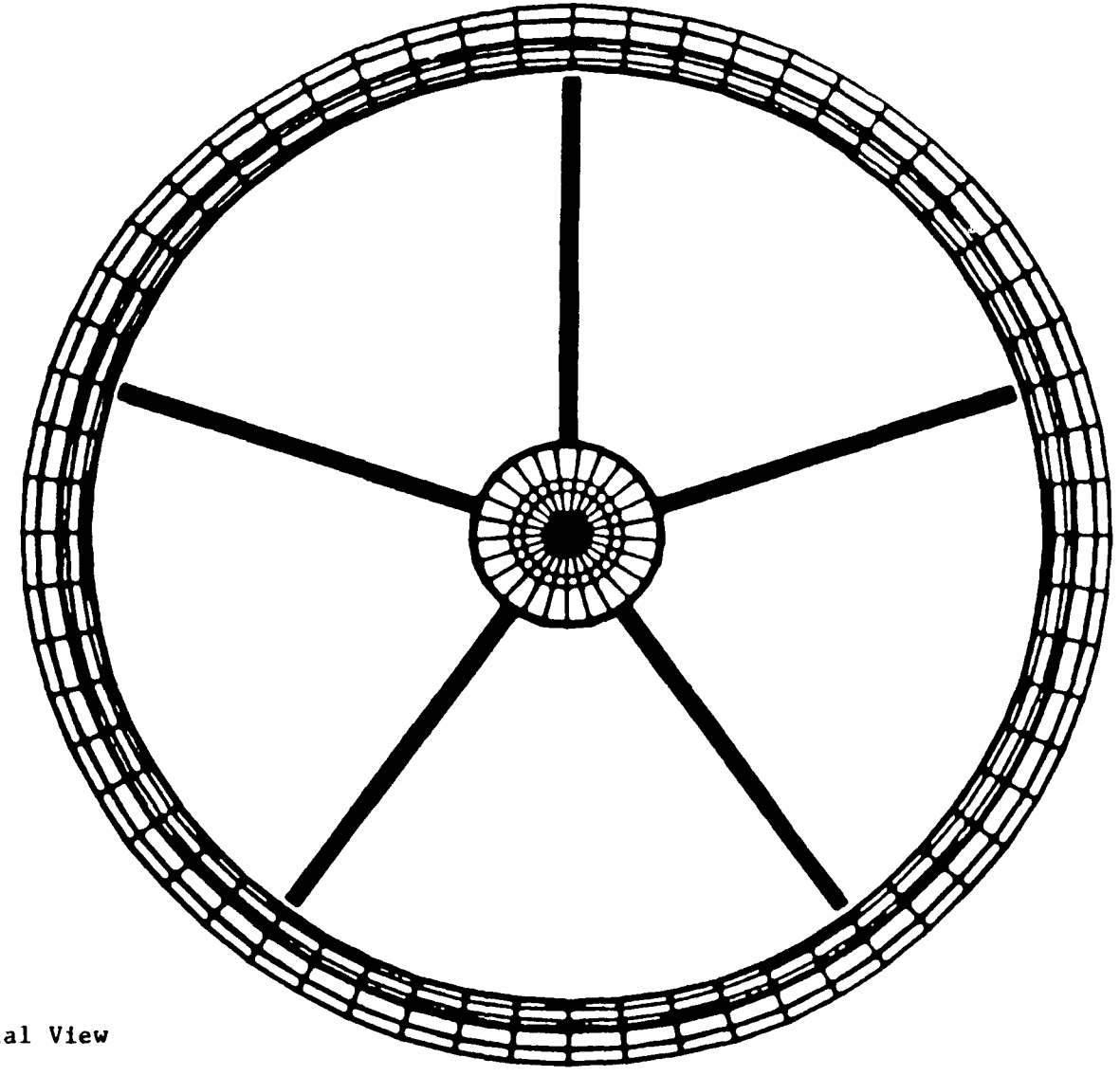

(a) Axial View

Figure 3.8. Stator, Hub and Shroud Assembly.

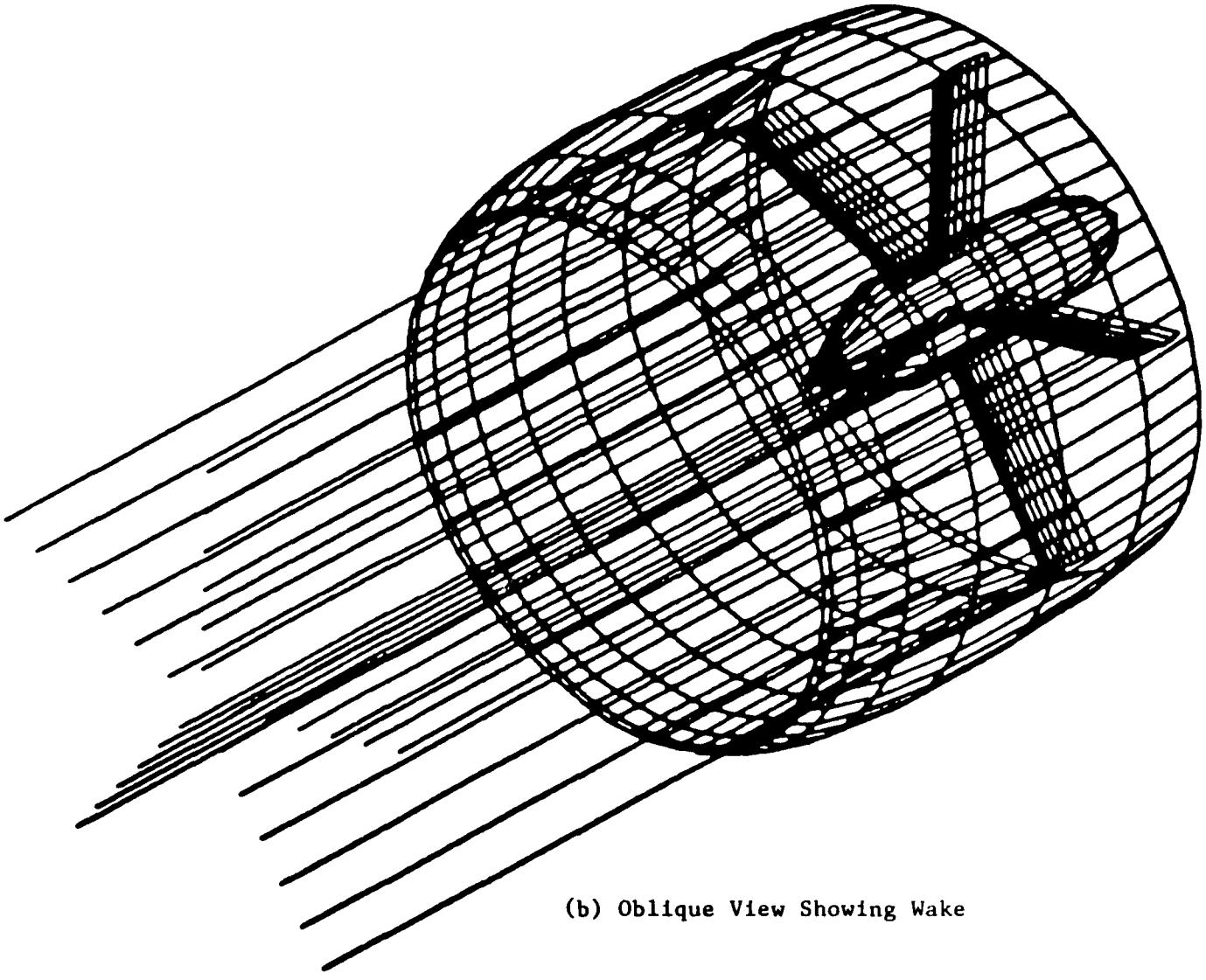

(b) Oblique View Showing Wake

Figure 3.8. Concluded.

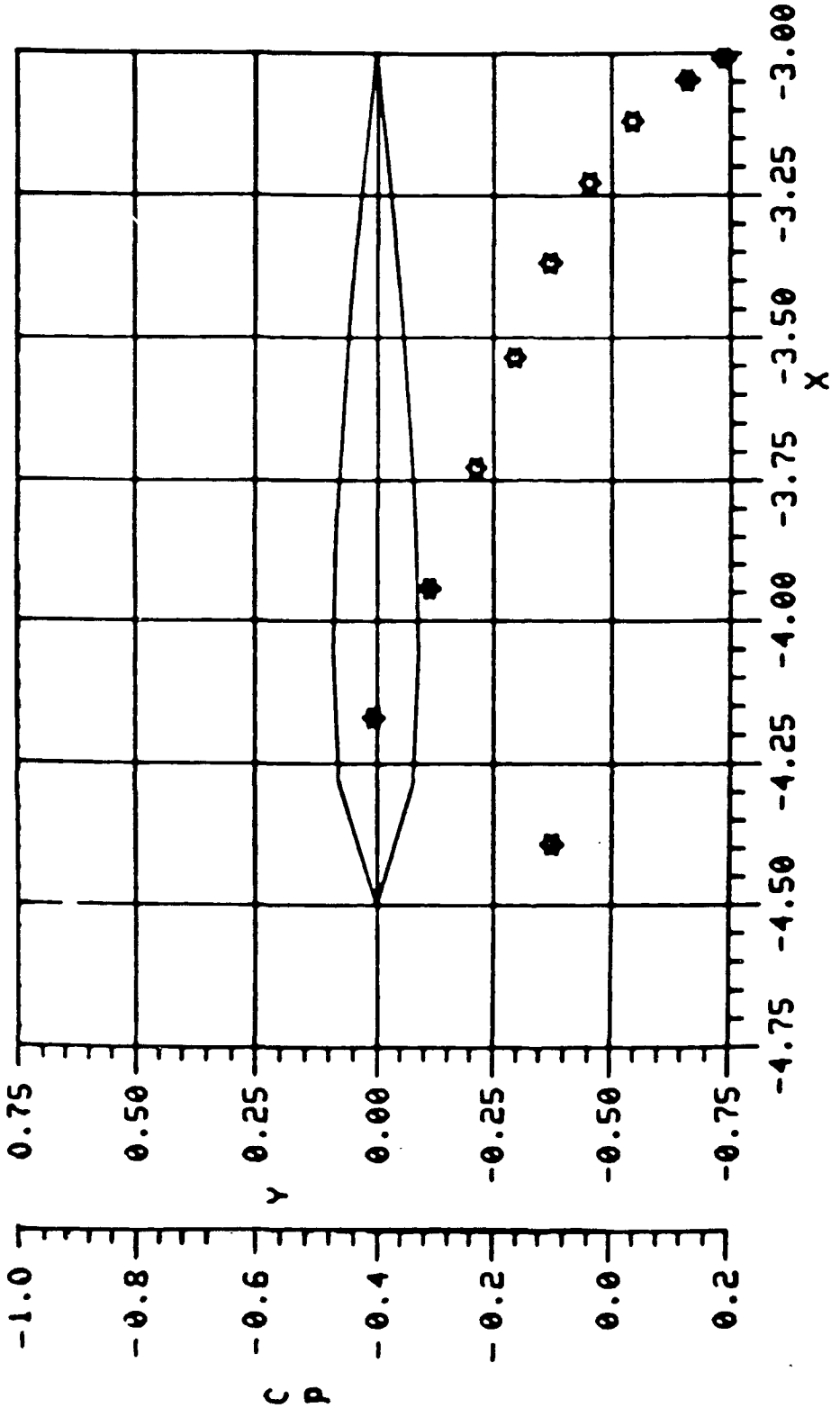

Figure 3.9 . Pressure Distribution on Stator Section.

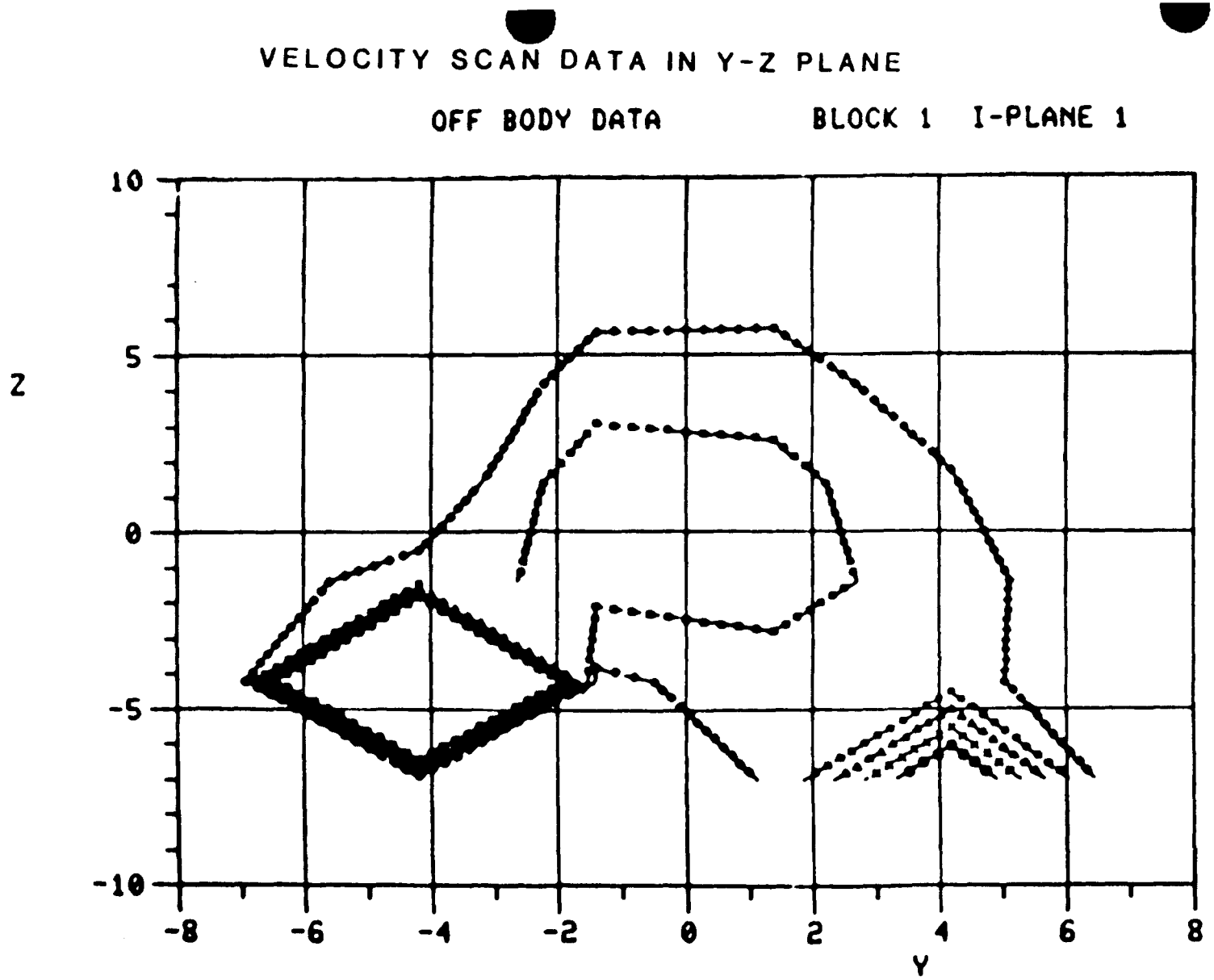

Figure 3.10. Velocity Scan Data Showing Flow Non-Uniformity.

4.0 ISOLATED HULL ANALYSIS

An accurate prediction of the flow at the stern is of great practical interest in the determination of propeller hull interaction. The improvements to the boundary layer and the streamline analysis reported in the previous chapter aid the correct modeling of hull flow. There is, however, an additional problem associated with the analysis of the viscous flow over the stern arising from the failure of conventional boundary layer calculation methods to account for thick boundary layers. In the literature this problem has been addressed in two general directions. One of these involves generalization and extension of the thin boundary layer methods, of both integral and differential types, to include such factors as changes in coordinate metrics normal to the surface, normal variation of pressure, and interaction between viscous and inviscid flow regions. The alternative approach to the calculation of stern flows involves numerical solutions to the complete Reynolds-averaged Navier-Stokes equations.

In the present work both of these approaches have been applied in a limited way. MPROP has been applied to calculate the potential flow about the hull form. The approximate boundary layer profiles calculated by MPROP have been used in an iterative scheme to model interaction between viscid and inviscid flows. The Reynolds-averaged Navier-Stokes solver developed by Patel et al. (32) was employed to calculate the viscous velocity profile in the plane of the propeller. Both approaches are briefly described below.

4.1 Potential Flow

The boundary layer characteristics of the Akron Airship (Figures 4.1(a), (b) and 4.2(a), (b)) were calculated before and after the changes to MPROP. The accuracy of the calculation method is demonstrated in Figure 4.3. This figure shows a comparison between measured and calculated boundary layer developments along a streamline on the U.S. Airship Akron.

The new and old calculations are compared at zero angle of attack and a Reynolds number of 4.56 million. As seen in Fig. 4.1, the momentum thickness is now considerably larger near the tail. The prediction was 25% below experiment; it is now 10% above the last experimental datum. The boundary layer thickness was also 25% below experiment with the wrong convergence term, Fig. 4.2(a). It is now 10% below. The skin friction and shape factor were only minutely affected by the change. Two comparisons with experiment are shown in Fig. 4.3: one near the midpoint of the hull, the other near the tail. It is worth noting that the good agreement would not be possible unless both the external velocity and boundary layer thickness matched that of experiment.

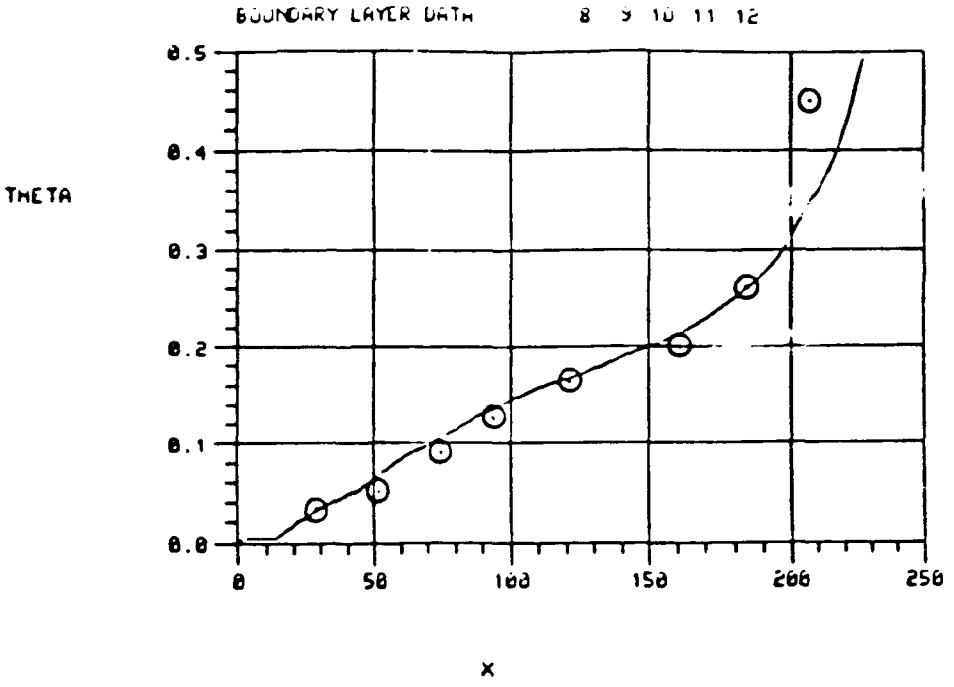

(a) Momentum Thickness before Changes to MPROP

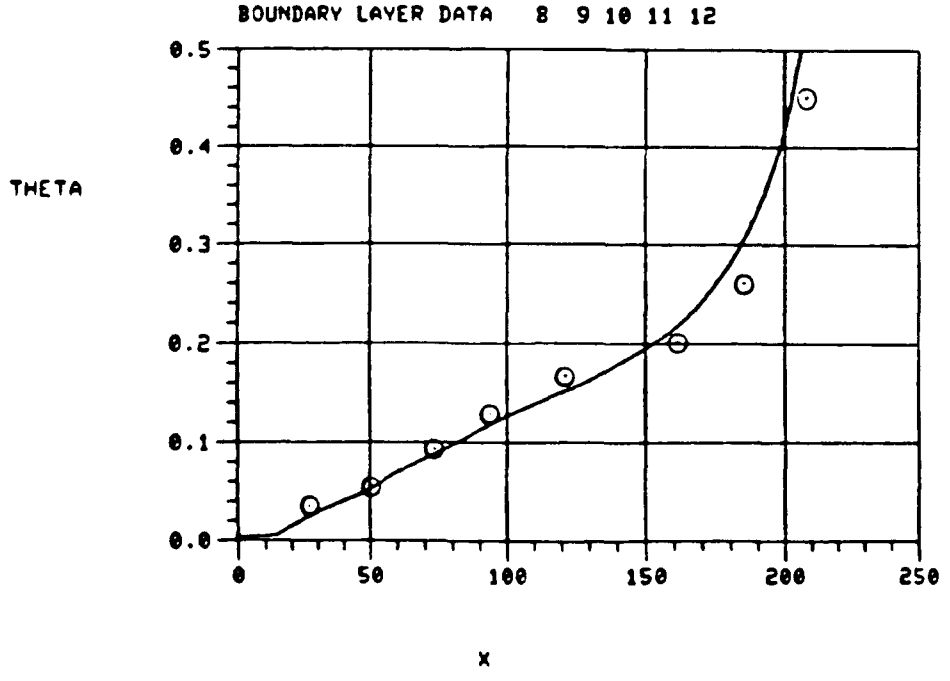

(b) Momentum Thickness after Changes to MPROP

Figure 4.1. Airship Akron Boundary Layer Characteristics Correlated with Experiment.

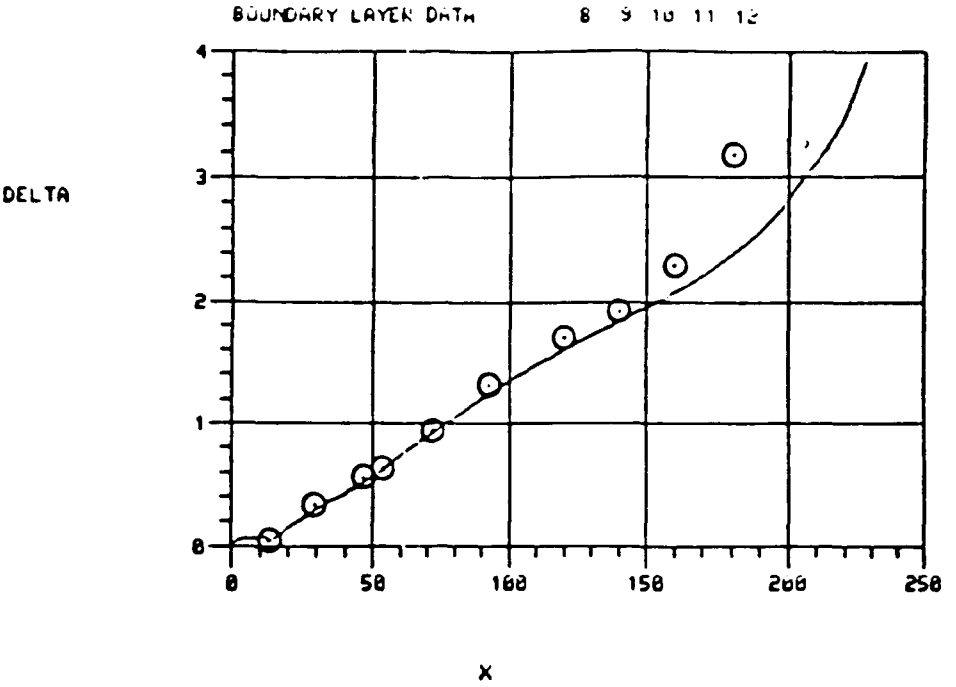

(a) Boundary Layer Thickness before Changes to MPROP

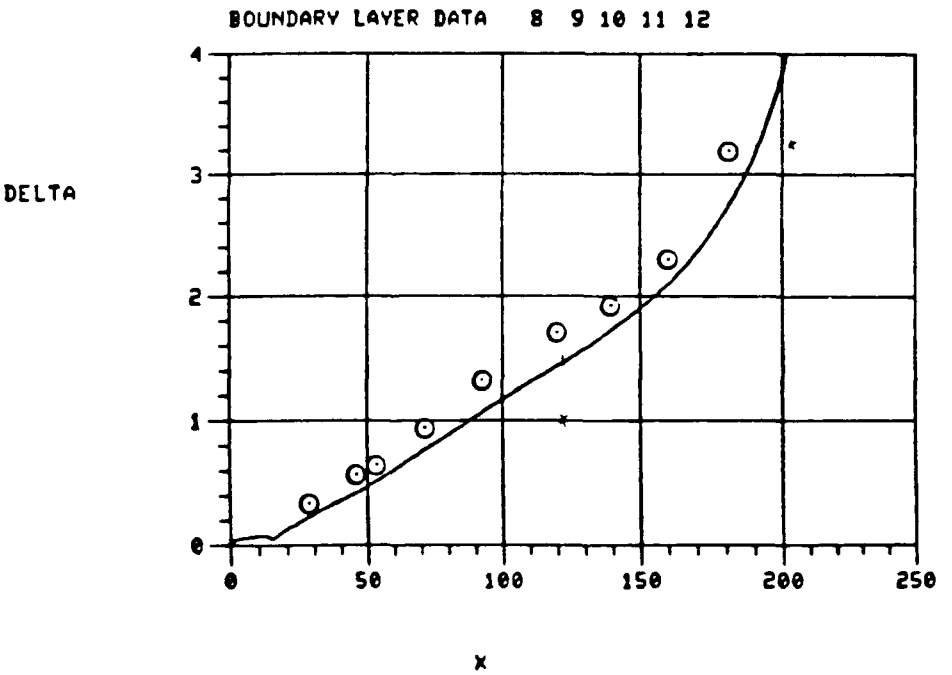

(b) Boundary Layer Thickness after Changes to MPROP

Figure 4.2. Experimental Correlation of Boundary Layer Characteristics.

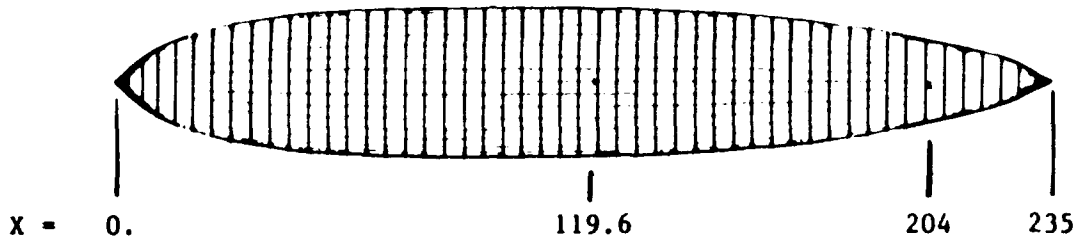

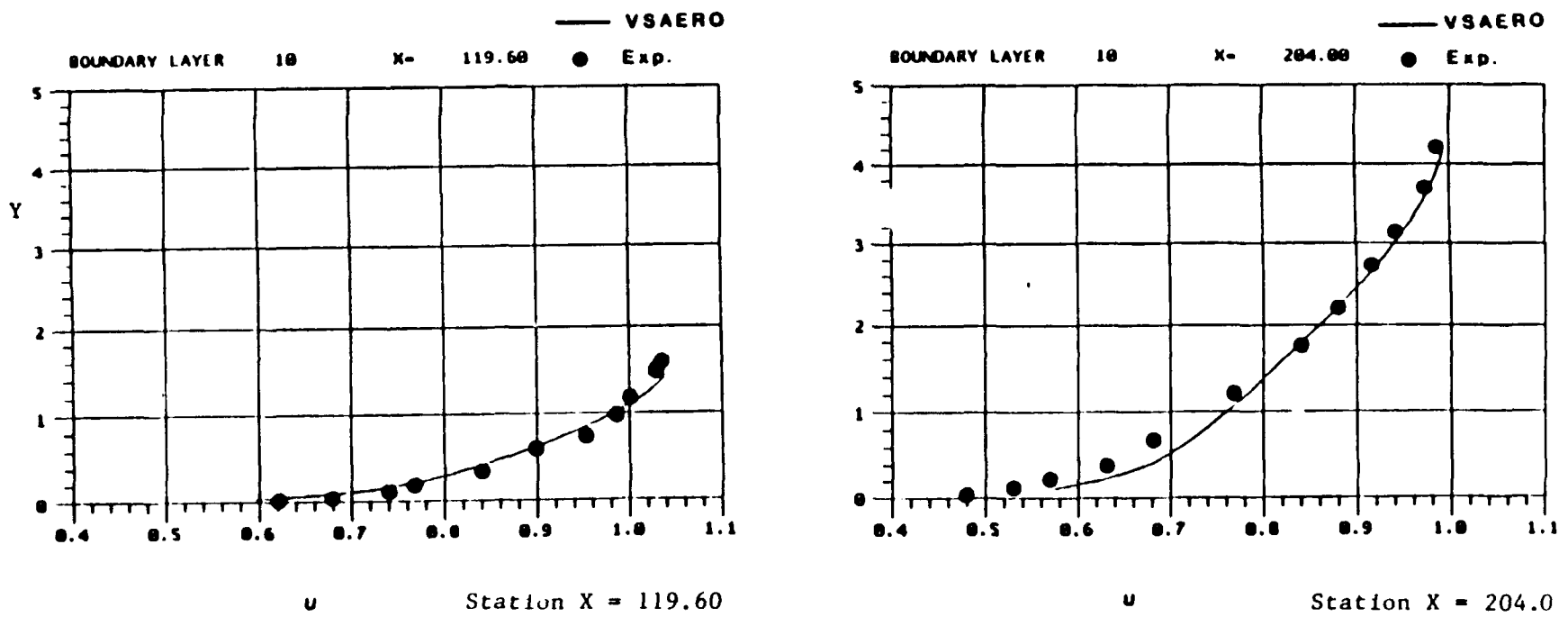

Figure 4.3. Velocity Profile Inside Boundary Layer Correlated with Experiment.

4.2 Viscous Flow

Axisymmetric bodies were chosen for this investigation in order to directly focus on the interaction between a propeller and a thick stern boundary layer. Experimental results for a set of body of revolution models are available (33). Figure 4.4 shows the geometry of the axisymmetric afterbodies. For the present investigation, Analytical Methods has considered two different codes to calculate the flow around the hull. These are the Reynolds-averaged Navier-Stokes solver (RANSTERN) and ARC3D. RANSTERN is a numerical method developed by Chen and Patel (34) for the solution of the fully-elliptic Reynolds-averaged Navier-Stokes equations. ARC3D, which was originally developed by Steger at NASA Ames Research Center (35) is based on the implicit approximate factorization algorithm of Beam and Warming (36) for unsteady compressible flow.

Figures 4.5(a) and (b) show the grid employed to calculate the flow on Afterbody 1. The pressure distribution on Afterbody 1 at a Reynolds number of 6.6 million is compared with experiment. Both ARC3D and RANSTERN correctly predict the pressure on the body surface. The second pressure peak is more accurately predicted by RANSTERN. Further analysis for the calculation of wake flow was made using RANSTERN.

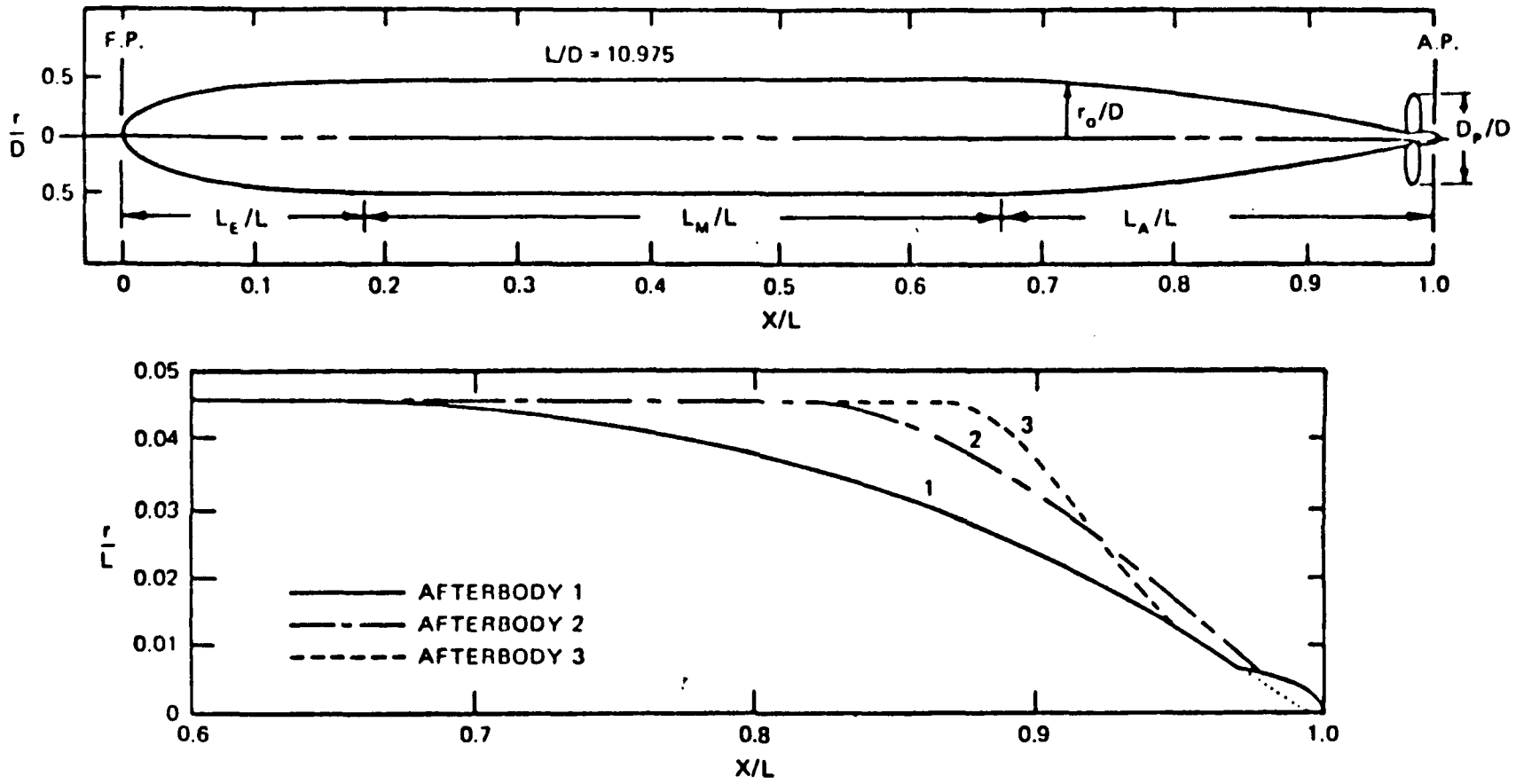

Figure 4.4. The Axisymmetric Afterbodies.

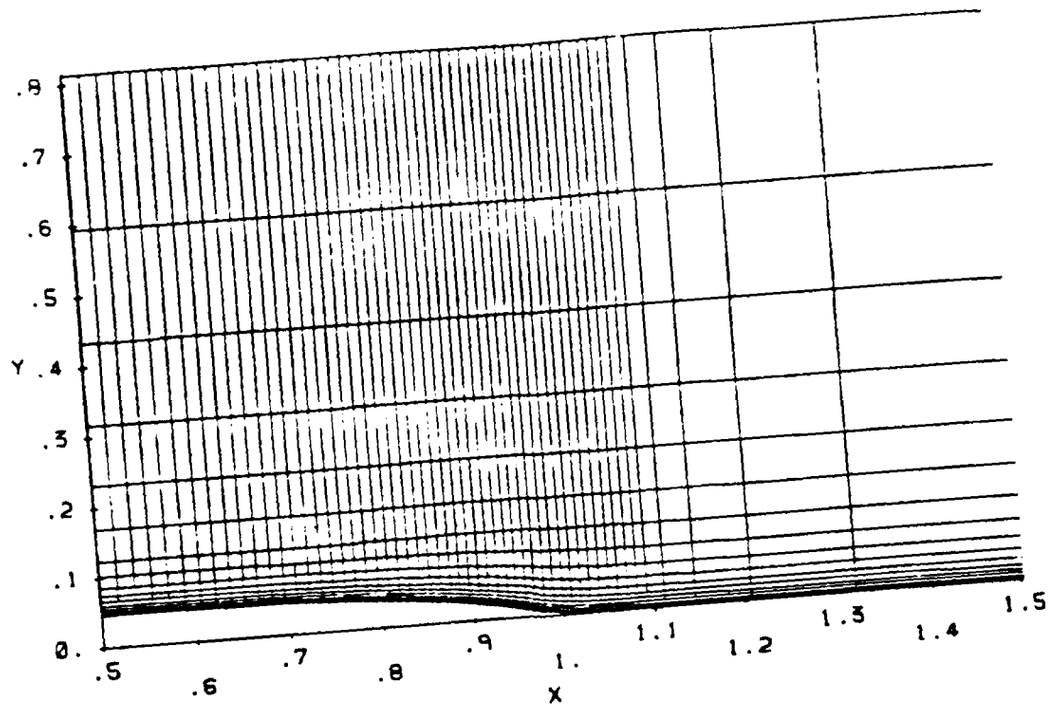

(a) Large-Domain Grid for Afterbody 1

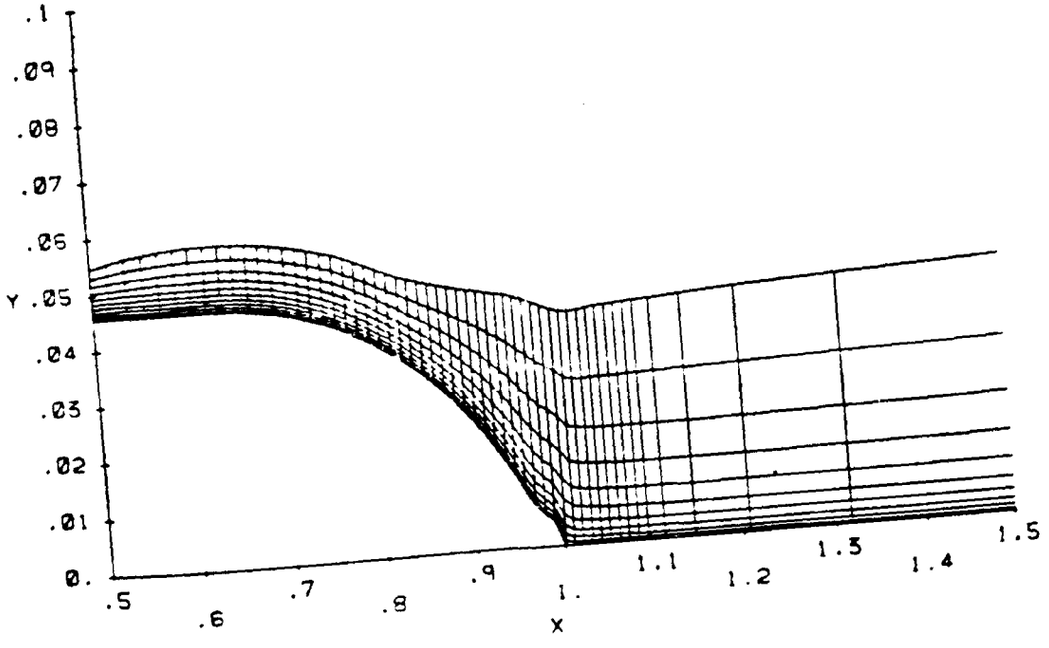

(b) Small-Domain Grid for Afterbody 1

Figure 4.5. Grid for Afterbody 1.

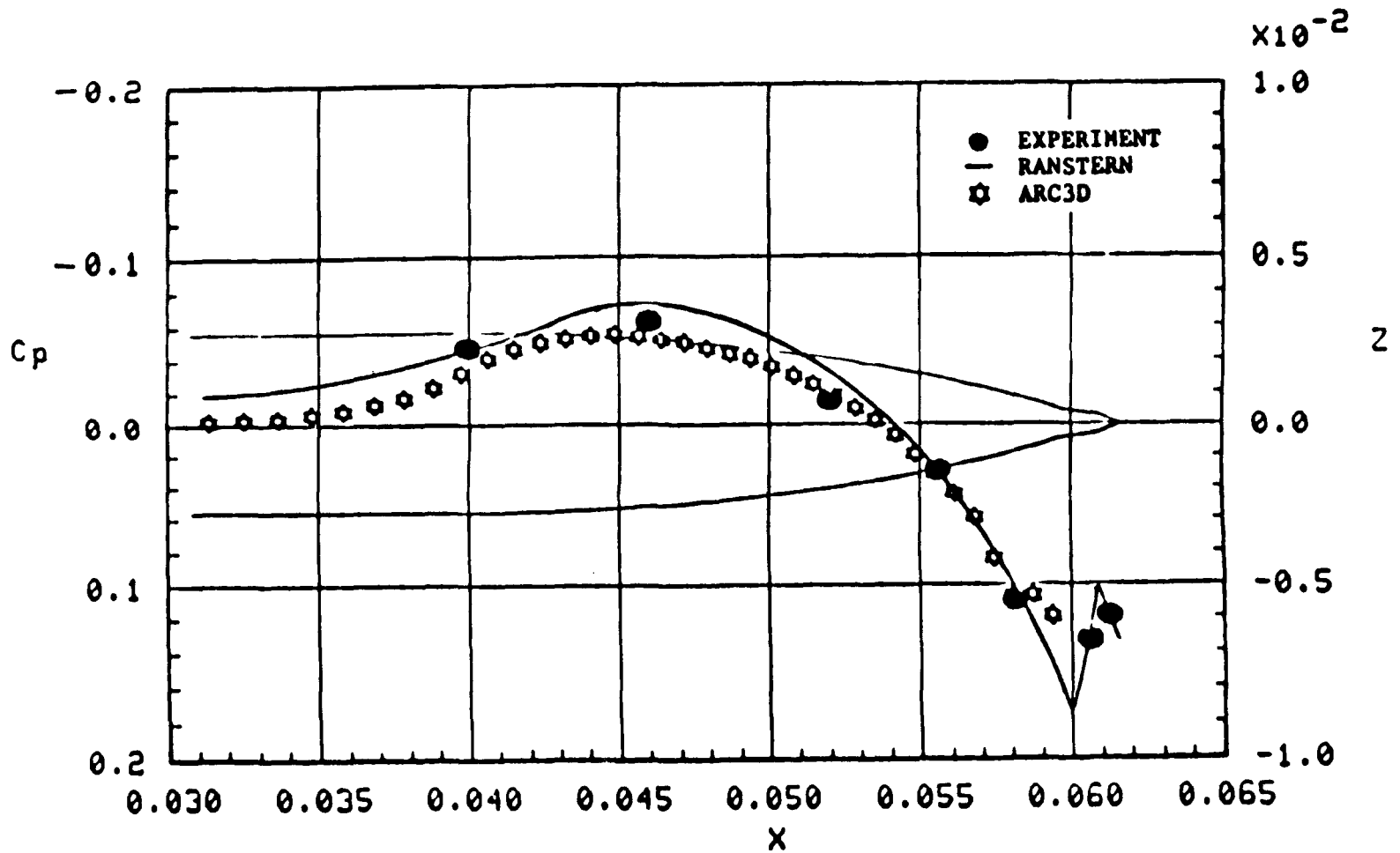

Figure 4.6. Pressure Distribution on Afterbody 1 at Re = 6.6 Million.

5.0 PROPELLER-HULL INTERACTION

The complete problem of propeller-hull interaction without restrictive assumptions on geometry, the nature of viscous effects and types of cavitation is both difficult and subject to prohibitive computational costs. Many of the physical processes involved in propeller-hull interaction are locally dominated by viscosity. However, it is still appropriate to represent the flow field due to the propeller action by means of a velocity potential satisfying the Laplace equation. Of the different computational approaches available to solve the resulting equations, the Green's function surface singularity method coupled with special routines for nonlinear effects has the promise of success.

5.1 Technical Approach

Consider a propeller operating in the wake of a long hull. The radius of the hull wake is assumed to be comparable in size to the propeller radius. In other words, the propeller is completely immersed in the boundary layer of the hull. For the purposes of the analysis the following two viscous assumptions are made.

(1) The viscous hull flow at the propeller plane is calculated by a three-dimensional finite difference code by neglecting the presence of the propeller.

(2) The unsteady propeller flow is modeled as a potential flow problem with nonuniform inflow describing the hull wake.

By the above two assumptions the overall problem of propeller-hull interaction becomes decoupled into two constituent parts. The first part is entirely viscous and three dimensional. Finite-difference codes solving Navier-Stokes equations are appropriate for the viscous analysis. The viscous analysis provides the wake fractions in the plane of the propeller. The propeller field is constructed by the method of surface singularity distribution satisfying an implicit boundary condition of the exit plane of the viscous domain. Inviscid flow techniques are applicable because the vorticity contained in the hull wake is neglected.

The scope of the present investigation is limited to calculating the flow field around a propeller operating in the presence of a thick and possibly separated turbulent hull wake. The focus here is on the unsteady pressure distribution on the propeller surface and is caused by the azimuthal variation of inflow in the plane of the propeller. This problem has been modeled in two different ways. Firstly, MPROP has been modified to calculate a series of solutions as a perturbation over a basic uniform flow solution. Secondly, the entire problem has been analyzed by USAERO, an unsteady code marched in time through several revolutions of the propeller. In the following paragraphs, a brief description of the two methods are given.

5.2 Frequency Band Analysis

Consider an assemblage of several three-dimensional closed bodies with an outer boundary, S, moving through a large mass of constant density fluid. Let W denote the wake surface of bodies with non-zero circulation. The velocity potential across the wake is discontinuous. In the region excluding the potential barrier of the wake, the flow is non-circulatory and the velocity potential at any point, P, in the flow (following Lamb's (15)) is:

$$\phi_p\left[x_p, y_p, z_p, t\right] = \frac{1}{4\pi} \iint_S \frac{1}{r} \frac{\partial \phi}{\partial n} \, dS + \frac{1}{4\pi} \iint_{S+W} \phi \, \frac{\partial}{\partial n} \left[\frac{1}{r}\right] dS \qquad (5.1)$$

where

$$r = \frac{1}{\sqrt{\left(x_p - x_1\right)^2 + \left(y_p - y_1\right)^2 + \left(z_p - z_1\right)^2}} \qquad (5.2)$$

and x_1, y_1 and z_1 represent a point on the body surface corresponding to the variable of integration. The integration must extend over all points on the body and wake surface. ϕ is the disturbance potential due to body motion and vanishes at infinity. When point P is on the surface, the locally singular kernel, $1/r$, must be replaced by the appropriate limiting value and should be excluded from the region of integration.

Discretization of S into N panels, assuming that ϕ is constant on each of the panels and $\partial\phi/\partial n$ takes the value of prescribed normal velocity, provides the following matrix equation for the unknown velocity potential on the surface, ϕ_s.

$$[A]\ [\phi_s] = [\phi_N]$$

Elements of matrix A are geometric quantities defined by

$$\iint \partial/\partial n\ (1/r)\ dS$$

and ϕ_N is the velocity potential induced at a control point by the sum of all constant strength sources of known strength. The former may be recognized as the velocity potential induced at a control point by a unit strength doublet whose axis is normal to the panel surface. The above matrix equation is the basic equation.

The inclusion of a spatially non-uniform velocity distribution resulting from hull wake may now be considered. The flow in the steady state must repeat itself every $2\pi/N$ degrees of rotation even when spatially non-uniform inflow from the hull wake is present. By comparison with the steady propeller problem, the major change is circumferential variation of velocity normal to the propeller. As the blade rotates it encounters a change in the normal velocity as a function of θ, the angular position of the blade. The general problem would appear to rule out the possibility of employing a

method based on steady flow analysis. However, there appears to be a way whereby the steady flow procedure can be applied to model general non-uniform flow. The application of that procedure will be outlined below. It is assumed that non-uniform flow is prescribed.

Let the non-uniform inflow be prescribed as a function of r and θ; i.e., $V = f(r,\theta)$.

Let the propeller rotate at n revolutions per second. $\int_0^{2\pi}\int_0^R V\, dr\, d\theta = Q$, say. Now, define $V_Q = Q/\pi R^2$, where R is the propeller radius. Now the prescribed non-uniform inflow can be represented as

$$V - V_Q = a_1 \cos\theta + a_2 \cos 2\theta + a_3 \cos 3\theta + \ldots$$

$$+ b_1 \sin\theta + b_2 \sin 2\theta + b_3 \sin 3\theta \qquad (5.3)$$

Typically, a_1, a_2, ..., b_1, b_2, etc. are functions of r and small in magnitude compared to V_Q.

A solution is next sought for the propeller in non-uniform inflow as follows.

$$\phi = \phi_q + \phi_{1c} \cos\theta + \phi_{2c} \cos 2\theta + \phi_{3c} \cos 3\theta \ldots$$

$$+ \phi_{1s} \sin\theta + \phi_{2s} \sin 2\theta + \phi_{3s} \sin 3\theta \qquad (5.4)$$

ϕ is the unknown doublet potential on a panel. ϕ_q is the potential value based on steady propeller flow at an advance coefficient, $J_q = V_Q/nD$. ϕ_{1c}, ϕ_{2c}, ..., ϕ_{1s}, ϕ_{2s}, etc. are unknowns to be determined. Here the relationship between blade-fixed coordinate system and space-fixed coordinate system may be noted. The onset flow is defined by Eq. (5.3) above in which θ is measured counterclockwise from the z-axis. A panel on a propeller rotating at w radians per second will negotiate an onset velocity corresponding to $\psi - wt$, where ψ is the angle made by the panel control point relative to the blade fixed axis; i.e., $\theta = \psi - wt$.

The coefficients of ϕ_{1c} and ϕ_{1s} are to be determined from a knowledge of source strengths required to account for the circumferential variation of onset flow. For a simple example, assume the onset flow is given by

$$V = V_Q + a_1 \cos\theta$$

A solution is sought in the form

$$\phi = \phi_Q + \phi_1 \cos \theta$$

Now, on the blade surface,

$$\partial\phi/\partial n = \mathbf{V} \cdot \mathbf{n}$$

or

$$\left(\frac{\partial \phi_Q}{\partial n} + \frac{\partial \phi_1}{\partial n} \cos \theta \right) = V_Q + a_1 \cos \theta \qquad (5.5)$$

Thus, $\partial\phi_1/\partial n = a_1$ will satisfy the boundary conditions on normal velocity. Based on Eq. (5.1),

$$\phi_{1c} = -\frac{1}{4\pi} \iint \frac{1}{r} a_1 \, dS + \frac{1}{4\pi} \iint_{s+w} \phi_{1c} \frac{\partial}{\partial n} \left(\frac{1}{r}\right) dS$$

The above equation is exactly equivalent to a doublet solution in response to a panel source strength of a_1. Though a_1 is a constant, it actually varies as a function of panel angular position, $\theta = wt$. In other words, with the source strength, a_1 being known, it is possible to solve for ϕ_{1c} in a manner similar to that of steady flow analysis.

An important aspect of unsteady flow is the shedding of variable strength vorticity. Ideally, a harmonic wake (i.e., a wake in which the strength varies as cos (x/ℓ) where x is the distance along the wake and ℓ is the net distance travelled by the wake in one revolution of the blade) must be modeled. In practise, these integrals can be constructed in a closed form. At this point a simplifying assumption is introduced--the response of the propeller perturbation potential to the circumferential velocity component is assumed to be <u>in phase</u>. The phase difference between the onset flow and wake strength has been neglected. Under this assumption the problem becomes similar to that of finding the solution for a steady onset flow of magnitude a_1. Now, the unsteady pressure, $\partial\phi/\partial t$, can be evaluated, remembering that $\theta = wt - \psi$.

$$\partial\phi/\partial t = -aw \cos (wt - \psi_1)$$

for the simple example.

5.3 Time-Dependent Analysis

5.3.1 Background

The time-dependent analysis of a propeller in nonuniform flow was computed using an existing program, USAERO. This code was developed at Analytical Methods, Inc. originally for helicopter blade tip analyses (37). Later, the method was extended to treat more general problems. The current version calculates the unsteady subsonic flow characteristics for multiple bodies in general motion. The motions may be prescribed or they can be calculated internally using a six-degree-of-freedom flight path integration routine which is an optional module.

Based on a time-stepping approach, USAERO provides a very general capability for applications to such transient problems as helicopter rotor/fuselage interactions (38), vehicle-on-vehicle interactions, propeller/stator problems, maneuvering vehicle (39) and store release problems. Output from the program includes time histories of integrated force and moment characteristics for selected parts of a **CONFIGURATION** together with the corresponding velocity and pressure distributions. These results, together with the three-dimensional geometry of the CONFIGURATION (including the generated wakes), may be displayed graphically step by step using the interactive program, OMNIPLOT, on a graphics workstation or in an "animated" sequence using interactive program, OMNI3D, on a Silicon Graphics IRIS 4-D series workstation.

5.3.2 Method Outline

The basis of the method is a time-stepping, surface singularity method which uses quadrilateral **PANELS** of uniformly distributed doublets and sources. The surface integrals in Green's theorem are evaluated in a piecewise manner over each PANEL to form panel influence coefficients. These are evaluated for each PANEL acting at the central control points on all the surface PANELS, thus forming a matrix of influence coefficients. Usually the source values are determined at the start of each time step according to the local velocity component normal to the PANEL surface (the source values include terms for normal inflow/outflow as well as boundary layer displacement). The doublet values are then solved using the matrix equations.

There is also provision to solve the source values (i.e., normal velocity) given the panel doublet strengths (potential). This is done on a **PATCH** by PATCH basis (a PATCH is a collection of panels in a rectangular array). Thus mixed boundary condition problems may be treated. Some PATCHES may have user input values of both source and doublet for special flow modeling options.

Extensive component copying facilities are provided at the input level. These not only provide a convenient way of describing the multiple blades of a propeller, but also provide an option for blades to copy earlier doublet solutions from a "primary" blade in situations where the solution repeats as blades pass the same azimuthal station. This capability is applicable in the case of the propeller in nonuniform flow provided the nonuniformity is

steady in the ground-fixed frame. This reduces the number of unknowns, and hence computing time, considerably.

The tangential velocity at the solid surfaces of the CONFIGURATION is obtained from the doublet gradient. The normal component (which can be non-zero for inflow/outflow and transpiration modeling) is provided by the source value. Off-body velocity perturbations are evaluated by summing all doublet and source singularity contributions. These velocities are used for general flow field information as well as for wake point convection. The WAKES grow with each time step, with new wake points being propagated from wake-shedding lines, while all the previous wake points are convected at the local fluid velocity.

5.3.3 Method Formulation

Basic Equations

Consider the CONFIGURATION moving with velocity, $\mathbf{V}_B$, through an unbounded fluid initially at rest, Figure 5.1. The basic assumptions are that the effects of viscosity are largely confined to thin boundary layers on the CONFIGURATION surface and that wake vorticity is essentially concentrated in thin, free-shear layers and discrete vortex filaments. The majority of the flow is, therefore, regarded as inviscid, irrotational and incompressible. Laplace's equation can then be applied,

$$\nabla^2\phi = 0 \tag{5.6}$$

The convention adopted here is that the perturbation velocity is the negative gradient of ϕ:

$$\mathbf{v} = -\nabla\phi \tag{5.7}$$

Green's Theorem is applied next. Note that with $\nabla^2\phi = 0$ the volume integral disappears. The flow is therefore uniquely determined by surface integrals of ϕ and its normal derivative over the surface of the CONFIGURATION and its WAKE. Thus the velocity potential, ϕ_p, for a point, P, on the wetted side of the surface is

$$\phi_p = \frac{1}{4\pi}\int\int_{S-P} \phi\, \mathbf{n}\cdot\nabla\left(\frac{1}{r}\right) dS + \frac{\phi_P}{2} - \frac{1}{4\pi}\int\int_{S} \frac{1}{r}\,\mathbf{n}\cdot\nabla\phi\, dS$$

$$+ \frac{1}{4\pi}\int\int_{W} (\phi_U - \phi_L)\,\mathbf{n}\cdot\nabla\left(\frac{1}{r}\right) dW \tag{5.8}$$

where $\mathbf{n}$ is the outward normal from the surface and r is the length of the vector from the surface element, dS, to the point, P. S-P signifies that the point, P, is excluded from the surface integral--the limiting process for the singular point when $r \to 0$ yields the local contribution, $\phi_p/2$.

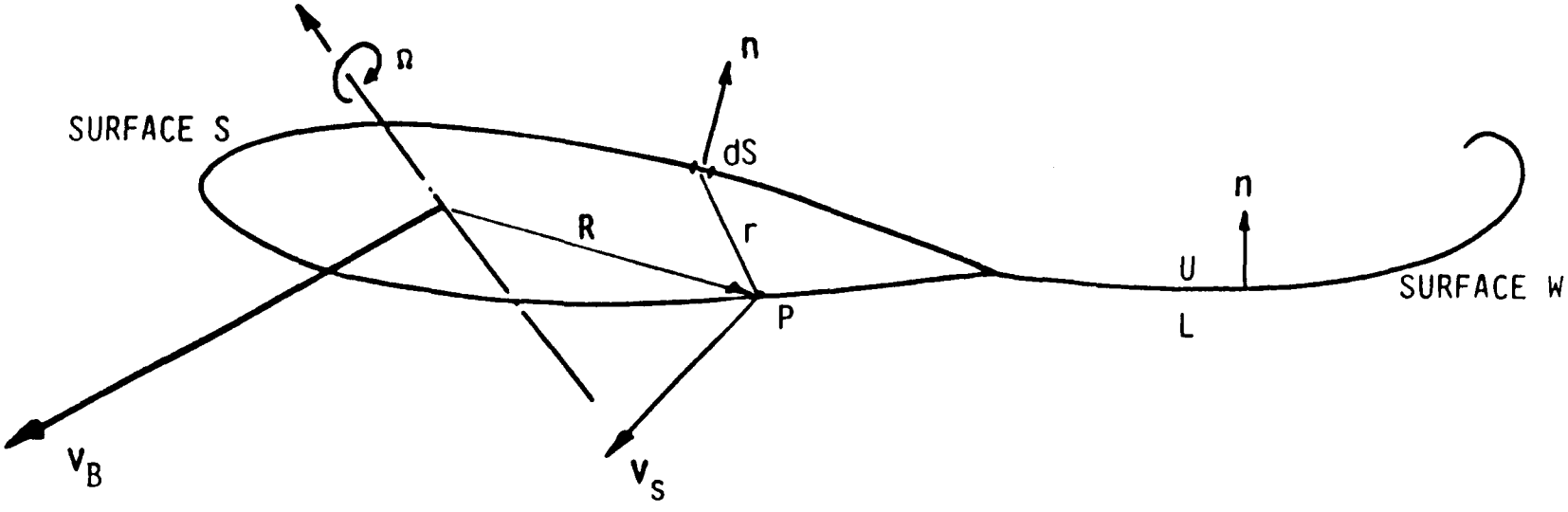

Figure 5.1. General Arrangement.

The first integral in Eq. (5.8) is the contribution from a surface distribution of normal doublets of strength,

$$\mu = \phi/4\pi \tag{5.9}$$

The second integral is the contribution from a surface distribution of sources of strength,

$$\sigma = -\frac{\mathbf{n} \cdot \nabla\phi}{4\pi} \tag{5.10}$$

The third integral in Eq. (5.8) is the contribution from the wake surface. Here, the upper and lower surfaces have been combined, taking the upward facing normal. The upper and lower potentials have been combined yielding a wake doublet distribution of strength,

$$\mu_W = \frac{(\phi_U - \phi_L)}{4\pi} \tag{5.11}$$

This is the potential jump across the wake. In combining the upper and lower surfaces the source term has been discarded, implying that there is no normal flow relative to the wake--the wake points, in fact, convect with the flow and so the wake surface is always aligned with the local flow. (The entrainment effect due to turbulent mixing is neglected for the moment.)

Thus, Eq. (5.8) becomes

$$\iint_{S-P} \mu\, \mathbf{n} \cdot \nabla \left(\frac{1}{r}\right) dS - 2\pi\mu_P + \iint_S \frac{\sigma}{r}\, dS + \iint_W \mu_W\, \mathbf{n} \cdot \nabla \left(\frac{1}{r}\right) dW = 0 \tag{5.12}$$

In the general case of analyzing the flow about a given configuration the doublet distribution on the surface is unknown while the source distribution is determined directly by the external Neumann boundary condition specifying the resultant normal velocity at the boundary. The flow velocity relative to the surface is,

$$\mathbf{V} = \mathbf{v} - \mathbf{V}_s \tag{5.13}$$

where $\mathbf{v}$ is the perturbation velocity (Eq. (5.7)), and

$$\mathbf{V}_s = \mathbf{V}_B + \boldsymbol{\Omega} \times \mathbf{R} - \mathbf{V}_\infty \tag{5.14}$$

is the surface velocity relative to the undisturbed fluid. $\mathbf{V}_B$ is now measured in an inertial frame (GFF) which may have an onset flow, $\mathbf{V}_\infty$. $\boldsymbol{\Omega}$ is the velocity of rotation of the body, and $\mathbf{R}$ the position of a surface point relative to the rotational axis. The normal component of $\mathbf{V}$ is, from Eq. (5.13),

$$\mathbf{V} \cdot \mathbf{n} = \mathbf{v} \cdot \mathbf{n} - \mathbf{V}_s \cdot \mathbf{n} = V_N \tag{5.15}$$

V_N is the resultant normal velocity at the surface. This is usually zero (solid boundary), but it can have a number of nonzero parts, e.g.,

$$V_N = VNORM + V_{BL} \tag{5.16}$$

where VNORM is the user specified inflow/outflow representing an engine inlet/exhaust modeling, and V_{BL} is the boundary layer displacement effect using the transpiration technique,

$$V_{BL} = \frac{\partial}{\partial s} (V_e \delta^*) \tag{5.17}$$

where V_e is the local speed at the edge of the boundary layer and δ^* is the displacement thickness. The derivative is taken in the direction of the local external flow.

Using Eqs. (5.7), (5.10) and (5.15), the source term is,

$$\sigma = (\mathbf{n} \cdot \mathbf{V}_B + \boldsymbol{\Omega} \cdot \mathbf{R} \times \mathbf{n} - \mathbf{n} \cdot \mathbf{V}_\infty + VNORM + V_{BL})/4\pi \tag{5.18}$$

When the onset flow is nonuniform in the ground-fixed frame, the $\mathbf{n} \cdot \mathbf{V}_\infty$ term for a particular panel is time dependent as that panel moves through space. The local instantaneous value is picked up by spatial interpolation in the defined onset flow according to the location of the panel center.

The wake development is followed over a number of time steps. At each step a new set of wake points is propagated from the wake shedding lines, each point taking with it the local doublet strength (see later under Kutta condition). Thus, at each time step the wake doublet strength in Eq. (5.12) is known. The only unknown is the surface doublet distribution which is now obtained as the solution to Eq. (5.12).

Surface Pressure

With the solution known, the surface velocities and pressures can be evaluated. The tangential component of perturbation velocity is obtained from the surface gradient of the potential. The normal component comes from the source term. The pressure coefficient is evaluated using the Bernoulli equation for a moving frame,

$$C_P = V_s^2 - V^2 + 2 \frac{\partial \phi}{\partial \tau} - \frac{z}{Fr^2} \tag{5.19}$$

This may be displayed in its separate component parts:

Dynamic Term	$CPD = V_s^2 - V^2$
Impulsive Term	$CPI = 2 \frac{\partial \phi}{\partial \tau}$
Hydrostatic Term	$CPH = \frac{-z}{Fr^2}$

Here, the velocities are normalized by a reference speed, VREF. Time is normalized by REFL/VREF, REFL being a reference length, e.g., propeller radius. τ = t*VREF/REFL. The velocity potential, ϕ, is normalized by VREF and REFL. The geometric height to the free surface, z, is normalized by REFL, and Fr = Froude Number = VREF/$\sqrt{gL}$, where L=2*REFL.

Force and Moment

The forces and moments are obtained by integrating the pressure over the surface.

The force coefficient is,

$$C_F = -\int\int_S C_P \, \mathbf{n} \, \frac{dS}{SREF} \tag{5.20}$$

SREF is the reference area.

The moment coefficient is,

$$C_M = \int\int_S \frac{C_P \, \mathbf{n} \times \mathbf{R} \, dS}{SREF \; L} \tag{5.21}$$

where L is a reference length--usually the mean chord, CBAR, for pitching moment and SSPAN (semispan) for yawing and rolling moments.

Kutta Condition

If we apply the condition of equal upper and lower pressure (using Eq. (5.19)) at a thin trailing edge, we obtain the unsteady Kutta condition,

$$\frac{\partial \mu_W}{\partial \tau} + V_M \frac{\partial \mu_W}{\partial s} = 0 \tag{5.22}$$

V_M is the mean convection speed and the s direction is the local mean flow direction. μ_W is the jump in doublet strength across the trailing edge, Eq. (5.11), i.e., μ_W is the newly emerging wake strength. Equation (5.22) essentially states that the rate of change of circulation at the trailing edge must match the transport of circulation into the wake.

Wake Movement

When a solution has been obtained, velocities are computed at all existing wake points using a summation of all singularity contributions in the model. All wake points are then propagated along the local velocity vector for a small time step. Simultaneously, a new set of wake panels is created along the separation lines, Figure 5.2. The current trailing-edge doublet values (i.e., the doublet jump across the wake at the trailing edge) is transferred to the newly created wake points. The doublet strength on each wake point remains constant for the remainder of the calculation. The wake vorticity effectively varies in time and space according to the local stretching or contraction of the wake sheet as the wake points convect at the local velocities.

A new set of doublet influence coefficients is calculated for the new wake configuration at each time step.

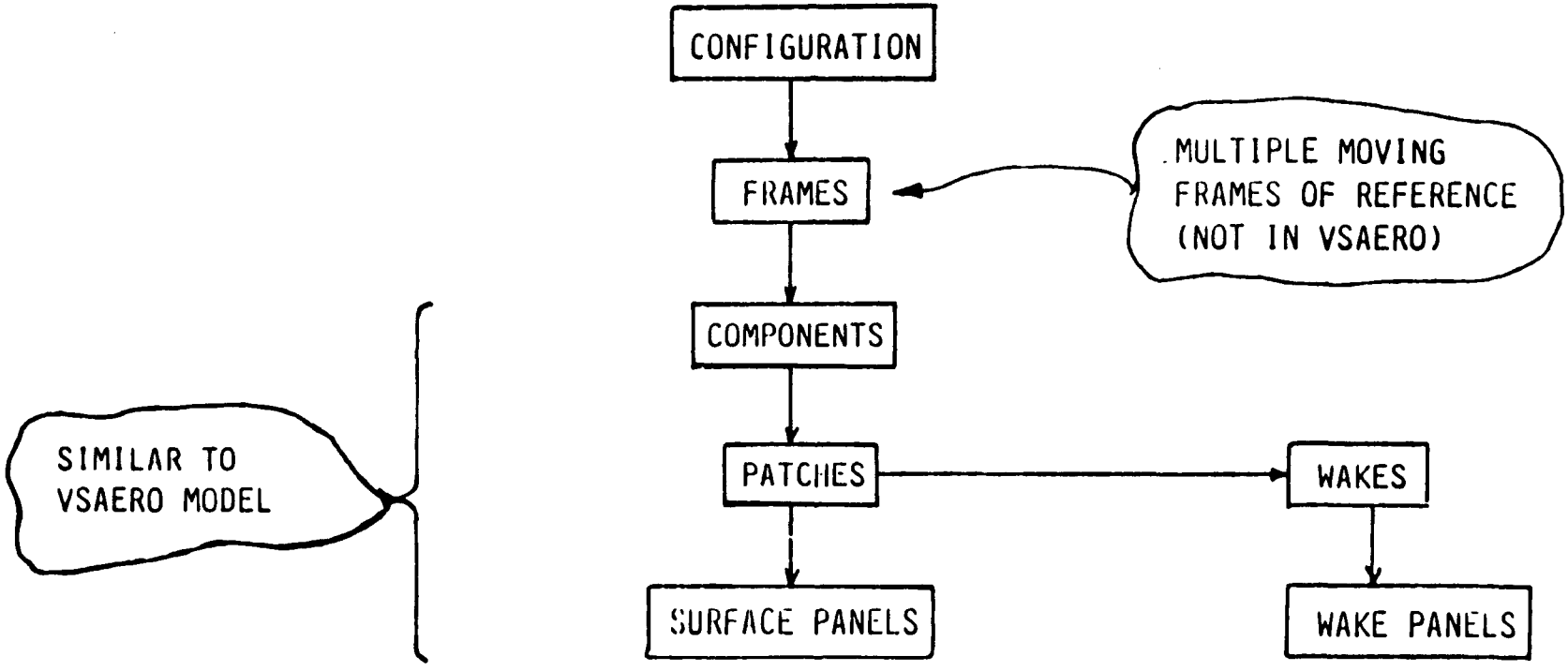

Figure 5.2. USAERO Configuration Breakdown.

6.0 DISCUSSION OF RESULTS

Five test cases were chosen to validate different aspects of the calculation. These are listed below.

(1) Propeller in uniform flow
(2) Propeller in simple nonuniform flow
(3) Propeller in fully nonuniform flow--MPROP modeling
(4) Unsteady propeller flow--USAERO modeling
(5) Simple propeller-hull interaction

6.1 Propeller in Uniform Flow

MPROP as modified and extended for propeller-hull interaction was validated against a set of multi-bladed propulsors. Accurate prediction of surface pressures is a crucial test of the overall modeling capability. Agreement with experiment for a range of propeller models and advance ratios is excellent.

Figure 6.1 shows the paneling for a six-bladed marine propeller. Limited blade surface pressure data was available for this case (40), and the comparison shown in Figures 6.2(a) and (b) for a typical radial station for both an on- and off-design condition shows good agreement.

A second propeller has been analyzed using MPROP. This is a five-bladed propeller for which experimental results are available at several off-design conditions (Hoshino). Some of these calculations are enclosed as part of a further demonstration of the code's capability. Figure 6.3 shows a five-bladed propeller. Pressure correlation with experiment is shown for the advance coefficients, J = 0.3, 0.5 and 0.7, at each of two radii locations in Figures 6.4 through 6.9. This propeller has a finite thickness at the trailing edge, and the code now has the capability to treat correctly the Kutta condition for such a geometry. The satisfaction of the Kutta condition is achieved through iterative determination of the sectional circulation. The successful calculations for this propeller validate the newly coded procedure.

The paneling for a four-bladed propeller is shown in Figure 6.10. Extensive data on surface pressure is available for this propeller tested in Amsterdam (41). Figures 6.11 through 6.18 plot calculated and measured Cp at several radial locations for the advance coefficients, J = 0.4 and J = 0.6, respectively. Agreement between theory and experiment for this propeller is particularly good. The improved correlation is due to the Y-wake model developed for thick trailing edges.

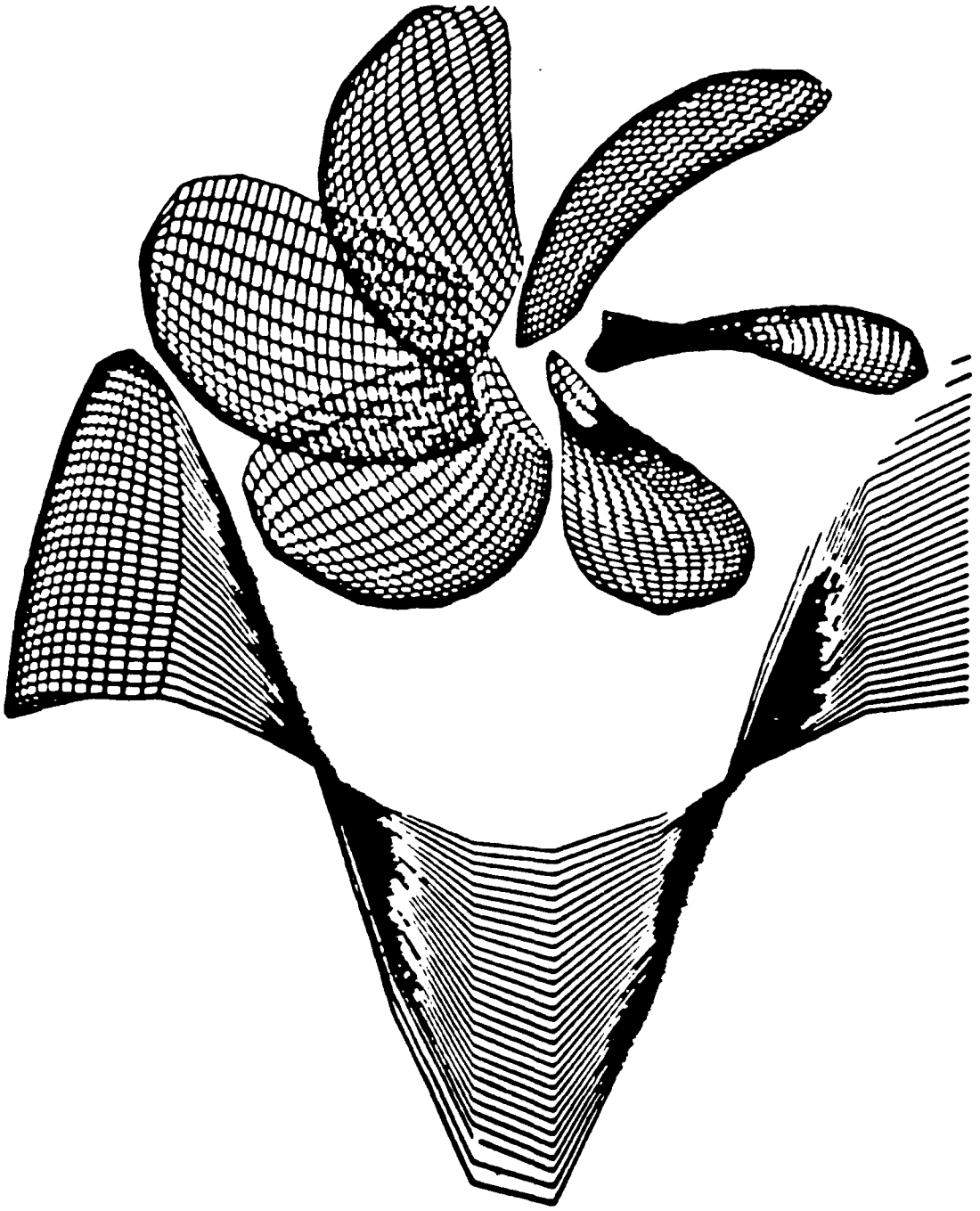

Figure 6.1. Blade Paneling and Wake. Propeller Model No. 0123, Ship Research Institute, Tokyo, Japan (40).

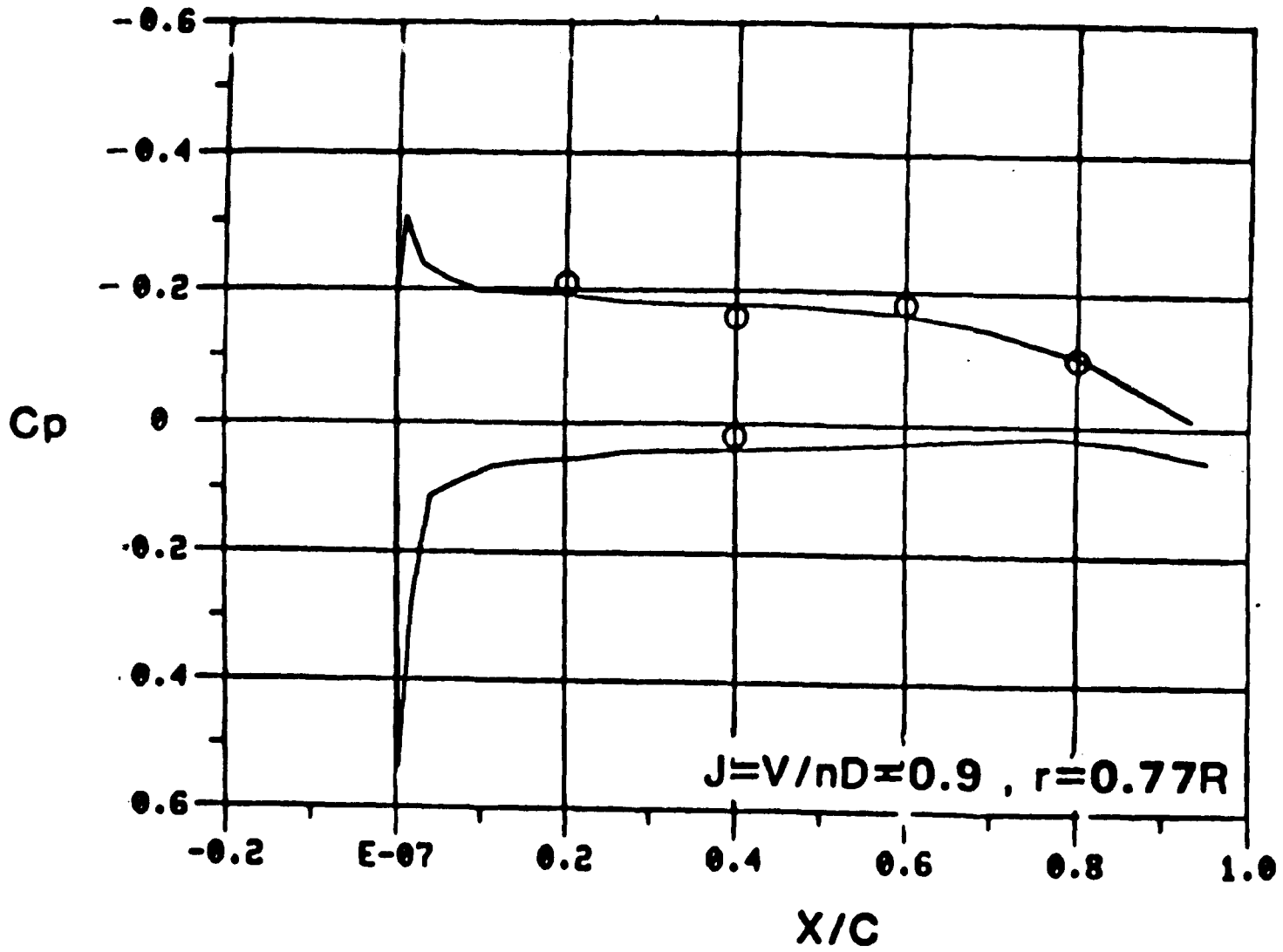

(a) J = V/nD = 0.9, R = 0.77R

Figure 6.2. Surface Pressure Correlation on Propeller 0123 (40).

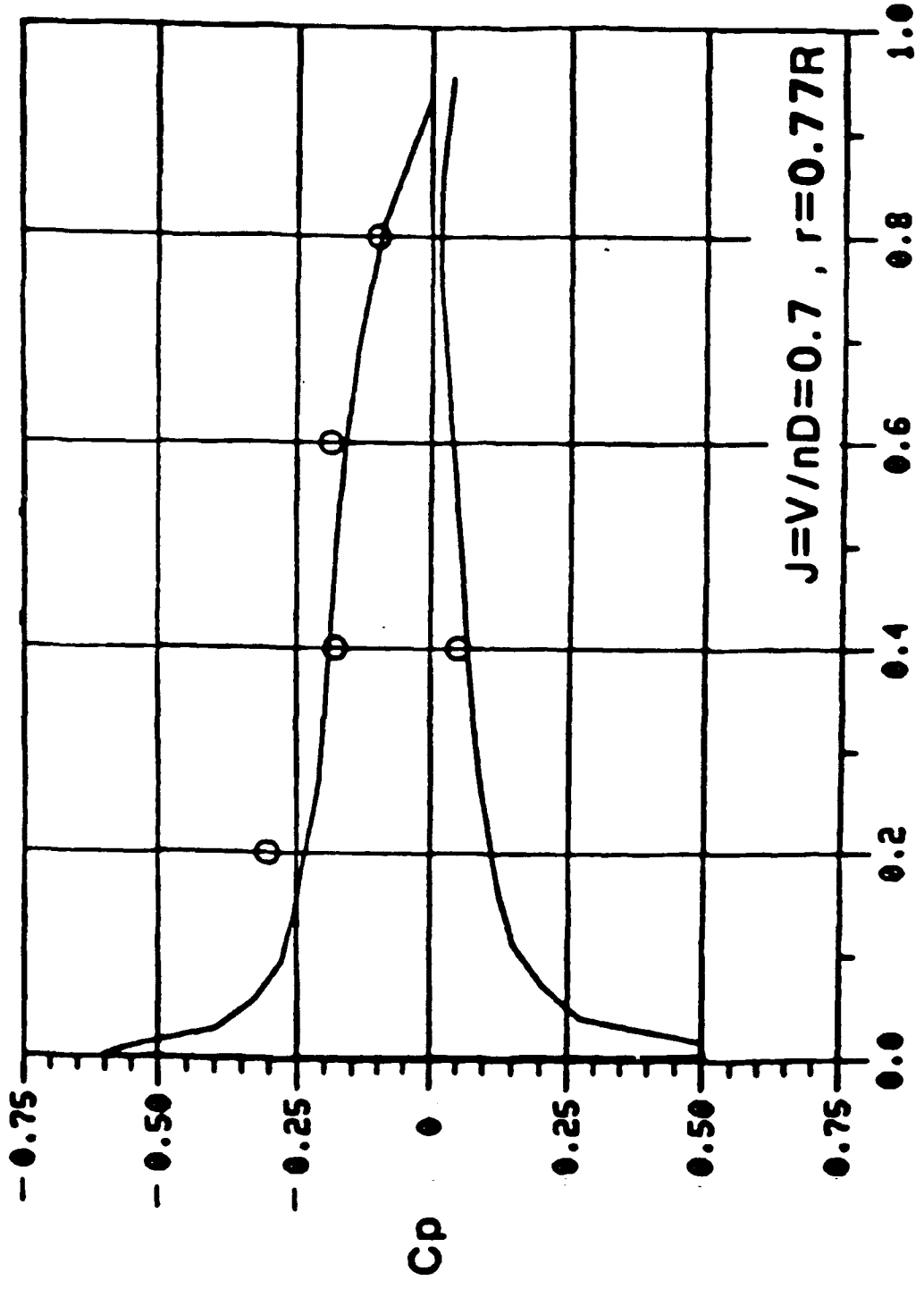

(b) J = V/nD = 0.77, r = 0.77R

Figure 6.2. Concluded.

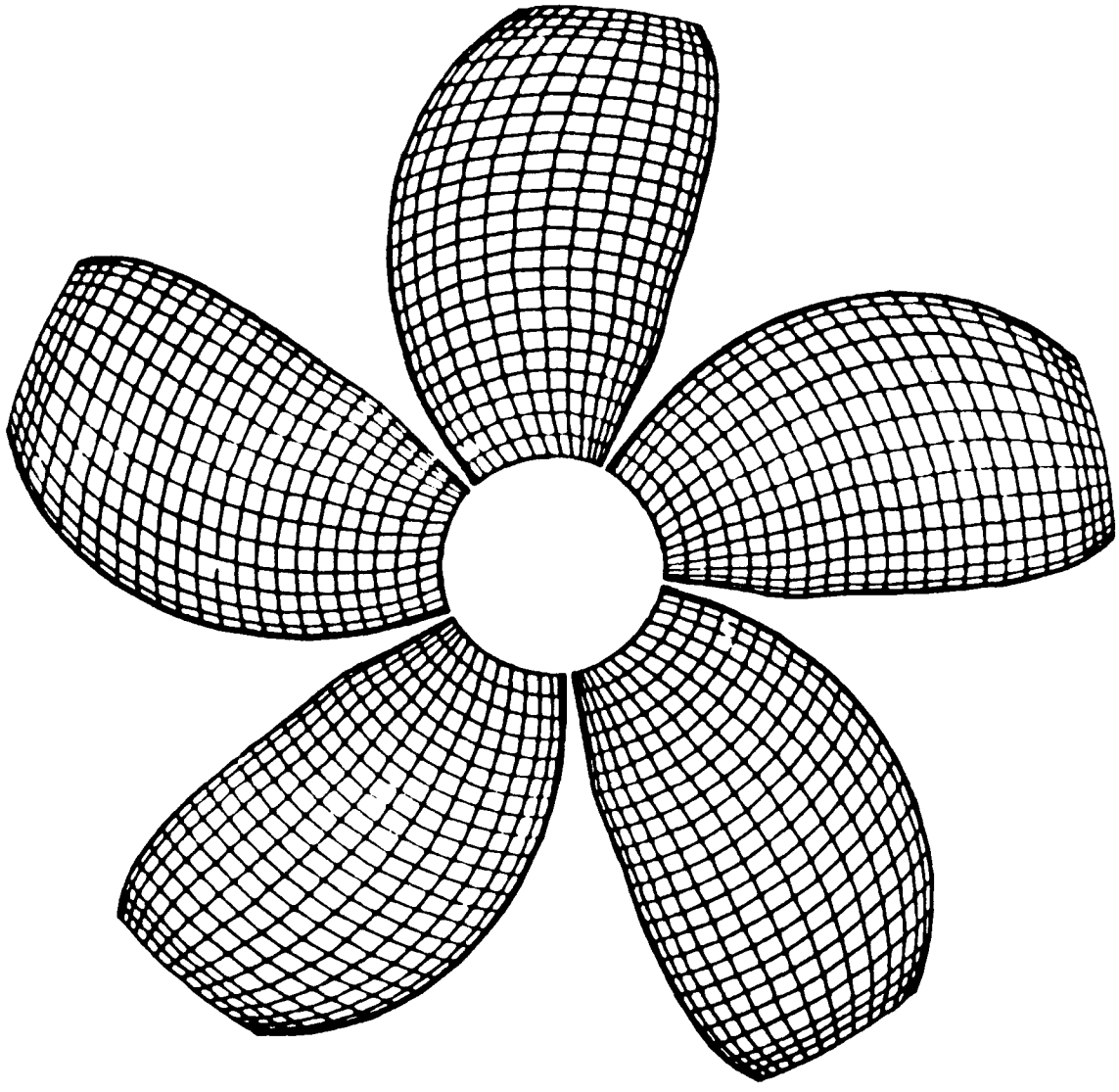

Figure 6.3. Hoshino Propeller Paneling for Analysis.

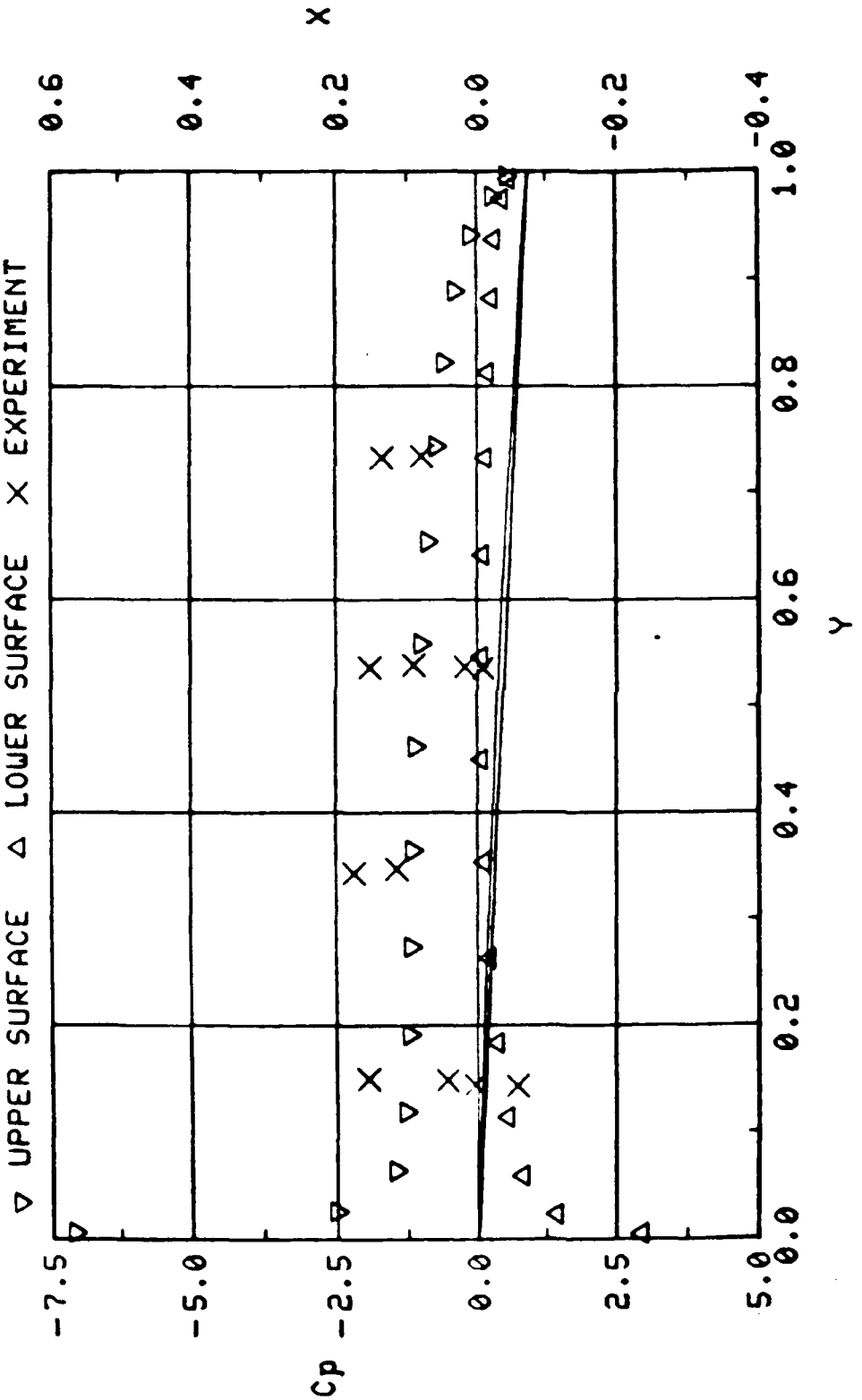

Figure 6.4. Experimental Correlation, 5-Bladed Hoshino Propeller; Advance Ratio = 0.7, R = 11.80.

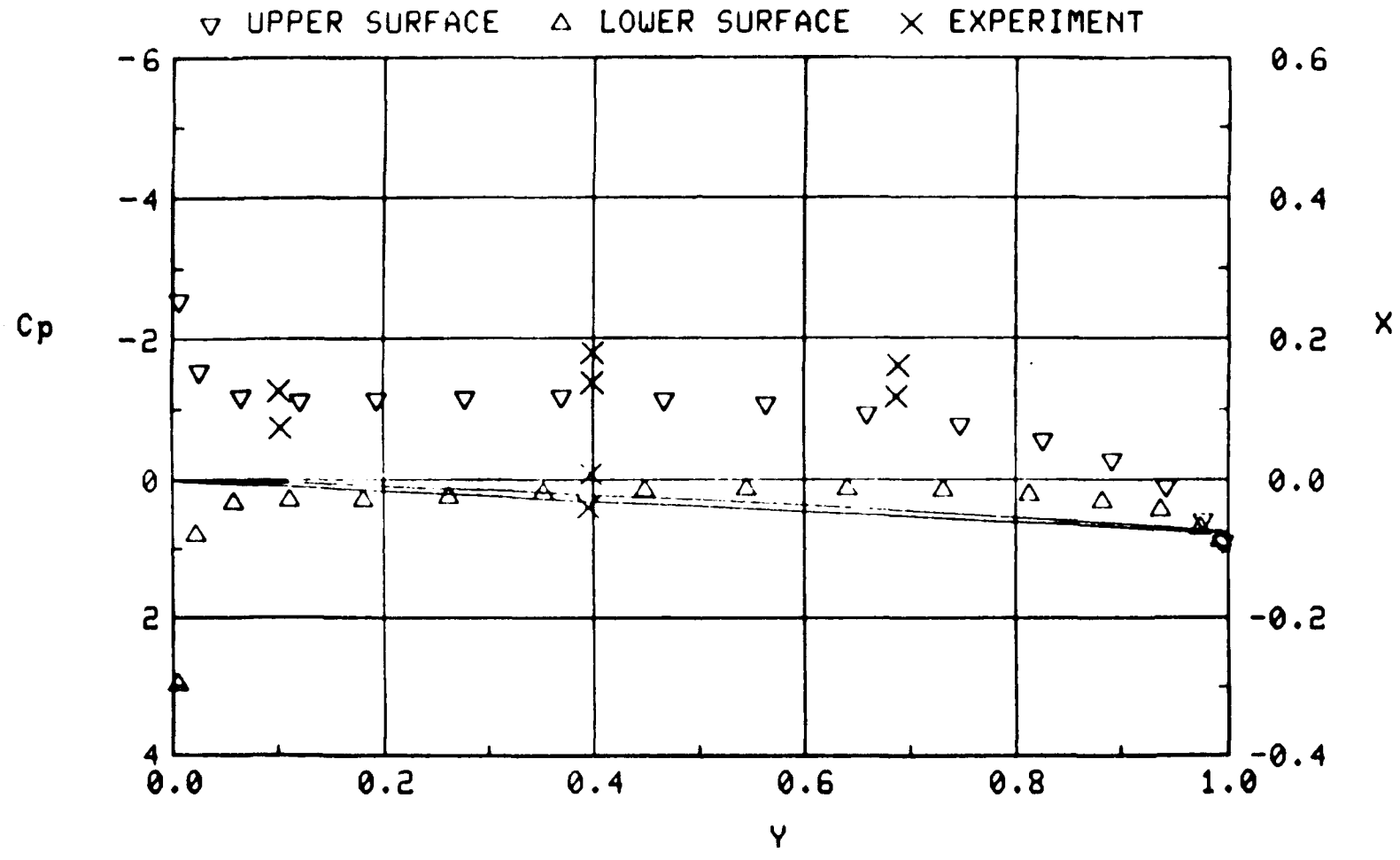

Figure 6.5. Experimental Correlation, 5-Bladed Hoshino Propeller; Advance Ratio = 0.7, R = 10.05.

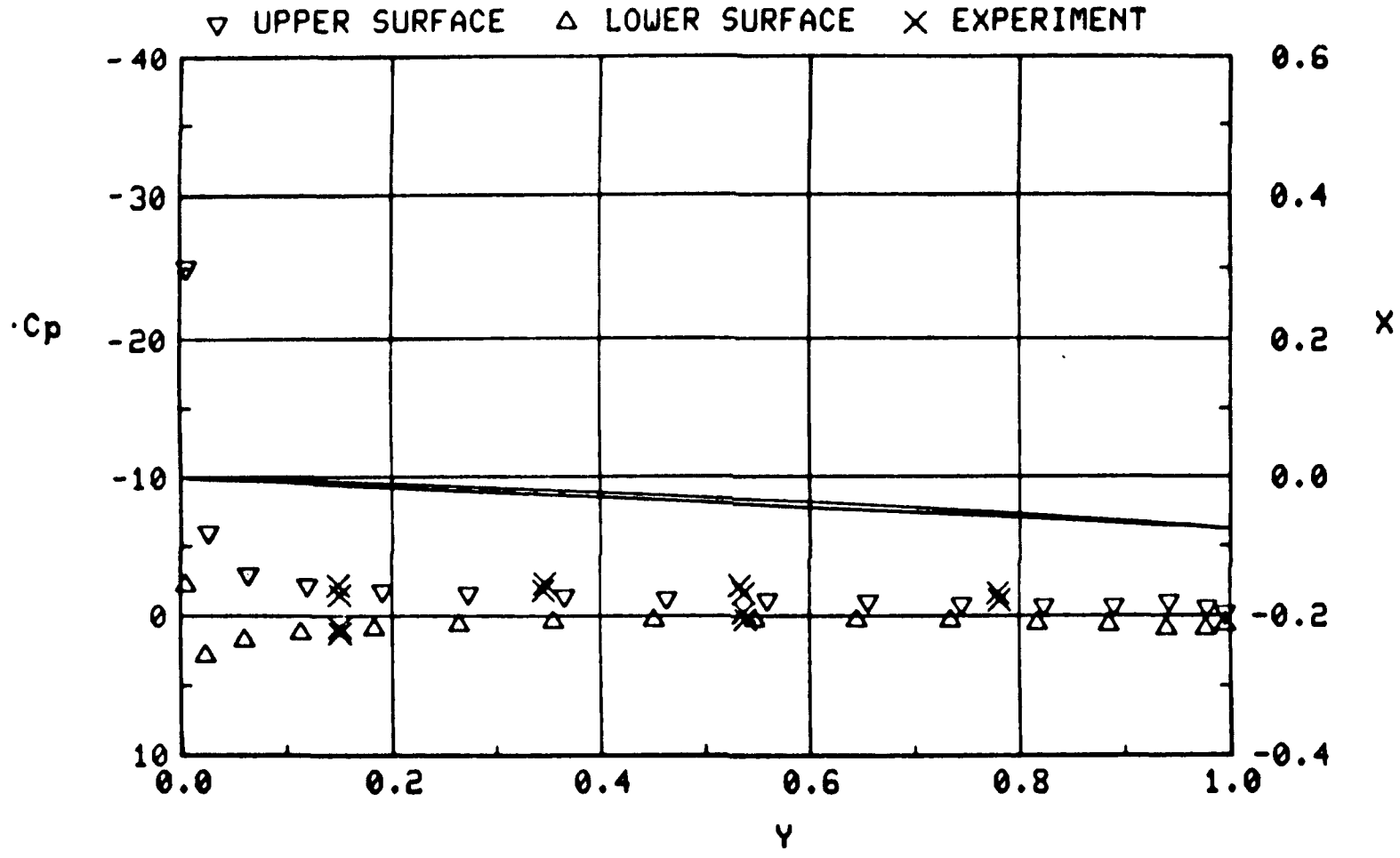

Figure 6.6. Hoshino Propeller Experimental Correlation; Advance Coefficient = 0.5, R = 11.80.

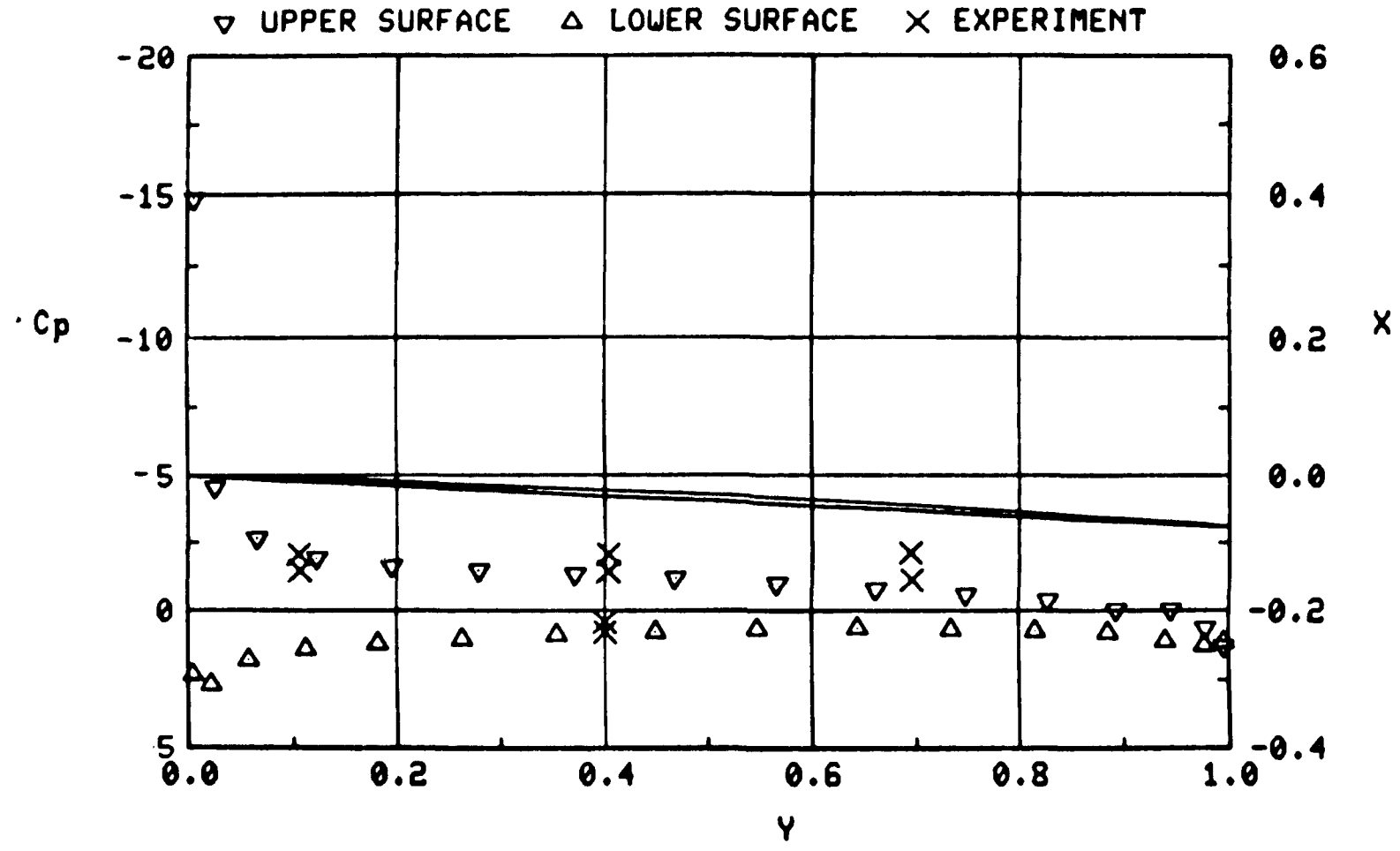

Figure 6.7. Hoshino Propeller Experimental Correlation; Advance Coefficient = 0.5, R = 10.05.

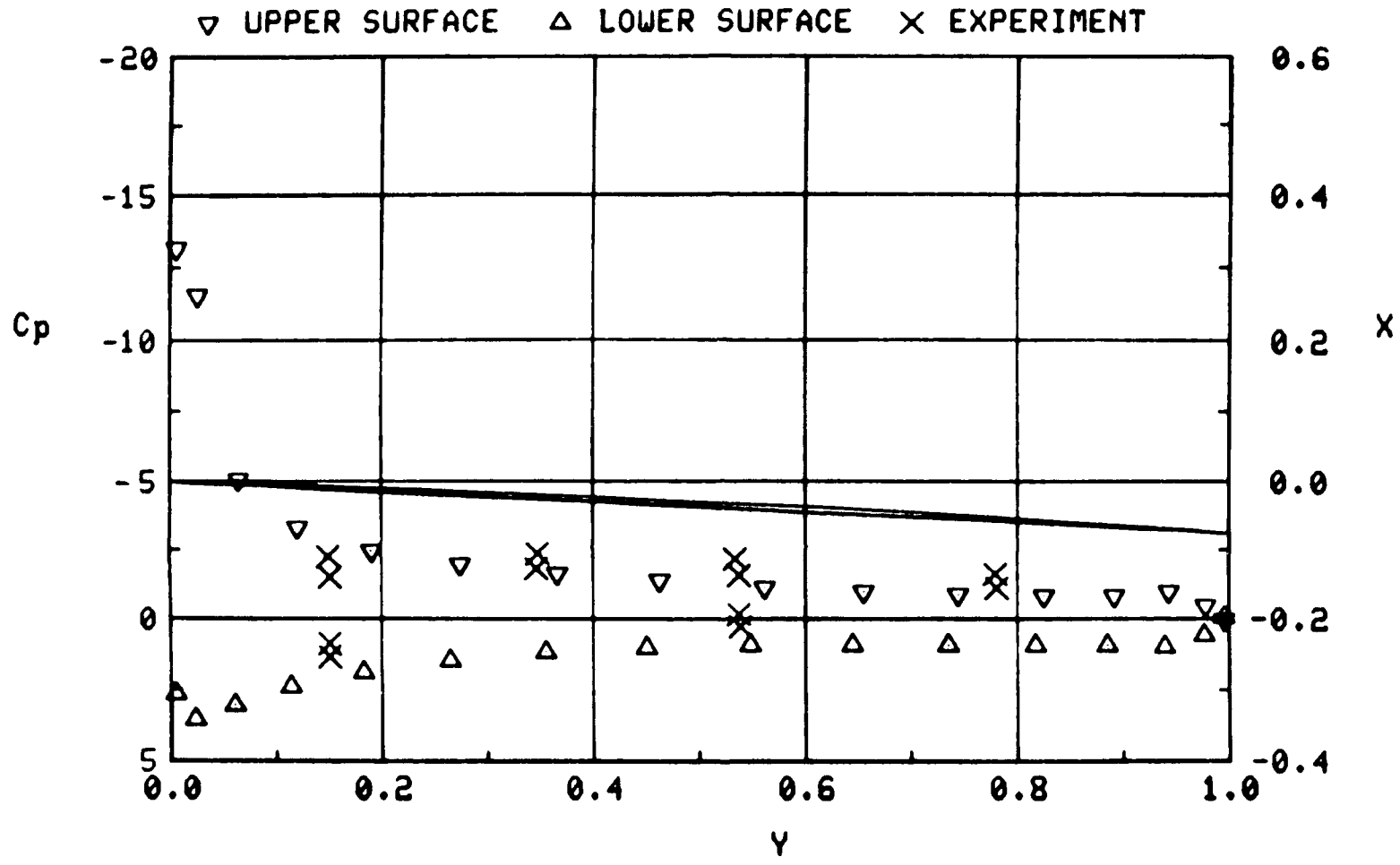

Figure 6.8. Hoshino Propeller Experimental Correlation; Advance Coefficient = 0.3 (Off Design), R = 11.80.

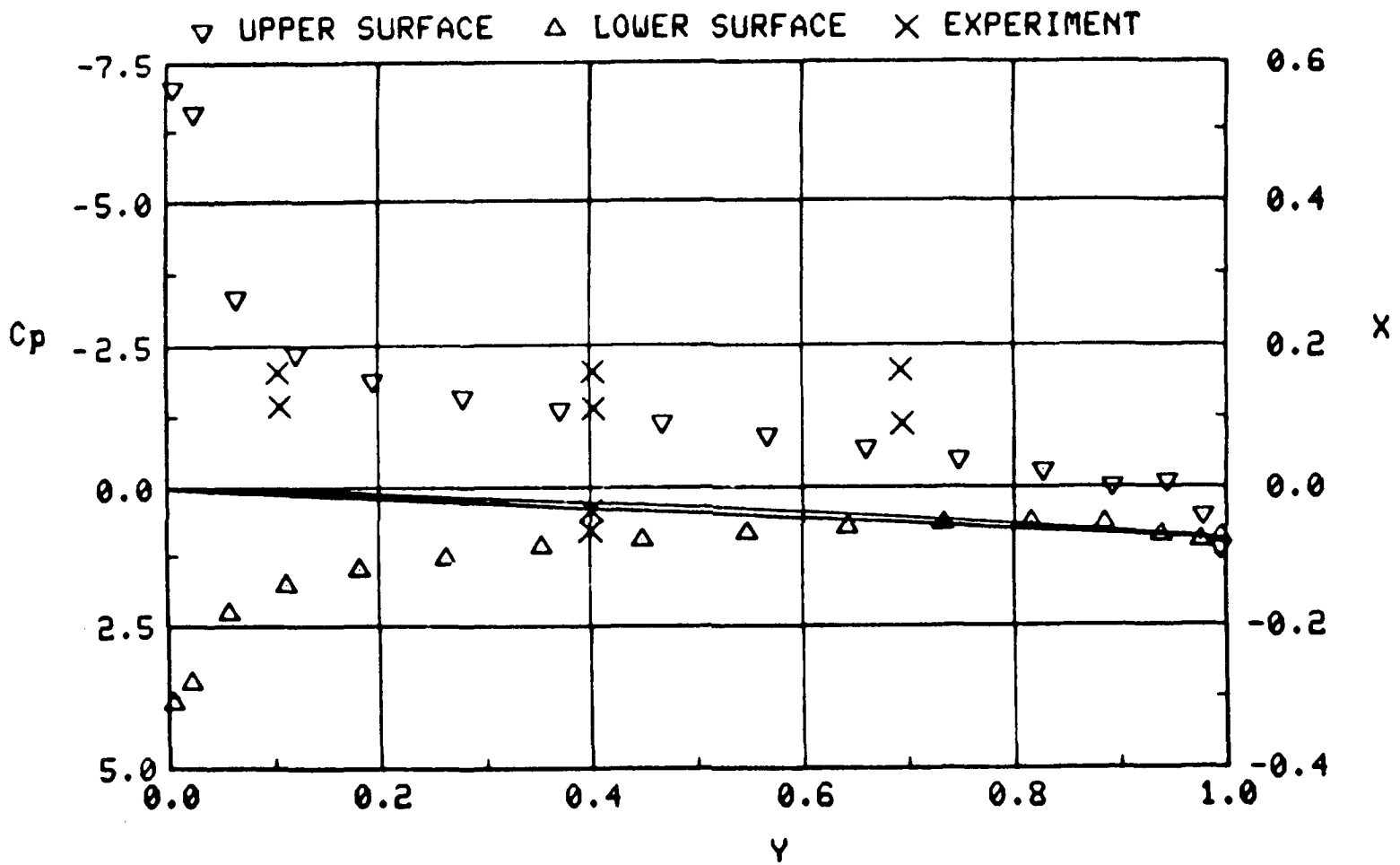

Figure 6.9 . Hoshino Propeller Experimental Correlation; Advance Coefficient = 0.3 (Off Design), R = 10.05.

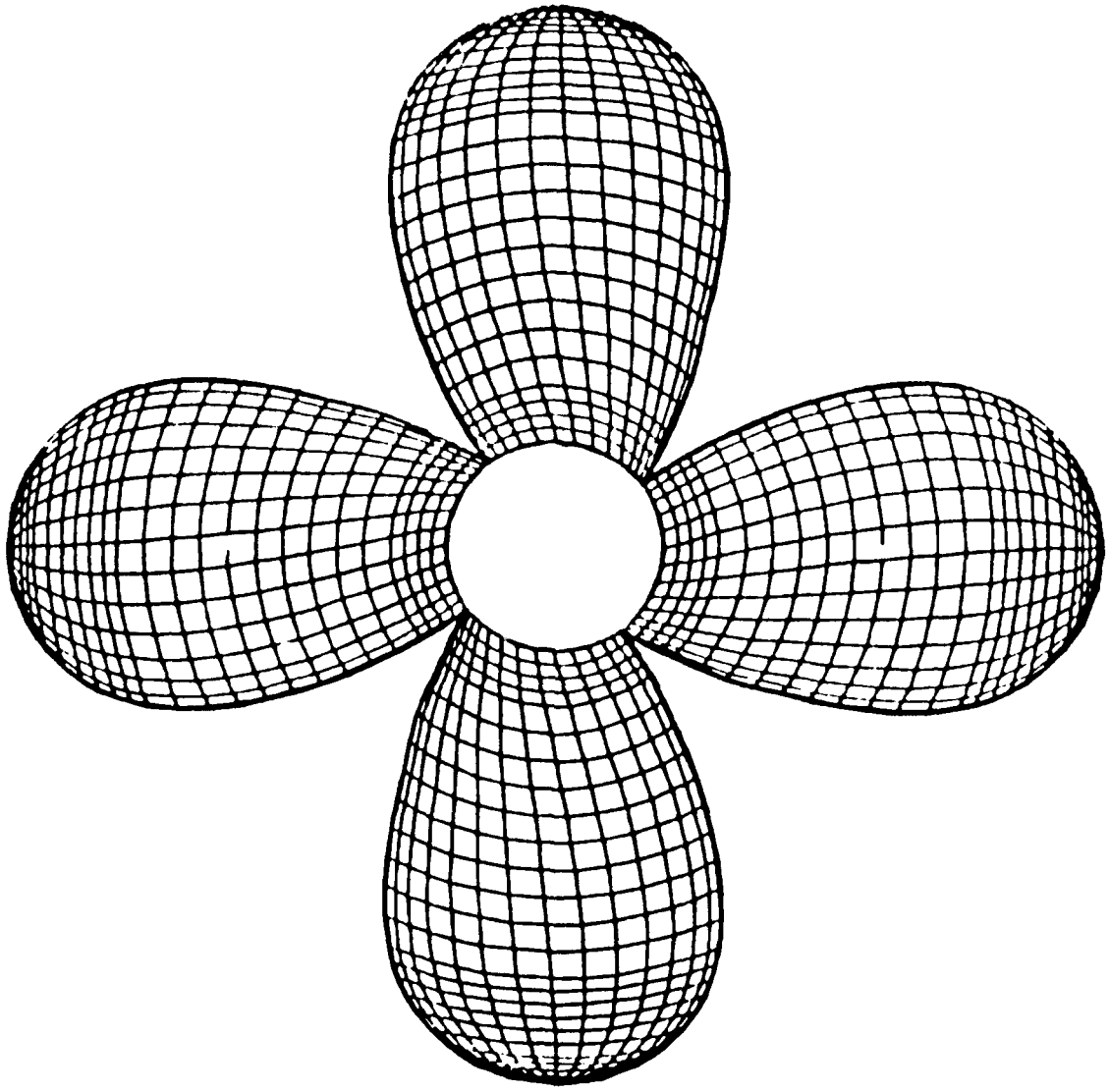

Figure 6.10. van Gent 4-Bladed Propeller Paneled for Analysis.

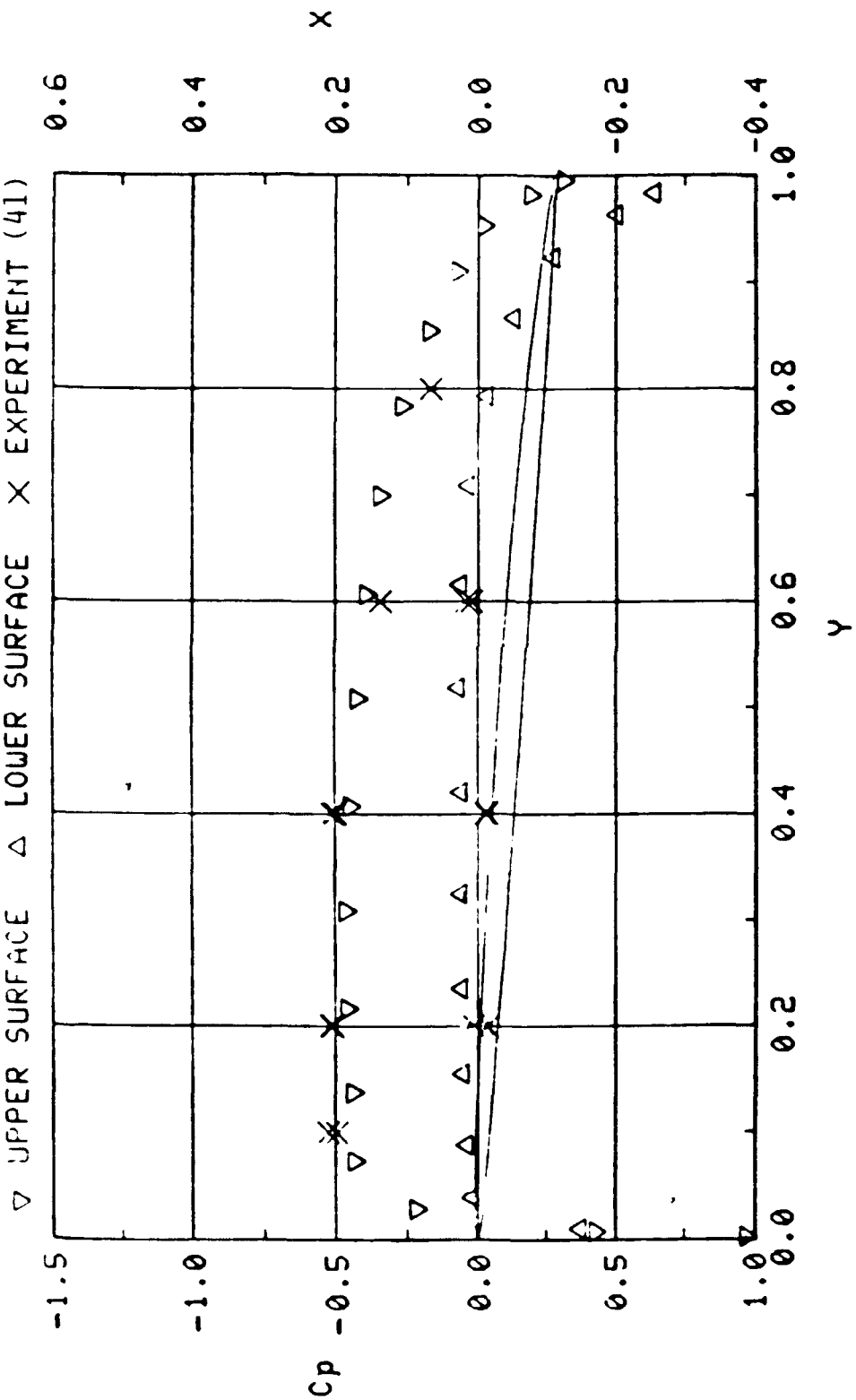

Figure 6.11. Experimental Correlation for van Gent Propeller at Radial Section, R = 10.19, Advance Coefficient = .4.

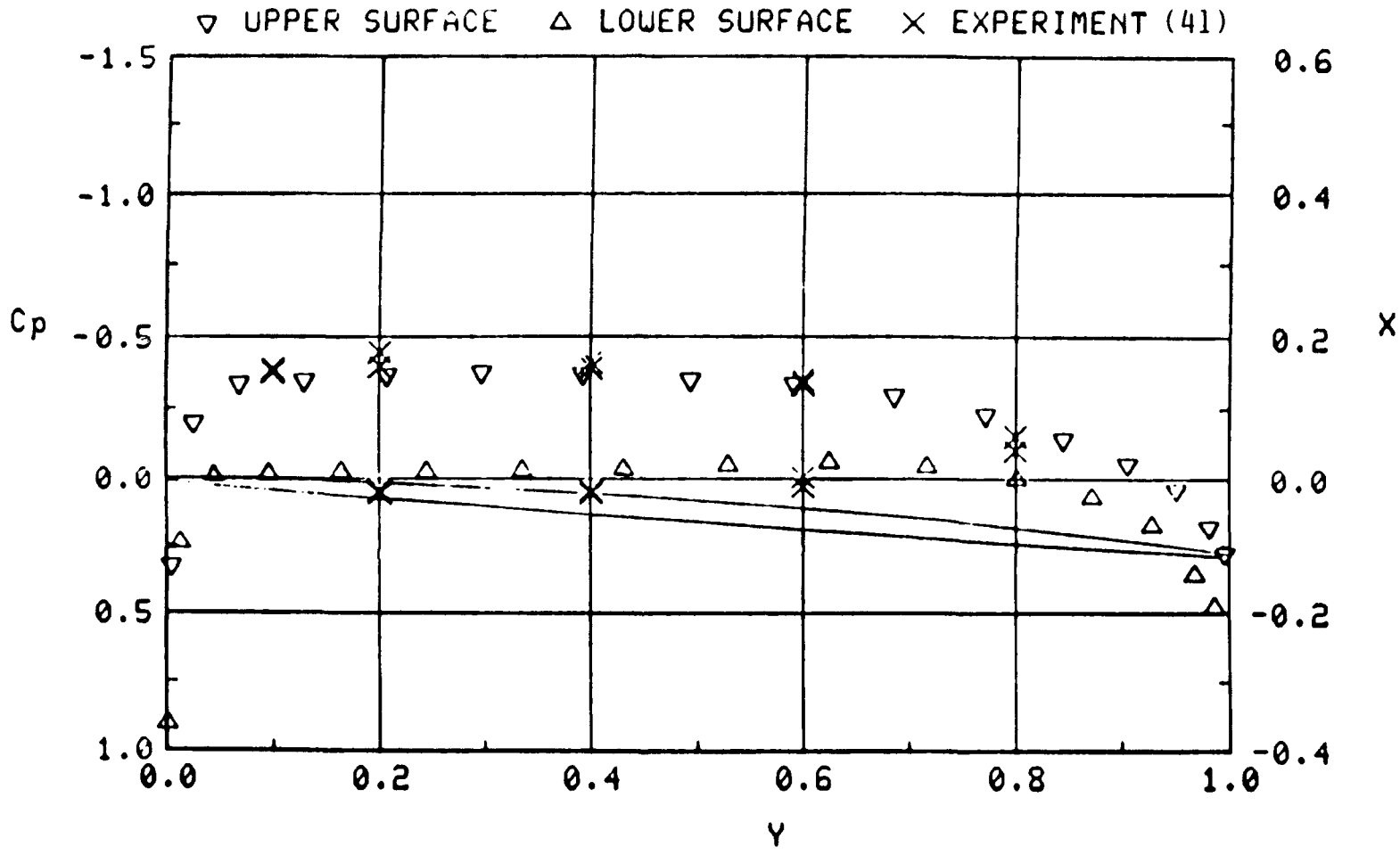

Figure 6.12. Experimental Correlation for Van Gent Propeller at Radial Section, r = 12.20, Advance Coefficient = .4.

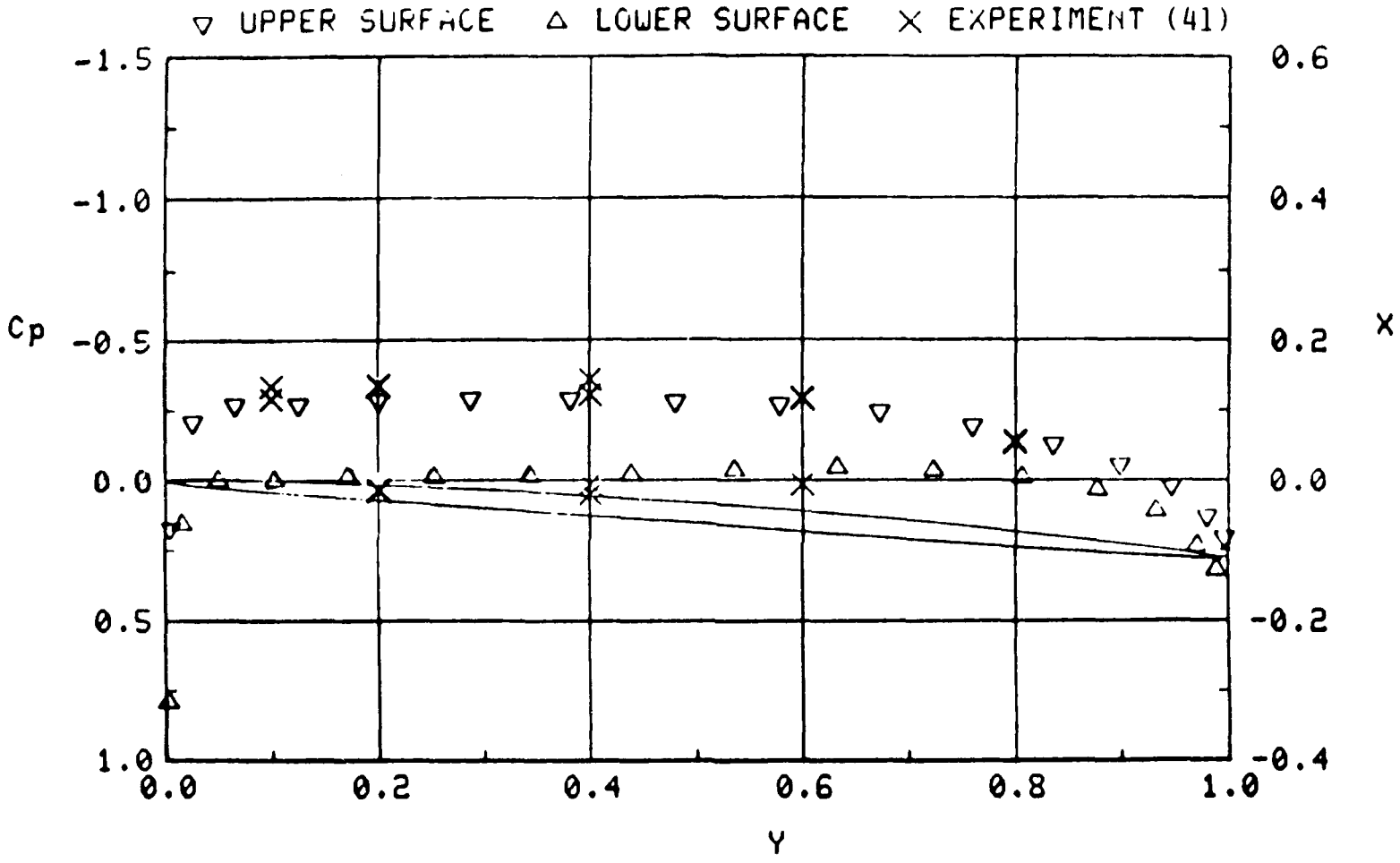

Figure 6,13. Experimental Correlation for van Gent Propeller at Radial Section, r = 14.50, Advance Coefficient = .4.

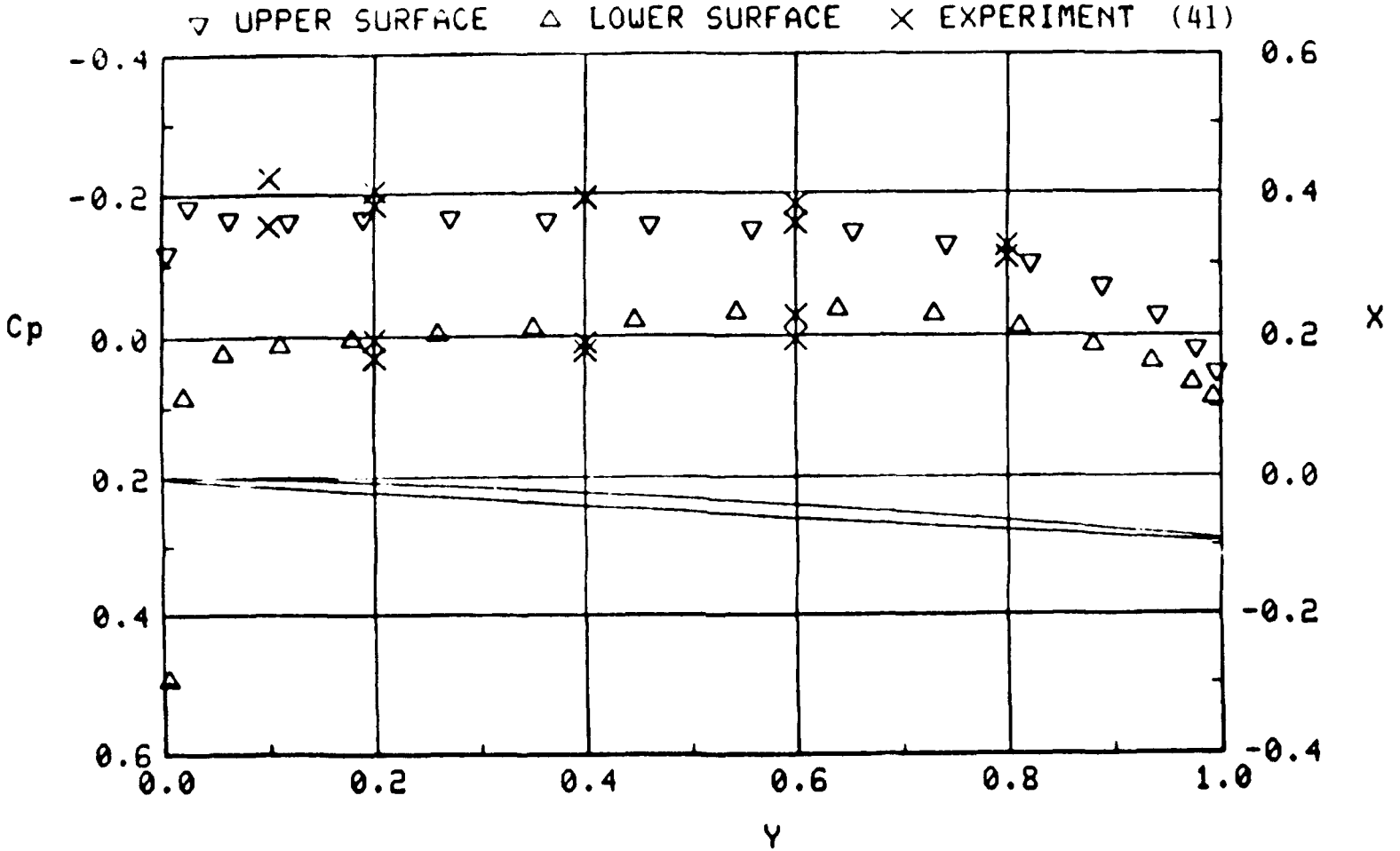

Figure 6.14. Experimental Correlation for Van Gent Propeller at Radial Section r = 19.40, Advance Coefficient = .4.

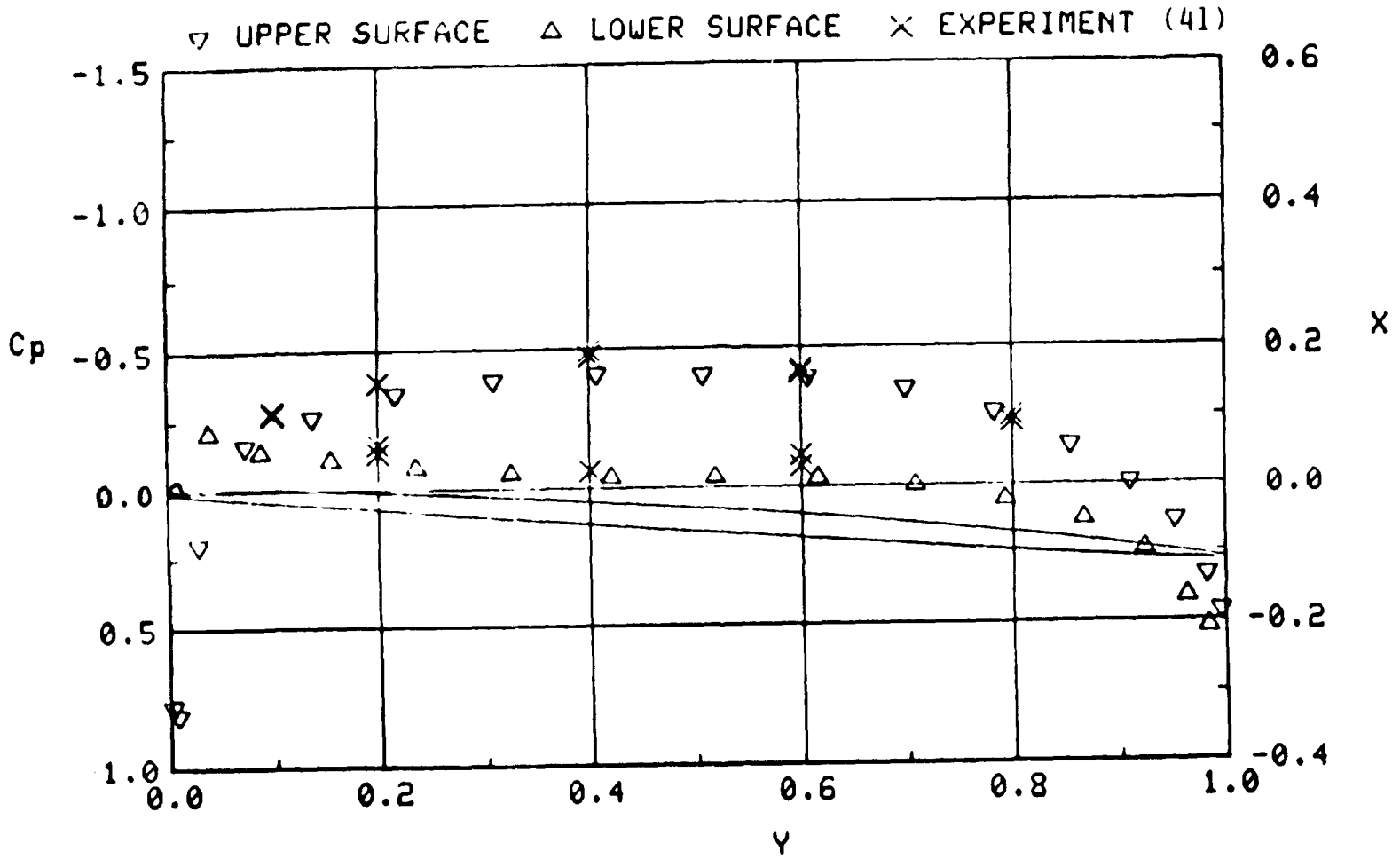

Figure 6.15. Experimental Correlation for van Gent Propeller at Radial Section, r = 10.19, Advance Coefficient = 0.6.

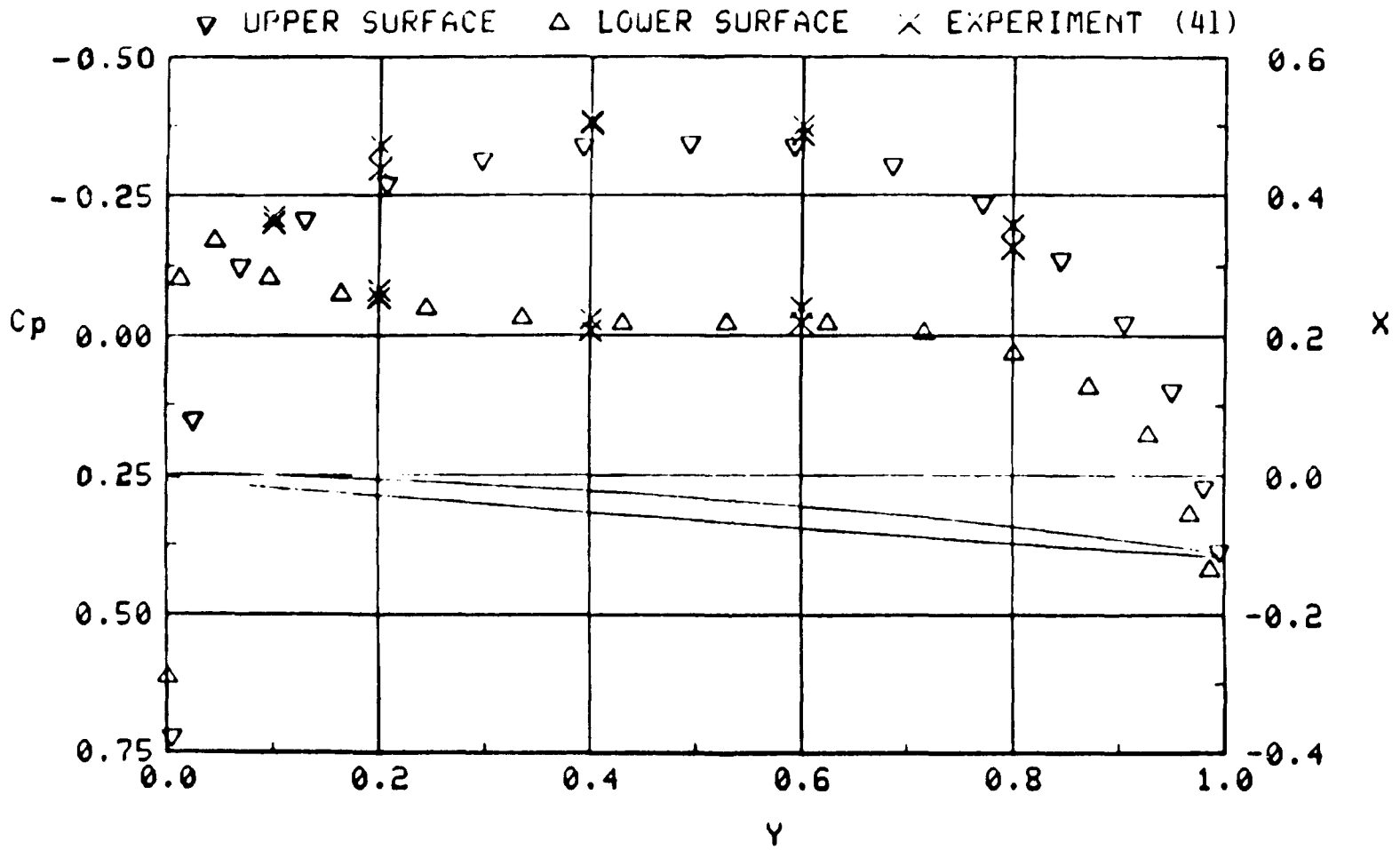

Figure 6.16. Experimental Correlation for van Gent Propeller at Radial Section, r = 12.20, Advance Coefficient = 0.6.

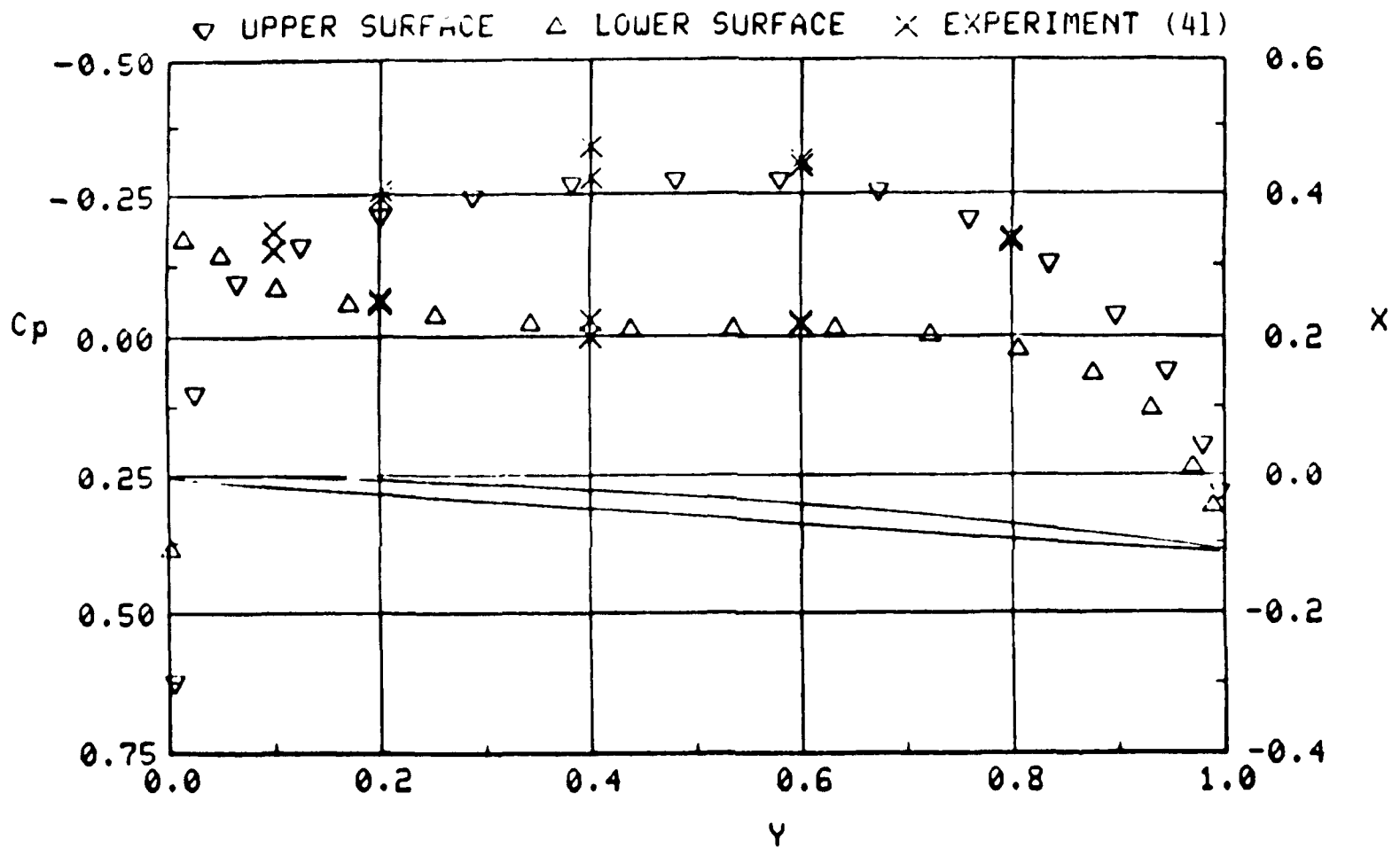

Figure 6.17. Experimental Correlation for van Gent Propeller at Radial Section, r = 14.50, Advance Coefficient = 0.6.

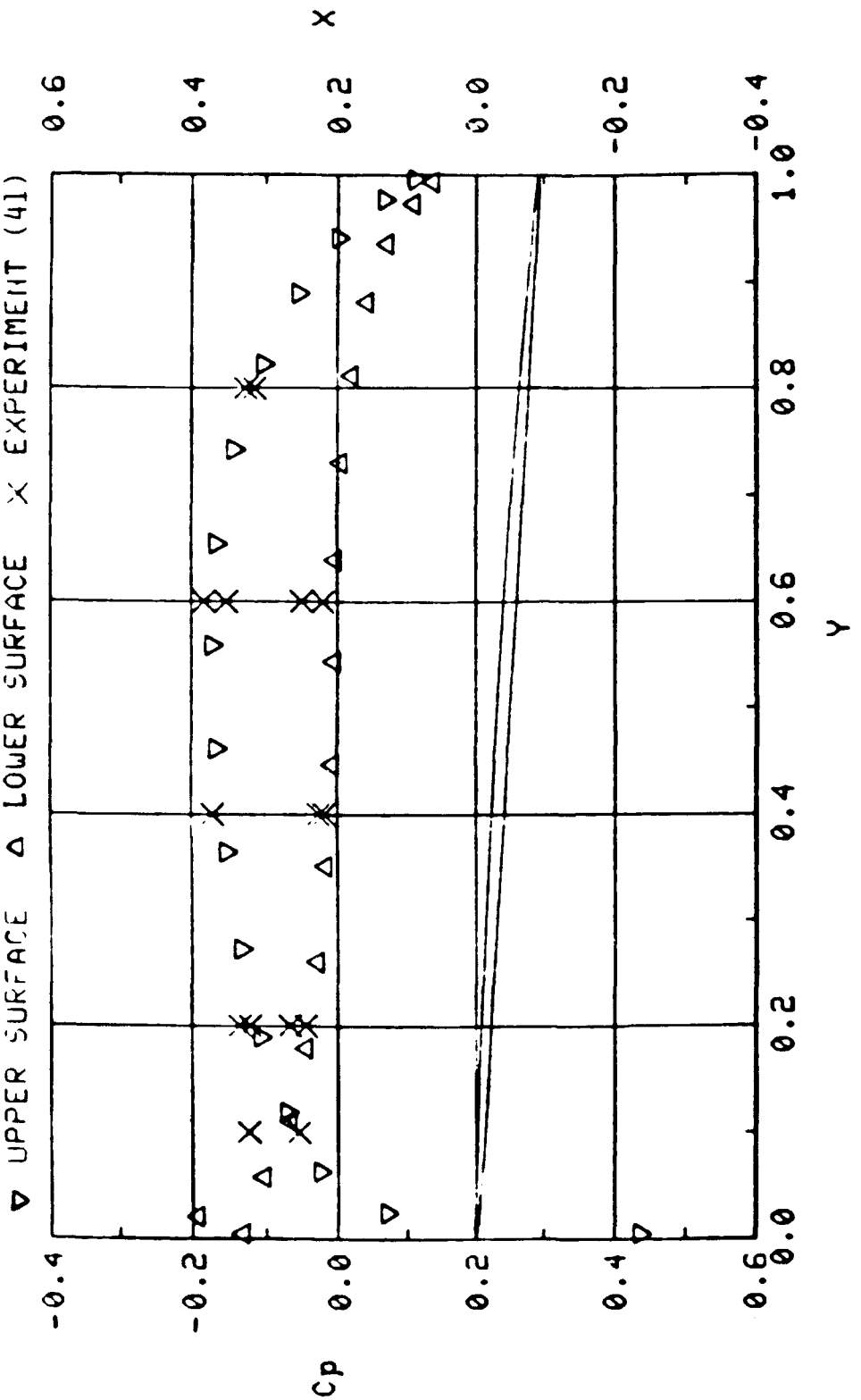

Figure 6.18. Experimental Correlation for van Gent Propeller at Radial Section, r = 19.40, Advance Ratio = 0.6.

6.2 Propellers in Simple Nonuniform Flow

Propellers operating in the boundary layer of simple hull forms without extensive separation regions can be very simply modeled with MPROP. The nonuniformity can be modeled as outlined in Section 2.2. The vorticity associated with the shear flow is neglected in this modeling. The change in the boundary condition normal to the propeller surface is accurately modeled. Experimental results for specific comparison are not available for general documentation. A typical calculation for a propulsor in radially nonuniform flow is presented. Figure 6.19 shows a front view of a five-bladed, high-skew propeller designed by Brockett (P4383). The nonuniformity is linear with a lower free-stream velocity (approximately 12%) near the tip compared to the axial value. The total pressure is assumed constant in the radial direction and the flow is nondimensionalized with respect to the axial velocity. Figures 6.20(a) and (b) show sectional Cp distributions at a chosen location (r = 4.4) for the basic propeller in uniform and nonuniform flow, respectively. The change in Cp distribution due to nonuniformity is indicative of the kind of detail that is calculated by the code. The original propeller is believed to be designed for a marginally nonuniform inflow. Analysis predicts a larger suction peak with nonuniformity. Further application of this modeling will reveal the extent to which the neglect of vorticity is valid.

6.3 Propeller in Fully Nonuniform Flow

Experimental results are available for two propulsors in circumferentially varying nonuniform inflow. The nonuniformity was simulated in the test (40) to study cavitation under actual operating conditions.

6.3.1 Frequency Band Analysis

Both propellers have been analyzed with the frequency band theory outlined in Section 5.2. In Figure 6.21 the experimental wake fractions are reproduced from Ref. 40. The nonuniformity was represented by a Fourier cosine series. The second harmonics or the cos (2wt) term is the most dominant. Figure 6.22 shows the comparison between calculated and measured pressure at a radial section, r = 0.77R for J = .9. The experimental pressure data is available at a gauge located at 20% downstream of the leading edge. The dotted line in Figure 6.22 shows a three-component solution for the velocity potential. The calculated pressure is in good agreement with experiment. The slight overprediction of the peak pressure is not fully understood. It is believed that the theory forces a continuous analytical function for the velocity potential which introduces inaccuracies in the time derivative of the potential which influences the pressure calculated. A five-term solution is also represented in Figure 6.22 by the solid line. The change in solution is not significant because the amplitude of the higher harmonics is very small. Full details of the experimental setup are not available. There is a change in hydrostatic pressure across the radius of the propeller which has not been accounted for in the theory.

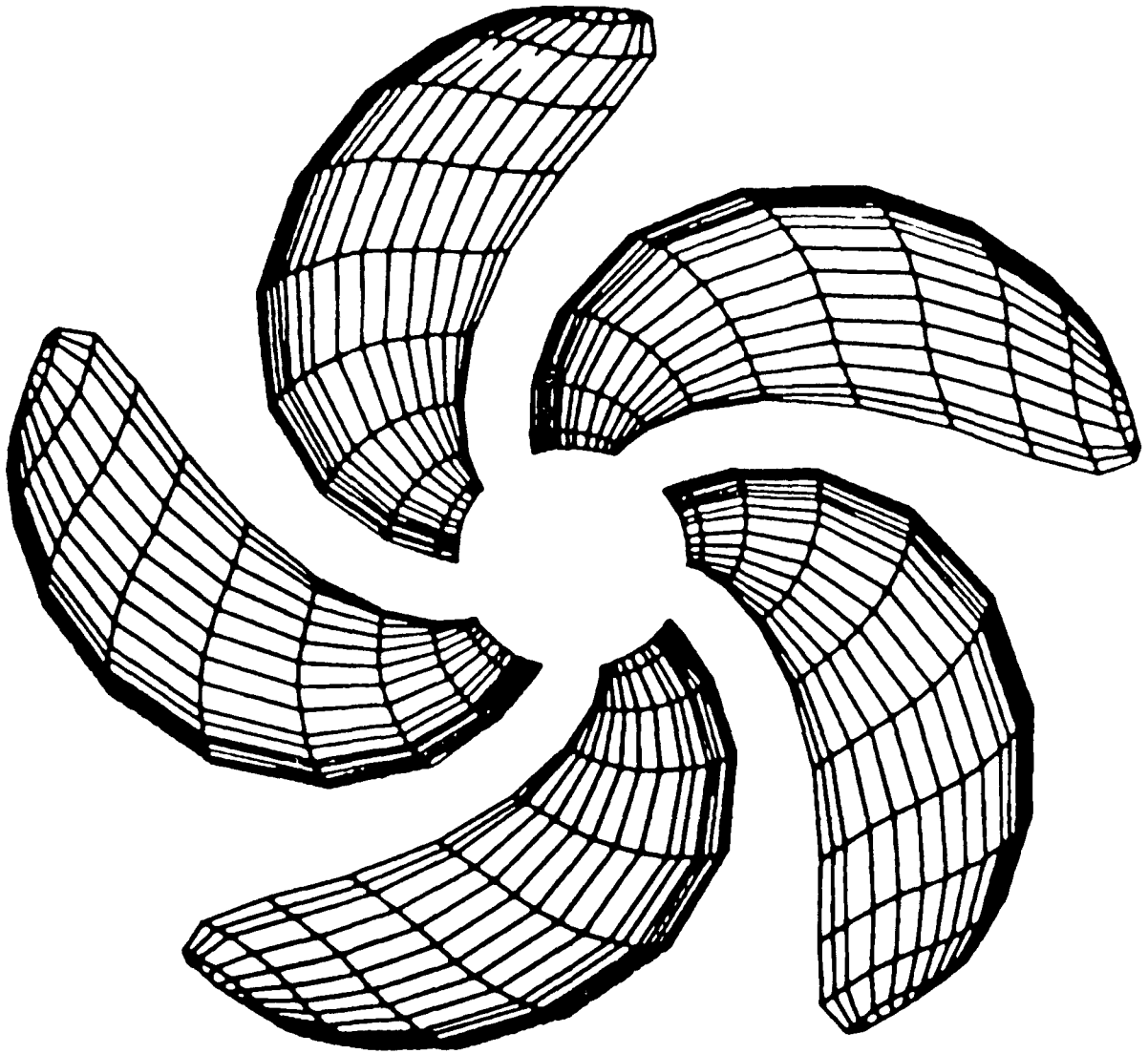

Figure 6.19. Propeller with a Skew of 72 Degrees in Uniform Flow.

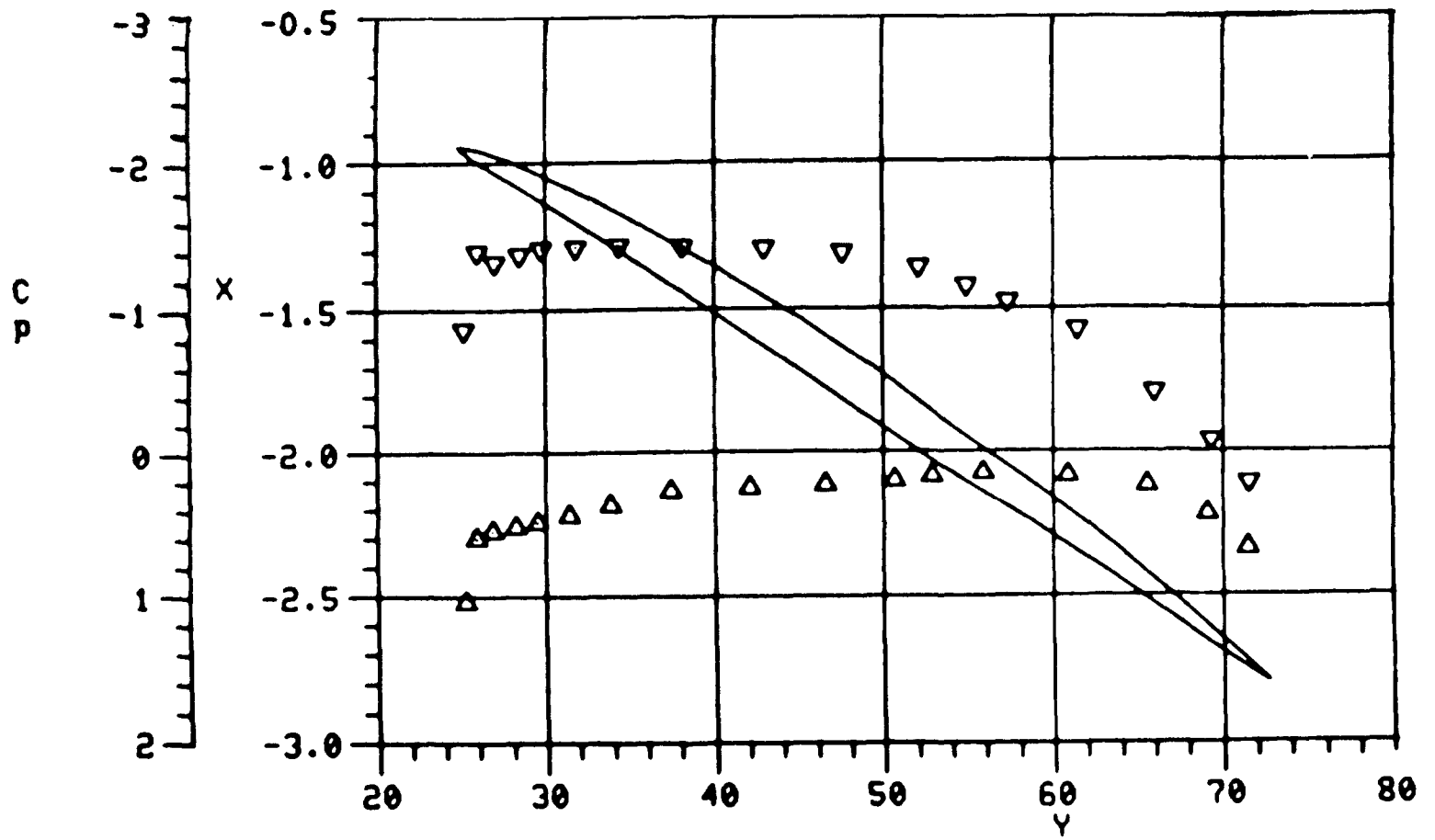

(a) Uniform Flow

Figure 6.20. C_p Distribution on the Blade Section at r = 4.4.

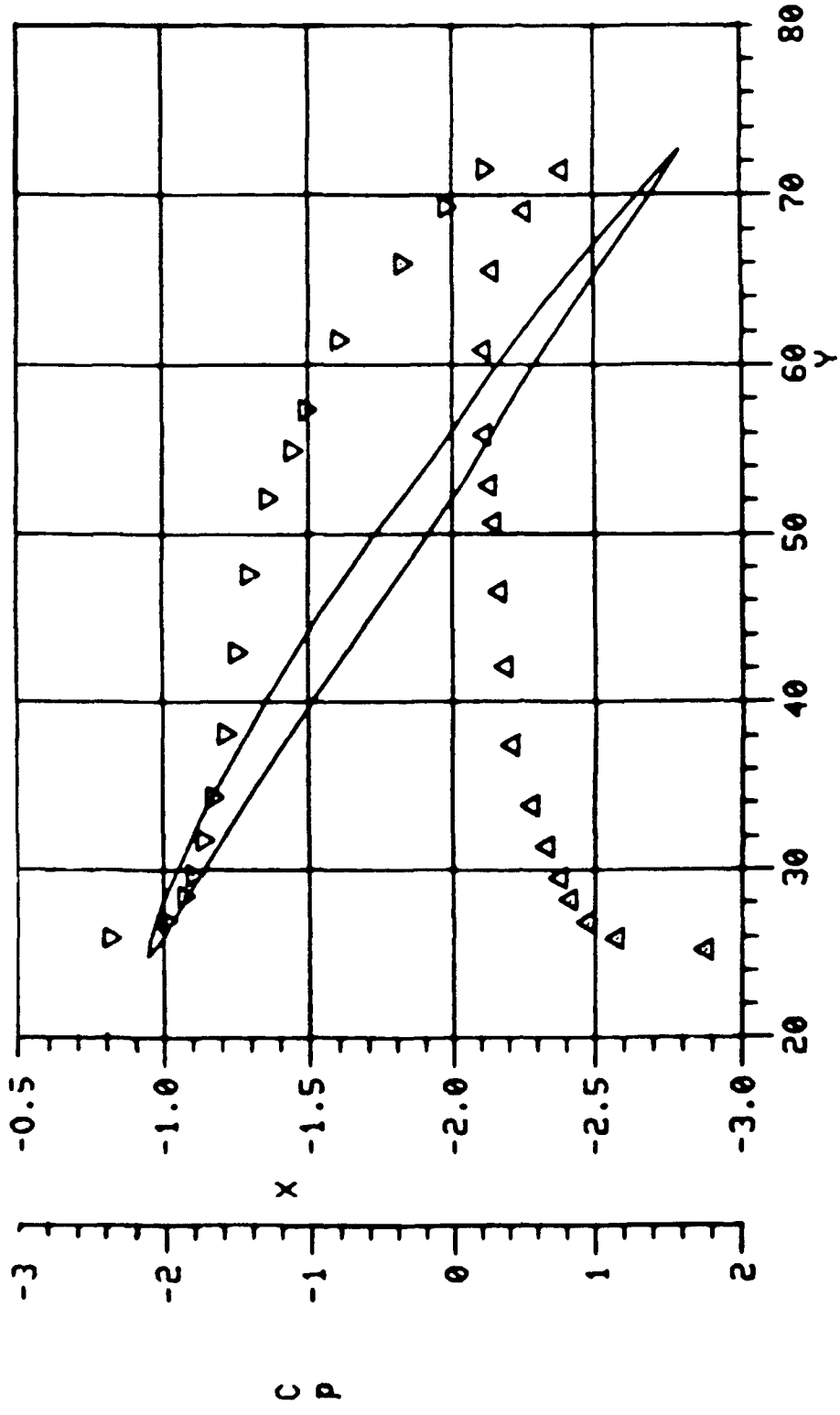

(b) Radially Non-uniform Flow

Figure 6.20. Concluded.

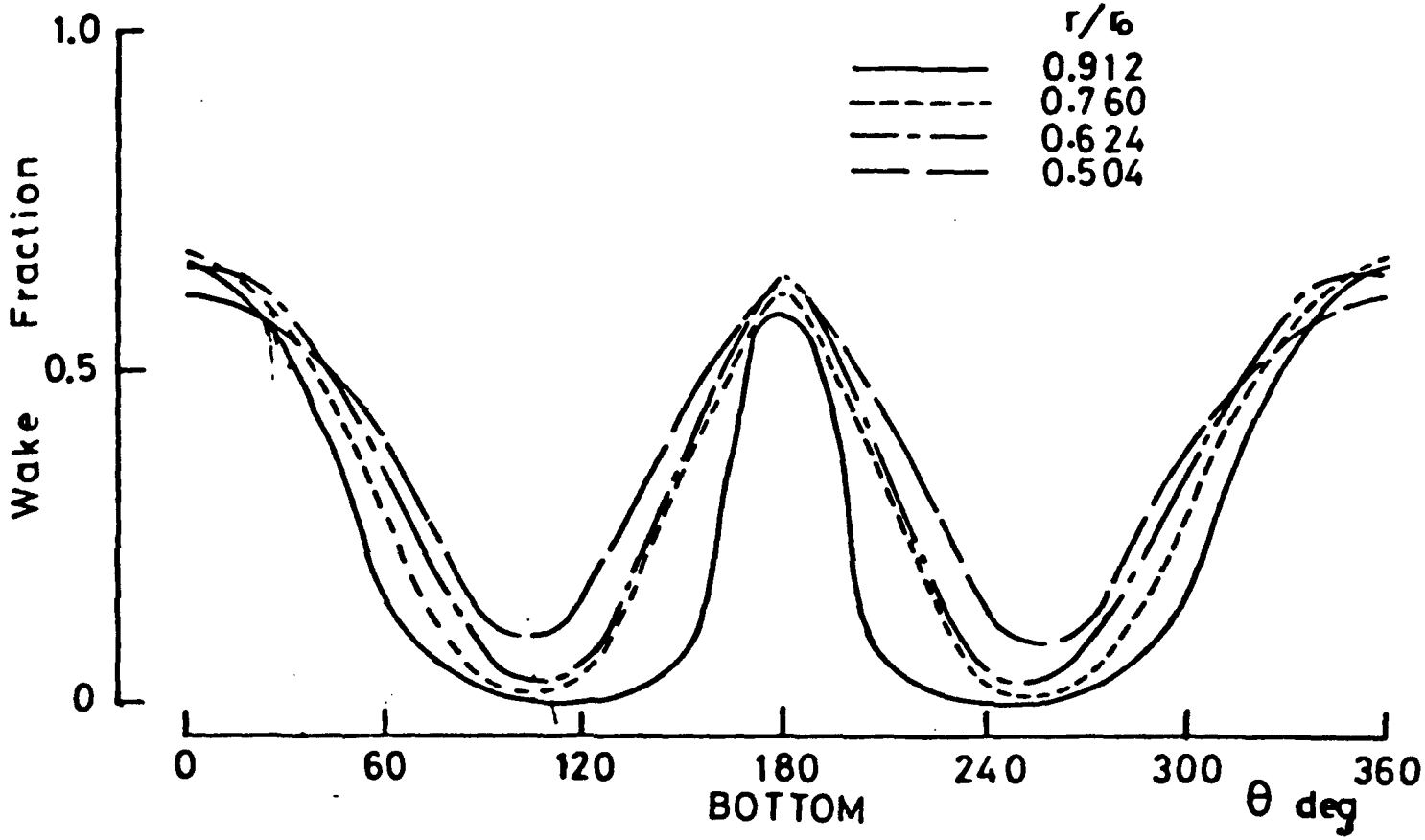

Figure 6.21. Wake Fractions, Reporduced from Reference 40.

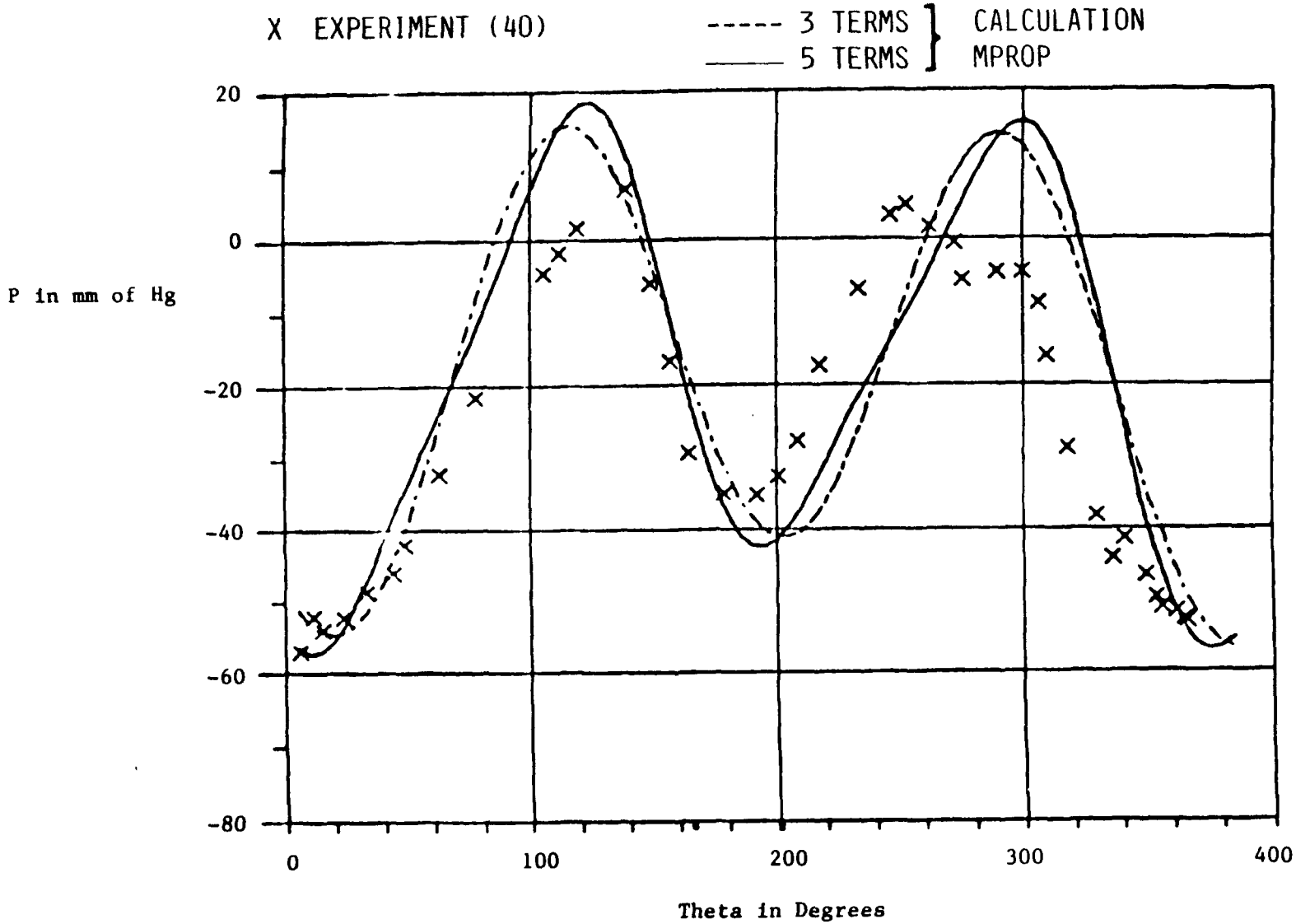

Figure 6.22. Pressure Correlation on a Six-Bladed Propeller in Nonuniform Wake; r = 0.77R, x/c = 0.2, Suction Side.

The nonuniformity associated with a five-bladed Hoshino propeller is shown in Figure 6.23. The description of nonuniformity is less precise than the previous case. The contour plots were ditigized and represented by an 8-term Fourier series. The wake fraction locally drops to 0.7 in a narrow region around the vertical axis. This makes it necessary to have many terms before an acceptable solution can be calculated. Figure 6.24 shows the calculated results plotted against experimental results taken from Ref. 42. Experimental probes were located at a radial section 0.75 R outboard. The suction side probe was located at 10% downstream of the leading edge while the pressure side probe was located 40% downstream of the leading edge. The calculated pressures are in good agreement for the complex inflow. The basic assumptions and approximations of the theory may be considered indirectly validated by these calculations.

6.3.2 Time-Dependent Analysis

The existing time-dependent program, USAERO, described in Section 5.3, was applied to the SRI MP0123 propeller (40).

6.3.2.1 Uniform Flow

First, as in the case of the frequency band analysis, the uniform flow case (40) was examined to establish a basic level of accuracy. A relatively low panel density representation of the blades was used (Figure 6.25), i.e., 208 panels on each blade in a 16 (chordwise) x 12 (radially) array plus a 2 x 8 array on the tip. A simple hub was also included to improve the blade root representation. The propeller was started impulsively from rest and run for three revolutions at 10 rps with 12 steps in each of the first two revolutions and 24 steps in the third. These runs were made with different onset flows to give advance ratios of 0.7, 0.9 and 1.1.

Figure 6.26(a) shows a general view of the pressure coefficient distribution after three revolutions at J = 0.7. (Note that hydrostatic pressure is included and therefore the Cp varies with azimuthal location.) Streamwise lines indicate the computed location of the wake surfaces. A buttline cut through the wake indicates a higher rate of convection in the root region compared with the tip region, Figure 6.26(b). The starting vortex from the impulsive start has convected about 2 1/2 diameters downstream. A station cut through the wake at one diameter downstream from the propeller, Figure 6.26(c), shows a large middle region in essentially "solid-body" swirl and a thin outer region where the tip vortex flow is becoming sheared due to lower swirl rate there. An inner region involved with the hub root vortex is also evident.

Figure 6.26(d) shows the time history of x-wise force (-CD) and normal (CMX) coefficients from the USAERO calculation. They converge to steady state values in 12 steps, i.e., one revolution. The wake has convected by less than one diameter in that time. Reduced to the standard thrust (KT) and torque (KQ) coefficients, these and similar values obtained at J = .9 and 1.1 compare very favorably with the experimental measurements, Figure 6.26(e), in view of the relatively low panel density used. Viscous effects were not included in the calculation and so the slightly higher thrust value obtained is to be expected. However, the slightly higher torque coefficient

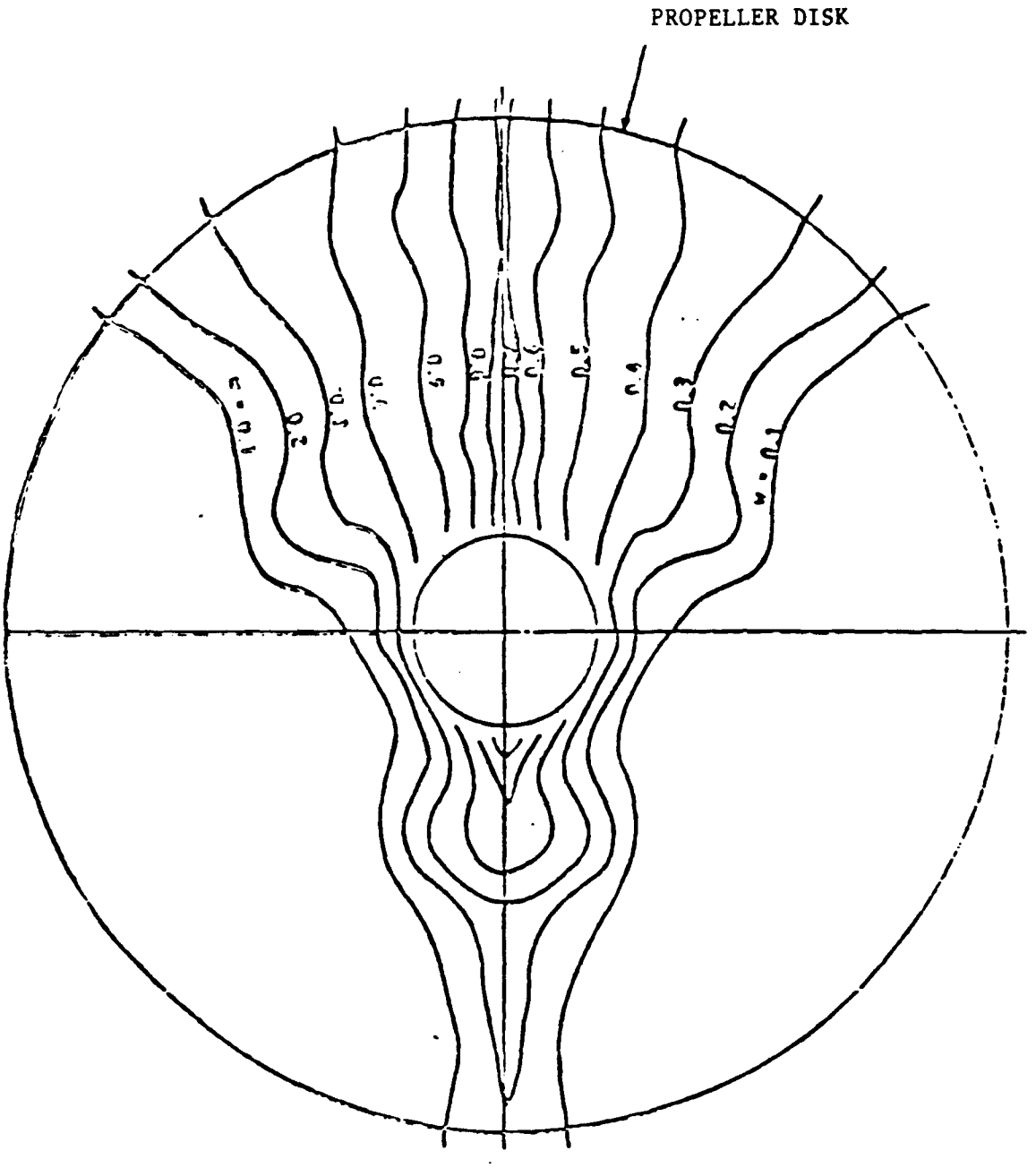

P. 1787 (HOSHINO 1981)

Figure 6.23. Wake Fraction Contours for Nonuniform Inflow, Reproduced from Reference 42.

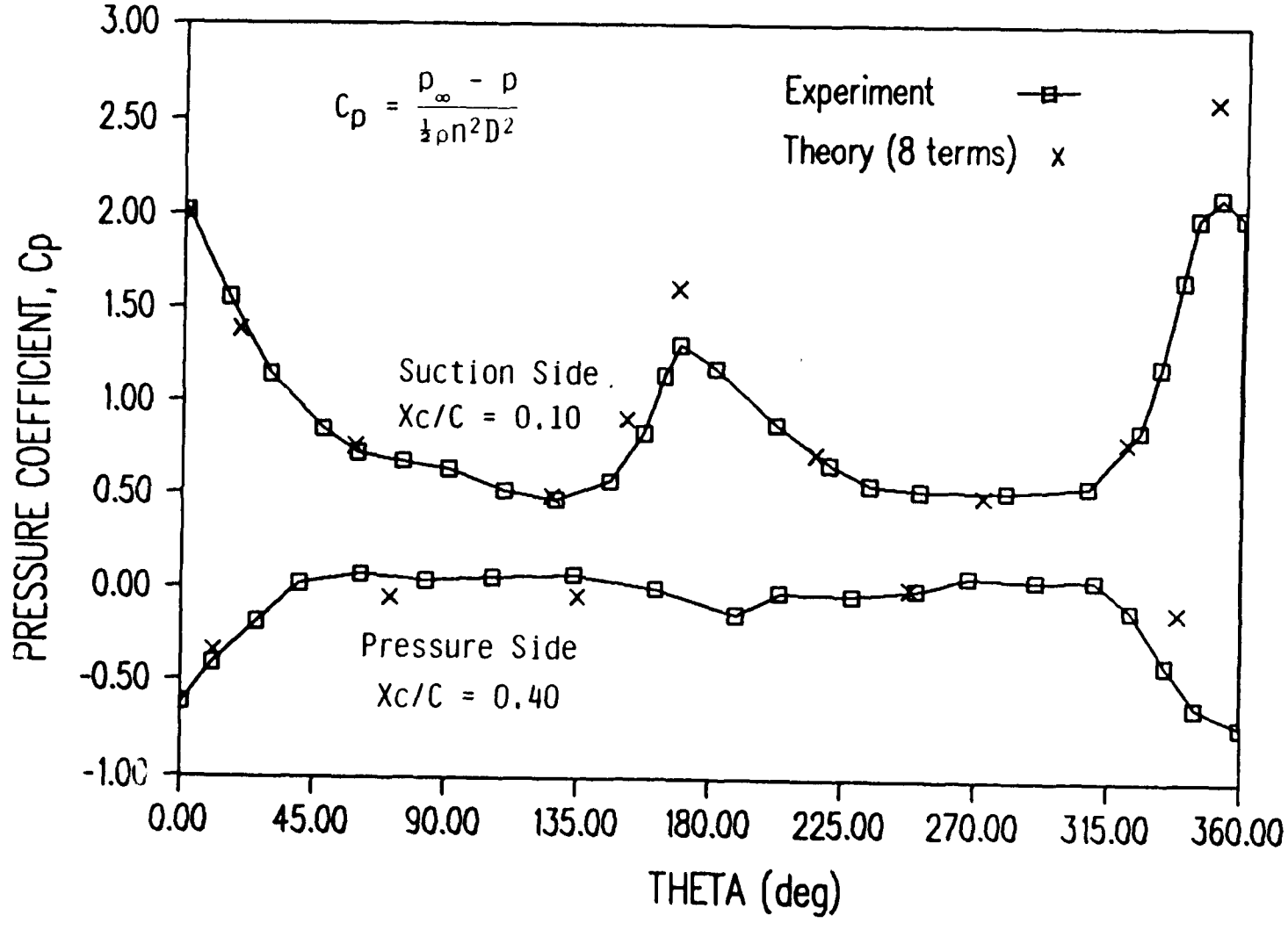

Figure 6.24. Comparison between 8-Term Solution and Experiment (Ref. 42).

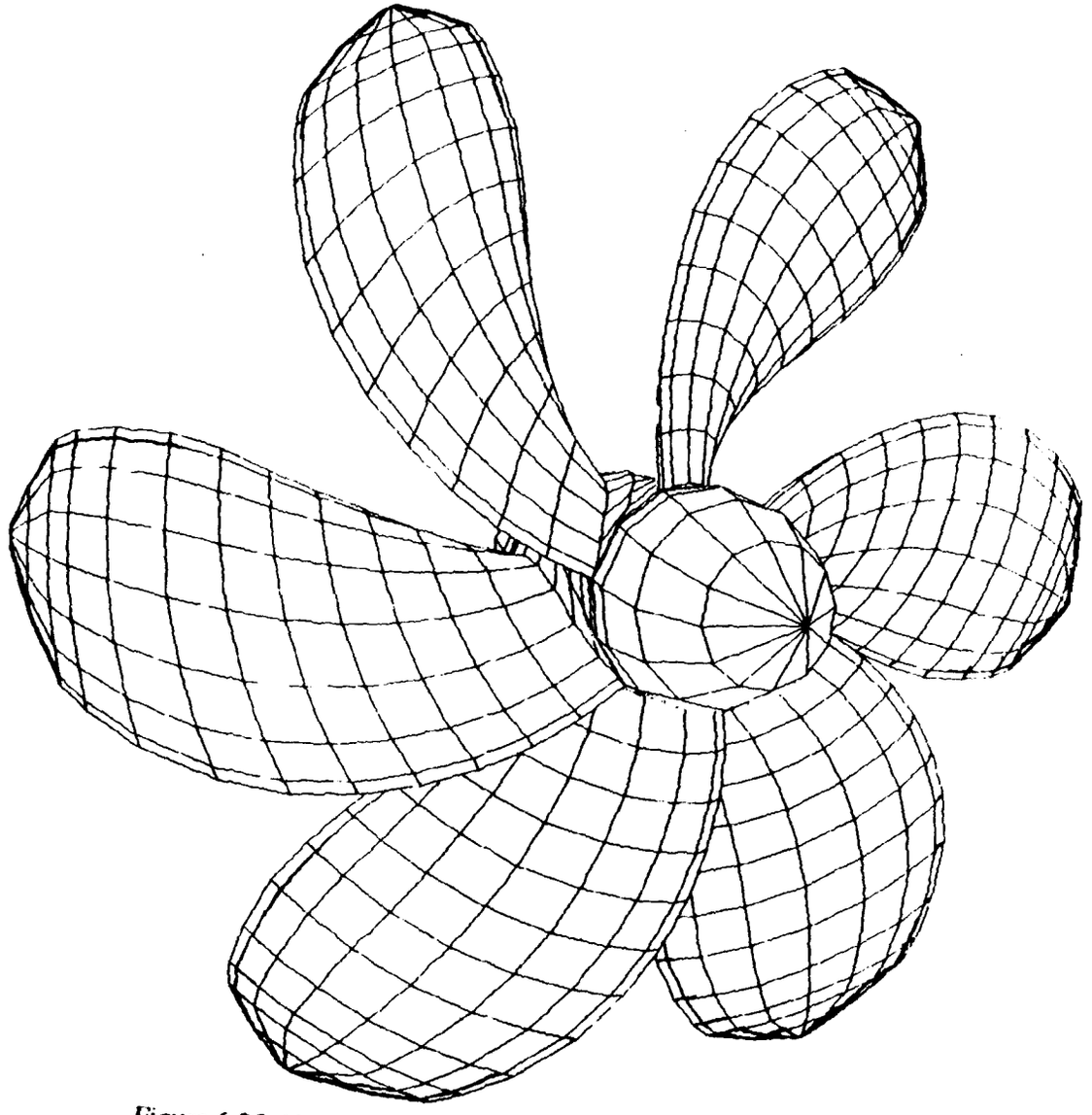

Figure 6.25. USAERO Paneling for the SRI MP0123 6-bladed Propeller

Feb 10 16:28:59 1991
OMNI3D (AMI)
ITER= 1

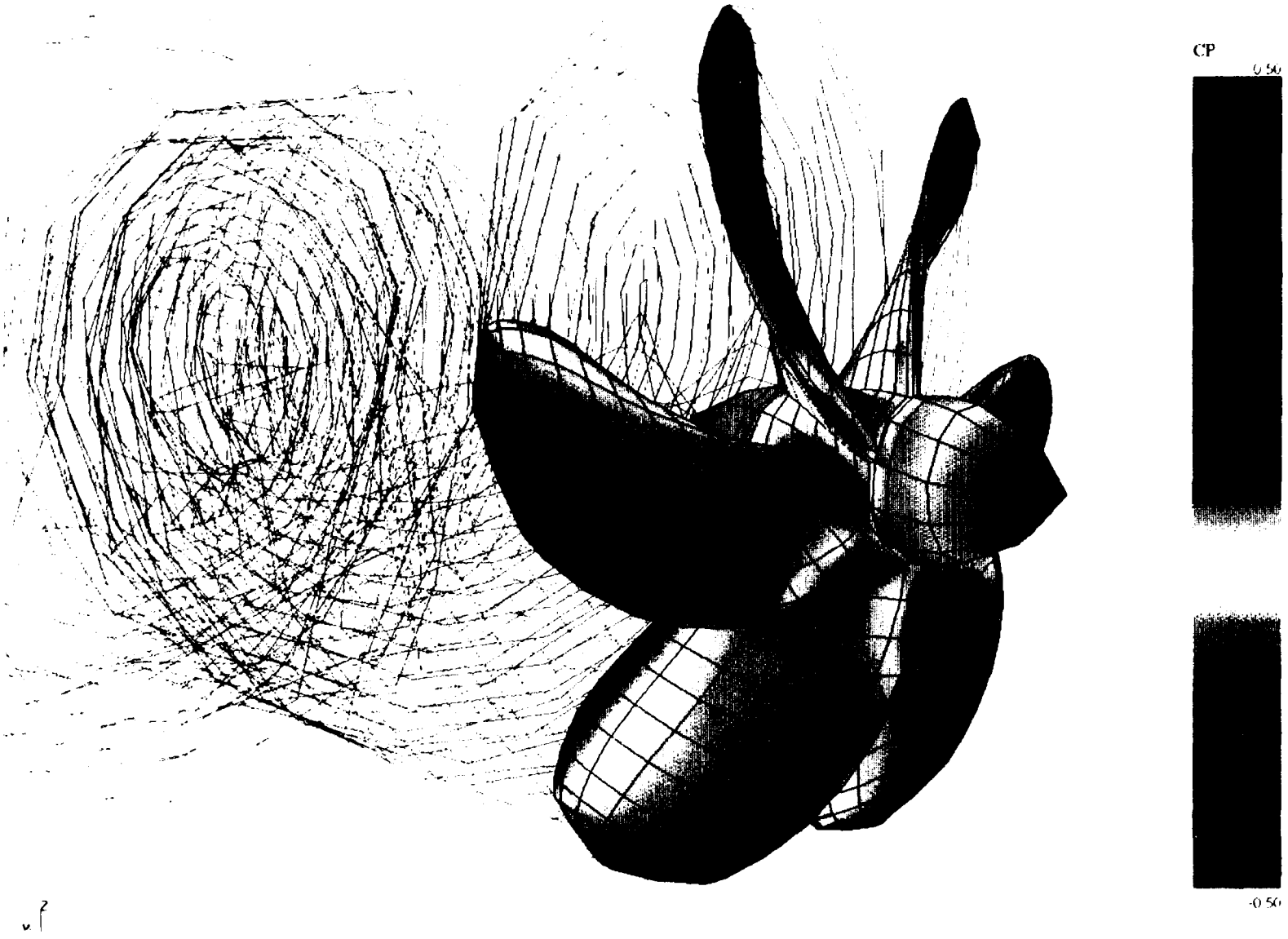

(a) General View Showing Computed Wake and Spectrum Plot of Surface Pressure (Hydrostatic Term Included)

Figure 6.26. USAERO Calculations for the SRI MP0123 6-Bladed Propeller in Uniform Flow at J = .7.

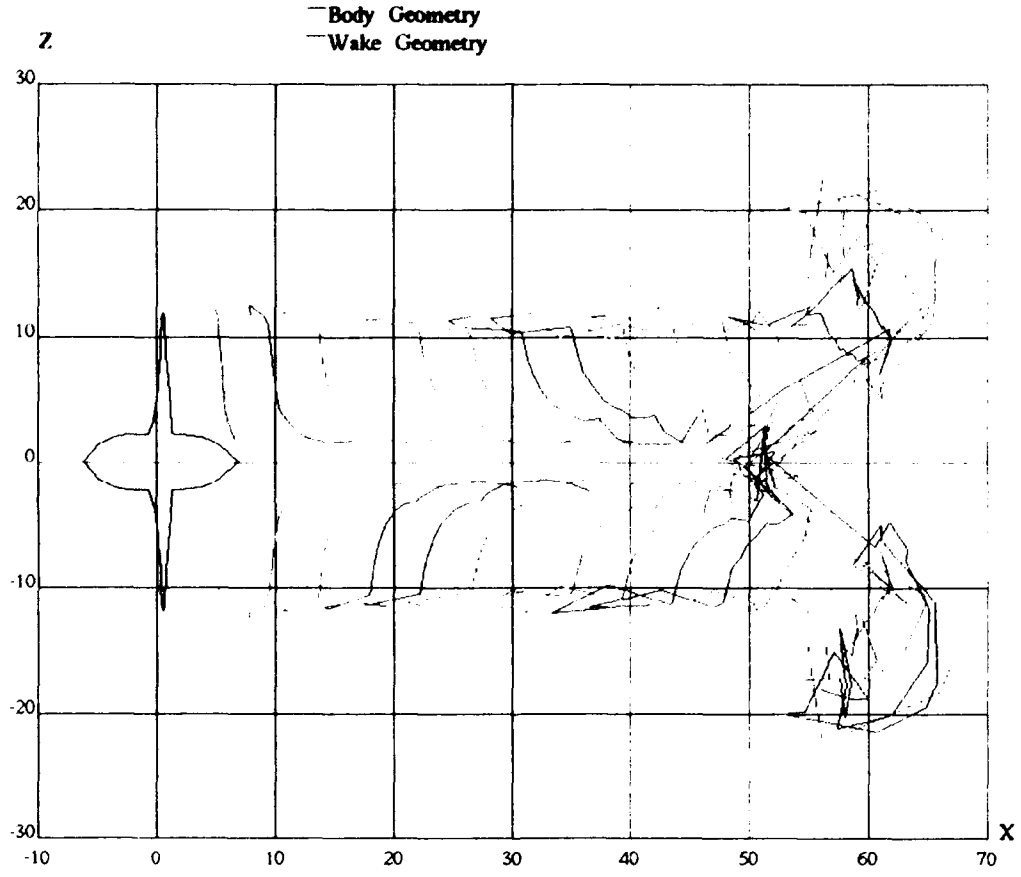

(b) Buttline Cut through Wake

BUTTLINE CUT
Y- 0.00

SRI MP0123 6-BLADED PROPELLER in uniform flow J=0.7

Oct 25 08:50:13 1990
OMNI3D (AMI)
ITER- 37

Figure 6.26. Continued.

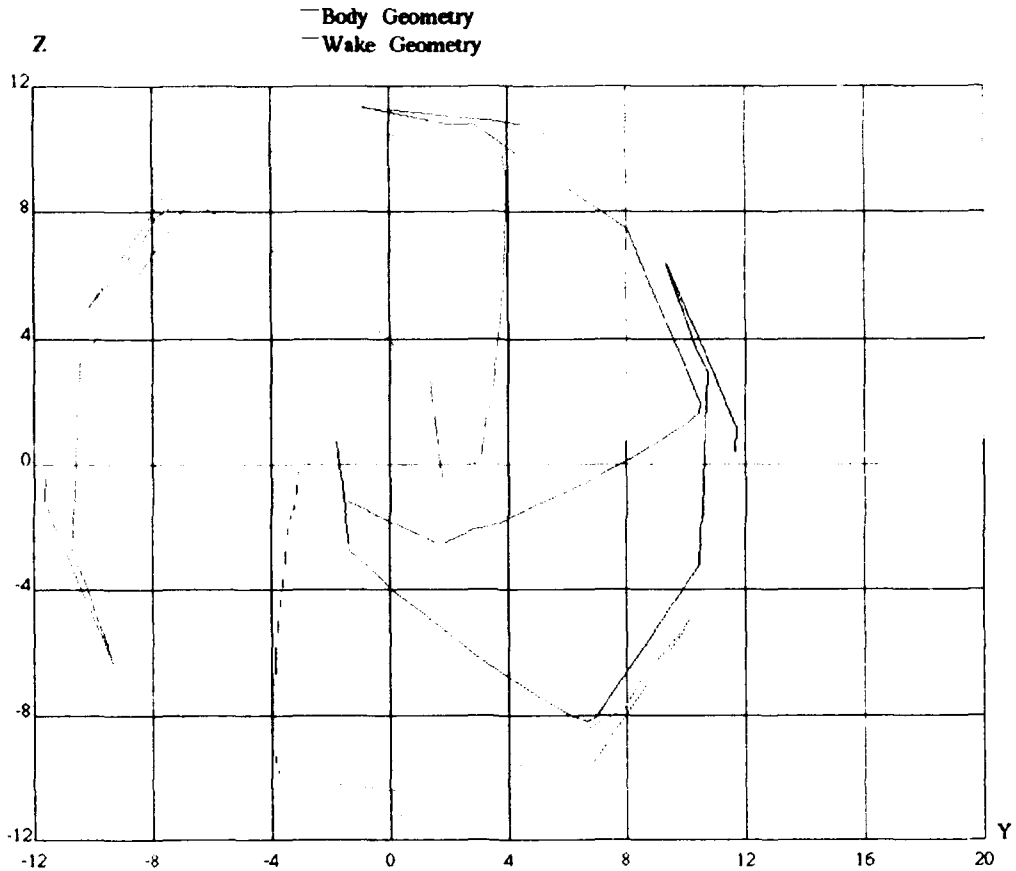

(c) Station Cut One Diameter Downstream from Propeller

STATION CUT
X- 25.00

SRI MP0123 6-BLADED PROPELLER in uniform flow J=0.7

Oct 25 08:52:22 1990
OMNI3D (AMI)
ITER- 37

Figure 6.26. Continued.

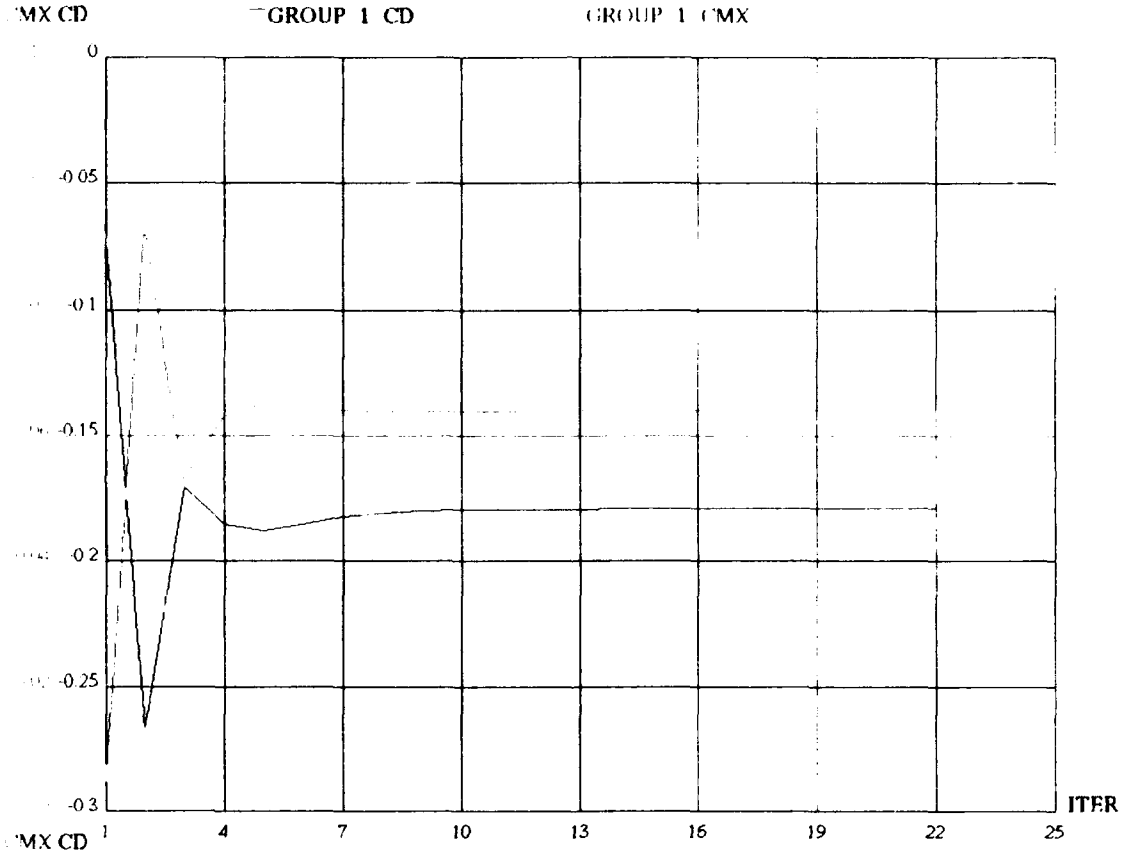

(d) Time History of CD and CMX

Groups of Panels

SRI MP0123 6-BLADED PROPELLER in uniform flow J=0.7

Oct 25 12:08:25 1990
OMNI3D (AMI)
ITER= 22

Figure 6.26. Continued.

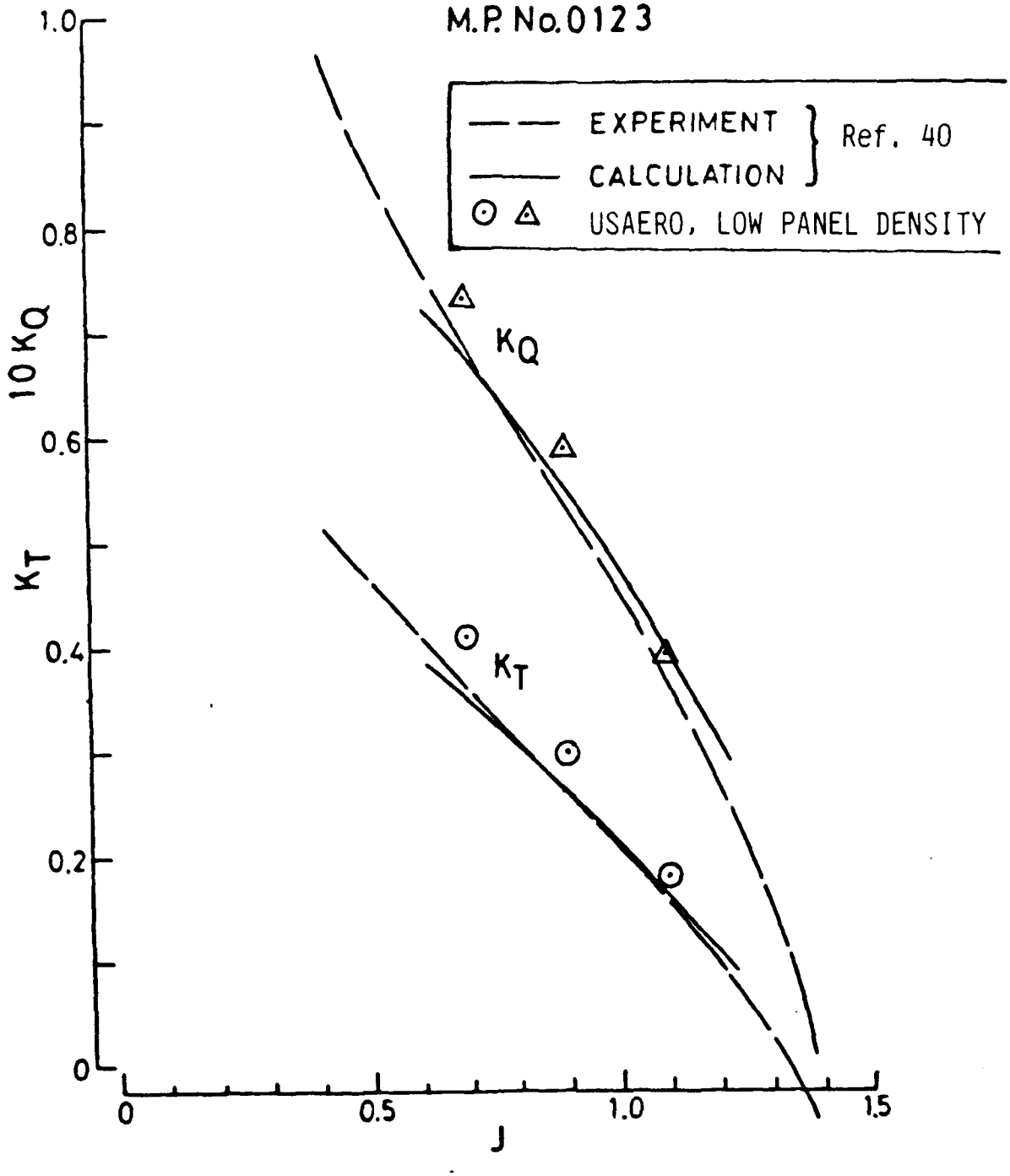

(e) Comparison of Calculated and Measured Thrust and Torque Coefficients

Figure 6.26. Continued.

obtained from the calculation is not consistent with the expected correction due to viscous effects; it is likely that the calculation has underestimated the leading-edge thrust because of poor panel resolution around the leading edge. A higher panel density, at least in the chordwise direction, would be essential in order to predict torque correctly. This would also be a requirement when including boundary layer calculations in the analysis.

Figures 6.26(f), (g) and (h) show a very reasonable correlation between the calculated pressure distribution and measured values at .77 radius for advance rations of .7, .9 and 1.1, respectively. The normalizing velocity for the experimental pressure coefficient is the local inflow velocity plus an induced term computed by a lifting surface theory. The latter term is unknown here but should be small at the advance ratios considered. For the present calculation, therefore, the normalizing velocity for pressure coefficient is just the local inflow velocity, i.e., the combination of the onset flow and the velocity due to rotation at .77 radius.

The results discussed above establish a basic level of accuracy for the code. Although the application of a time-stepping method to the analysis of propellers in uniform flow would normally be regarded as "overkill", it is interesting to note that for the advance ratios covered, steady state solutions were reached in less than 15 minutes on an SGI IRIS Power workstation. Moreover, the calculations include the natural convection of the wakes.

6.3.2.2 Nonuniform Flow Analysis

In the nonuniform onset flow case the experimental (40) wake fractions (Figure 6.21) were digitized and placed directly into the USAERO flow corresponding to J = .9. The resulting axial onset flow is displayed in a spectrum plot in Figure 6.27. Red indicates the low flow region while blue represents the undisturbed flow. The velocity is normalized by the speed of rotation at .77 of the propeller radius. The circular survey plane has a diameter 1.2 times that of the propeller and is placed just upstream of the propeller.

Figure 6.28 shows a general view of the propeller with a moderate panel density; 480 panels were used on each blade in a 30 x 15 array plus 2 x 15 on the tip. This is approximately double the panel density used for the uniform flow case but is still about half the density used earlier in the MPROP frequency band analysis. The propeller was started impulsively from rest to 10.8 rps at J = .9 and was run for three revolutions with 24 steps per revolution. Only results from the last complete revolution were passed to the plot file. Figure 6.28 shows the computed surface pressure distribution at the end of the third revolution. The pressure values include the dynamic, impulsive and hydrostatic terms. Note the relatively high leading-edge suction levels (red) on the blades near the top and bottom azimuthal positions compared with lower suction levels (green) on the two blades in the high flow region: the rotational velocity combined with the full onset flow produces a lower local angle of attack than when combined with the smaller onset flow in the "wake". The propeller wake itself is displayed by streamwise lines. These indicate the computed locations of the wake doublet sheets which are propagated from each blade trailing edge and convected

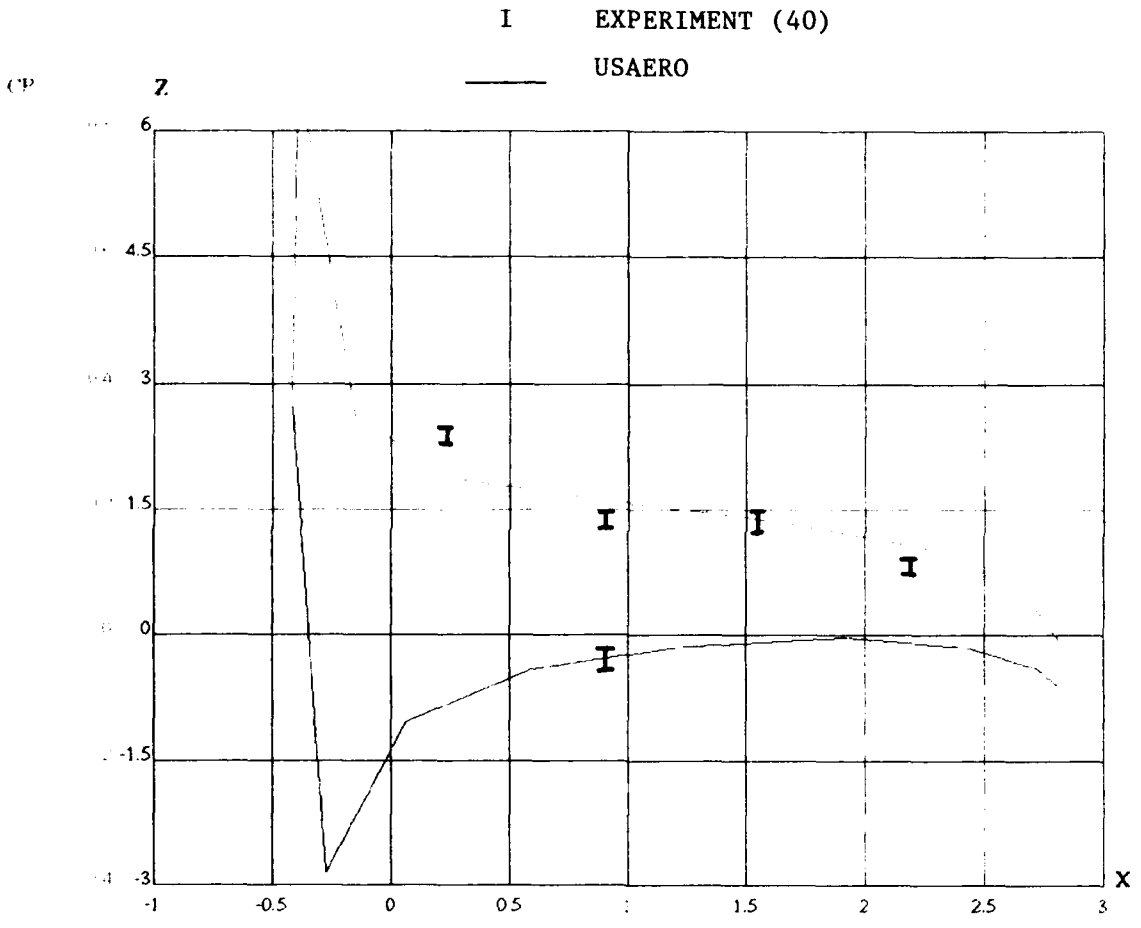

(f) Comparison of Calculated and Measured Chordwise Pressure Distribution at 0.77 Radius at J = 0.7

BUTTLINE CUT
Y- 9.60

SRI MP0123 6-BLADED PROPELLER in uniform flow J=0.7

Oct 25 12:06:46 1990
OMNI3D (AMI)
ITER- 22

Figure 6.26. Continued.

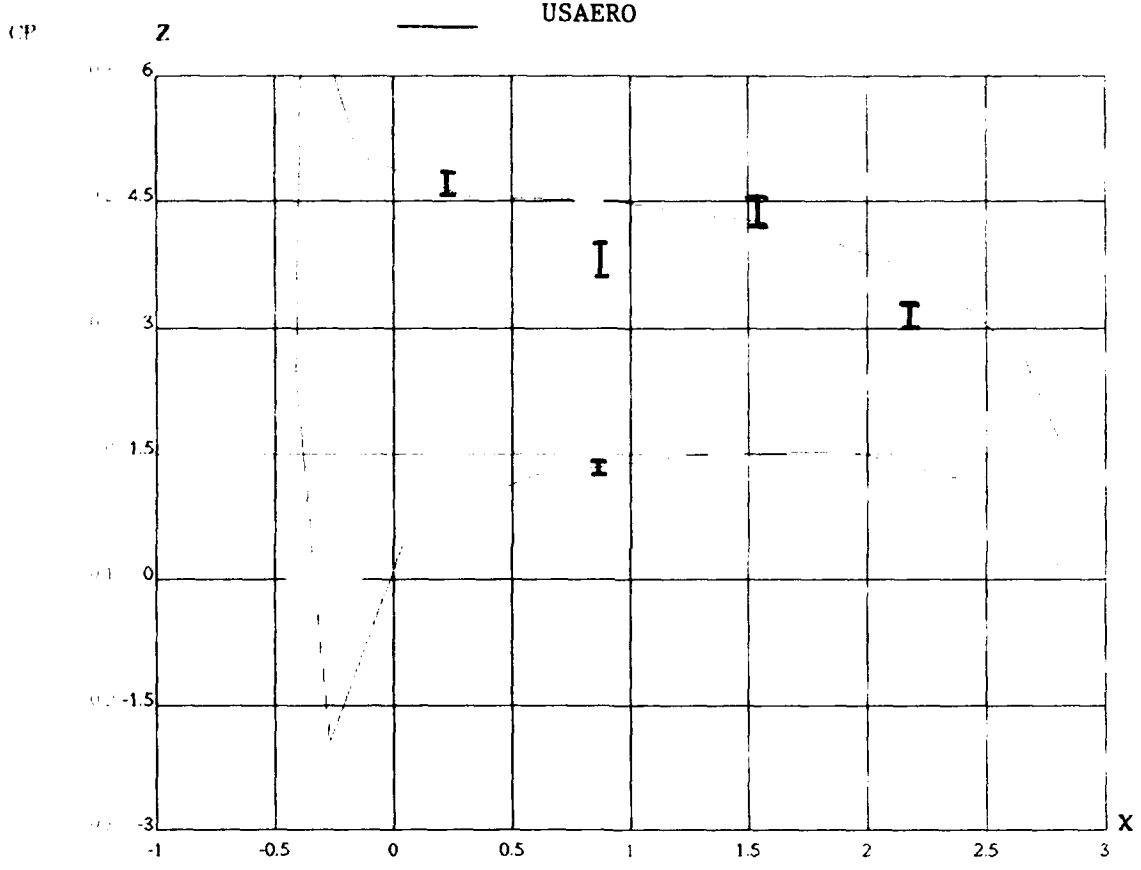

(g) Comparison of Calculated and Measured Chordwise Pressure Distribution at .77 Radius for J = 0.9

BUTTLINE CUT
Y- 9.60

SRI MP0123 6-BLADED PROPELLER in uniform flow J=0.9

Oct 25 12:26:10 1990
OMNI3D (AMI)
ITER- 12

Figure 6.26. Continued.

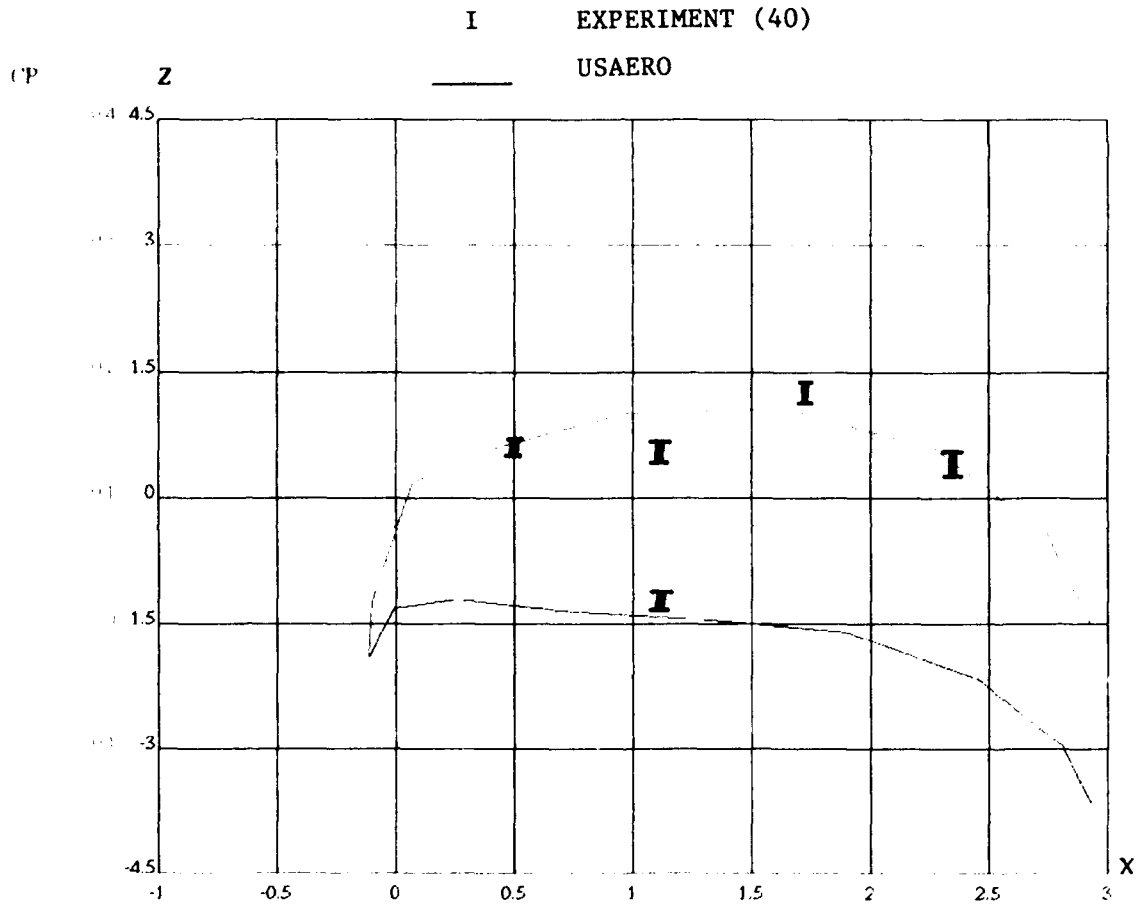

(h) Comparison of Calculated and Measured Chordwise Pressure Distribution at 0.77 Radius at J = 1.1

Figure 6.26. Concluded.

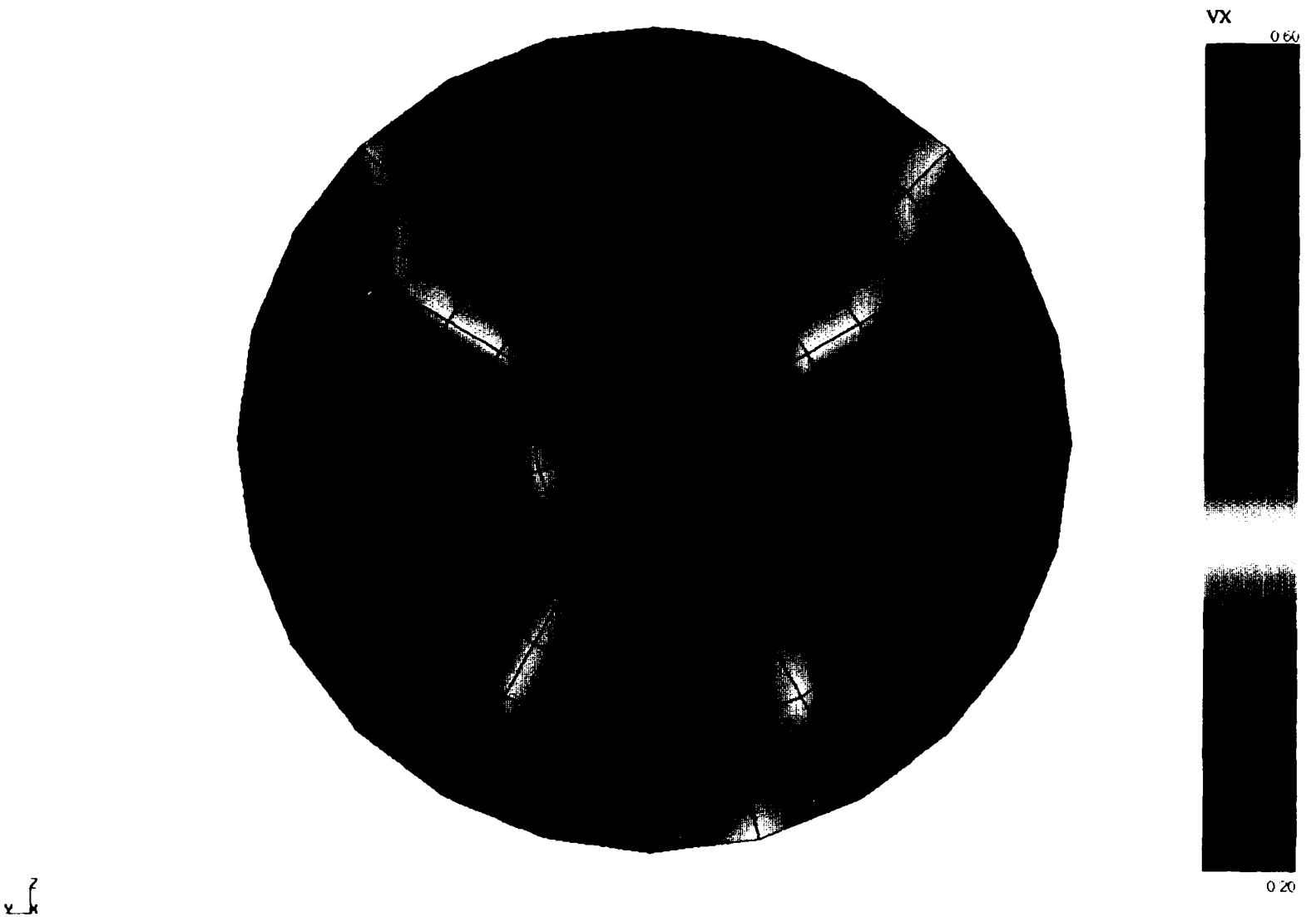

Figure 6.27. Resulting Onset Flow Computed on a 1.2 D Disc Just Upstream of Propeller (Vx Normalized by Speed of Rotation at .77 R).

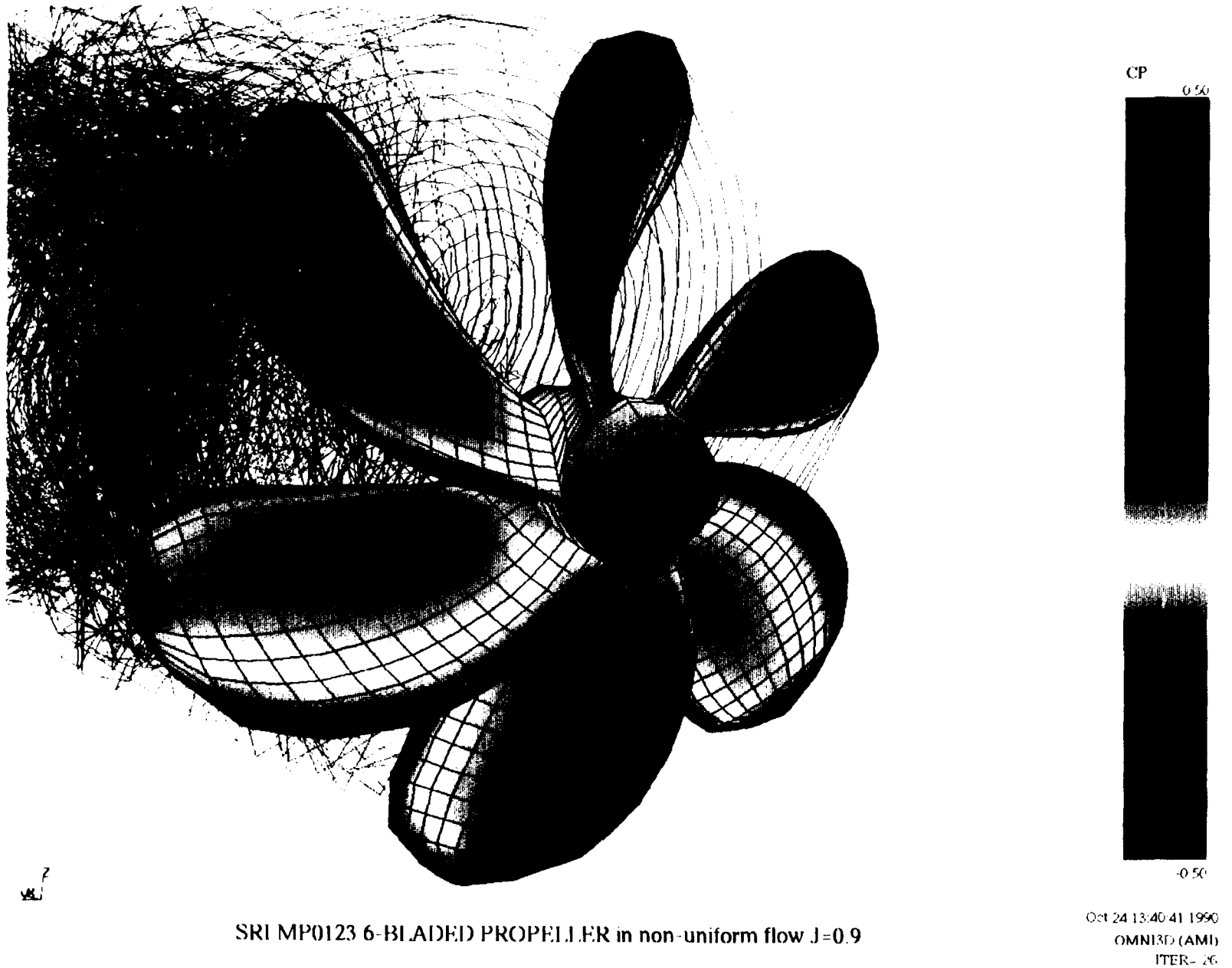

Figure 6.28. General View of the MP0123 Propeller in Nonuniform Flow Showing the USAERO Computed Surface Pressure Distribution.

downstream step-by-step at the local velocities. In this case the convection rate is slower at the top and bottom azimuthal stations compared with those at the sides and so there is a tendency to bunch up near the vertical plane. Figures 6.29(a) and (b) show two waterline cuts at Z = 3.0 and 7.0 (.24 and .56 of blade radius, respectively) in the low flow region and indicate a smooth wake propagation from the blade trailing edges at the various conditions captured by the cuts on different blades.

Because of earlier problems encountered in MPROP in regard to the Kutta condition in the blade root region, the computed pressure distribution was also inspected at the Z = 3.0 waterline cut (Z/R = .24; the hub is at .18). Figure 6.30 indicates a very good behavior of the unsteady Kutta condition employed in USAERO. The impulsive term (included in the total) is also displayed (at the same scale) to indicate the magnitude of the unsteady effect at this position.

Typical chordwise pressure distributions at approximately .77 radius are given in Figure 6.31(a), (b), (c) and (d) for a blade at azimuthal stations 0, 90, 180 and 270 degrees, respectively. They are all plotted to the same Cp scale to indicate visually the range of pressure variation in one revolution. They all indicate a good behavior of the unsteady Kutta condition over a wide range of conditions. The impulsive term is included as well as the complete pressure coefficient. A load reversal is evident at the 90° and 270° positions, i.e., in the full onset flow. This is consistent with the general view in Figure 6.28°.

Experimental pressure measurements (40) were taken at five chordwise positions at .77 radius on the blade. Positions A, B, C and D are on the "upper" or "suction" side at .2, .4, .6 and .8 of the chord, respectively, from the local leading edge and position E is at .4 of the chord on the "pressure" side. Comparisons between measured and calculated pressures for one complete revolution are shown in Figure 6.32(a), (b), (c), (d) and (e) for positions A, B, C, D and E, respectively. The calculations include curves for a lower panel density case which used 240 panels in a 16 x 14 array plus 2 x 8 on the tip. At position A (-2c) there is very little effect of panel density but the calculated pressures are generally more negative than the experimental values. (The frequency band analysis tended to be more positive, Figure 6.22.) Although the main features of the pressure variation are captured by the calculation there is a general appearance of a phase lead. Basically, the calculation follows the experiment fairly closely in the region of <u>decreasing</u> peak suction (i.e., when entering the high onset flow region), but it leads the experiment on the <u>increasing</u> peak suction region (entering the low onset flow region). The effect of viscosity could be a factor here; boundary layer effects were not included in the present calculations. At position B (-4c), the calculation is again more negative than the measured values but in this case the discrepancy is an almost constant 10 mm. of Hg. In this case the main features of the pressure variation--which is less extreme than at postion A--are captured by the calculation and are more or less in phase. The lower panel density calculation at this position is again fairly close to the high density case; the main deviations occur near the bottom azimuthal position where the blade is leaving the low onset flow region. This deviation of the low panel density case is somewhat more obvious for position C (-6c) at the same azimuthal station.

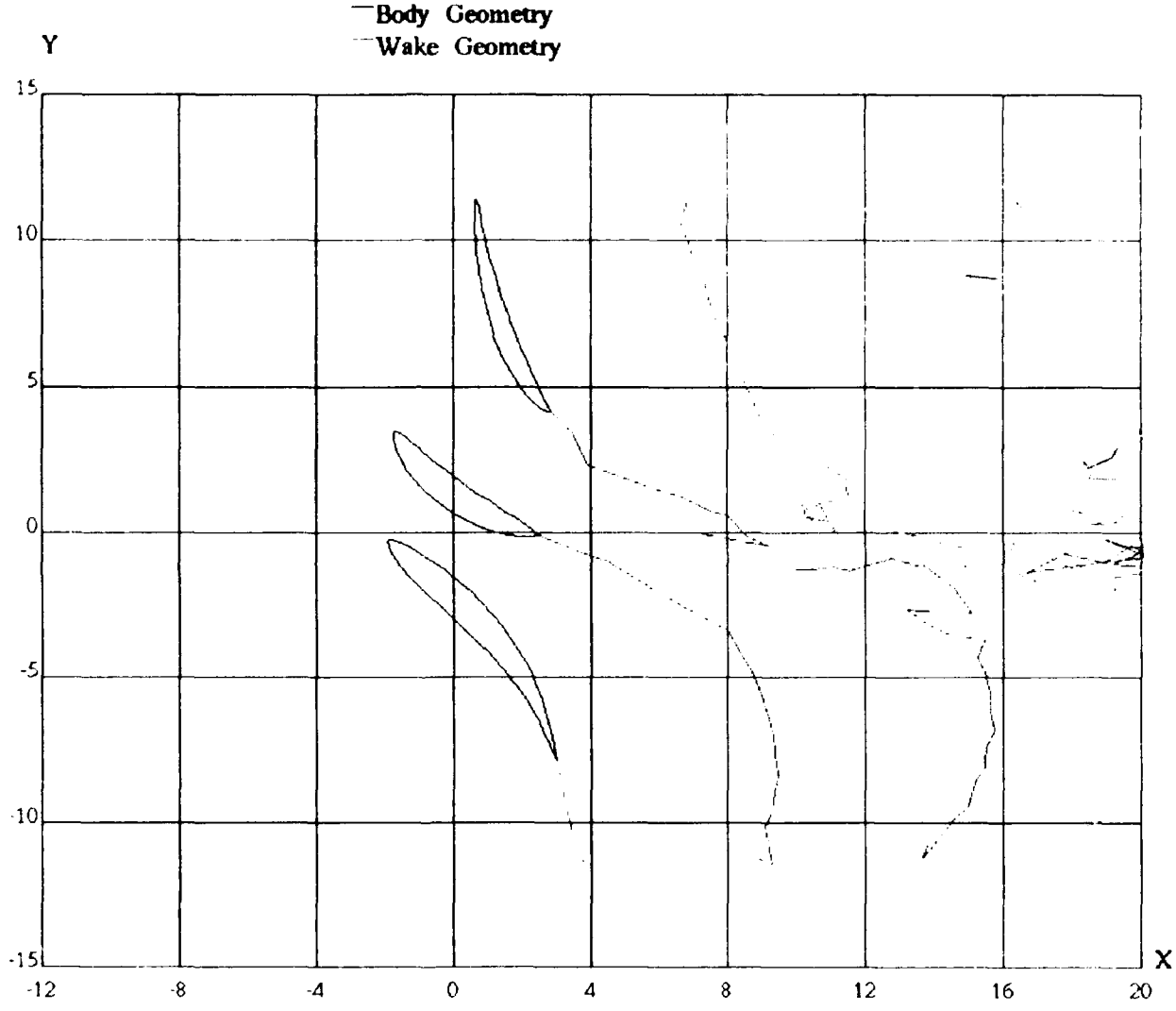

(a) Z/R = 0.24

Figure 6.29. Waterline Cuts through the Blades and Local Wake.

WATERLINE CUT

SRI MP0123 6-BLADED PROPELLER in non-uniform flow J=0.9

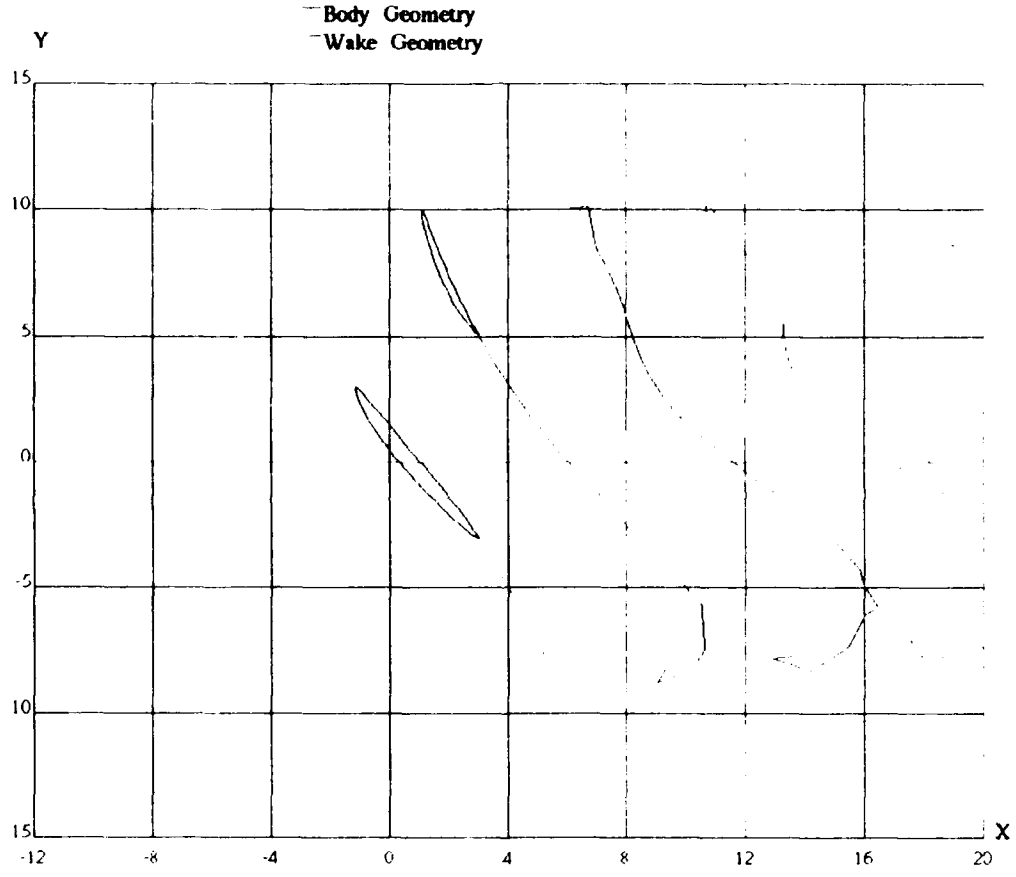

(b) Z/R = 0.56

WATERLINE CUT
Z= 7.00

SRI MP0123 6-BLADED PROPELLER in non-uniform flow J=0.9

Oct 24 14:11:06 1990
OMNI3D (AMD)
ITER= 26

Figure 6.29. Concluded.

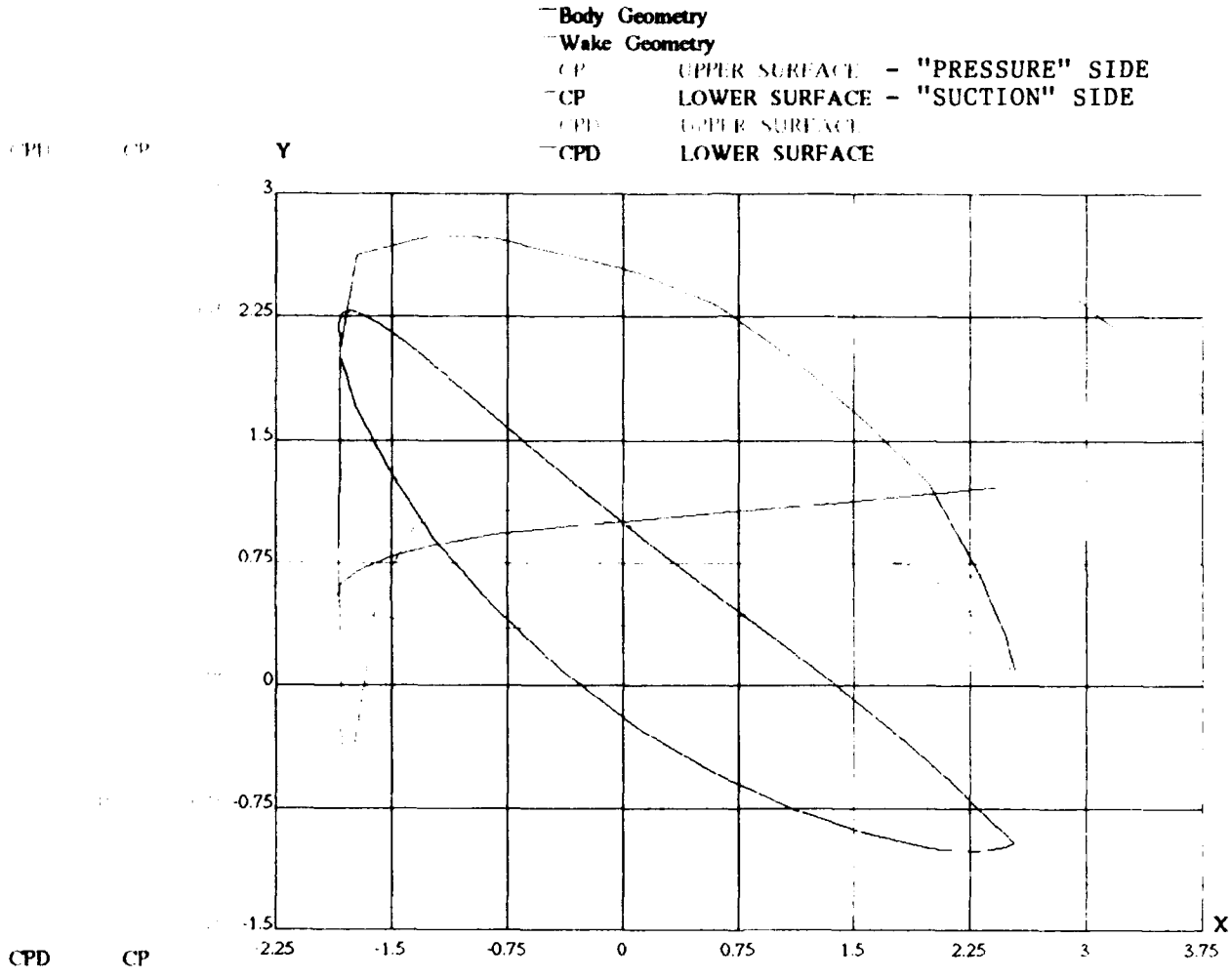

Figure 6.30. Details of the Computed Pressure Distribution near the Blade Root.

WATERLINE CUT
Z- 3.00

SRI MP0123 6-BLADED PROPELLER in non-uniform flow J=0.9

Oct 24 14:05:34 1990
OMNI3D (AMI)
ITER- 26

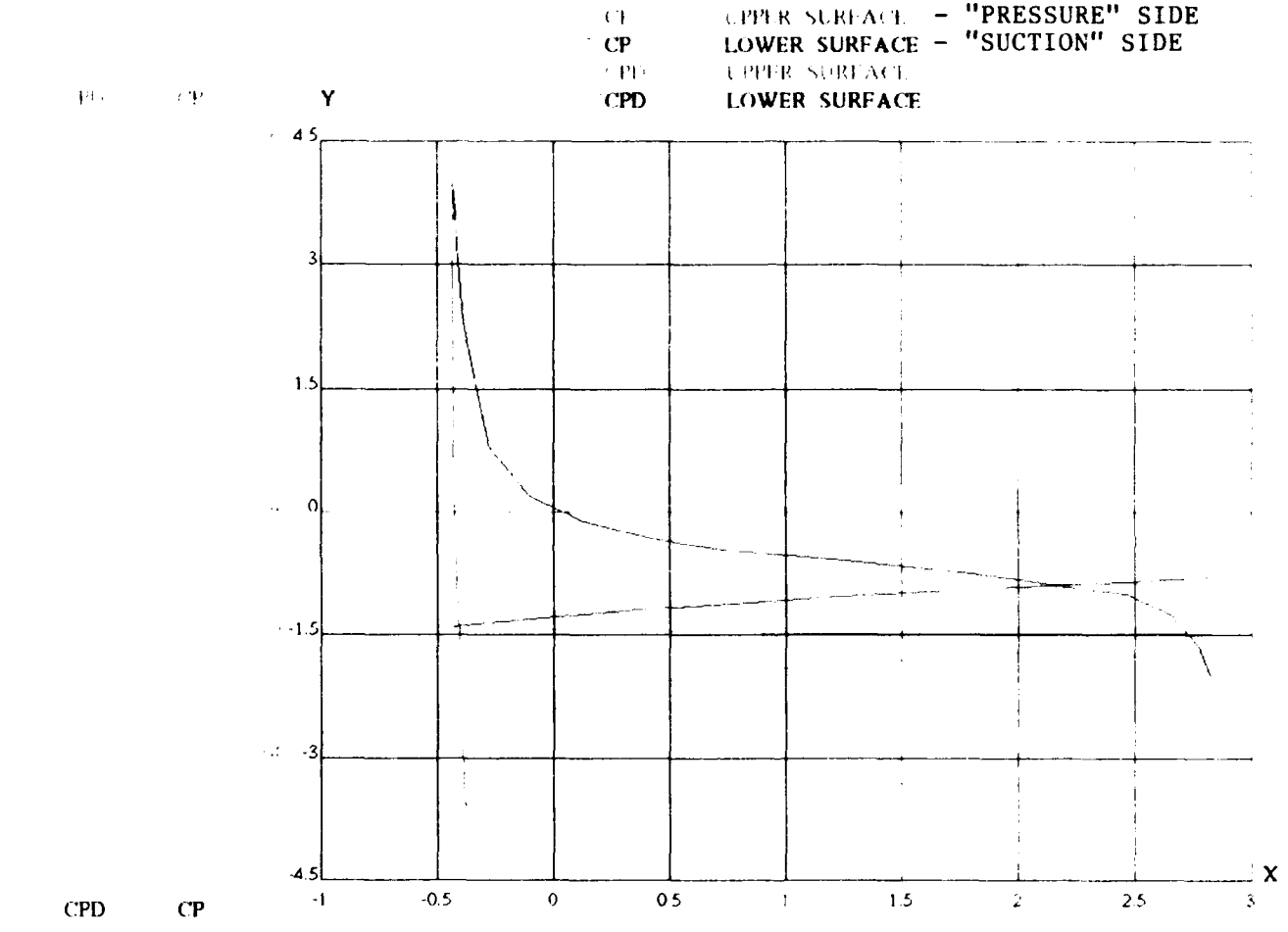

(a) 0° (Top)

WATERLINE CUT
Z- 9.60

SRI MP0123 6-BLADED PROPELLER in non-uniform flow J=0.9

Oct 24 13:47:49 1990
OMNI3D (AMI)
ITER- 2(

Figure 6.31. Computed Chordwise Pressure Distribution at .77R at Various Azimuthal Stations.

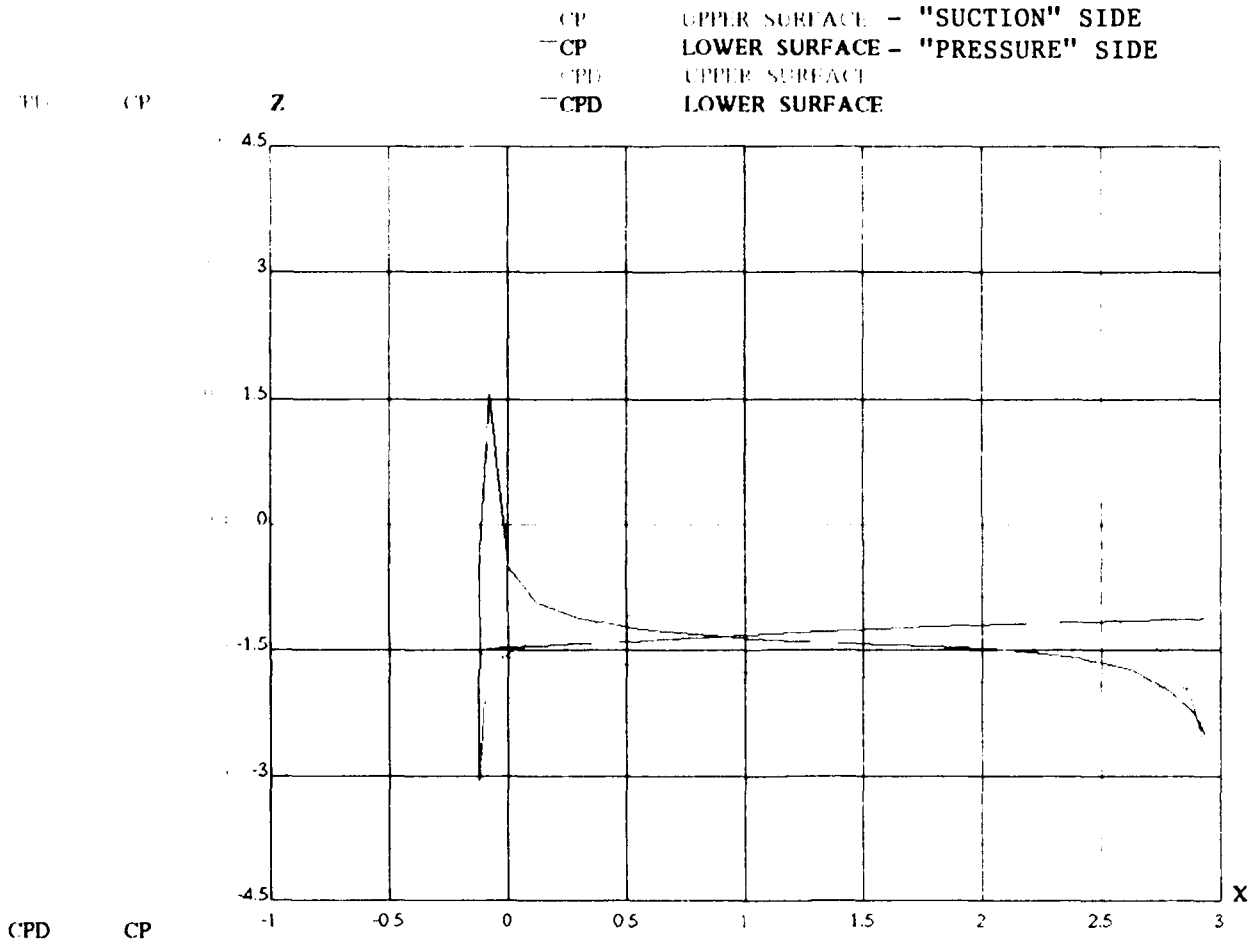

(b) 90° (Side)

BUTTLINE CUT
Y- 9.60

SRI MP0123 6-BLADED PROPELLER in non-uniform flow J=0.9

Oct 24 13:54:31 1990
OMNI3D (AMI)
ITER- 9

Figure 6.31. Continued.

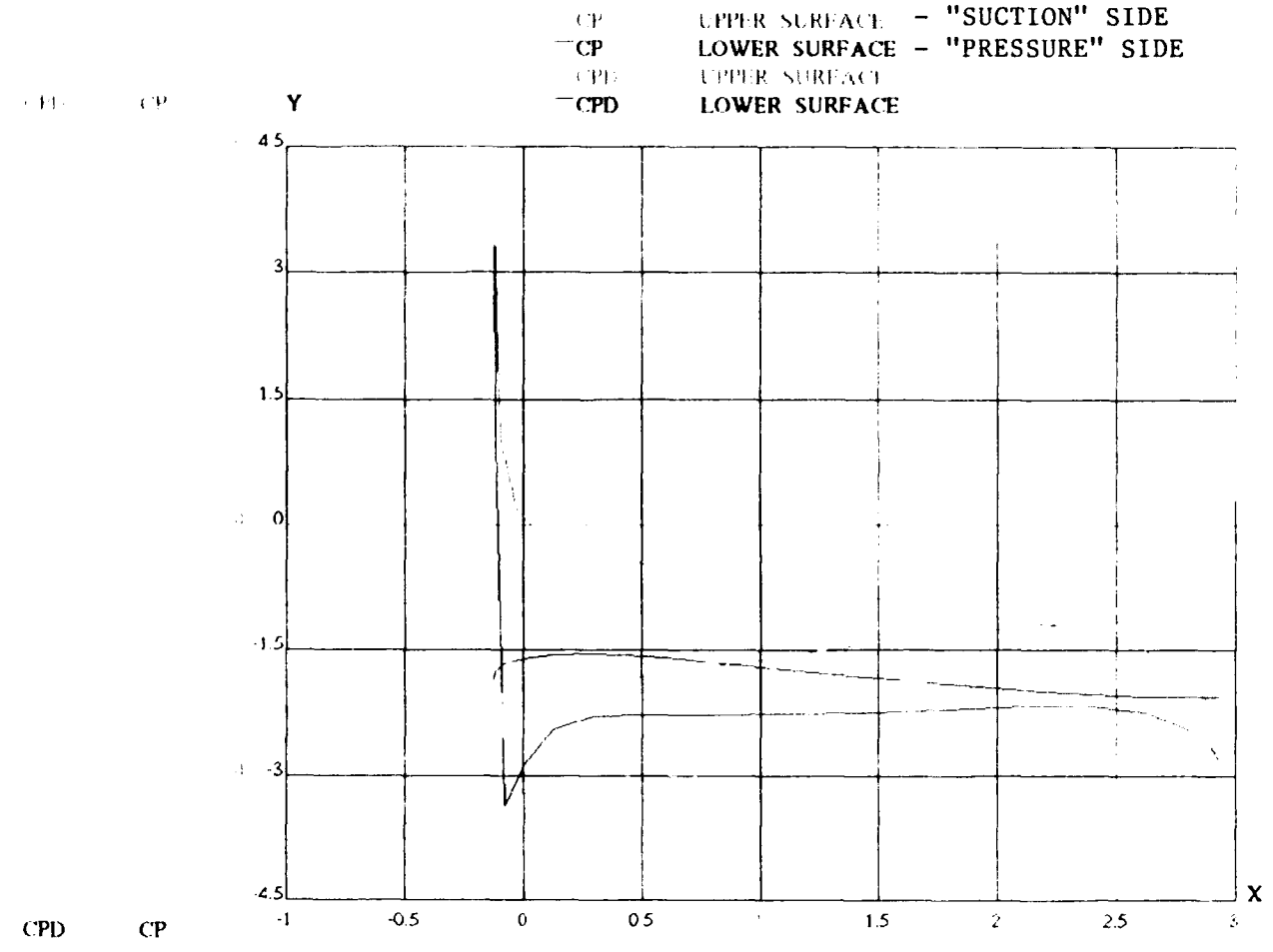

(c) 180° (Bottom)

Figure 6.31. Continued.

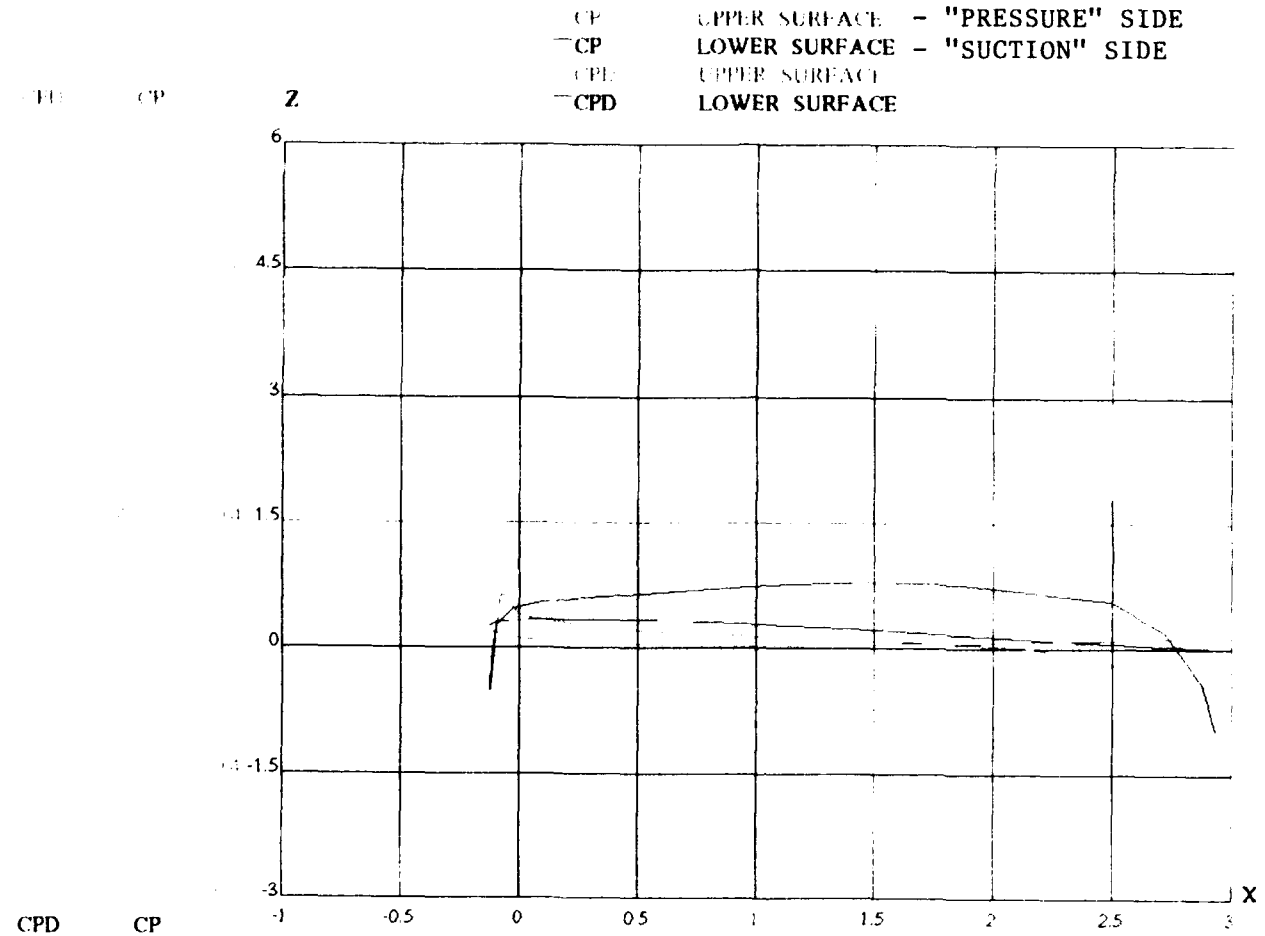

(d) 270° (Side)

BUTTLINE CUT
Y= -9.60

SRI MP0123 6-BLADED PROPELLER in non-uniform flow J=0.9

Oct 24 14:00:38 1990
OMNI3D (AMI)
ITER= 21

Figure 6.31. Concluded.

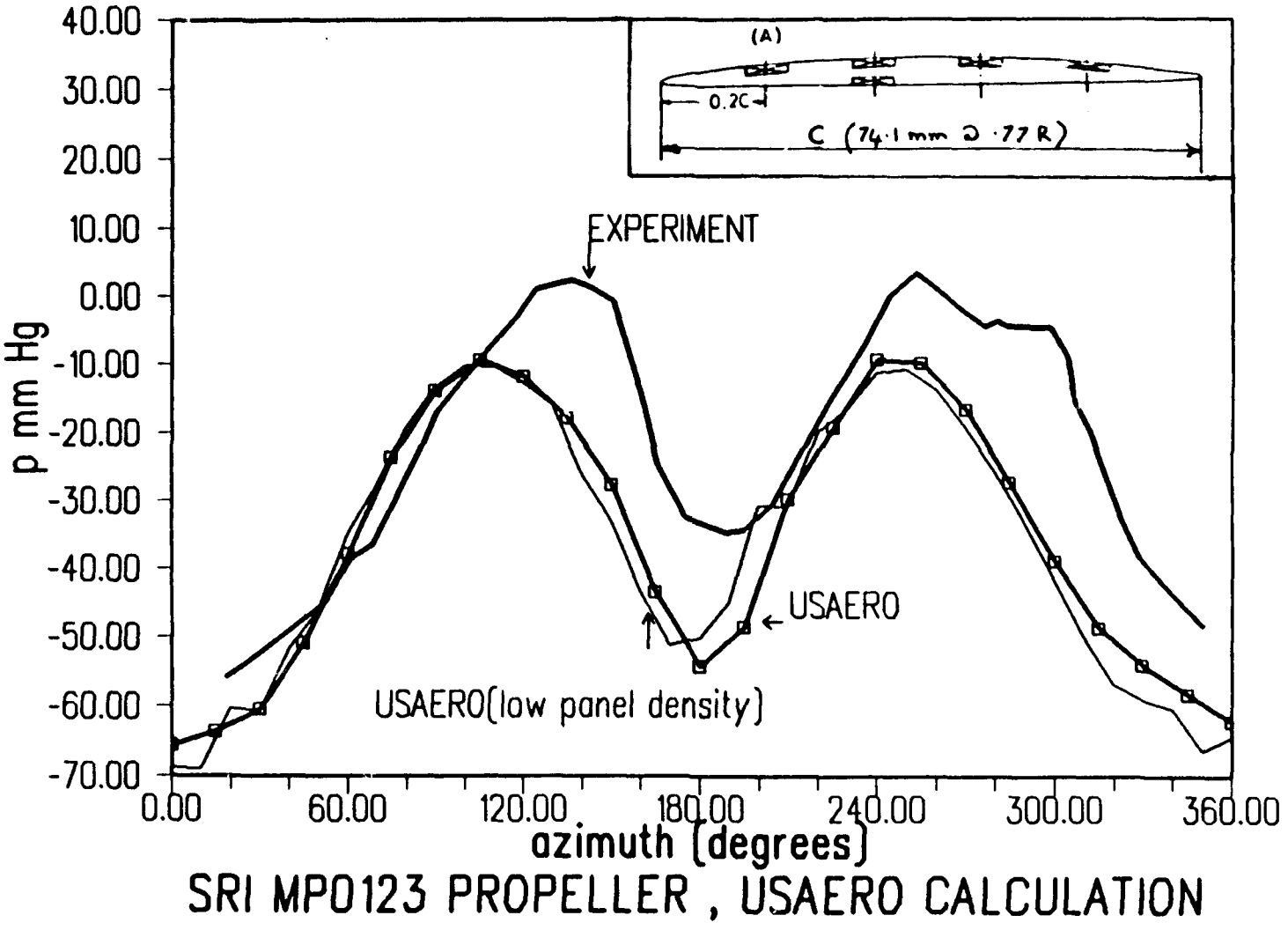

(a) Position A

Figure 6.32. Comparison of Calculated and Measured Pressure Histories--Time-Dependent Analysis.

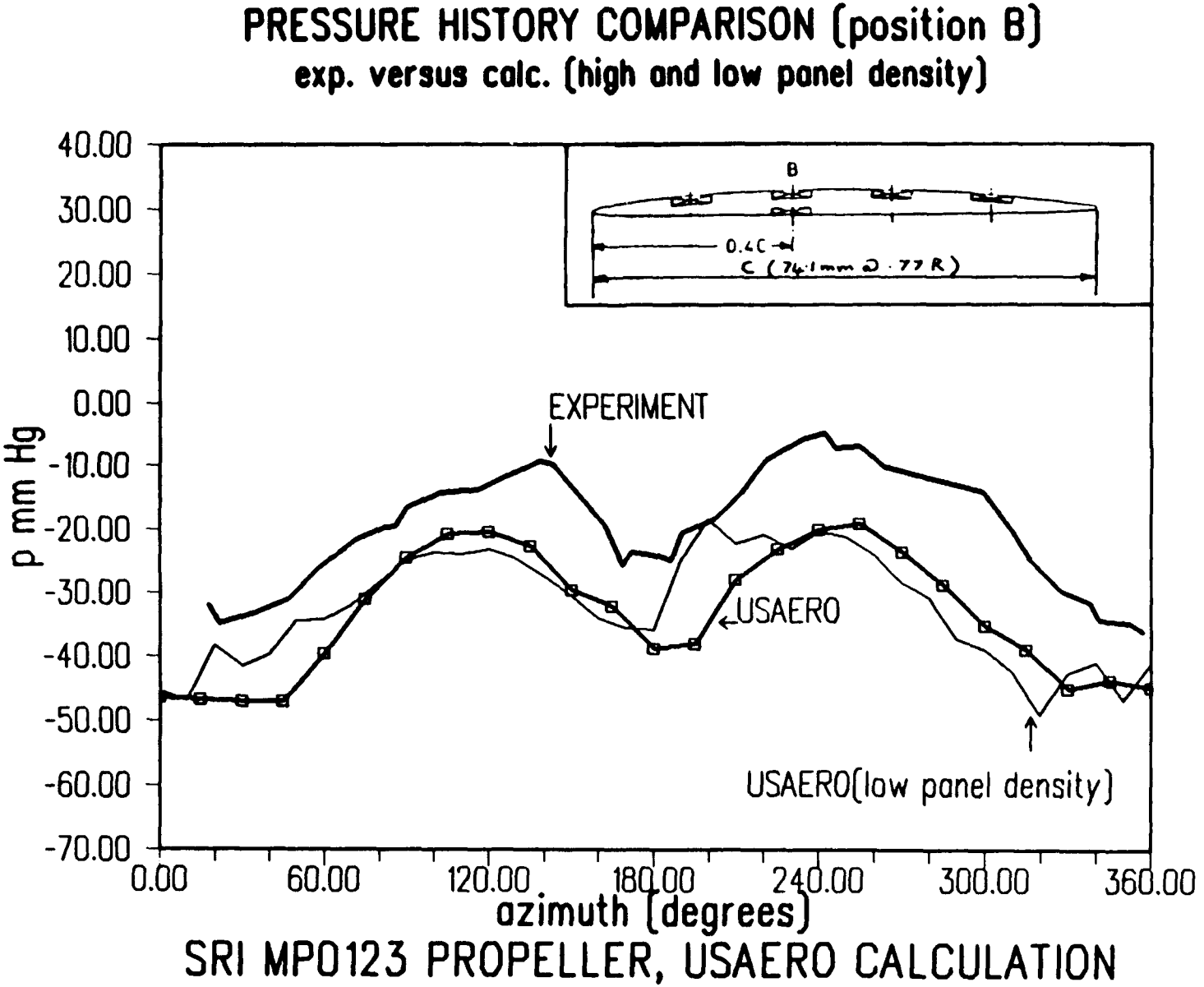

(b) Position B

Figure 6.32. Continued.

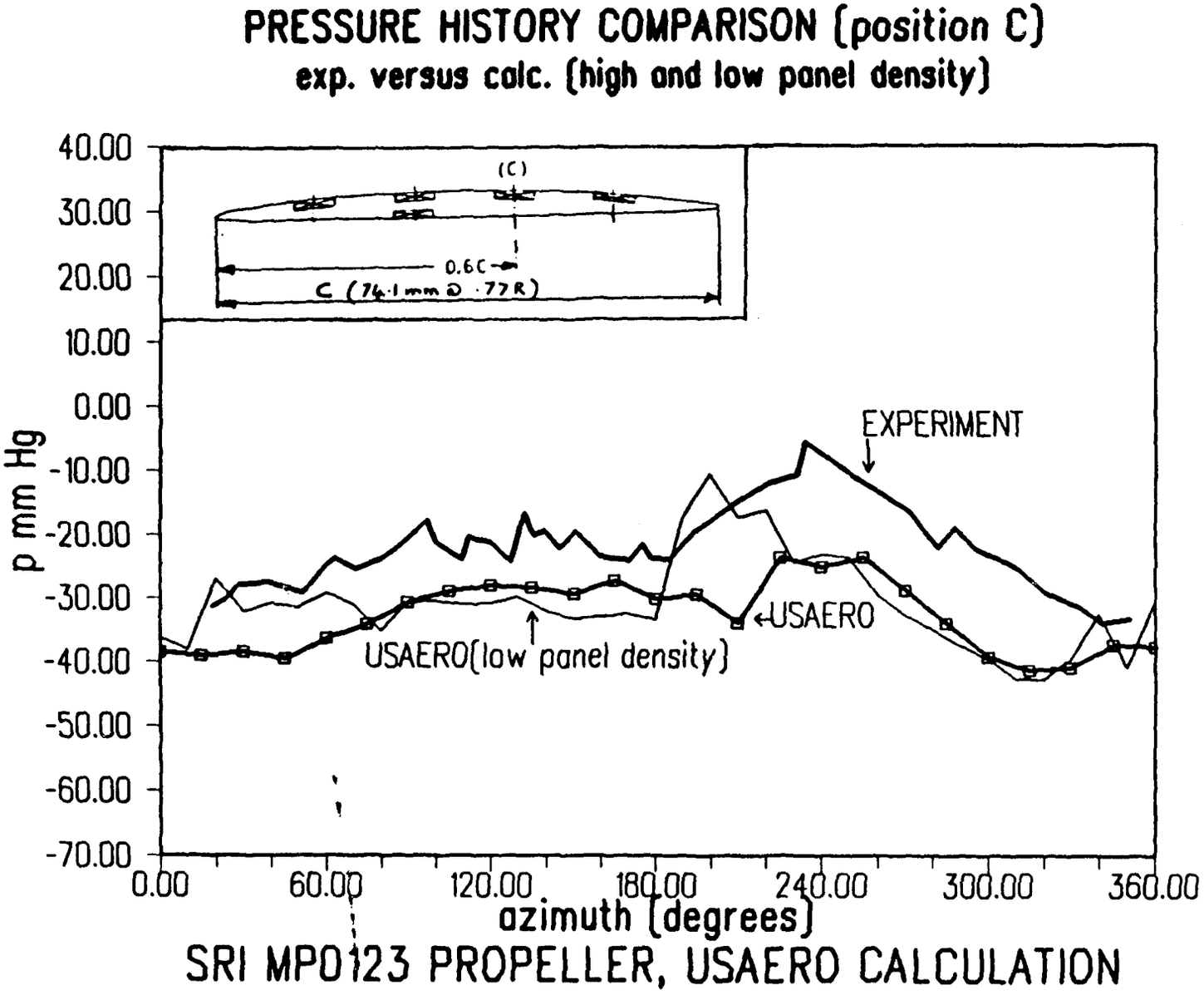

(c) Position C

Figure 6.32. Continued.

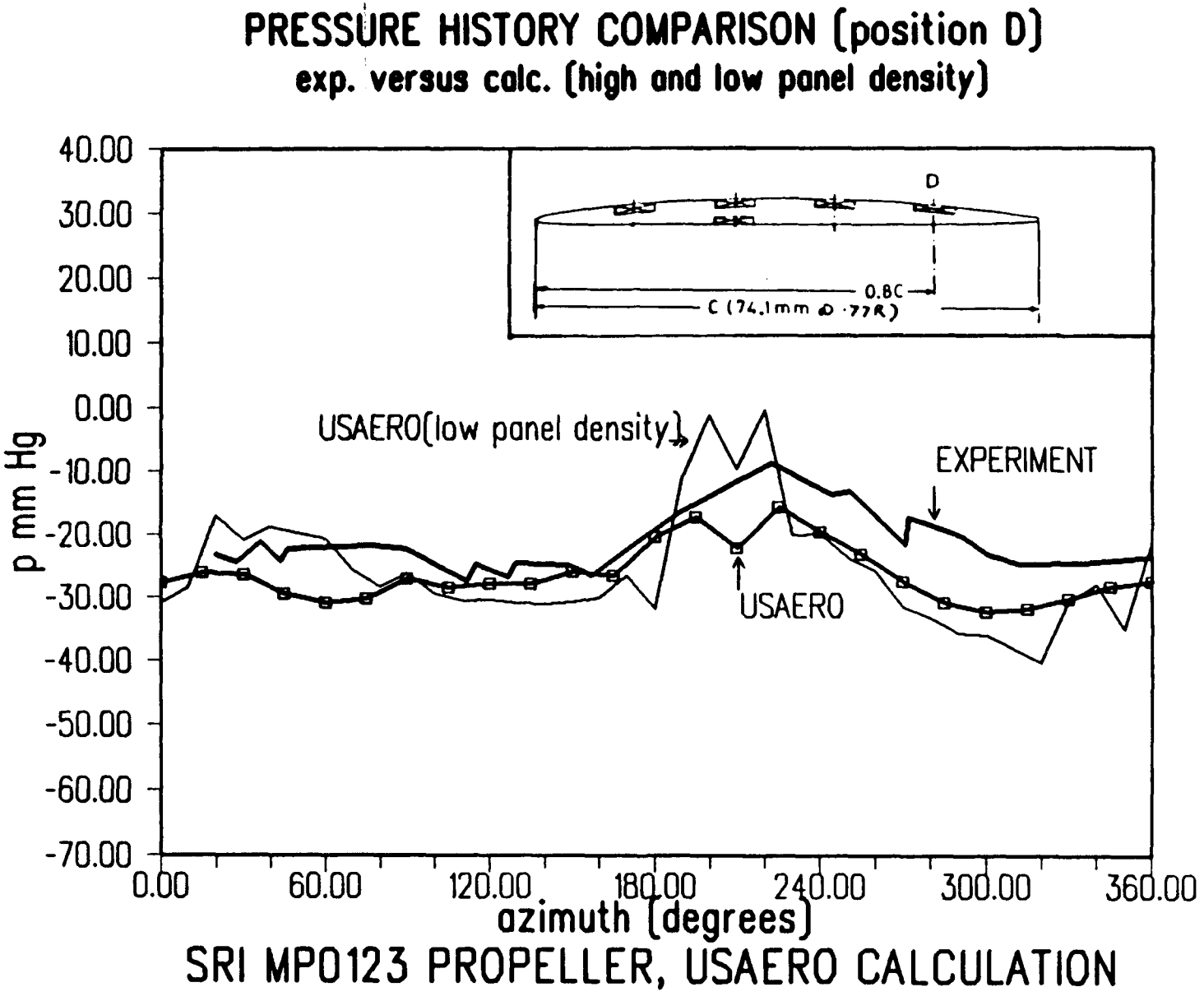

(d) Position D

Figure 6.32. Continued.

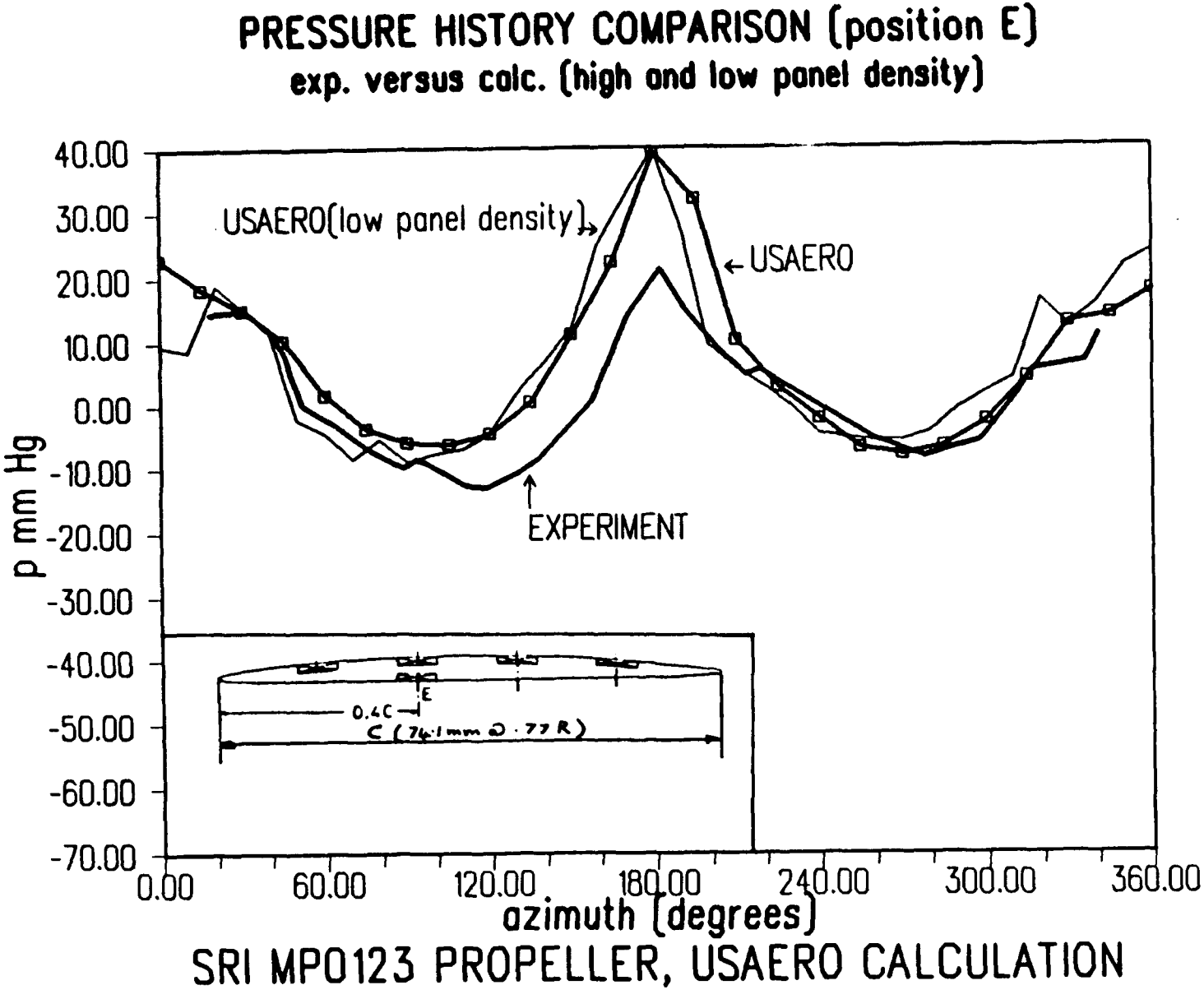

(e) Position E

Figure 6.32. Concluded.

Again, the high density case follows the experimental pressure variation at position C very closely but with a general negative offset of about 10 mm. Hg.

At position D, Figure 6.32(d), the high density case again follows the experimental pressure variation very closely but with a small negative offset. The variation of pressure here is relatively benign compared with that at position A. The shift of the low panel density calculation when leaving the low-onset-flow region is even more pronounced than at positions B and C. This is caused by a small shift in the phase of the impulsive term in the lower density case compared with that of the higher density paneling.

Finally, at position E (-4c on the "pressure" side) the calculation again captures the main features of the measured pressure variation. This time there is a tendency for a positive shift in pressure. There is little effect of panel density evident at this position. Overall, the tendency for a negative pressure shift on the upper surface and positive shift on the lower surface are consistent with viscous effects and so it would be expected that the inclusion of boundary layer calculations in the unsteady calculation would improve the correlation with experiment.

It is instructive to examine the detailed breakdown of the pressure variation into its component parts, i.e., dynamic, impulsive and hydrostatic, as outlined in Eq. (5.19). Figure 6.33(a) shows the details for position A. The dynamic term has a peak-to-trough variation of about 70 mm. Hg and lags behind the impulsive term by about 75° of azimuth. The impulsive term has a peak-to-trough variation of about 40 mm. Hg. Both the dynamic and impulsive terms have two cycles per revolution while the hydrostatic term, which has a peak-to-trough variation of about 16 mm. Hg, has one cycle. With such large variations in the major terms and in view of the phase difference between them, it is remarkable that the combined total is as close to the experiment as it is (Figure 6.32(a)). It is even more remarkable at position D (Figure 6.33(b)) where the resultant pressure variation is relatively benign. Here the peak-to-trough variations in the dynamic and impulsive terms are 50 and 70 mm. Hg, respectively, and they are essentially 90° out of phase.

Figure 6.34 displays the dynamic and impulsive pressure variations in relation to the onset flow sensed at position A. If we think in terms of the angle-of-attack variation due to the nonuniform onset flow, i.e., α small in the high flow region and α large in the low flow region, then the dynamic pressure is lagging α by about 25° while the impulsive term is leading by about 50°.

While it is true that the phasing between the dynamic and impulsive pressure terms is strongly connected to the reduced frequency of the effective α variation at each station, it is not clear to what extent the features of blade design, i.e., rake, skew, twist, camber and thickness distribution, affect the relationship. The time-stepping approach provides a means of examining these factors with a view towards achieving a blade design which minimizes the load variations for a given performance on a given hull (i.e., in the presence of a given nonuniform onset flow).

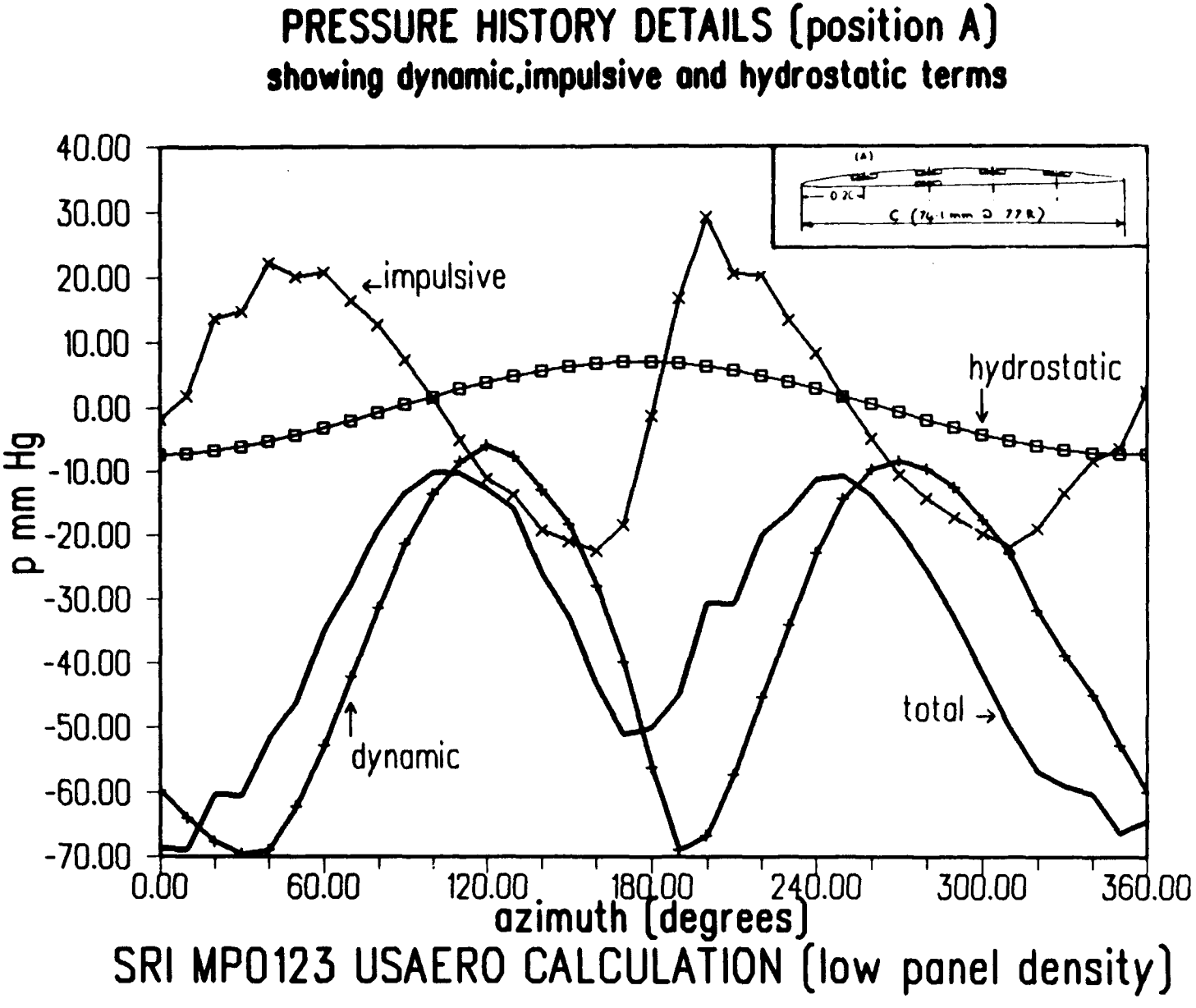

(a) Position A

Figure 6.33. Details of the Pressure History Terms.

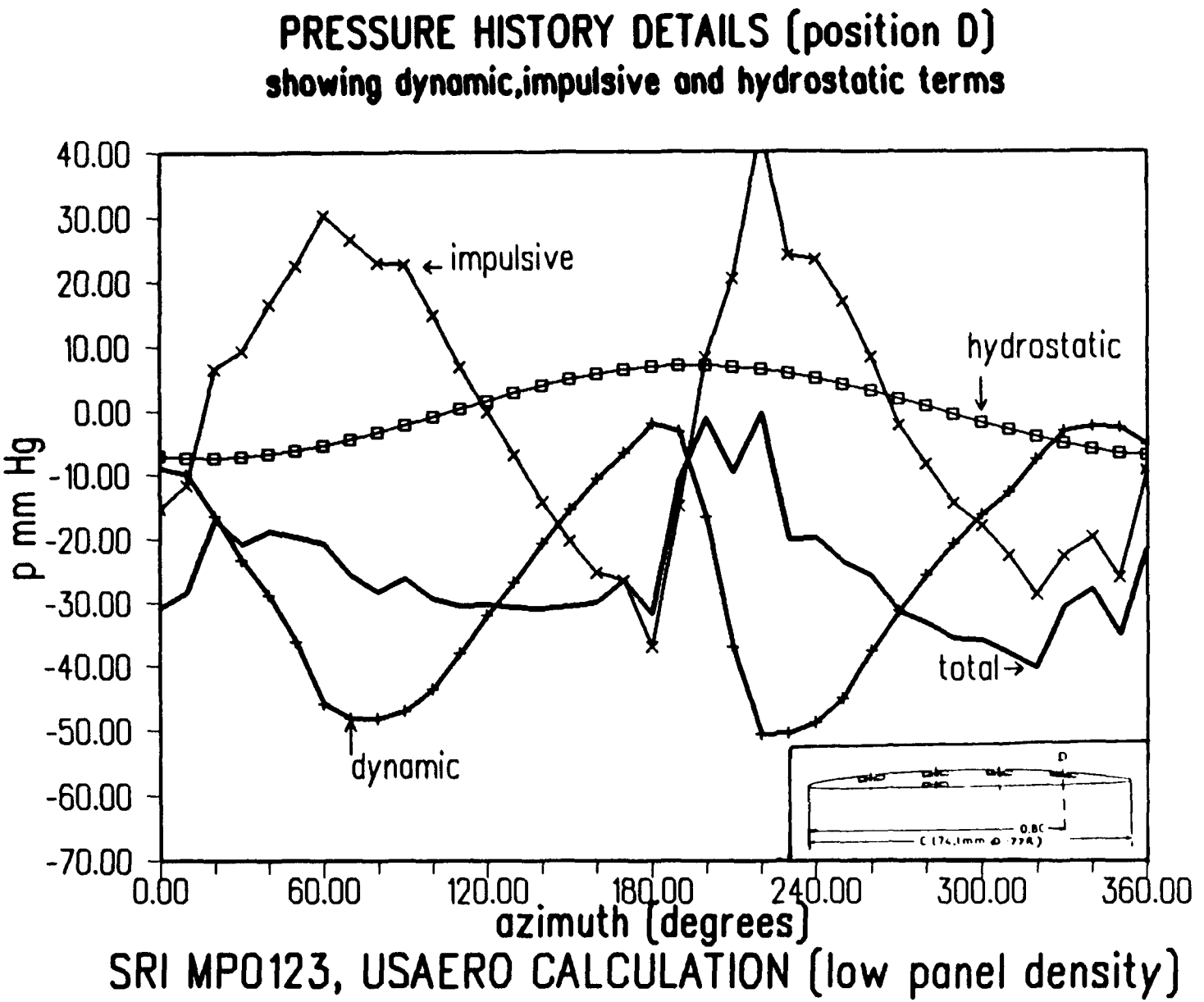

(b) Position D

Figure 6.33. Concluded.

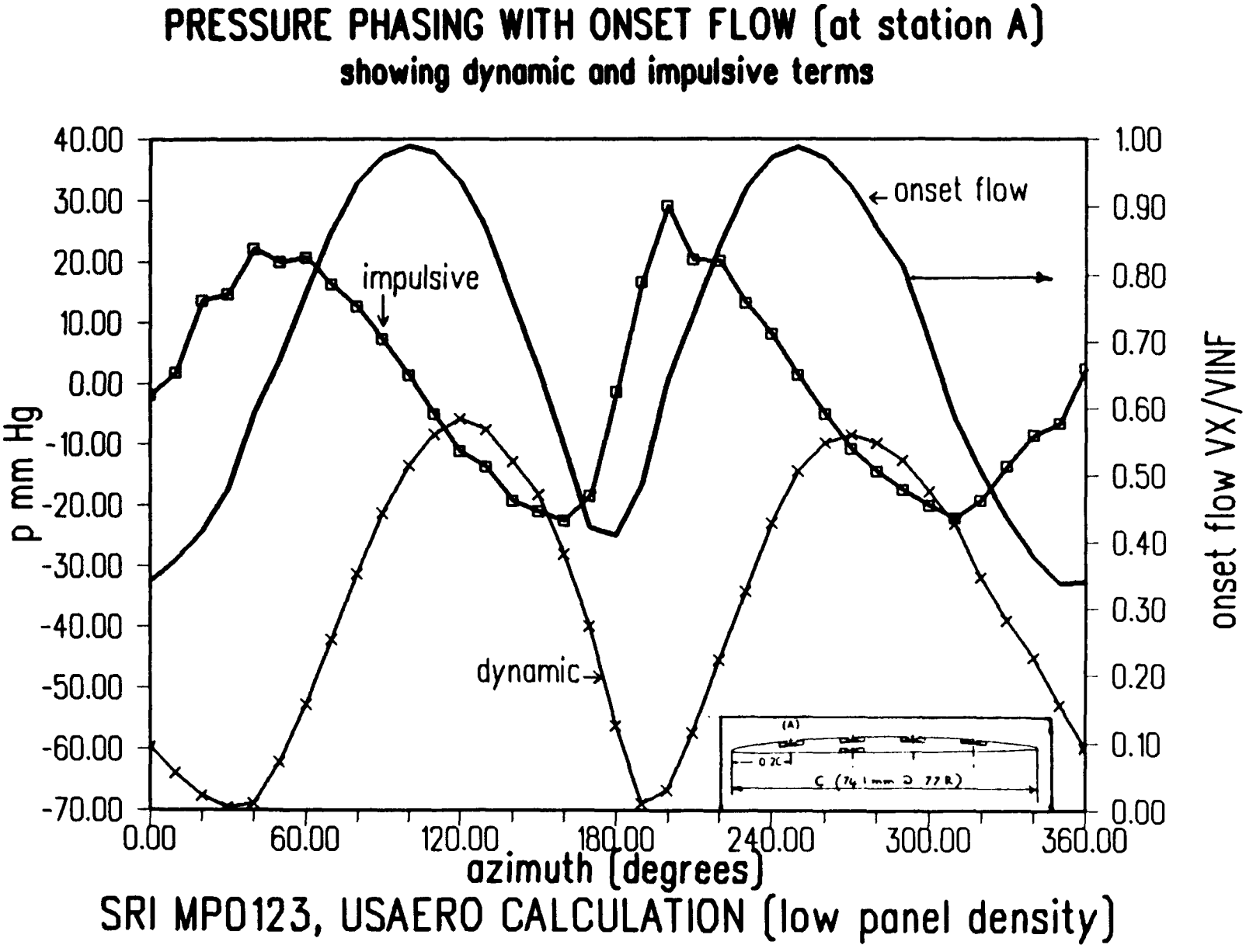

Figure 6.34. Computed Phasing of the Pressure Terms Relative to the Onset Flow Variation.

6.4 Simple Propeller-Hull Interaction

Figure 6.35 shows a four-bladed propulsor operating in the wake of a long hull. The hull geometry is similar to that described in Ref. 33 as Afterbody 1. The propeller geometry is derived from Ref. 41 with appropriate scaling to match the maximum hull diameter. The calculation of viscous flow on the hull for a Reynolds number of 4.56 million was accomplished with RANSTERN as described in section 4.2. The calculation of propeller flow with MPROP in the absence of the hull has been extensively correlated with experiment as discussed in Section 6.1. In this section the effect of hull wake flow on the propeller is considered.

Figure 6.36 shows the axial velocity distribution as a function of radius. "Full" velocity profile refers to the case where the propeller diameter is equal to the maximum hull diameter. "Partial" velocity profile refers to the case where the hull diameter is a fifth of the propeller diameter. The nonuniformity of the flow is limited to the hub region in the latter case with uniform flow over most of the propeller. The hull stern velocity profiles were calculated using RANSTERN as previously described. Pressure contours for two advanced coefficients (J = 0.4, and 0.5) were calculated with MPROP for prescribed nonuniformity. Figures 6.37(a) through (j) present spectrum plots of calculated pressures for a variety of cases ranging from uniform flow (no hull interaction) to full presence of hull wake. For uniformity the scale chosen for all pressure contours is -4.0 to 4.0. For this choice of pressure range, the contours on the "pressure" side of the propeller (Figures 6.37(b), (d), (f), (h) and (j)) do not show much variation. A comparison of Figure 6.37(a) with Figure 6.37(c) indicates the effect of hull wake on the calculated pressure distribution for the J = 0.4 case. A similar comparison of Figure 6.37(g) with 6.37(i) indicates the increased effect of hull wake on the propeller for higher advance coefficients. Figures 6.37(e) and (f) show a case with very slender hull, i.e., partial nonuniformity. The changes to the pressure levels as compared with the uniform flow case would be expected to be small for this case. This expectation is borne out in general. However, a particular feature of the effect of the reduced hull flow on the propeller in the region near the hub actually shows a higher circulation and greater suction pressure. This is due to the increased angle of attack of the flow relative to the local suction.

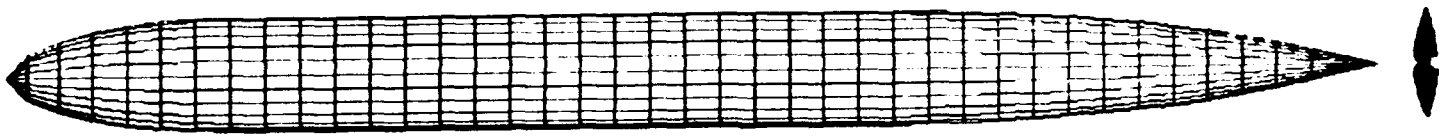

Figure 6.35. Propeller/Hull Arrangement for Propeller-Hull Interaction.

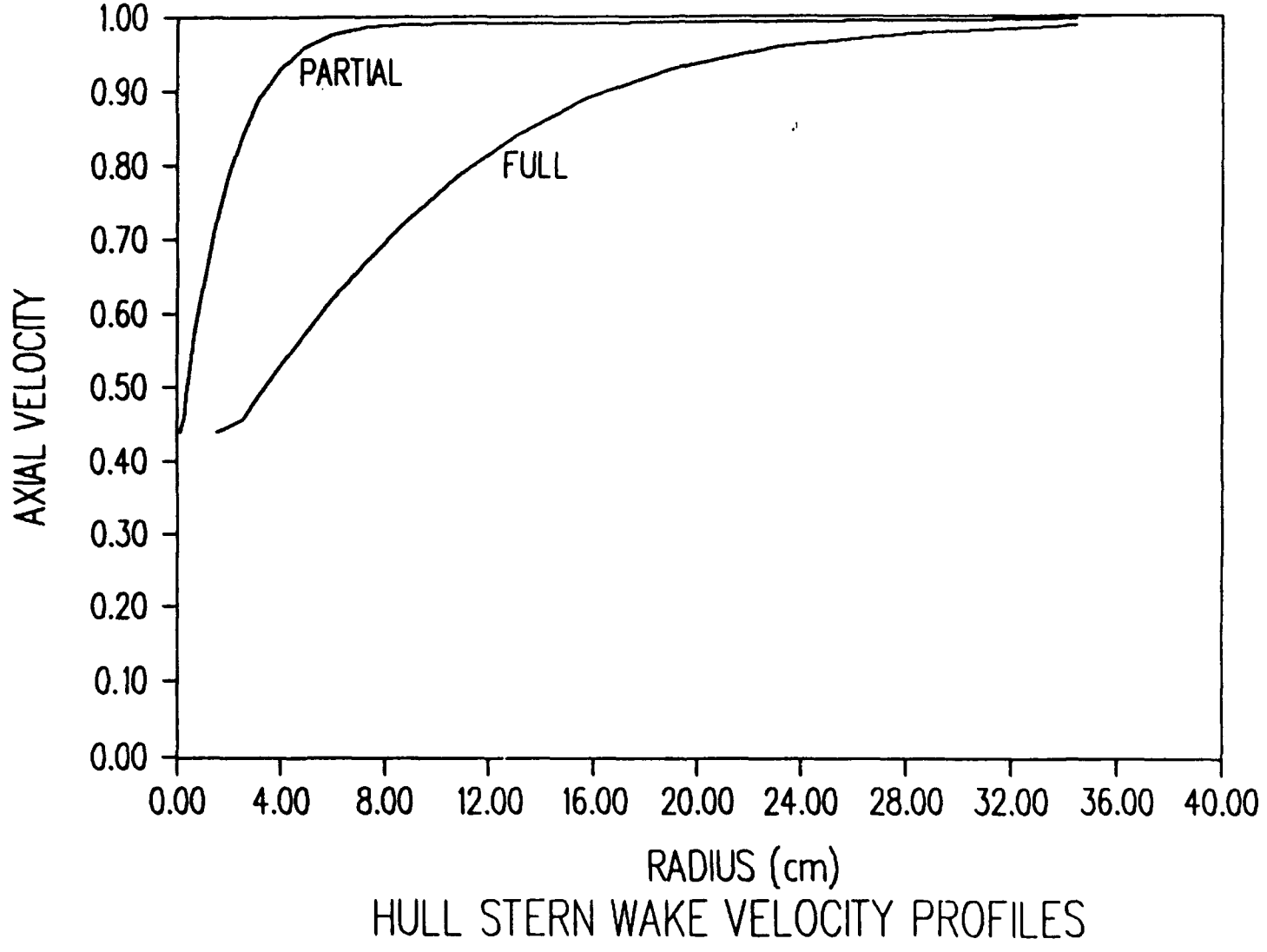

Figure 6.36. Axial Velocity Distribution in the Plane of the Propeller Calculated by RANSTERN; Re = 4.56 Million.

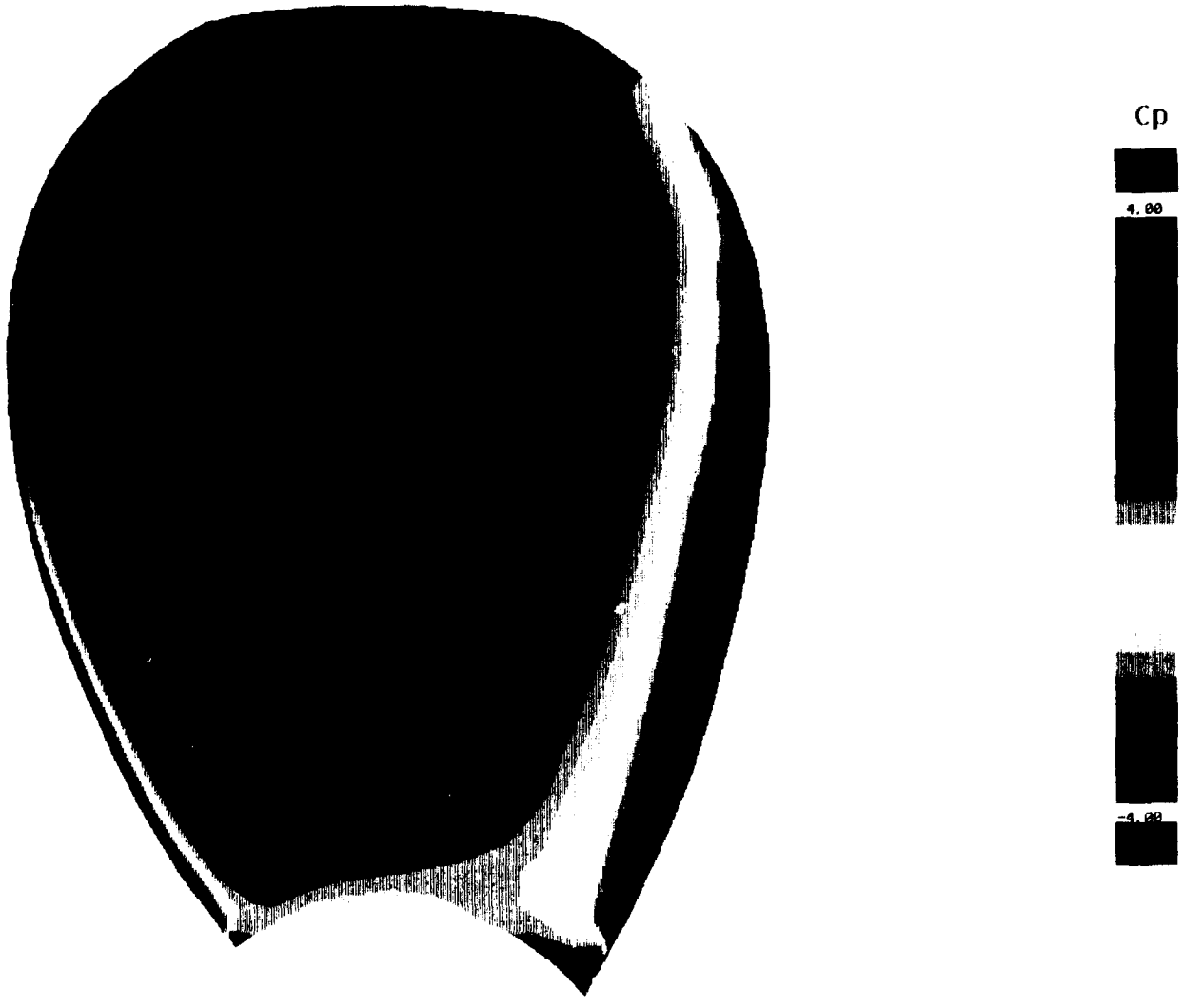

(a) No Hull; J = 0.4, Suction Side

Figure 6.37. Propeller Pressure Contours Calculated by MPROP to Highlight Viscous Hull Interactions.

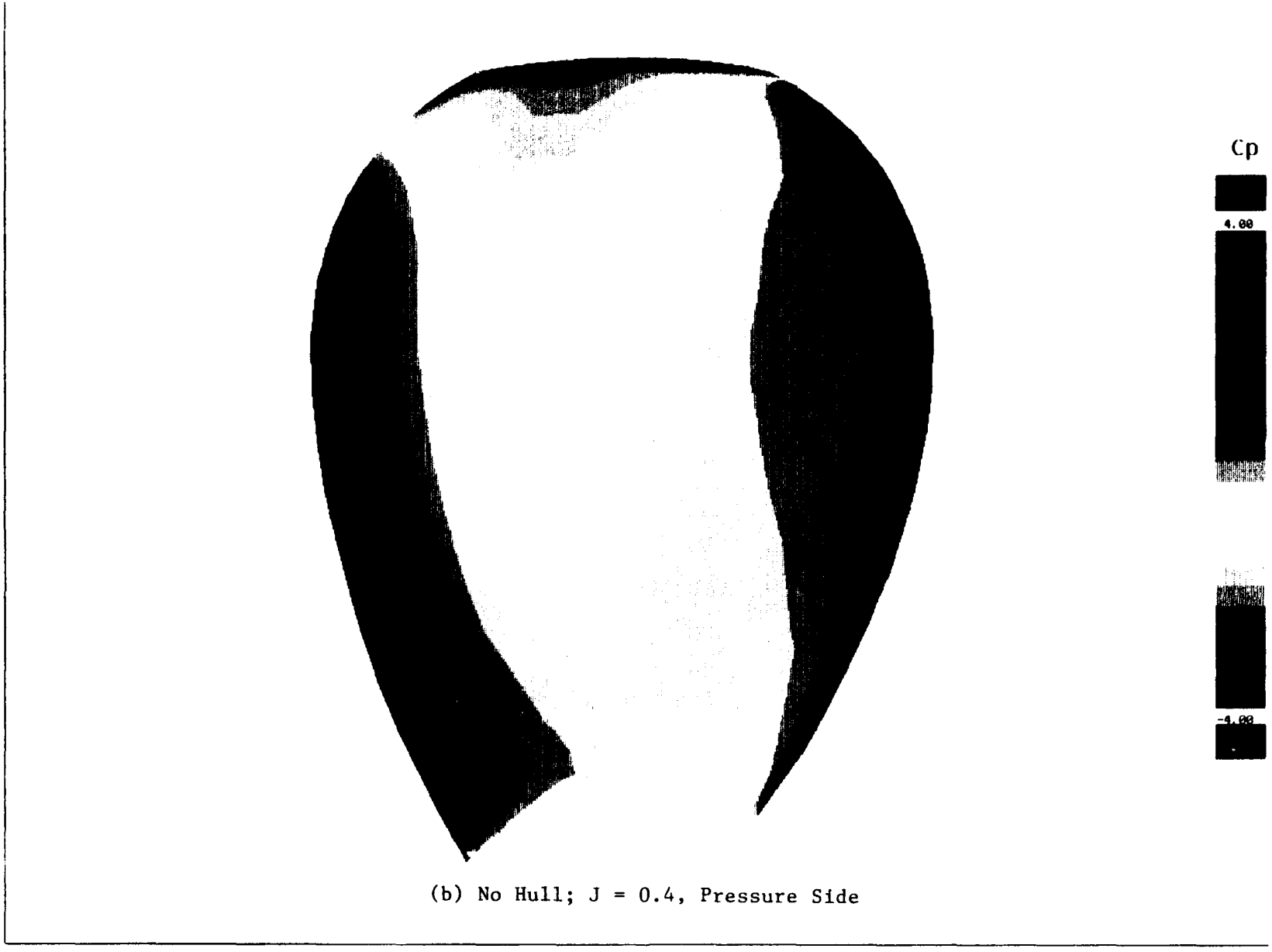

(b) No Hull; J = 0.4, Pressure Side

Figure 6.37. Continued.

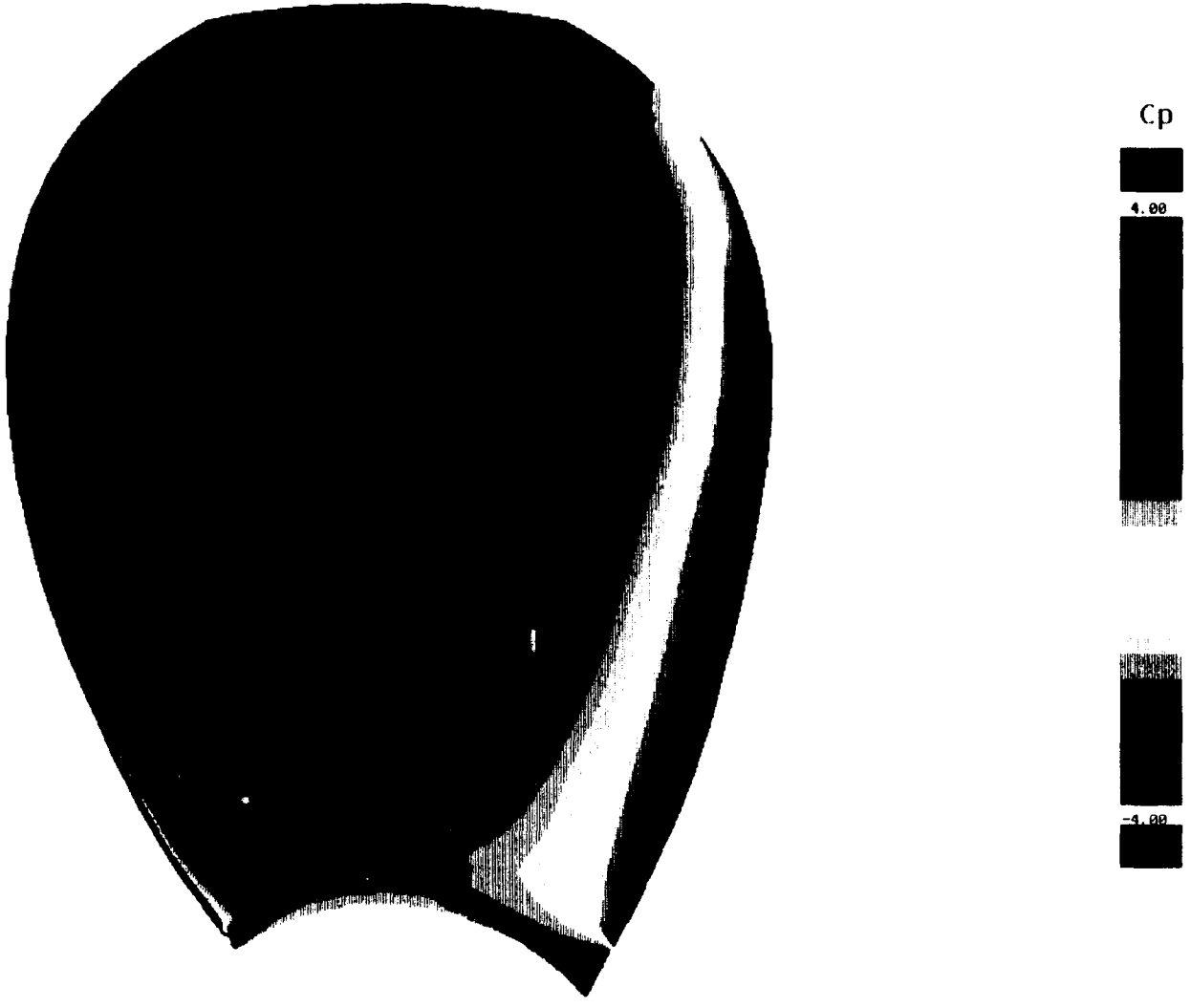

(c) Full Hull; J = 0.4, Suction Side

Figure 6.37. Continued.

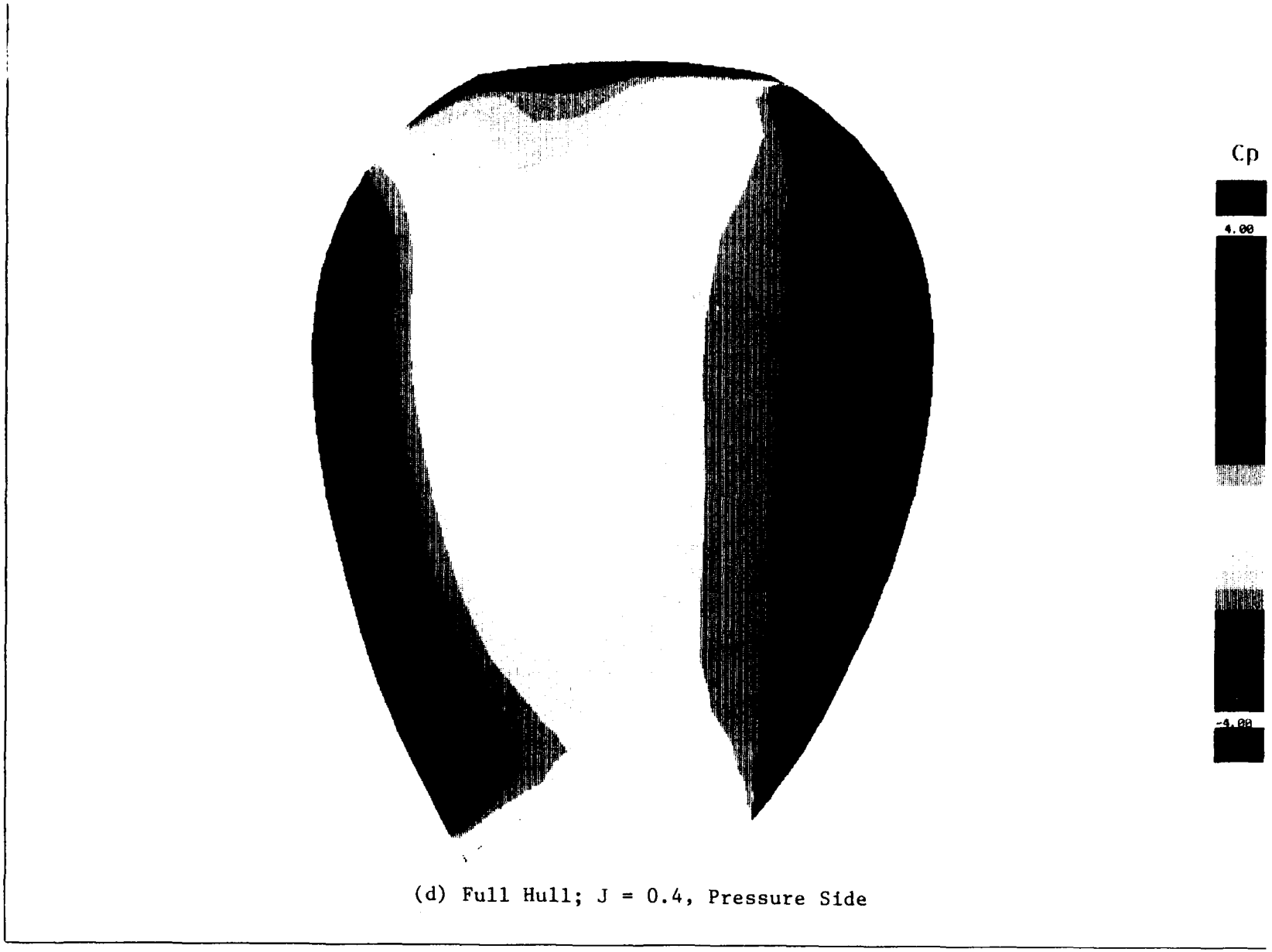

(d) Full Hull; J = 0.4, Pressure Side

Figure 6.37. Continued.

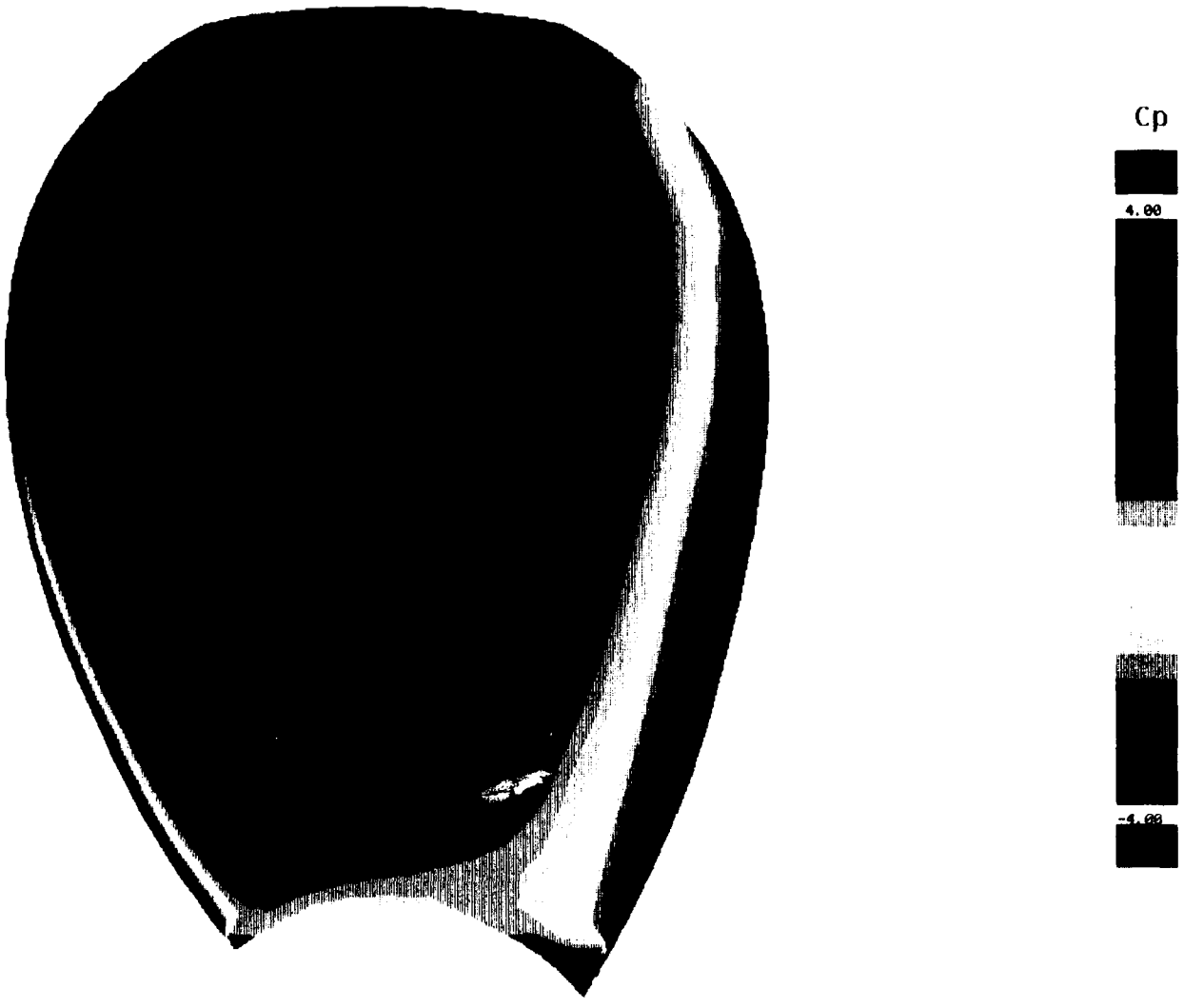

(e) Slender Hull; J = 0.4, Suction Side

Figure 6.37. Continued.

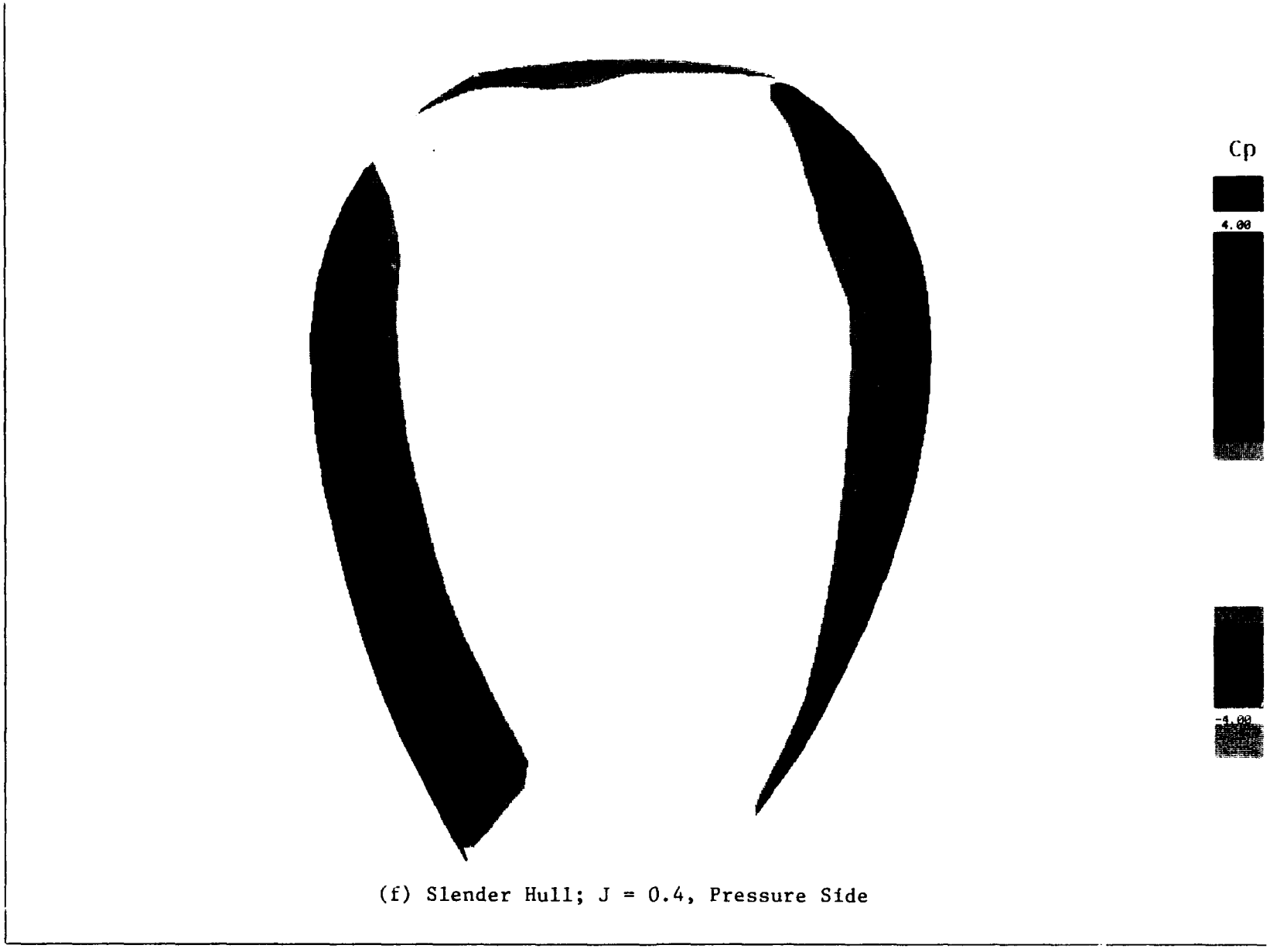

(f) Slender Hull; J = 0.4, Pressure Side

Figure 6.37. Continued.

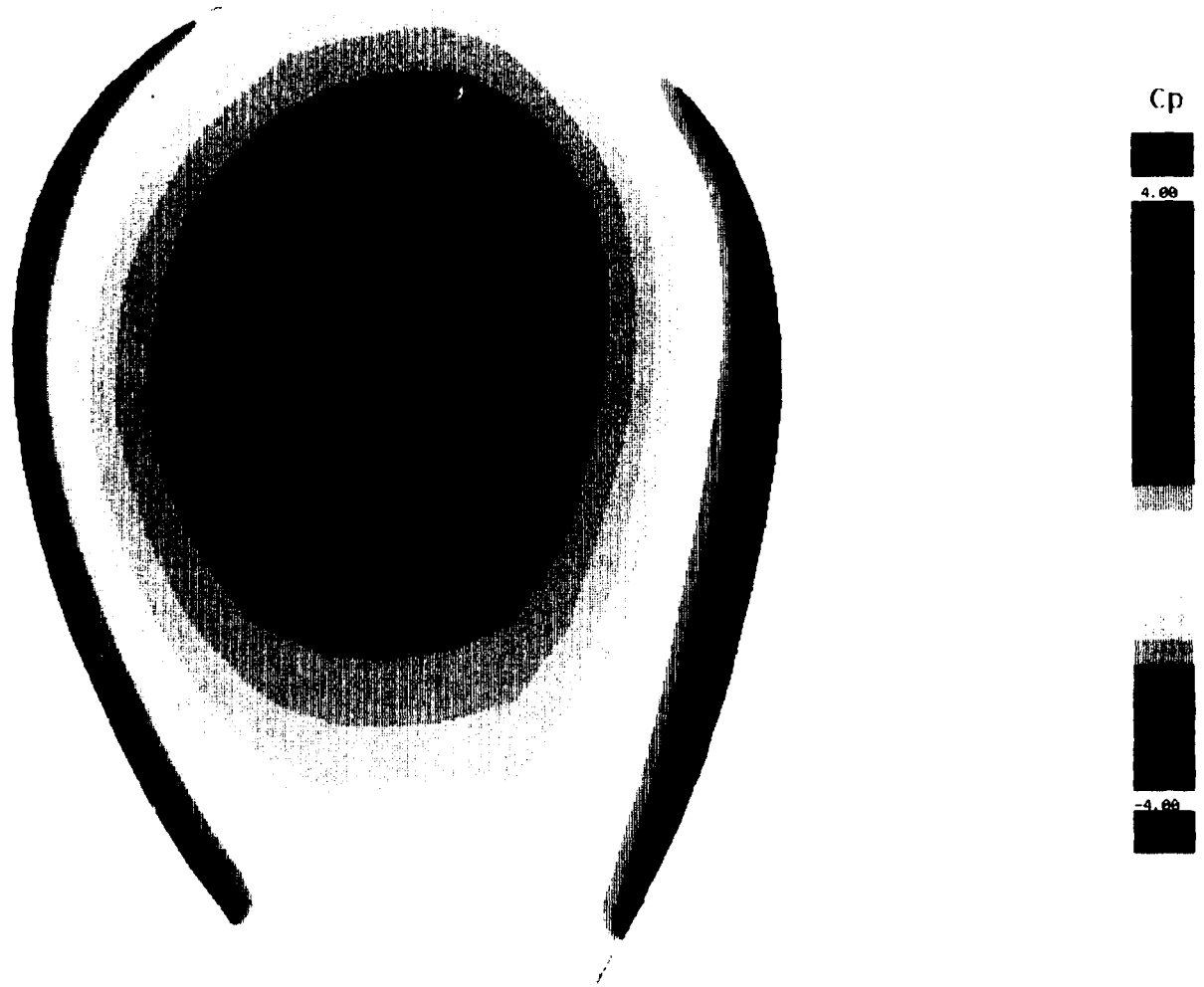

(g) No Hull; J = 0.6, Suction Side

Figure 6.37. Continued.

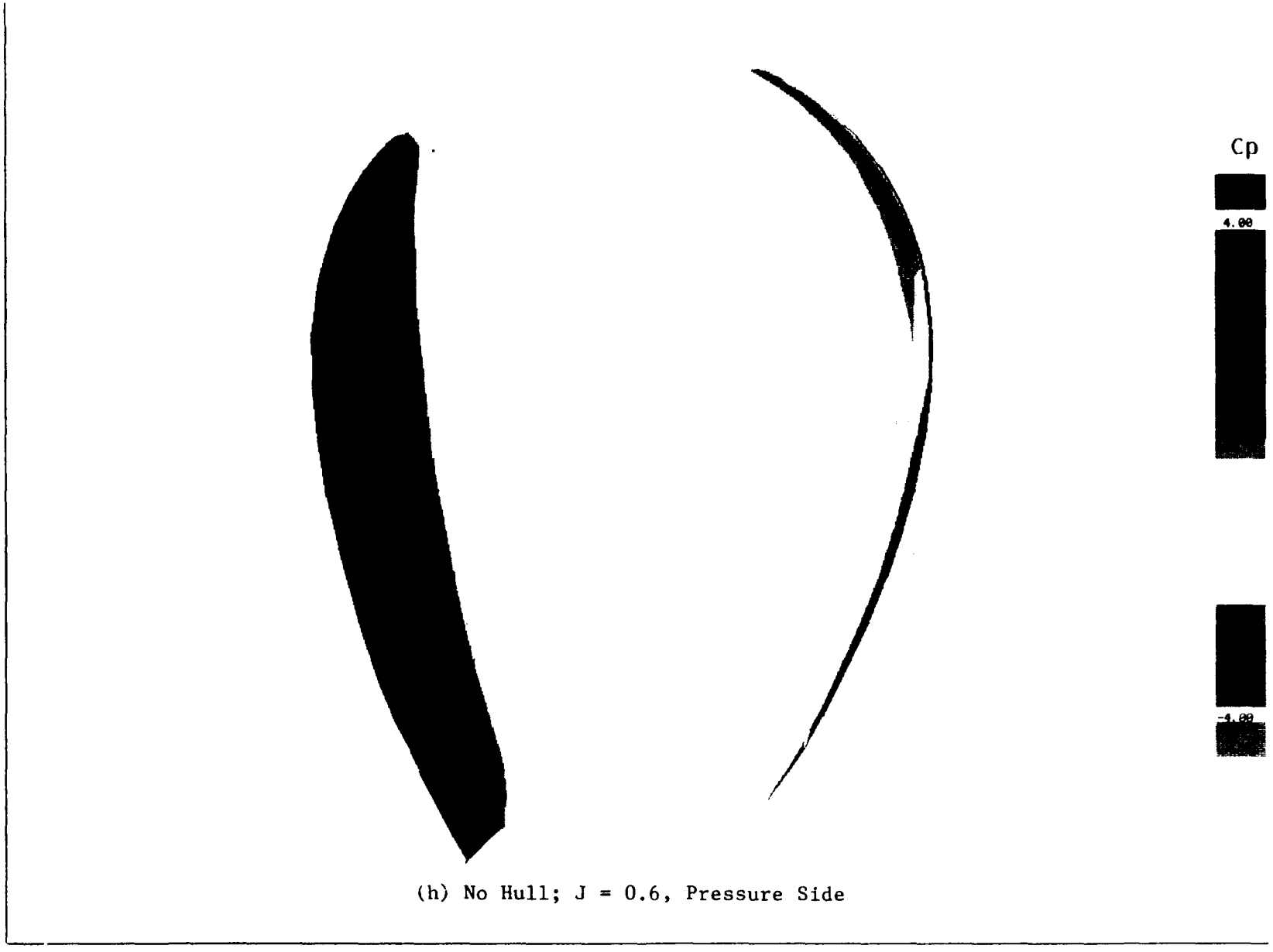

(h) No Hull; J = 0.6, Pressure Side

Figure 6.37. Continued.

(i) Full Hull; J = 0.6, Suction Side

Figure 6.37. Continued.

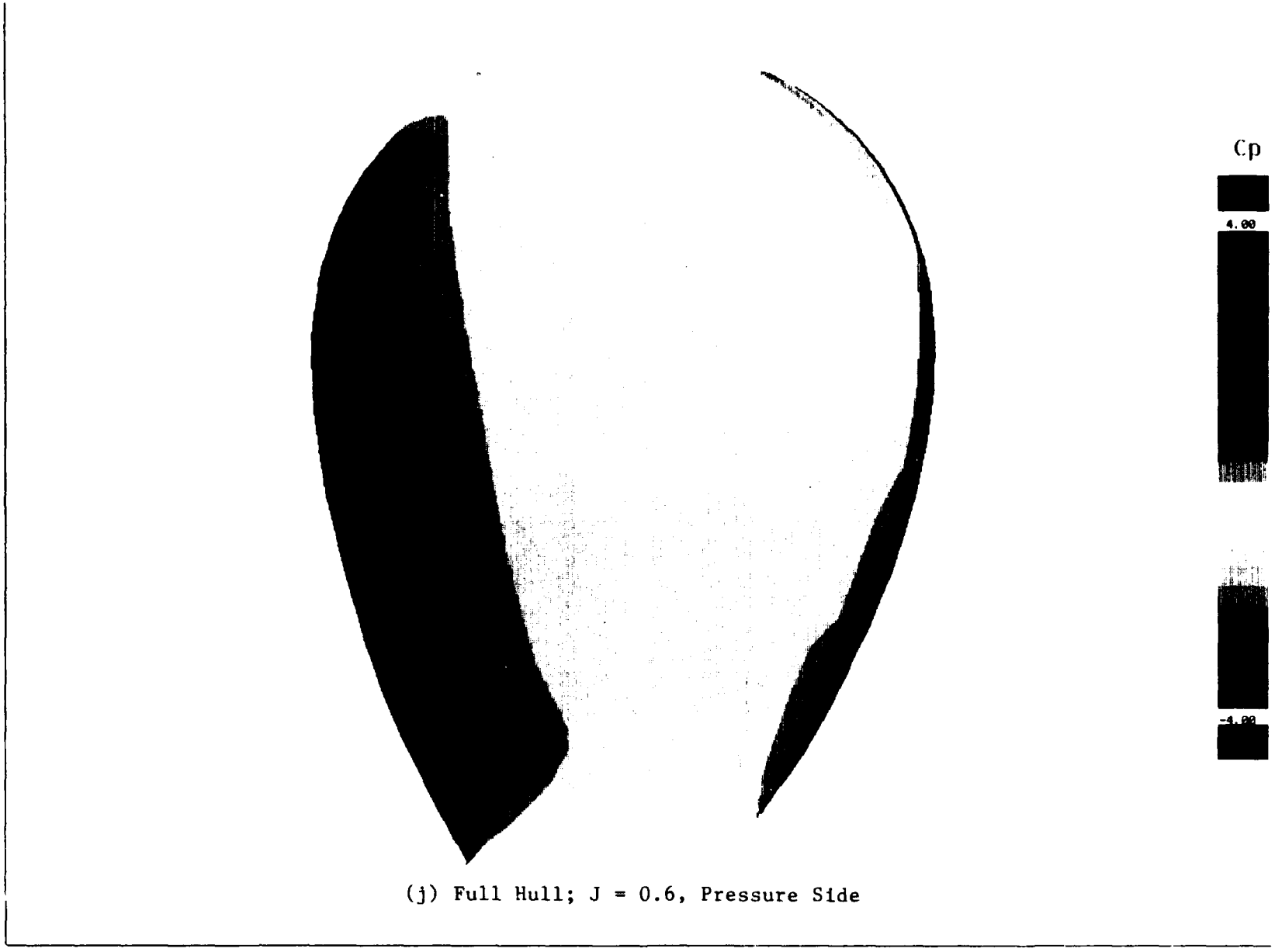

(j) Full Hull; J = 0.6, Pressure Side

Figure 6.37. Concluded.

7.0 CONCLUSIONS AND RECOMMENDATIONS

The complex problem of propeller/hull interaction has been examined in separate parts, i.e., (i) a propeller operating in a flow generated by a hull, and (ii) a hull operating in the effect of a propeller.

Details of velocity profiles in the hull-generated viscous flow approaching the propeller location were computed using the Reynolds-Averaged, Navier-Stokes program, RANSTERN.

The basic flow characteristics of a hull are treated adequately using VSAERO, a panel method with coupled boundary layer calculations. Example calculations of a propller operating in such a nonuniform flow were demonstrated for the axisymmetric case using the marine propeller version of VSAERO, MPROP, with plausible results. The code was also used to demonstrate the simple (axisymmetric) case of a hull operating in the presence of a propeller.

The MPROP program was also used to explore calculations of radially varying onset flows for a propeller/hub/shroud/stator configuration. Again, plausible results were obtained but comparisons with measurements are needed to complete the study.

The more general condition of a propeller operating in a nonaxisymmetric hull wake is more challenging because the propeller sees time-dependent conditions as it rotates in the arbitrary inflow distribution. Two approaches were applied to this problem, both with very encouraging results. The first approach used a frequency-band analysis of the azimuthal variation of the inflow and solved for doublet Fourier coefficients in the MPROP program. This very cost effective analysis gave results which compare very well with experimental measurements even though certain wake assumptions are needed in the model. A second, more time consuming, but still practical calculation was conducted with USAERO, a time-stepping panel method, which rotates a fully paneled propeller in finite steps through the nonuniform flow. The output from this is a detailed time history of velocities, pressures and integrated forces and moments. This approach also gave good agreement with experimental measurements; moreover, it provided a detailed breakdown of the pressure components, i.e., the dynamic, impulsive, and hydrostatic terms, plus their varying phase relationships for different positions across a blade chord. Unlike the frequency-band analysis, the time-stepping program requires no assumptions as to wake position or periodic strength variation since the wake is generated step by step according to local conditions.

7.1 Recommendations

(1) In view of its capability and cost effectiveness, the MPROP version of VSAERO should be developed further to improve its usability and applicability. Certain refinements in the wake model would improve its treatment of propellers at low advance coefficients. Also, the modeling of the periodic wake strength in the frequency band analysis of nonuniform flows could be improved. The basic program should also be updated to take advantage of more recent developments in the VSAERO program, especially in regard to the coupled boundary layer analysis. Overall, more comparisons with measured data are needed in order to establish its range of validity.

(2) A hybrid coupling between RANSTERN and VSAERO should be pursued with a view to providing a cost effective zonal approach to computing viscous velocity profiles in the propeller region.

(3) The USAERO program should be applied to more cases for comparison with measured data. In particular, boundary layer calculations should be included. The boundary layer routines, although coupled in an earlier version of USAERO, have been temporarily out of action during an extensive rewrite and restructuring of the basic code. These routines are about to be reactiveated.

The very general modeling capability of the program offers a potentially broad range of propeller/hull interaction problems that could be employed: for example,

(a) a propeller in general orientation/motion, e.g., in yaw, in surge, heave and sway, etc., simulating the effect of hull motions on the rotation propeller;

(b) a propeller with hub, shroud, and stators;

(c) complete propeller/hull configuration for simultaneous solution of the mutual interaction effects including periodic pressures on the hull surface; and

(d) a propeller operating near a free surface.

USAERO should also be used to study in more detail the complex phasing of the dynamic and impulsive pressure terms on a propeller operating in a nonuniform flow. The objective would be to improve the understanding of the influence of various blade parameters (skew, rake, twist, camber, etc.) on this phasing in order to reduce the resultant load oscillations for a given performance in blade design.

8.0 REFERENCES

1. Wilson, M.B., McCallum, D.N., Boswell, R.J., Bernhard, D.D. and Chase, A.B., "Causes and Corrections for Propeller-Excited Airborne Noise on a Naval Auxiliary Oiler", SNAME Transactions, Vol. 90, 1982, pp. 277-320.

2. Takahashi, H. and Ueda, T., "Cavitation on Fluctuating Pressures around a Marine Propeller", Paper No. 33 of the Ship Research Institute, Tokyo, March 1972.

3. Breslin, J.P., Van Houten, R.J., Kerwin, J.E. and Johnsson, C.A., "Theoretical and Experimental Propeller-Induced Hull Pressures Arising from Intermittent Blade Cavitation, Loading and Thickness", SNAME Transactions, Vol. 90, 1982, pp. 111-151.

4. Cox, B.D., Vorus, W.S., Breslin, J.P. and Rood, E.P., "Recent Theoretical and Experimental Developments in the Prediction of Propeller-Induced Vibration Forces on Nearby Boundaries", Proc. 12th Symposium on Naval Hydrodynamics, Office of Naval Research, Washington, D.C., June 1978.

5. Kaplan, P., Bentson, J. and Benatar, M., "Analytical Prediction of Pressures and Forces on a Ship Hull Due to Cavitating Propellers", paper presented at 14th Symposium on Naval Hydrodynamics, University of Michigan, Ann Arbor MI, August 1982.

6. Noordzij, L., "Pressure Field Induced by a Cavitating Propeller", International Shipbuilding Progress, Vol. 6, No. 260, 1976.

7. Huse, E., "Propeller-Induced Excitation Forces and Vibrations, Cavitation Noise and Erosion", Proc. International Symposium on Advances in Marine Technology, Vol. 1, Trondheim, Norway, 1979.

8. Tsakonas, W., Jacobs, W.R. and Ali, M.R., "An 'Exact' Linear Lifting-Surface Theory for a Marine Propeller in a Nonuniform Flow Field", J. Ship Research, Vol. 17, No. 4, 1973.

9. Kerwin, J.E. and Lee, C.S., "Prediction of Steady and Unsteady Marine Propeller Performance by Numerical Lifting-Surface Theory", SNAME Transactions, Vol. 86, 1968.

10. Vorus, W.S., "A Method for Analyzing the Propeller-Induced Vibratory Forces Acting on the Surface of a Ship Stern", Trans. Soc. Naval Arch. and Marine Engrs., Vol. 82, 1974.

11. Maskew, B., "Program VSAERO, A Computer Program for Calculating the Nonlinear Aerodynamic Characteristics of Arbitrary Configurations: Users' Manual", NASA CR-166476, November 1982.

12. Johnson, F.T. and Rubbert, P.E., "Advanced Panel-Type Influence Coefficient Methods Applied to Subsonic Flows", Proc AIAA 13th Aerospace Sciences Meeting, January 1975.

13. Vaidyanathan, T.S., Maskew, B. and Dvorak, F.A., "Application of Advanced Nonlinear Panel Methods to the Analysis of Marine Propellers", Analytical Methods Report 8404, Final Report, Contract N00014-83-C-0031, David Taylor Research Center, Bethesda MD, March 1984.

14. Vaidyanathan, T.S., "Potential Flow Calculation Methods and Computer Programs and Analysis and Computations of Viscid Tip Vortex Flows", Final Report, Contract N00167-85-C-0005, August 1988.

15. Lamb, H.Y., Hydrodynamics, 6th ed., Dover Publications, New York, 1945.

16. Min, K.S., "Numerical and Experimental Methods for the Prediction of Field Point Velocities around Propeller Blades", M.I.T. Department of Ocean Engineering Report 68-12, Cambridge MA, June 1978.

17. Curle, H., "A Two-Parameter Method for Calculating the Two-Dimensional Incompressible Laminar Boundary Layer", J.R. Aero Soc., Vol. 71, 1967.

18. Thwaites, B., "Approximate Calculation of the Laminar Boundary Layer", Aero Quart., Vol. I, 1949.

19. Rott, N., and Crabtree, L.F., "Simplified Laminar Boundary Layer Calculations for Bodies of Revolution and for Yawed Wings", J. Aero. Sci., 19, 553, 1952.

20. Granville, P.S., "The Calculation of the Viscous Drag of Bodies of Revolution", David Taylor Model Basin Report 849, 1953.

21. Schlichting, J. and Ulrich, A., "Zur Berechnung Des Unsellages Laminar-Turbulenten" (On the Calculation of Laminar-Turbulent Transition), Jahrbuch 1942 Der Deutschen LuftFahrt-Forschung.

22. Smith, A.M.O., "Transition Pressure Gradient and Stability Theory", Proc. 9th International Congress of Applied Mechanics, Brussels, Vol. 7, 1957.

23. Coles, D.E., "Measurements in the Boundary Layer on a Smooth Flat Plate in Supersonic Flow", Jet Propulsion Lab. Report No. 20-69, 1953.

24. Briley, W.R., "An Analysis of Laminar Separation--Bubble Flow Using the Navier-Stokes Equations", Proc. Fluid Dynamics of Unsteady, Three-Dimensional and Separated Flows, Georgia Tech., June 1971.

25. Gaster, M., "The Structure and Behavior of Laminar Separation Bubbles", ARC 28-226, 1967.

26. Kline, S.J., Morkovin, M.V., Sovran, G. and Cockrell, D.J., "Computation of Turbulent Boundary Layers", Proc. 1968 AFOSR-IFP Stanford Conference, Stanford University Press, Stanford CA, 1969.

27. Nash, J.F. and Hicks, J.G., "An Integral Method Including the Effect of Upstream History on the Turbulent Shear Stress", Proc. Computation of Turbulent Boundary Layers - 1968, Vol. 1, Standord University Dept. Mech. Engr., Stanford CA, 1968.

28. White, F.M.d, Viscous Fluid Flow, McGraw-Hill, New York, 1974.

29. Coles, D.E., "The Law of the Wake in the Turbulent Boundary Layer", J. Fluid Mech., Vol. 1, 1956.

30. Nash, J.F. and Macdonald, A.G.J., "A Calculation Method for the Incompressible Turbulent Boundary Layer Including the Effect of Upstream History on the Turbulent Shear Stress", N.P.L. Aero Report 1234, 1966.

31. McDonald, H. and Stoddart, J.A.P., "On the Development of the Incompressible Boundary Layer", British Aircraft Corp. (Preston) Aero Report AC 223, 1965.

32. Patel, V.C., Chen, H.C. and Ju, S., "Ship Stern and Wake Flows; Solutions of the Fully-Elliptic Reynolds-Averaged Navier-Stokes Equations and Comparisons with Experiments", IIHR Report No. 323, Contracts N00014-83-K-0136 and N00014-88-K-001, April 1988.

33. Huang, T.T., Wang, H.T., Santelli, N. and Groves, N.C., "Propeller/Stern/-Boundary Layer Interaction on Axisymmetric Bodies: Theory and Experiment", David Taylor Report 76-0113, December 1976.

34. Chen, H.C. and Patel, V.C., "Calculation of Stern Flow by a Time-Marching Solution of the Partially-Parabolic Equations", presented at 15th ONR Symposium, September 1984.

35. Pulliam, T.H. and Steger, J.L., "Implicit Finite Difference Simulations of Three-Dimensional Compressible Flow", AIAA J., Vol. 18, No. 2, February 1980.

36. Beam, R. and Warming, R.F., "An Implicit Finite-Difference Algorithm for Hyperbolic Systems in Conservation Law Form", J. Comp. Phys., Vol. 22, September 1976.

37. Maskew, B., "Influence of Rotor Blade Tip Shape on Tip Vortex Shedding--An Unsteady Inviscid Analysis", Paper 80-6 in Proc. 36th Annual AHS Forum, May 1980.

38. Clark, D.R. and Maskew, B., "Calculation of Unsteady Rotor Blade Loads and Blade/Fuselage Interference", paper presented at 2nd International Conference on Rotorcraft Basic Research, University of Maryland, College Park MD, February 1988.

39. Katz, J. and Maskew, B., "Unsteady Low-Speed Aerodynamic Model for Complete Aircraft Configurations", paper AIAA-86-2180CP, August 1986.

40. Takei, Y., Koyama, K. and Jurobe, Y., "Measurement of Pressures on a Blade of a Propeller Model", Papers of Ship Research Institute, No. 55, Tokyo, Japan, March 1979.

41. Vermissen, G.G.P. and van Gent, W., "Hydrodynamic Pressure Measurements on a Ship Model Propeller", presented at 14th Office of Naval Research Symposium, Ann Arbor MI, 1983.

42. Hoshino, private communication, 1981.